A thesis submitted for the fulfilment of the requirements for the academic degree of Doctor of Science at the University of Liège (College of Spatial Sciences)

Application of the WRF-GHG model for the interpretation of ground-based observations of atmospheric greenhouse gas concentrations

presented by

Sieglinde CALLEWAERT

Groupe Infra-Rouge de Physique Atmosphérique et Solaire (GIRPAS)
Department of Astrophysics, Geophysics and Oceanography
University of Liège
Liège, Belgium

Infrared observations
Sources and sinks of atmospheric constituents
Royal Belgian Institute for Space Aeronomy
Brussels, Belgium

Academic year 2024-2025

Thesis Jury

Emmanuel MAHIEU	ULiège	Promotor
Martine DE MAZIÈRE	BIRA-IASB	Co-promotor
Denis GRODENT	ULiège	Chairman
Bernard HEINESCH	ULiège	Secretary
Jochen LANDGRAF	SRON	
Jean-François MÜLLER	BIRA-IASB	

Contents

Acknowledgments

As I look back on my PhD journey, I want to thank all the people who helped me along the way.
First of all, I would like to express my intense gratitude to my co-promoter and supervisor at BIRA-IASB, Martine De Mazière. Her mentorship, extensive support, and invaluable feedback have been instrumental in shaping this research. It was Martine who set the course for this project and facilitated my visit to the Max Planck Institute for Biogeochemistry (MPI-GBC) in Jena, Germany back in 2018 to learn all about the WRF-GHG model. A visit that greatly sparked my interest in the subject. I am deeply grateful for our numerous scientific discussions and for the time she dedicated to me despite her many responsibilities. Her unwavering belief in my abilities has definitely helped me evolve into a better researcher.
I am equally thankful to my promoter at the University of Liège, Emmanuel Mahieu, whose encouraging attitude was a boost during challenging times and who was always available for questions. I also wish to acknowledge the other members of my thesis committee, Jean-François Müller and Bernard Heinesch, for their constructive feedback during our annual progress meetings. Special thanks go to Dominique Fonteyn, now enjoying his well-deserved retirement, for his wise words and guidance at the beginning of my PhD, a time filled with many questions.
On the international front, I am particularly grateful to my colleagues at MPI-GBC in Jena for their warm hospitality and willingness to share their expertise on WRF-GHG. I especially thank Julia Marshall (currently employed at the German Aerospace Center (DLR)), Michal Galkowski, and Amir Abdi, without them I would not have been able to understand the model as well as I do now. The online community later initiated by Michal has been an invaluable resource, fostering important technical discussions and creating a robust network for collaboration.
At BIRA-IASB, I have been fortunate to work alongside wonderful colleagues. I thank my office mates—Bart Dils, Sophie Vandenbussche, and Corinne Vigouroux—for creating a pleasant work environment, and by extension the entire infrared team: Bavo Langerock, Minqiang Zhou, Mahesh Kumar Sha, Filip Desmet, Nicolas Kumps, Charles Robert, Yvan Nollet, and Jonas Debosscher. Their expertise and feedback have been instrumental to my research. Huge thanks as well to Vincent Letocart and the rest of the IT team for supporting me in running the model on the High Performance Cluster of the Space Pole and managing the large amount of data on the BIRA-IASB servers.
Ofcourse, there is more in life than work, and I am grateful to my colleagues and fellow doctoral students at BIRA-IASB for making this experience memorable. To Ermioni Dimitropoulou, Daniele Minganti, Miriam Cisneros, Cedric Busschots, Sarah Vervalcke,

Maria Luisa Alonso Tagle, Oindrila Nath, Catalina Poraicu, Gytha Mettepenningen, Zachary Flimon, Arno Keppens, Tijl Verhoelst, Steven Compernolle, and many others—thank you for the refreshing lunch breaks and after-work activities that make BIRA-IASB such an enjoyable workplace.
Even though I rarely visited the university, I would like to thank Irene Pardo Cantos for feeling me welcome on those days that I did, such as the annual PhD days.
To my long-time friends—Gaëlle, Lisa, Justine and Laura—thank you for providing moments of leisure and opportunities to unwind. Similarly to my sister Sarah and my parents, who always had my back, even though I rarely ventured beyond "something with atmospheric science" when describing my work. Special thanks to my brother Pieter, whose genuine interest in my work and his own adventures in Norway have been a source of inspiration.
And last but not least, I want to thank my partner Andries. Thank you for your love, support, and for being an amazing father to Merel. Your efforts to understand my research, our shared adventures through travel and concerts, and your companionship during the isolating periods of the COVID pandemic have made this journey not just manageable, but enjoyable. Thank you all for being there on this journey with me.

Summary

Atmospheric transport models are essential tools for understanding and predicting greenhouse gas (GHG) concentrations throughout the atmosphere across different regions - a crucial requirement for effective climate change mitigation. However, these models need thorough evaluation to ensure their reliability and identify areas for improvement. This thesis addresses this need through a comprehensive study at two contrasting locations where the Belgian Institute for Space Aeronomy (BIRA-IASB) maintains long-term measurement programs in collaboration with local partners: the remote tropical island of Réunion in the Indian Ocean and the urbanized county of Xianghe near Beijing, China. Both measurement sites are part of international observing networks dedicated to long-term GHG monitoring. By examining the observed and simulated GHG concentrations at these sites, we pursue two interconnected goals: evaluating the capabilities of atmospheric transport models in these understudied regions, and advancing our understanding of how human activities, natural processes, and weather patterns influence local GHG concentrations at these sites.

Our research employs the WRF-GHG atmospheric transport model to simulate concentrations of carbon dioxide (CO_2), methane (CH_4), and carbon monoxide (CO). We analyze a comprehensive dataset combining two measurement techniques: ground-based in situ measurements that capture detailed near-surface concentrations, and remote sensing observations that provide information across the entire atmospheric column. This dual approach, coupled with high-resolution modeling, enables us to both validate model performance and examine GHG behavior from multiple perspectives.

The results reveal distinct patterns at each location. At Réunion Island, where local emission sources are minimal, column measurements reflect broader regional patterns, particularly capturing the impact of seasonal biomass burning from African and South American continents between August and December. In situ concentrations show a modest influence of local sources, and significant diurnal variation primarily driven by local wind patterns. In contrast, Xianghe exhibits higher concentrations and greater variability due to a huge variety of emission sources in the region. Our analysis attributes CH_4 concentrations at Xianghe primarily to agricultural activities, residential heating, fossil fuel extraction, and waste management, while CO_2 variations are largely driven by industrial activities, energy production, and biosphere interactions. Further, wind direction plays a crucial role at Xianghe: southwesterly winds transport polluted air from the heavily urbanized North China Plain to the site, while northerly winds bring cleaner air from remote regions such as Inner Mongolia. The study also reveals that column measurements are more sensitive to distant sources, as illustrated

by the significant contribution of energy emissions, likely from the Shanxi coal region, to Xianghe's CH_4 column concentrations.

The WRF-GHG model successfully reproduces many observed patterns, for both in situ and column measurements. Among the strengths of the model is the integration of VPRM (the Vegetation Photosynthesis and Respiration Model), which allows for a detailed and realistic simulation of biogenic CO_2 fluxes, a crucial component for simulating CO_2 concentrations. However, our evaluation identified several challenges: difficulty in representing local wind patterns on Réunion Island due to complex topography, seasonal deviations in CH_4 simulations linked to inaccurate boundary conditions and emission inventories, and uncertainties in biogenic flux calculations due to VPRM input data quality.

This research contributes to both atmospheric modeling and GHG monitoring communities by providing a detailed model evaluation in contrasting environments while advancing our understanding of regional GHG dynamics. Our findings demonstrate the capabilities and limitations of current modeling approaches, while identifying specific areas for improvement. These insights are valuable for enhancing emission inventories, refining atmospheric transport models, and ultimately supporting more effective climate change mitigation strategies.

Résumé

Les modèles de transport atmosphérique sont des outils essentiels pour comprendre et prédire les concentrations de gaz à effet de serre (GES) dans différentes régions et contribuer significativement à la lutte contre le changement climatique. Cependant, ces modèles doivent être évalués en profondeur pour garantir leur fiabilité et identifier les domaines à améliorer. Cette thèse répond à ce besoin par une étude approfondie de deux sites contrastés où l'Institut royal d'Aéronomie Spatiale de Belgique (IASB) maintient des programmes de mesure à long terme en collaboration avec des partenaires locaux: l'île tropicale isolée de La Réunion dans l'océan Indien et la zone urbanisée de Xianghe près de Pékin, en Chine. Les deux sites de mesure font partie de réseaux d'observation internationaux dédiés à la surveillance à long terme des GES. En examinant les concentrations de GES observées et simulées à ces sites, nous poursuivons deux objectifs interconnectés: évaluer les capacités de notre modèle de transport atmosphérique pour ces régions peu étudiées tout en faisant progresser notre compréhension de l'influence des activités humaines, des processus naturels et des conditions météorologiques sur les concentrations locales de GES pour deux situations distinctes.

Notre recherche utilise le modèle de transport atmosphérique WRF-GHG pour simuler les concentrations de dioxyde de carbone (CO_2), de méthane (CH_4) et de monoxyde de carbone (CO). Nous analysons un ensemble de données complet combinant deux techniques de mesure: des mesures in situ au sol qui capturent des concentrations détaillées près de la surface et des observations par télédétection qui fournissent des informations sur l'ensemble de la colonne atmosphérique. Cette double approche, associée à une modélisation à haute résolution, nous permet à la fois de valider les performances du modèle et d'examiner le comportement des GES sous plusieurs angles.

Notre étude révèle des situations distinctes. À La Réunion, où les sources d'émission locales sont minimes, les mesures de la colonne reflètent des distributions régionales plus homogènes, capturant notamment l'impact de la combustion saisonnière de la biomasse des continents africain et sud-américain entre août et décembre. Les concentrations in situ montrent une influence modeste des sources locales et une variation diurne significative principalement due aux régimes éoliens locaux. En revanche, Xianghe présente des concentrations plus élevées et une plus grande variabilité en raison d'une grande variété de sources d'émissions dans la région. Notre analyse permet d'attribuer les concentrations de CH_4 à Xianghe principalement aux activités agricoles, au chauffage résidentiel, à l'extraction de combustibles fossiles et à la gestion des déchets, tandis que les variations de CO_2 sont largement dues aux activités industrielles, à la production d'énergie et aux interactions avec la biosphère. De plus, la direction

du vent joue un rôle crucial à Xianghe: les vents du sud-ouest transportent l'air pollué de la grande plaine de Chine du Nord fortement urbanisée vers le site, tandis que les vents du nord apportent de l'air plus propre des régions éloignées comme la Mongolie-Intérieure. L'étude révèle également que les mesures de colonne sont plus sensibles aux sources éloignées, comme l'illustre la contribution significative des émissions d'énergie, probablement de la région charbonnière du Shanxi, aux concentrations de colonne de CH_4 de Xianghe.

Le modèle WRF-GHG reproduit avec succès de nombreux situations ou configurations observées à la fois pour les mesures in situ et en colonne. Parmi les points forts du modèle, on trouve l'intégration du VPRM (Vegetation Photosynthesis and Respiration Model), qui permet une simulation détaillée et réaliste des flux biogéniques de CO_2, un élément crucial pour simuler les concentrations de ce GES. Cependant, notre évaluation a identifié plusieurs défis: la difficulté de représenter les motifs de vent locaux à La Réunion en raison de la topographie complexe, des écarts saisonniers dans les simulations de CH_4 liés à des conditions limites et des inventaires d'émissions inexacts, et des incertitudes dans les calculs de flux biogéniques en raison de la qualité des données d'entrée du VPRM.

Cette recherche contribue à la fois aux communautés de modélisation atmosphérique et de surveillance des GES en fournissant une évaluation détaillée du modèle dans des environnements contrastés tout en faisant progresser notre compréhension de la dynamique régionale des GES. Nos résultats démontrent les capacités et les limites des approches de modélisation actuelles, tout en identifiant des domaines spécifiques à améliorer. Ces informations sont précieuses pour améliorer les inventaires d'émissions, affiner les modèles de transport atmosphérique et, en fin de compte, soutenir des stratégies d'atténuation du changement climatique plus efficaces.

Samenvatting

De concentratie van broeikasgassen in de atmosfeer, zoals koolstofdioxide (CO_2) en methaan (CH_4), maar ook van het indirecte broeikasgas koolstofmonoxide (CO), varieert sterk per locatie. Deze variatie ontstaat door een complexe wisselwerking van verschillende factoren: zodra deze gassen worden uitgestoten - door zowel menselijke als natuurlijke bronnen - worden ze door de wind verspreid in de atmosfeer. Door de grote verscheidenheid aan bronnen en weersomstandigheden kunnen de concentraties sterk verschillen, niet alleen per locatie maar ook van dag tot dag.
Het begrijpen van deze fluctuaties is essentieel, broeikasgassen spelen namelijk een cruciale rol in ons klimaatsysteem via het broeikaseffect. Ze houden warmte vast in de atmosfeer en dragen zo bij aan de opwarming van de aarde, hetgeen verstrekkende gevolgen heeft voor zowel de menselijke beschaving als natuurlijke ecosystemen. Aangezien de concentraties van deze gassen door menselijke activiteiten met ongekende snelheid blijven toenemen, is het voor de klimaatwetenschap en beleidsvorming cruciaal om meer inzicht te krijgen in hun geografische verspreiding en temporele variatie.
Wetenschappers maken gebruik van onder andere atmosferische transportmodellen om deze verspreiding te bestuderen. Deze computermodellen simuleren parameters zoals wind en temperatuur doorheen ruimte en tijd, gelijkaardig aan weermodellen. Daarnaast bevatten ze ook informatie over verschillende uitstootbronnen en berekenen ze de resulterende concentraties in de atmosfeer. Om de nauwkeurigheid en betrouwbaarheid van deze modellen te garanderen in verschillende situaties, is het essentieel om ze te evalueren aan de hand van observatiegegevens. Deze evaluaties helpen onder andere ontwikkelaars bij het identificeren van verbeterpunten.

Dit onderzoek richt zich op twee specifieke locaties waar BIRA-IASB (het Belgisch instituut voor ruimte-aeronomie) betrokken is bij lokale metingen: het Franse eiland Réunion, een afgelegen tropische locatie in de Indische Oceaan, en Xianghe, een verstedelijkt gebied nabij Peking in noordoost China. Het onderzoek in deze thesis heeft zowel als doel om meer inzicht te krijgen in de processen die de concentratieschommelingen op deze locaties beïnvloeden, als om het atmosferische transportmodel te evalueren op deze nog niet uitvoerig bestudeerde locaties.
Zowel de meetprogrammas's op Réunion als Xianghe maken deel uit van internationale observatienetwerken voor langetermijnwaarnemingen van broeikasgassen, en registreren concentraties aan de hand van twee verschillende meettechnieken: in situ metingen die gedetailleerde informatie geven over concentraties nabij het meetinstrument, en teledetectie-metingen die informatie verzamelen over de hele atmosferische kolom, van grondniveau tot de top van de

atmosfeer.
Voor dit onderzoek simuleren we minimaal één jaar aan metingen met het wereldwijd gebruikte WRF-Chem model (Weather Research and Forecasting model coupled with chemistry). We gebruiken specifiek de WRF-GHG optie, die ontwikkeld is voor het simuleren van regionaal transport van CO_2, CH_4 en CO, zonder de complexiteit van atmosferische chemische reacties die van minder belang zijn voor deze gassen. Door de concentraties van beide meettechnieken te combineren met simulaties van hoge resolutie, kunnen we een uitgebreide analyse maken van het gedrag van broeikasgassen op deze locaties.

De resultaten tonen duidelijke verschillen tussen beide locaties. Op Réunion zijn, door de afgelegen ligging en minimale lokale bronnen, de kolomconcentraties representatief voor de hele regio. Het belangrijkste signaal in de kolommetingen op Réunion is te wijten aan het jaarlijks terugkerende fenomeen van het verbranden van biomassa op de Afrikaanse, of zelfs Zuid-Amerikaanse continenten (voornamelijk voor landbouwdoeleinden) tussen augustus en december. Deze praktijk stoot enorm veel broeikasgassen uit en is zichtbaar in de kolommetingen op Réunion. Voor de in situ metingen hebben de lokale bronnen een bescheiden invloed, en worden daarnaast sterk beïnvloed door lokale windpatronen die aanzienlijke schommelingen in concentraties doorheen de dag kunnen teweeg brengen.
In Xianghe zorgt een enorme verscheidenheid aan bronnen voor hogere concentraties en meer variatie. De modelsimulaties laten onder andere toe om een verdeling te maken van de verschillende emissie sectoren die bijdragen tot de totale concentratie. Zo blijkt bijvoorbeeld dat de CH_4 concentraties in Xianghe voornamelijk afkomstig zijn van landbouwactiviteiten, verwarming van gebouwen, fossiele brandstofwinning en afvalbeheer, terwijl industriële processen, electriciteitsproductie en interactie met de biosfeer de belangrijkste componenten zijn voor CO_2. Verder toont onze analyse aan dat de kolommetingen gevoeliger zijn voor bronnen op grotere afstand dan in situ waarnemingen, vergelijkbaar als op Réunion. Wij vonden bijvoorbeeld dat de energiesector een groter aandeel heeft in de totale CH_4 kolomconcentraties, vergeleken met deze dicht bij het oppervlak (in situ), omdat de meeste uitstoot in deze sector gebeurt op grotere afstand van de meetinstrumenten, namelijk in het intensieve steenkoolgebied van Shanxi. Ook heeft de windrichting een grote invloed: zuidwestelijke wind brengt vervuilde lucht uit het sterk verstedelijkte Chinese Laagland naar Xianghe, terwijl noordelijke wind schonere lucht aanvoert uit afgelegen gebieden zoals Binnen-Mongolië.

Het WRF-GHG model bleek over het algemeen accuraat in het reproduceren van de gemeten concentraties en hun schommelingen, zowel in situ als over de hele atmosferische kolom. Eén van de sterke punten van het model is onder andere de integratie van VPRM (het Vegetation Photosynthesis and Respiration Model), dat een gedetailleerde en realistische simulatie van biogene CO_2 fluxen mogelijk maakt, een cruciaal onderdeel voor het reproduceren van CO_2 concentraties. Er kwamen echter ook uitdagingen naar voren. Op het eiland Réunion had het model bijvoorbeeld moeite om de lokale windpatronen nauwkeurig weer te geven, wat leidde tot afwijkingen in de nachtelijke CO_2 concentraties dichtbij het oppervlak. Dit is waarschijnlijk te wijten aan de grote hoogteverschillen op het kleine eiland, die ondanks de hoge resolutie niet nauwkeurig genoeg gerepresenteerd zijn in het model. Verder vertoonde het model een eerder zwakke correlatie met de verschillende CH_4 waarnemingen op beide lo-

caties. Dit kon telkens gelinkt worden aan een seizoensafwijking in de randvoorwaarden van de modelsimulaties afkomstig van externe globale datasets. Voor Xianghe kwamen daar extra afwijkingen bij door onjuiste seizoensvariaties in CH_4 emissiebronnen. Anderzijds komen de grootste onzekerheden voor CO_2 voort uit de parameters en input gegevens van VPRM, die van invloed zijn op de nauwkeurigheid van simulaties van biogene fluxen. Dit demonstreert dat de nauwkeurigheid van modelsimulaties sterk samenhangt met de kwaliteit van de input gegevens.

Het onderzoek in deze thesis toont aan dat WRF-GHG de belangrijkste aspecten van broeikasgasdynamiek kan simuleren in verschillende omgevingen. Het model biedt waardevolle inzichten in de waargenomen variabiliteit op beide bestudeerde locaties. Daarnaast werden verschillende aandachtspunten voor toekomstige modelontwikkeling geïdentificeerd: onder andere de verfijning van CH_4 emissie-inventarissen en randvoorwaarden, verbetering van VPRM input gegevens voor CO_2 simulaties, en een betere weergave van lokale windpatronen. Het aanpakken van deze uitdagingen zal het model verder optimaliseren, waardoor het op andere locaties toegepast kan worden om broeikasgasvariabiliteit te onderzoeken. Dit zal uiteindelijk bijdragen aan een beter begrip van de koolstofcyclus en ondersteunt bredere inspanningen om de impact van klimaatverandering te beperken.

Chapter 1

Research context

1.1 The significance of greenhouse gases

Greenhouse gases (GHGs) play a vital role in the Earth's climate system due to their contribution in the *greenhouse effect*. Infrared active gases in the atmosphere such as water vapor (H_2O), carbon dioxide (CO_2), methane (CH_4) and nitrous oxide (N_2O) allow incoming shortwave solar radiation to reach the Earth's surface but absorb and re-emit part of the outgoing longwave thermal radiation. This process creates an insulating layer around the Earth, preventing some of the planet's infrared radiation from escaping directly into space. Without greenhouse gases, the Earth's average surface temperature would be approximately -18 °C, instead of the current 15 °C, making it uninhabitable. In addition to H_2O, CO_2, CH_4 and N_2O, other gases such as tropospheric ozone (O_3) and manmade chlorofluorocarbons (CFCs) also contribute to this effect and are classified as greenhouse gases.

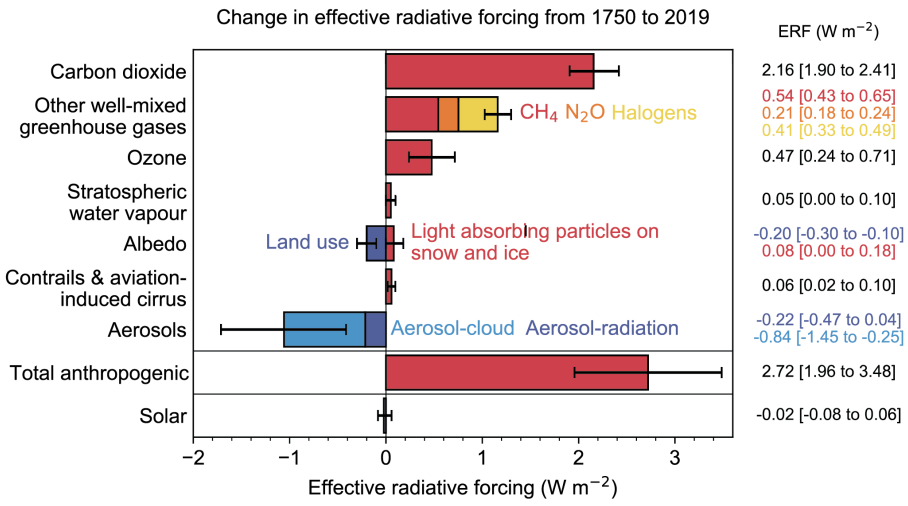

Figure 1.1: Drivers of climate change, with their respective change in radiative forcing from 1750 to 2019. Figure taken from Chapter 7 (Fig. 7.6) of the sixth assessment report of the Intergovernmental Panel on Climate Change (IPCC AR6, Masson-Delmotte et al., 2021).

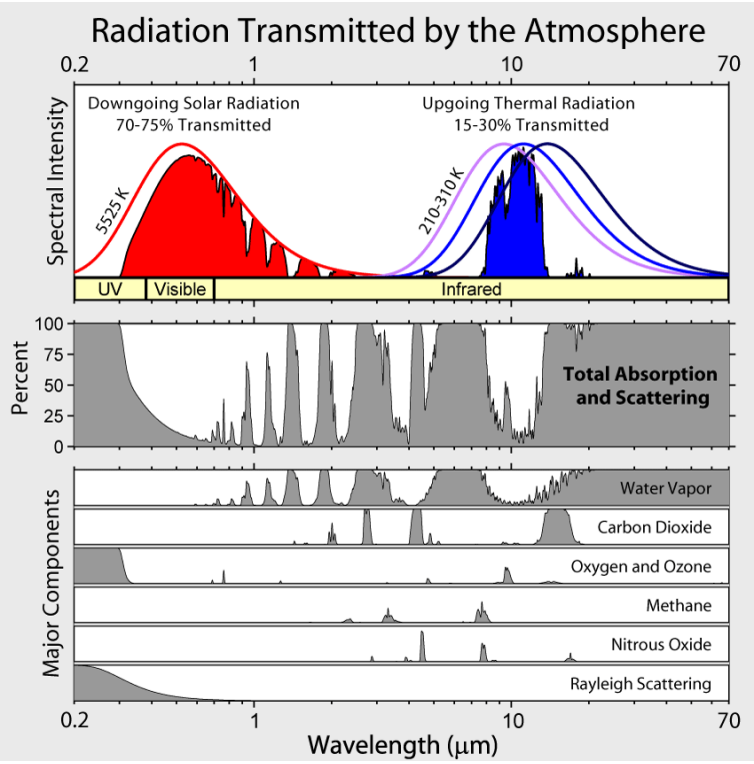

Figure 1.2: Top panel: Incoming solar radiation and outgoing thermal radiation, together with the Planck law's curves for their associated blackbodies, on a normalized scale. Middle and bottom panels: Absorption bands of the (cloud free) Earth's atmosphere and from specific gases (same scales as for the total absorption panel). Taken from Robert A. Rohde for the Global Warming Art project. CC BY-SA 3.0, via Wikimedia Commons.

In the last few centuries, human activities (such as the use of fossil fuels, deforestation and agricultural practices) have significantly increased the levels of greenhouse gases, especially CO_2 and CH_4. This increase has amplified the natural greenhouse effect, a phenomenon now referred to as the *enhanced greenhouse effect*, leading to positive radiative forcing. Radiative forcing quantifies the imbalance in the Earth's energy budget caused by various factors, including greenhouse gases, aerosols, solar radiation, and surface albedo. Although H_2O is the most prevalent greenhouse gas in the atmosphere (varying between 0 to 4%, depending on time and location), its contribution to the enhanced greenhouse effect is minimal. This is because human activities have not significantly altered its concentrations, and it has a short atmospheric lifetime of just a few days. In contrast, CO_2 and CH_4 are the most significant contributors to the enhanced greenhouse effect, accounting for over 70% of the total radiative forcing, see Fig. 1.1. This is largely due to their much longer atmospheric lifetimes —ranging from one year to millennia for CO_2 and around a decade for CH_4— and the significant increase in their concentrations since the Industrial Era, see below. Furthermore, CO_2 has a broad absorption band around 15 μm, which is close to the peak wavelength of outgoing thermal radiation (see Fig. 1.2).

Figure 1.3 depicts the rising trends of the major greenhouse gases (CO_2 and CH_4) in the at-

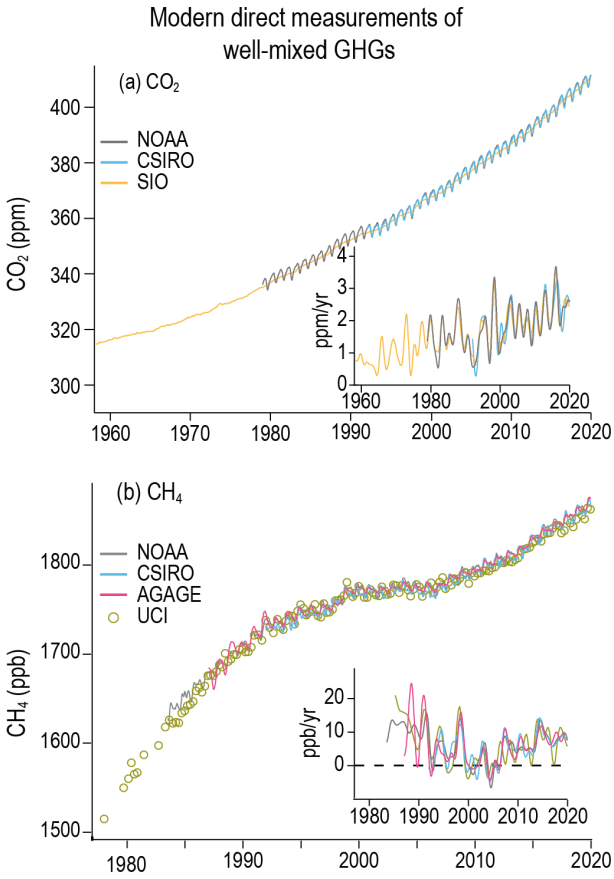

Figure 1.3: Globally averaged concentration trend and absolute growth rate of the most abundant greenhouse gases: CO_2 (top) and CH_4 (bottom), as observed by different measurement networks with global spatial coverage. Adapted from Figure 2.5 of Gulev et al. (2021).

mosphere over recent decades. The global averaged CO_2 concentration is estimated at 417.9 $\pm$ 0.2 ppm (parts per million per unit of volume, also ppmv) in 2022, while it was relatively stable at around 278 ppm before the industrial revolution (Masson-Delmotte et al., 2021; WMO, 2023). Due to the continuous extraction and burning of fossil fuels, atmospheric CO_2 is still rising with on average 2.4 $\pm$ 0.5 ppm per year, since 2011. Studies of ice cores and other data suggest that current atmospheric CO_2 levels are the highest they have been in at least 2 million years.

According to the latest Greenhouse Gas Bulletin of the World Meteorological Organization (WMO, 2023), the global average concentration of CH_4 in the atmosphere was approximately 1923 $\pm$ 2 ppb (parts per billion per unit of volume, also noted as ppbv) in 2022, reflecting an increase of over 150% since pre-industrial times (before 1750). The yearly increase of atmospheric CH_4 shows more variability than that of CO_2, as presented in the latest report from the Intergovernmental Panel on Climate Change (IPCC AR6, Masson-Delmotte et al., 2021). In the 1980s, the average growth rate of CH_4 was 15 $\pm$ 5 ppb per year. This rate dropped to 0.48 $\pm$ 3.2 ppb per year during the quasi-equilibrium phase from 2000 to 2006, and then rose again to an average of 7.6 $\pm$ 2.7 ppb per year over the past decade (2010–2019). Methane

concentrations in the atmosphere significantly surpass the natural fluctuations observed over the past 800,000 years.

This rapid increase of greenhouse gases in the Earth's atmosphere leads to an accumulation of energy and an imbalance in the Earth's climate system: anthropogenic forcing has given rise to global warming. Over the past 120 years, the average global surface temperature has already increased by more than 1.0 °C. This warming has caused significant sea-level rise and the rapid melting of polar ice and glaciers.
A major consequence of current climate change is the increase in the frequency and intensity of various weather extremes, such as heatwaves (Pörtner et al., 2023). Furthermore, climate change affects the global water cycle, leading to more frequent and intense heavy precipitation events (including major tropical cyclones) and droughts, as well as shifting precipitation patterns. These extreme events disrupt ecosystems worldwide: e.g. causing a loss of biodiversity, coral bleaching and mortality, ocean acidification, and tree mortality due to droughts and wildfires, ultimately deteriorating their structure, function, and resilience. Additionally, human societies already feel an impact through increased heat-related mortality, infectious diseases, changes in water and food security, and damage to cities and infrastructure from events like flooding and cyclones. Climate change profoundly impacts the current world on many levels and presents humanity with unprecedented challenges.

If CO_2 and other greenhouse gas concentrations continue to rise at current or higher rates, global surface temperatures will increase by anything between 1.4 and 4.4 °C (depending on the emission scenario) by the end of this century, relative to the 1850-1900 average (Gulev et al., 2021). Current observed extremes will likely intensify even further: more and stronger heatwaves, excessive precipitation, acute droughts and reduction of ice sheets and permafrost. Therefore the Paris Agreement, adopted at the COP21 of December 2015 under the United Nations Framework Convention on Climate Change (UNFCCC), aims to limit global warming to well below 2 °C above pre-industrial levels, with efforts to further limit it to 1.5 °C. In this agreement, 195 countries committed to set and regularly update their own national targets for reducing greenhouse gas emissions and enhance adaptation efforts in the so-called Nationally determined contributions (NDCs). Moreover, the treaty presents a framework to provide financial support to developing countries, and establish transparent reporting and review mechanisms to track progress.

1.2 Key sources and sinks of CO_2, CH_4 and CO

As potent greenhouse gases, CO_2 and CH_4 are the main focus of this thesis. Furthermore, this work studies time series of carbon monoxide (CO), which is considered an *indirect greenhouse gas*: while CO does not absorb infrared radiation, its presence in the atmosphere affects the concentration of other GHGs, thereby indirectly impacting the overall greenhouse effect.

Various natural and anthropogenic processes influence the exchange of these gases between the Earth's surface, which includes both land and ocean, and the atmosphere, ultimately

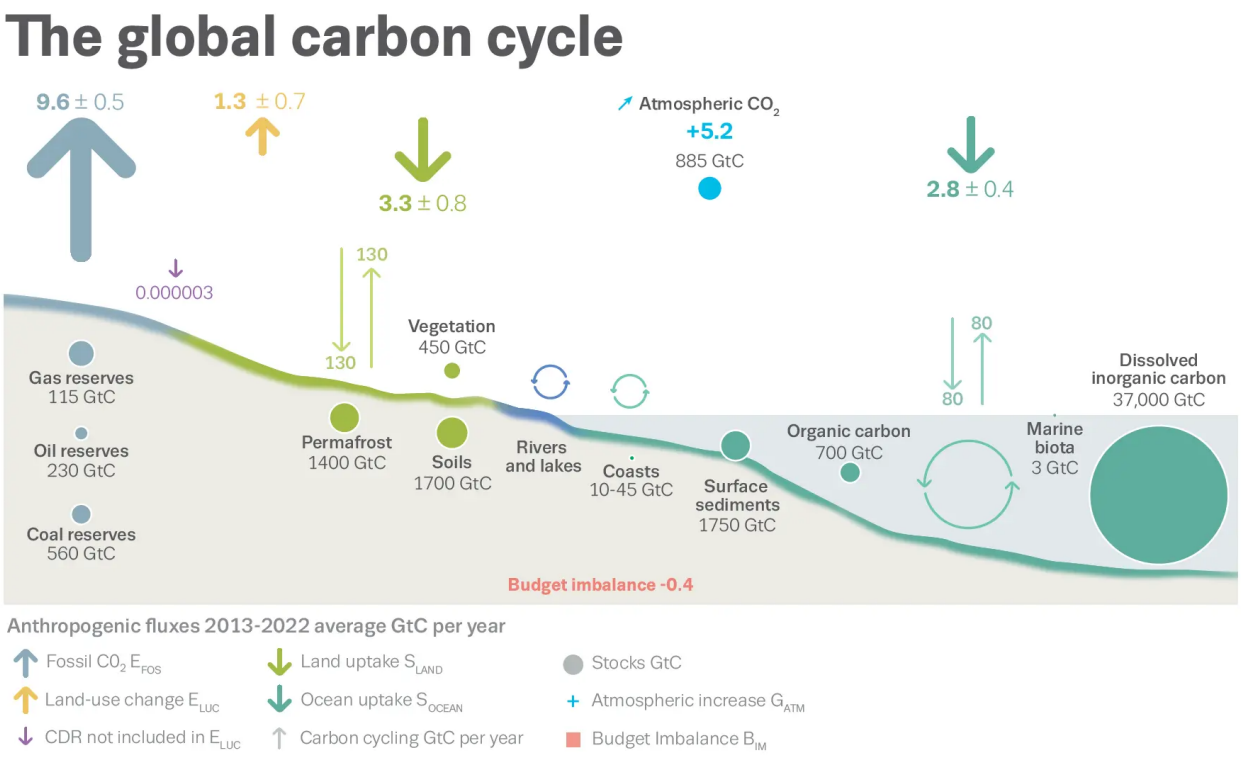

Figure 1.4: Global CO_2 budget in GtC per year, average over 2013-2022 from Friedlingstein et al. (2023).

influencing their atmospheric abundance. Processes that remove gases from the atmosphere are called *sinks*, whereas those that release gases into the atmosphere are known as *sources*. While these processes are relatively well understood and estimated on a global scale, uncertainties remain, with some processes (particularly those of natural origin) being less certain, and even more so at regional scales. Below, we discuss the primary sources and sinks of CO_2 CH_4, and CO, together with their global annual estimates.

1.2.1 Carbon dioxide

Carbon dioxide, or CO_2, is the fourth most abundant molecule in dry air, after nitrogen (N_2, 78.08%), oxygen (O_2, 20.95%) and argon (Ar, 0.93%), and is chemically inert whereby it can remain in the atmosphere for hundreds of years.
The main sources of CO_2 are:

- **Combustion of fossil fuels.** This is the most important anthropogenic source of CO_2 and includes the burning of coal, natural gas and oil for power generation, vehicles and heating of residential houses and commercial buildings.
- **Industrial processes.** The largest industries emitting CO_2 are the production of cement and other minerals, production of chemicals, metals and paper, petroleum refining and food processing.

- **Land use, land-use change and forestry (LULUCF).** This represents the direct human interference with vegetation such as the conversion of forested area to agriculture by deforestation, cutting trees for commercial use (logging) as well as forest management, regrowth and changes therein. Trees capture CO_2 from the atmosphere during their lifetime by photosynthesis (see below) and a part of this carbon is released back when they die. This category could in theory also be a net sink (if more trees are planted than cut down), however it is currently a source on the global level.

- **Forest fires.** A much smaller source compared to the others is biomass burning. This can be caused by both natural factors such as drought, heat or lightning as well as by anthropogenic factors such as the burning of agricultural waste or to clear land for agricultural purposes (so-called slash-and-burn method).

- **Other natural sources.** Natural sources of minor importance are for example volcanic eruptions and decomposition and respiration of the terrestrial biosphere.

The total global anthropogenic CO_2 source is estimated to be 10.9 ± 0.8 GtC (gigatonnes of carbon) per year (Fig. 1.4), of which 9.6 ± 0.5 is attributed to fossil fuels and industry (Friedlingstein et al., 2023).

The most important processes where CO_2 is removed from the atmosphere, or sinks, are:

- **Photosynthesis by forests and other vegetation.** (also called land uptake or land sink). During the day, plants use sunlight to convert CO_2 in glucose and biomass and thereby they grow. The land sink is stronger in the Northern Hemisphere (due to a larger area of land surface) and during the growing season. This terrestrial sink is estimated at 3.3 ± 0.8 GtC per year (Fig. 1.4).

- **Ocean uptake.** The ocean is an important carbon reservoir where CO_2 is exchanged with the surface layer and the air above, followed by vertical transport to deeper layers of the ocean. The estimated ocean sink is 2.8 ± 0.4 GtC per year (Fig. 1.4).

Currently, about half of the CO_2 that is emitted into the atmosphere by anthropogenic processes is compensated by the land and ocean sink. The rest accumulates in the atmosphere with a growth rate of about 5.2 GtC per year, thereby contributing to human-induced climate change.

1.2.2 Methane

About 40 % of the CH_4 sources is of natural origin while 60 % is emitted by human activities (Saunois et al., 2024). In general, the most important sources of CH_4 are:

- **Natural wetlands and inland waters.** This is biogenic CH_4 which is formed by the decomposition of organic matter in anaerobic environments, also called *methanogenesis*. It is the largest natural source of CH_4, estimated at about 248 Tg per year (Fig. 1.5).

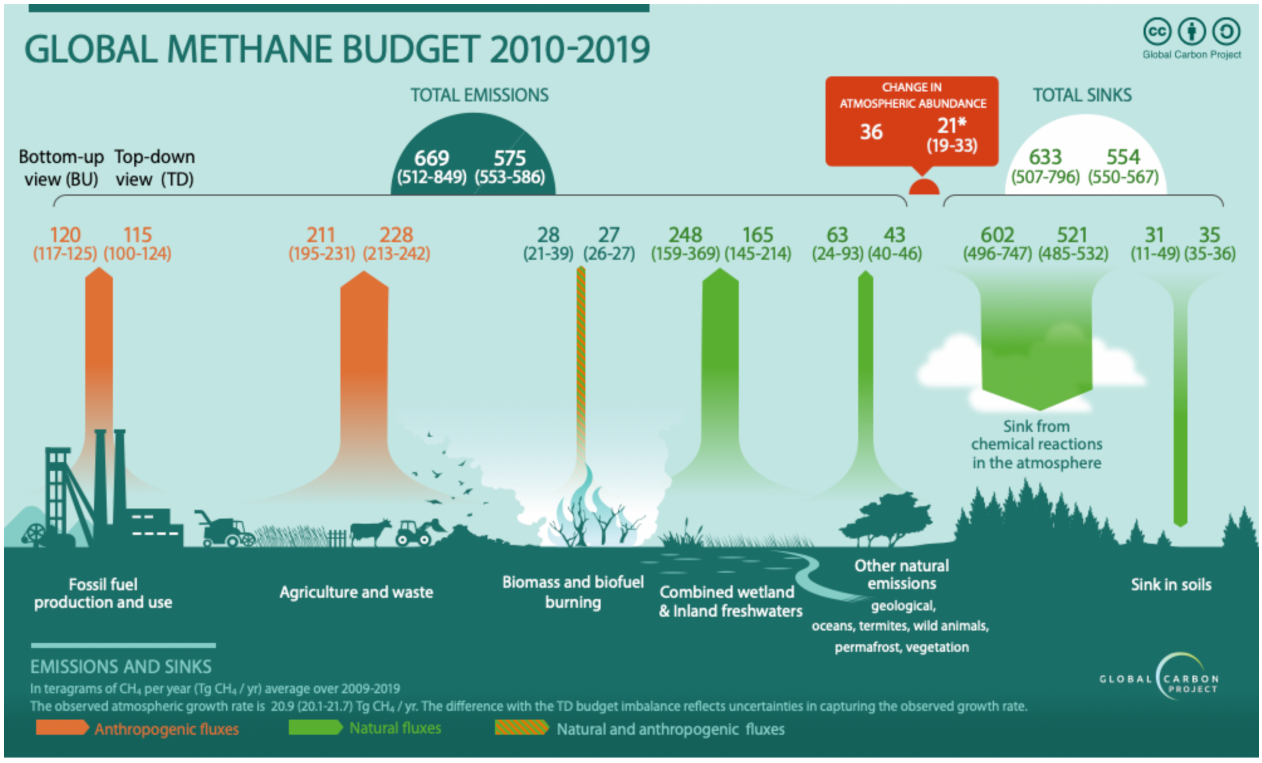

Figure 1.5: Global CH_4 budget in Tg per year, average over 2010-2019 from Saunois et al. (2024).

- **Agriculture.** This includes emissions from livestock (enteric fermentation in ruminants), manure management and rice cultivation. The latter is an important source due to the long-term flooding of rice paddies, creating the ideal conditions for methanogenesis. These sources are one of the largest anthropogenic sources of CH_4.

- **Waste management.** Another form of methanogenesis of anthropogenic origin, where CH_4 is emitted due to decaying organic material in environments lacking oxygen, are landfills and wastewater treatment systems. Together with agriculture, annual waste emissions are estimated at about 211 Tg (Fig. 1.5).

- **Fossil fuels.** CH_4 is the main constituent of natural gas which is formed over millions of years when organic matter is decomposed under intense heat and pressure underground, similar to oil. The extraction (including fracking) of gas, oil, and also coal, emits large portions of CH_4 into the atmosphere as it escapes from underground during drilling and mining operations. Further, CH_4 is also emitted during transport (gas pipe leaks) and incomplete combustion of fossil fuels that are further used for energy, transport and heating purposes. The total emissions of CH_4 of fossil fuel exploitation and use are estimated to be 120 Tg per year (Fig. 1.5).

- **Biomass burning.** As for CO_2, fires can originate from both natural and anthropogenic sources. Wildfires, peat fires, biomass and biofuel burning produce pyrogenic CH_4 due to incomplete combustion of organic material. This source is believed to emit about 28 Tg of CH_4 per year.

- **Other natural emissions.**There are many other sources of CH_4 that occur naturally and are estimated to emit about 63 Tg of CH_4 annually altogether. These sources include wild animals, termites, gas seeps, volcanoes, and thawing permafrost. While these natural processes are typically seen as having a minor role in climate change since only disturbances in these sources would lead to a rise in atmospheric CH_4, the thawing permafrost stands out as potentially more impactful. This is because it can intensify rapidly through positive climate change feedback mechanisms.

Methane is removed from the atmosphere by chemical reactions and by uptake in soils:

- **Atmospheric chemistry.** The largest CH_4 sink is oxidation by the hydroxyl radical (OH) in the troposphere. OH is created as a result of a chemical reaction between O_3, H_2O and ultraviolet (UV) sunlight. The formed OH radicals are highly reactive, they have an atmospheric lifetime of about a second, and react with trace gases such as CH_4 and CO. Because of this cleansing property, OH is often called the "detergent" of the atmosphere. About 90 % of CH_4 is destroyed by OH oxidation (Saunois et al., 2024). There are also chemical reactions with atomic chlorine (Cl) in the troposphere and with excited atomic oxygen $O(^1D)$, atomic fluorine (F) and OH in the stratosphere but these are of minor importance. The total loss of CH_4 from chemical reactions is estimated at 602 Tg per year.

- **Soil uptake.** Methanotrophs, or methane oxidizing bacteria in soils, consume CH_4 for survival leading to a removal of about 31 Tg CH_4 per year from the atmosphere.

1.2.3 Carbon monoxide

CO is created by incomplete combustion, mainly in the following processes:

- **Fossil fuels.** Incomplete combustion occurs when there is insufficient O_2 available. This mainly happens in engines of motorized vehicles and machinery. Thereby the transport sector (cars, trucks, airplanes, boats etc.) is an important source of CO. Further, burning of wood or gas for cooking or heating purposes also releases a lot of CO.

- **Industry.** The production of for example metals and chemical manufacturing releases CO into the atmosphere.

- **Biomass burning.** Wildfires are an important source of CO due to incomplete combustion of organic material, and can be caused by both natural and anthropogenic factors

- **Oxidation of CH_4 and NMVOCs.** Approximately half of the CO present in the atmosphere is produced through the oxidation of CH_4 and non-methane volatile organic compounds (NMVOCs).

CO is mainly removed from the atmosphere by dry deposition and chemical reactions in the troposphere. The most important sink is its reaction with OH. As a result, the emission of CO reduces the abundance of OH in the atmosphere and thus affects the atmospheric CH_4 lifetime and concentration (as less OH is available to remove CH_4). It also plays a role in the formation of tropospheric O_3 and urban smog.
In addition to being an important air pollutant, CO is considered an indirect greenhouse gas as it serves as a precursor to several direct climate forcers. Due to its chemical reactivity, CO has a much shorter atmospheric lifetime than CO_2 and CH_4, ranging from approximately 1 to 4 months, compared to CO_2 and CH_4. This shorter lifetime leads to less uniform mixing in the atmosphere, resulting in higher spatial and temporal variability.

1.3 Observing greenhouse gases

In the context of climate change, it is crucial to monitor greenhouse gas concentrations in the atmosphere. The unprecedented levels of GHGs, driven by anthropogenic emissions (Masson-Delmotte et al., 2021), necessitate detailed observation to understand their contribution to global warming, identify trends, ingest reliable data into climate prediction models, and pinpoint emission sources for effective mitigation. Continuous monitoring helps to unravel local and regional budgets, to assess the impact of specific events, and to differentiate between natural variability and anthropogenic impacts. Moreover, it supports the assessment of the impact of policy regulations and ensures compliance with international agreements like the Paris Agreement and the EU's Green Deal, that strive to limit the growth of atmospheric GHGs.

Historically, monitoring of GHGs in the atmosphere began with in situ air sampling at remote locations to minimize the influence of local pollution and to obtain representative samples of the global background atmosphere. Mauna Loa Observatory in Hawaii, chosen for its isolation and stability of atmospheric conditions, became a benchmark site for such high-precision, continuous observations, initiated by Charles David Keeling in 1957. Generally, in situ air sampling occurs close to the surface or on tall towers, capturing the local air to provide detailed snapshots of atmospheric composition. Other in situ techniques include for example AirCore sampling using balloons, which provides vertical profiles of greenhouse gases, or instruments mounted on aircrafts, which collect data along the flight track, offering insights into the atmospheric composition at various altitudes. Organizations like the National Oceanic and Atmospheric Administration (NOAA) and the World Meteorological Organization (WMO) have since expanded on this foundational work, establishing a network of monitoring stations worldwide, such as the Global Atmosphere Watch (GAW) program. These sites utilize various observational methods, such as Non-Dispersive Infrared (NDIR) and Cavity Ring-Down Spectroscopy (CRDS) sensors, to measure GHGs with high precision and accuracy.

Starting in the 2000s, remote sensing techniques became crucial in observing GHGs, enabling the measurement of concentrations over larger spatial scales. Unlike in situ sampling, which provides detailed local measurements, remote sensing offers vertical profiles or column-averaged dry-air mole fractions of GHGs, representing the concentration from the ground up through the atmosphere. Ground-based remote sensing employs instruments such as Fourier Transform Infrared (FTIR) spectrometers, which measure solar absorption spectra by pointing towards the sun. These instruments are often organized into networks like the Total Carbon Column Observing Network (TCCON), the Network for the Detection of Atmospheric Composition Change Infrared Working Group (NDACC-IRWG), or the Collaborative Carbon Column Observing Network (COCCON), providing consistent, high-precision GHG data across various locations spread over the globe. Space-based remote sensing, conducted by similar instruments (usually grating spectrometers) aboard satellites, observes GHG absorption lines in back-scattered solar or emitted thermal radiation spectra, offering extensive global coverage. Prominent satellite missions such as the Orbiting Carbon Observatory (OCO-2/3), the Greenhouse Gases Observing Satellite (GOSAT and GOSAT-2), the Tropospheric Monitoring Instrument (TROPOMI) onboard Sentinel-5P, TanSat, and GHGSat extend the observational capabilities, enabling comprehensive monitoring of atmospheric GHGs nowadays.

Among the different techniques available for measuring atmospheric trace gases, this research focuses on ground-based observations. More specifically, we will exploit the observations from both in situ and remote sensing measurement systems at two specific observatories: Réunion Island in the Indian Ocean and Xianghe, near Beijing in China. More detail on these sites will be given in Sect. 1.6, while below we provide a brief description of the type of instruments employed at the these locations, together with an introduction of the international networks they are embedded in.

1.3.1 Ground-based in situ observations

The ground-based in situ observations that are analyzed in this work are made by Picarro Cavity Ring-Down Spectroscopy (CRDS) gas analyzers, see Fig. 1.6. This type of instrument is highly sensitive and precise and works as follows: the locally sampled air is brought into an optical cavity. Then, a laser beam is sent through the cavity and its intensity is measured by a detector. When the laser is shut down, the intensity of the light detected will decay over time, depending on the amount of absorbers in the sample. This decay time, also called the ring-down time, reveals the absorption rate of the air and thus the abundance of the gas species. CRDS gas analyzers can detect species at very low concentrations and are known for their accurate measurements of greenhouse gases. Depending on the specific instrument employed, dry air mole fractions of CO, CO_2 and CH_4 are reported every couple of minutes with a precision up to 2 ppb, 0.05 ppm and 1 ppb, respectively.

(a) (b) (c)

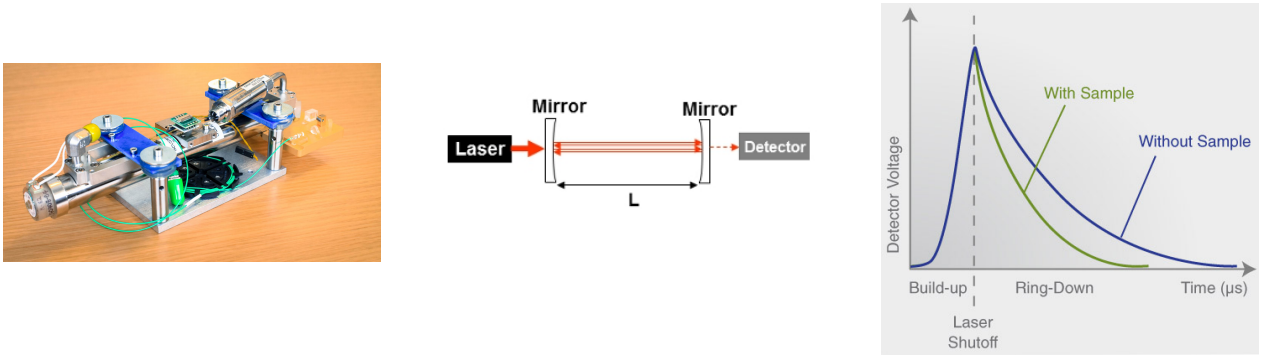

Figure 1.6: Illustration of Cavity Ring-Down Spectroscopy (CRDS) technique: (a) A Picarro CRDS analyzer and (b-c) Schematic overview of CRDS technique, and change in light intensity and ring-down time due to absorption.

ICOS

The Picarro CRDS analyzer at Maïdo, Réunion Island, is contributing to the Integrated Carbon Observing System (ICOS) research infrastructure. It is a European-wide facility dedicated to carbon cycle research in three domains: atmosphere, ecosystem and ocean. The observations are carried out at more than 170 stations in 16 European countries. The final quality-assured data products are publicly available according to the FAIR data principles (Findable, Accessible, Interoperable and Reusable) and the CC-BY-4.0 data license. More information can be found at https://www.icos-cp.eu/.

1.3.2 Ground-based remote sensing observations

The ground-based remote sensing observations of CO_2, CH_4 and CO that are analyzed in this study are made by FTIR spectrometers that are installed near the Earth's surface (i.e. ground-based), see Fig. 1.7. These devices are in fact Michelson interferometers that utilize

a connected solar tracker to direct sunlight into a beam splitter. The beam splitter then divides the incoming light into two beams, each directed toward separate mirrors. The combination of the two beams, of which one has a variable path due to a moving mirror, creates an interferogram. Finally, a Fourier transform is applied to convert the interferogram to a high resolution infrared spectrum. Using spectroscopic databases for atmospheric species, we can assign the wavelength-specific absorption to the gases (and aerosols) in the atmosphere, leading to the retrieval of trace gas concentrations. Note that, since FTIR spectrometers use sunlight, measurements can only be made during daytime and clear sky conditions.

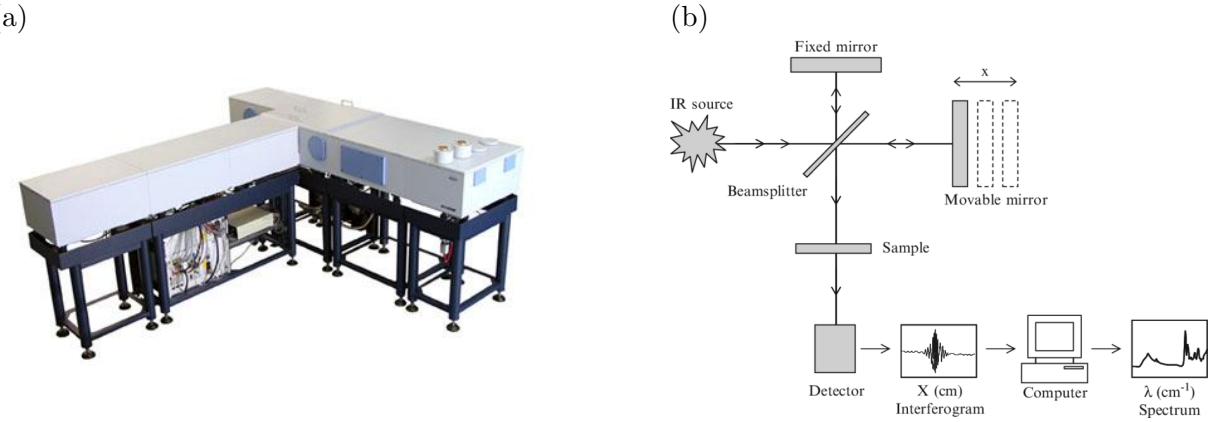

Figure 1.7: Illustration of Fourier Transform Infrared (FTIR) spectroscopy technique: (a) A Bruker IFS125HR instrument and (b) Schematic overview of FTIR.

The process of retrieving trace gas concentrations from absorption spectra is based on inversion theory, where a forward model, a priori information and the remotely sensed observation are combined to compute atmospheric concentrations. The forward model F links the atmospheric state space with the observation space and includes all parameters and processes affecting the observed signal (Maahn et al., 2020), such as a radiative transfer model: $F(\boldsymbol{x}) = \boldsymbol{y}$, where $\boldsymbol{x}$ is the atmospheric state (e.g. trace gas concentration profile) and $\boldsymbol{y}$ is the observed quantity (e.g. infrared spectrum).
Generally, we are interested in inverting this forward model to retrieve the concentration profile from the remotely sensed observation. As these inversion problems are often ill-posed (different atmospheric states $\boldsymbol{x}_i$ can all lead to the same measurement $\boldsymbol{y}$), and both the forward model and measurement have uncertainties, additional constraints are required, such as a priori information on the unknown atmospheric state ($\boldsymbol{x}_a$). A widely used retrieval method is Optimal Estimation (OE) where it is assumed that these uncertainties follow a Gaussian distribution (Rodgers, 2000). It is essentially an iterative process that starts from the a priori information and tries to minimize a constrained cost function to get to an optimal state that best matches the observation, see Fig. 1.8.

The retrieval method additionally provides a weighting function or averaging kernel matrix $\boldsymbol{A}$. This matrix represents the sensitivity of the retrieved profile to the true profile at each retrieval altitude. Ideally, every row is a delta function peaking at its corresponding altitude.

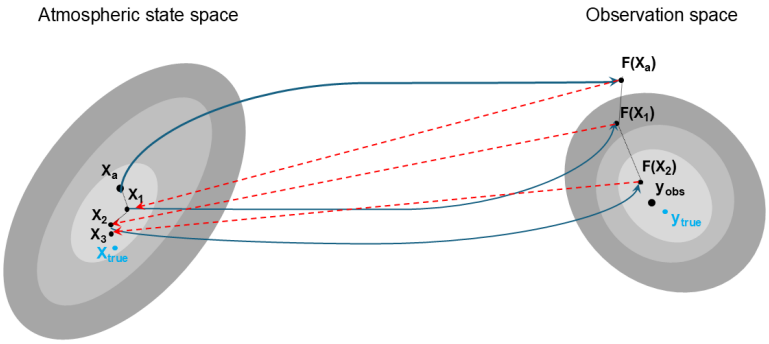

Figure 1.8: Principle of optimal estimation: the ellipses show the (left) prior state and (right) measurement uncertainty. The iterative process starts with applying the forward operator F to the first guess $\boldsymbol{x}_a$. Based on the difference of $F(\boldsymbol{x}_a)$ to $\boldsymbol{y}_{obs}$, $\boldsymbol{x}_1$ is obtained. This is repeated until the retrieval converges to a solution $\boldsymbol{x}_3$ that is close to the true state $\boldsymbol{x}_{true}$.

In reality however, remote sensing measurements are not equally sensitive to all levels of the atmosphere and have much broader sensitivity bands than delta functions. The relation between the true atmospheric profile $\boldsymbol{x}_{true}$ and the retrieved profile $\hat{\boldsymbol{x}}$ can be expressed as:

$$\hat{\boldsymbol{x}} - \boldsymbol{x}_a = \boldsymbol{A}(\boldsymbol{x}_{true} - \boldsymbol{x}_a) + \boldsymbol{\epsilon}, \tag{1.1}$$

where $\boldsymbol{\epsilon}$ is the retrieval error. The trace of $\boldsymbol{A}$ is the number of independent pieces of information that are retrieved, also called the degrees of freedom (DOF) for signal.

As noted earlier, these type of measurements are typically made in the context of international observation networks, such as TCCON (Wunch et al., 2011) and NDACC (De Mazière et al., 2018). At Réunion Island, FTIR instruments are located at two separate sites: in Saint-Denis and on the Maïdo mountain, contributing to TCCON and NDACC, respectively. Similarly, the instrument at Xianghe is affiliated with TCCON. Due to differences in retrieval strategies between these networks, a brief description of each network and the resulting product is given below. An example of their column averaging kernels for CO and CH_4 retrievals is show in Fig. 1.9, for different solar zenith angles (SZA). In contrast to the averaging kernel matrix $\boldsymbol{A}$, the column averaging kernel $\boldsymbol{a}$ represents the sensitivity of the retrieved total column to the true profile. For example the TCCON CO retrieval is more sensitive to the upper troposphere compared to the lower troposphere: it overestimates deviations from the a priori above $\pm$ 7 km (where $\boldsymbol{a}$ is 1.0), while it underestimates them below (see Fig. 1.9a).

TCCON

Currently, a total of 29 sites spread all over the globe (see Fig. 1.10) are equipped with solar-viewing FTIR spectrometers to continuously provide high accuracy remotely sensed

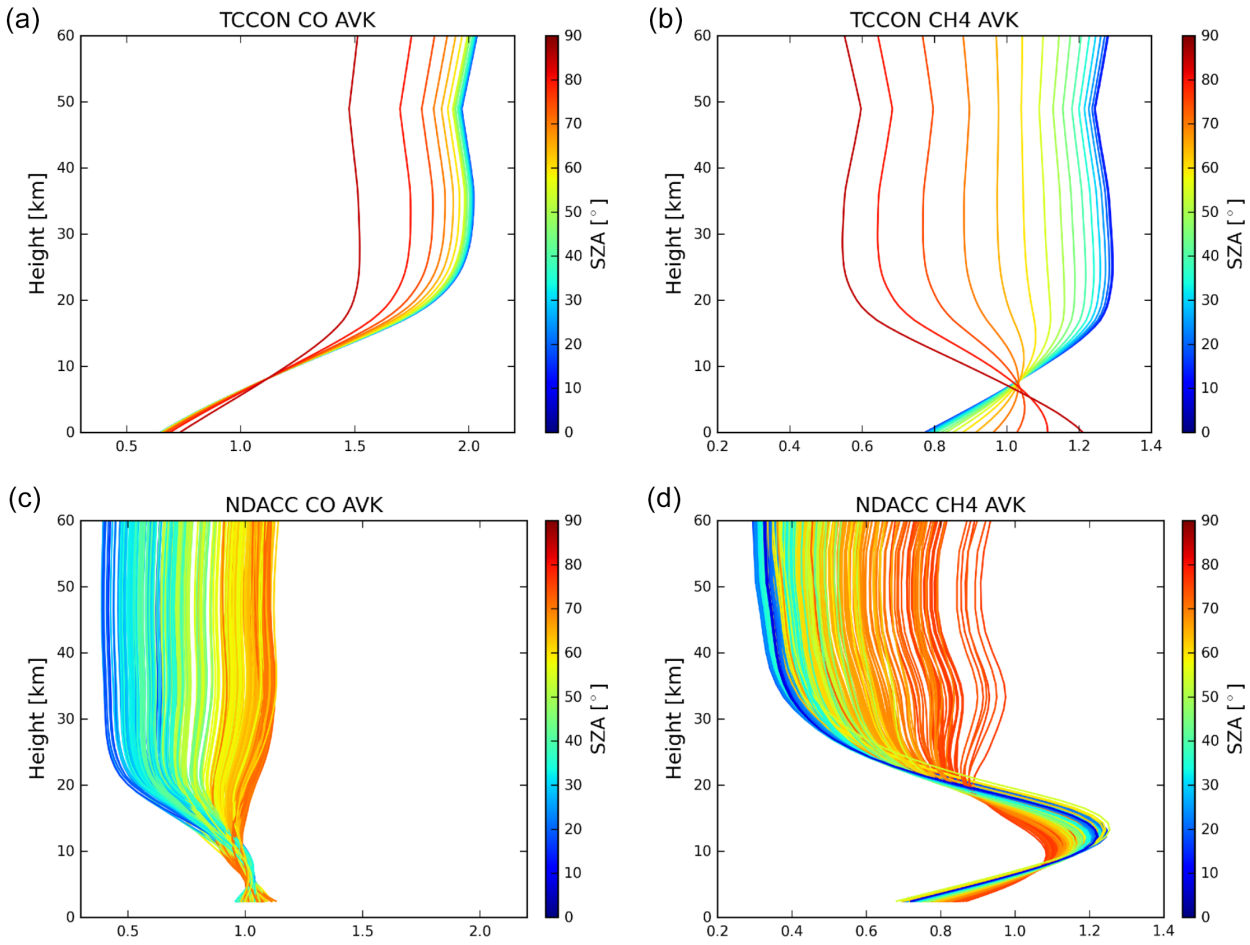

Figure 1.9: Example of column averaging kernels of CO and CH_4 retrievals in the context of TCCON and NDACC at Réunion Island, taken from Zhou et al. (2018).

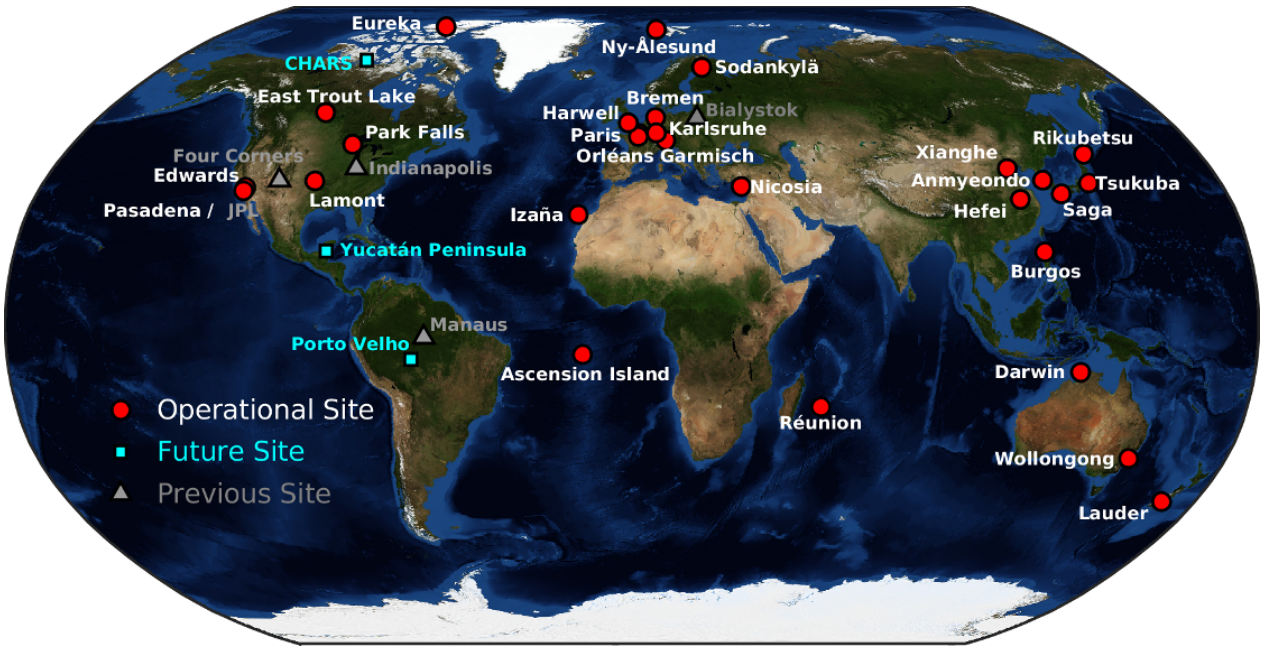

Figure 1.10: Map of the FTIR sites contributing to TCCON.

measurements of trace gases in the atmosphere. More specifically, near-infrared (NIR) solar spectra from Bruker IFS 125HR instruments are used to retrieve column-average dry air mole fractions, also called *Xgas*, of various gases. This type of concentration measure is denoted by an 'X' preceding the compound, i.e. XCO_2 for carbon dioxide. The available species further include CH_4, N_2O, H_2O, CO, HDO and HF. Remark that the TCCON retrieval does not provide atmospheric profiles. The used approach is centered around scaling the a priori profile to optimize the fit with the observed spectrum, which is then integrated over the total atmospheric column. It assumes the shape of the vertical profiles are known, and performs a so-called *scaling retrieval*. The *Xgas* of a target species G, X_G, is then computed from a combination of the total column (TC) of G and O_2:

$$X_G = 0.2095 \frac{TC_G}{TC_{O_2}}, \tag{1.2}$$

since the mole fraction of O_2 is stable in the atmosphere with a value of 0.2095. The observed column of O_2 is used to represent the column of dry air and to eliminate systematic uncertainties in the retrieval method. A more detailed mathematical formulation of the total column and the dry air column-average mole fraction is given in Appendix B. All data in the network is processed with the GGG software, of which the latest version is GGG2020 (Laughner et al., 2024), leading to column-averaged dry air mole fractions with a precision of 0.25% for XCO_2, 0.3% for XCH_4 and 1% for XCO. More information can be found at https://tccondata.org/, where the data is also publicly available to download.

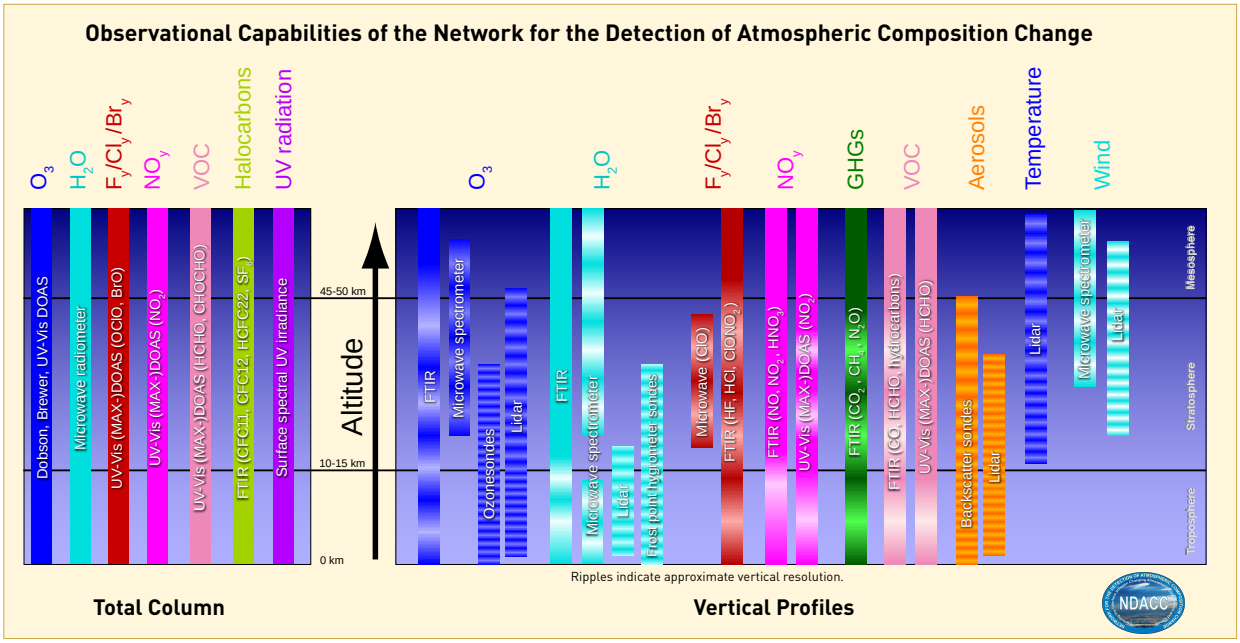

Figure 1.11: Overview of the different types of observations performed in the context of NDACC.

NDACC

NDACC is a network of over 90 stations worldwide focusing on the establishment of long-term time series to detect changes and trends in the chemistry and physics of the atmosphere (De Mazière et al., 2018). Both total columns and vertical profiles of a variety of species are measured by several ground-based observational techniques: not only FTIR spectrometers, but also Dobson-Brewer and UV/Visible DOAS (differential optical absorption spectroscopy) type instruments are applied, as are sonde, lidar and UV and microwave radiometers. Besides greenhouse gases and CO, aerosols, UV irradiance, O_3, H_2O and NO_y, many other species are being observed, see Fig. 1.11. These different techniques are gathered in corresponding instrument working groups. The Infrared Working Group (IRWG) is responsible for over 22 solar-viewing FTIR instruments spread over the globe, see Fig. 1.12. They measure solar transmission in the mid-infrared (MIR) spectral window, of which volume mixing ratio profiles are retrieved using the optimal estimation approach as implemented into the SFIT4 or PROFITT9 software. These retrieved profiles have on average 2.3 DOF for CO and 2.5 for CH_4, meaning that there are roughly two individual layers of information. Finally, column-averaged dry air mole fractions are computed from the total column of the species and of dry air. The latter is calculated from the surface pressure, gravitational acceleration and total column of H_2O. The NDACC data is known for its high-quality data where the accuracy and precision is below 3% for XCH_4 and XCO. Note that the NDACC-IRWG retrievals do not officially provide XCO_2 values. More information can be found at https://ndacc.larc.nasa.gov/.

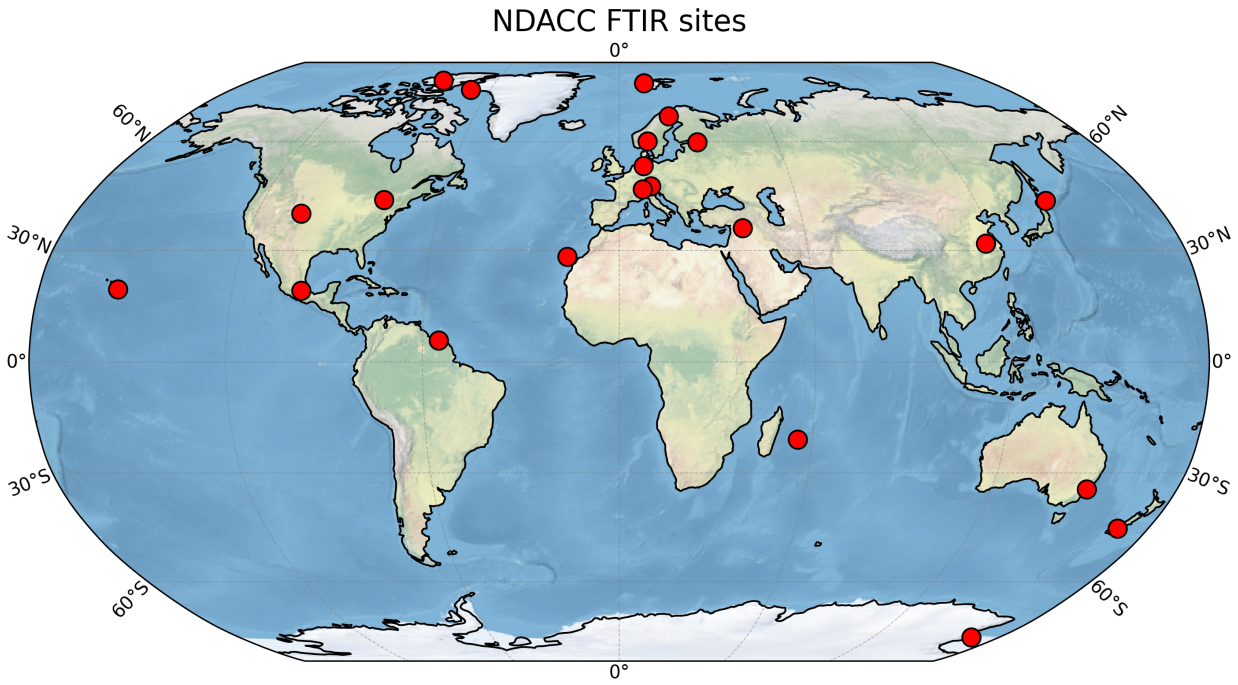

Figure 1.12: Map of the FTIR sites contributing to NDACC.

1.3.3 In situ versus remote sensing

Ground-based in situ and remote sensing techniques each offer distinct advantages and limitations. In situ sampling provides direct, high-accuracy measurements of GHG concentrations at specific locations, delivering high temporal resolution data that captures rapid changes and local fluctuations in GHG levels. These observations are heavily influenced by nearby sources and sinks, except at remote marine or mountain sites where they can be more representative of large-scale atmospheric distributions (Levin et al., 2020).

In contrast, remote sensing, whether ground-based or space-based, typically measure column-averaged mole fractions, which represent broader atmospheric patterns by integrating concentrations through the entire atmospheric column. This method is advantageous for understanding large-scale spatial patterns and trends, as it is relatively insensitive to local surface fluxes and vertical mixing (Keppel-Aleks et al., 2011; Wunch et al., 2011). Consequently, spatial and temporal variations in column-averaged mole fractions are typically smaller than those observed near the surface. It is important to recognize that remote sensing involves indirect measurements that require complex retrieval algorithms to convert raw spectral data into usable GHG concentrations. Effective interpretation of these data necessitates consideration of retrieval characteristics such as prior information, sensitivity, and potential errors.

1.4 Dispersion of gases in the atmosphere

Once emitted into the atmosphere, gases disperse downwind, where they may undergo chemical reactions or be removed by processes such as uptake by vegetation (e.g., photosynthesis for CO_2). In this section, the most important atmospheric processes governing the transport of gases are briefly described. These processes occur across different spatial and temporal scales, affecting how gases move through the atmosphere. Meteorological phenomena are often categorized by scale:

- *Synoptic-scale* processes, such as high- and low-pressure systems and weather fronts, typically cover distances of 1,000 km or more and last several days. These systems can transport pollutants across continents, making them key players in large-scale advection.

- *Mesoscale* processes, ranging from a few kilometers to several hundred kilometers, act over hours to a day. These include localized phenomena like thunderstorms, sea breezes, and mountain-valley circulations.

1.4.1 Factors influencing dispersion

Several key factors influence how gases are dispersed in the atmosphere, including wind speed, atmospheric stability, and topography (Ahrens and Henson, 2021). Below, we describe how each affects the concentration and spread of species.

- **Wind speed**: Wind speed plays a critical role in both the rate at which gases disperse from their source and how well they mix with the surrounding air. Strong winds tend to lower concentrations of pollutants by spreading them over a larger area and enhancing vertical mixing through increased turbulence. In contrast, weak winds lead to atmospheric stagnation, allowing pollutants to accumulate locally, often resulting in higher concentrations.

- **Atmospheric stability**: The vertical temperature gradient determines atmospheric stability. When the temperature decreases with height, the atmosphere is unstable, promoting vertical mixing and dispersion. In contrast, when temperature increases with height (this is called an *inversion*), the atmosphere is stable, inhibiting vertical movement. Pollutants trapped below an inversion layer spread horizontally but cannot rise, leading to potential accumulation near the surface. Inversions are common under high-pressure systems, where subsiding air warms as it descends, creating a "lid" over cooler air below. Similarly, frontal inversions, such as those associated with warm fronts, can create stable layers that suppress vertical mixing. On a smaller scale, radiational inversions frequently occur at night when the ground cools more rapidly than the air above, particularly under clear skies and light winds, enhancing stability and reducing mixing.

- **Topography**: Terrain plays a significant role in shaping airflow and pollutant dispersion. Mountains, for example, can block prevailing winds, trapping pollutants in

valleys, which can result in poor ventilation. Mountain-valley circulations also affect pollutant transport: during the night, cold air flows downhill, potentially strengthening surface inversions and concentrating pollutants within valleys. By day, solar heating of mountain slopes generates upslope winds (anabatic winds), which can carry pollutants out of valleys, redistributing them elsewhere. Similarly, coastal topography can influence dispersion through sea breezes, which carry pollutants inland or out to sea, depending on the time of day.

1.4.2 Planetary boundary layer

The Planetary Boundary Layer (PBL), also called the atmospheric boundary layer, is the lowest part of the atmosphere, directly influenced by its interaction with the Earth's surface (Foken, T., 2008). Most anthropogenic and natural emissions are released into this layer. It is characterized by turbulence due to wind shear (the difference in wind speed between the surface and the air aloft) and the surface roughness created by natural and man-made features such as buildings and trees. This turbulence promotes strong vertical mixing, playing a key role in the dispersion of gases and pollutants. The PBL typically ranges between 1 and 3 km in thickness, though it varies significantly depending on atmospheric conditions.
At a certain height, the atmosphere transitions from the turbulent PBL into the *free atmosphere*, where turbulence diminishes, and the flow becomes more stratified. In this layer above the PBL, vertical motion is more limited, and gases are mainly transported by large-scale advection rather than turbulent mixing.
The PBL undergoes a distinct diurnal cycle driven by solar radiation:

- Daytime: when the sun rises, the surface warms, causing convection that mixes the air vertically. This creates a well-mixed boundary layer with relatively uniform temperature, humidity, and pollutant concentrations throughout its depth. However, during winter or on cloudy days, convection is weaker, leading to a shallower mixed layer. As a result, the PBL height and the degree of mixing can be significantly reduced, which impacts how effectively pollutants are dispersed during the day.

- Nighttime: after sunset, the surface cools rapidly through emission of longwave radiation, while the air above cools more slowly, creating a nocturnal inversion near the surface. This results in a shallow, stable boundary layer that limits vertical mixing and tends to trap pollutants close to the ground. The depth of this layer depends on factors like cloud cover and wind speed, with clear skies and light winds favoring stronger inversions.

These dynamics mean that the PBL acts as a variable lid on the atmosphere, controlling how pollutants are mixed and dispersed both vertically and horizontally. The evolution of the PBL, illustrated in Fig. 1.13, plays a critical role in determining the extent to which pollutants are dispersed or confined near the surface.

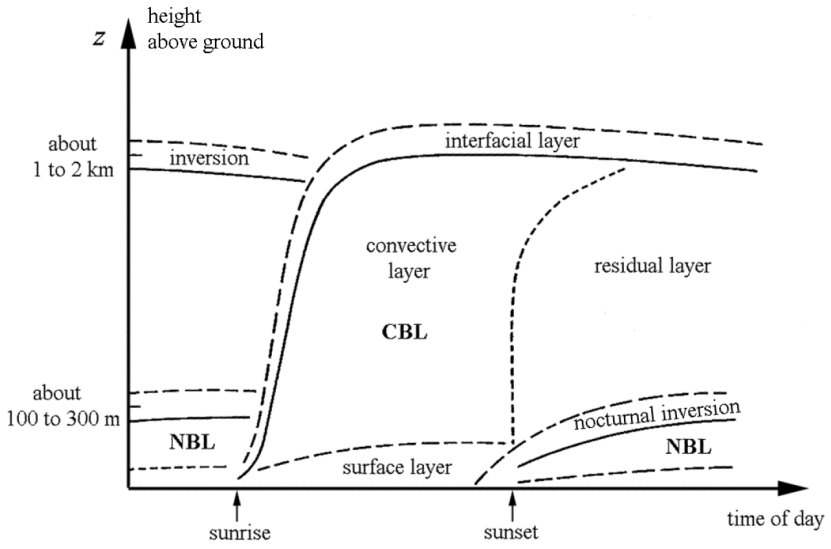

Figure 1.13: Diurnal evolution of the planetary boundary layer (PBL).

1.5 Atmospheric modeling and WRF-GHG

Modeling Earth's atmosphere involves simulating the interactions of various physical and chemical processes using mathematical equations and how they evolve over time. These equations are based on the fundamental laws of physics and (photo-)chemical reactions, enabling scientists to explore atmospheric phenomena, interpret them and predict future conditions. As a result, atmospheric models are essential tools for a wide range of applications, including weather forecasting, climate studies, air quality management, and environmental policy development. Chemical Transport Models (CTMs) are a specialized subset of atmospheric models that focus on the dispersion and transformation of atmospheric gases and aerosols. They are widely used to study pollutant distribution, identify sources, analyze chemical reactions, and assess impacts on air quality and human health. This work examines the use of the Weather Research and Forecasting Model coupled with Chemistry (WRF-Chem) in its greenhouse gas option, hereafter referred to as WRF-GHG.

WRF-Chem is an open-source community model that continuously advances with annual updates and offers a wide range of options for simulating gas-phase and aqueous chemistry and aerosols (Grell et al., 2005). WRF-GHG was officially created in 2012 when two separate modules for calculating the biogenic fluxes of CO_2 and CH_4 online were implemented into WRF-Chem V3.4, based on the work of Beck et al. (2011) and Ahmadov et al. (2007): the Vegetation Photosynthesis and Respiration Model (VPRM) for CO_2 and the wetland inventory of Kaplan (2002) for CH_4. Together with meteorology, this model simulates the passive tracer transport of CO_2, CH_4 and CO in different components —such as background, anthropogenic and biogenic sources— enabling to disentangle the total simulated concentration. Designed to simulate emission, mixing, and transport of these species without chemical transformations, WRF-GHG is computationally more efficient than other WRF-Chem op-

tions that account for full chemistry. This simplification is based on the assumption that these gases are long-lived in the atmosphere. The model relies on initial and boundary conditions and external emission inventories as key inputs, producing high-resolution 4D concentration fields within a regional domain. Typically, users opt for spatial resolutions of several kilometers and temporal resolutions of an hour. A more detailed description of the WRF modeling system will be provided in Chapter 3.

Originating from the need to simulate CO_2 transport with higher resolution than global models (which usually have a coarse resolution), WRF-GHG aims to better capture mesoscale transport patterns and surface flux exchanges and ultimately improve emission estimates. Indeed, Ahmadov et al. (2007, 2009) showed that, by coupling VPRM to WRF, processes like the sea-land breeze circulation and spatiotemporal variability of biospheric CO_2 fluxes during the CERES (CarboEurope Regional Experiment Strategy) campaign in France could be well captured.
This ability of WRF-GHG to simulate CO_2 concentrations at high spatial resolution is particularly valuable in regions with complex terrains and urban environments.
Pillai et al. (2011) demonstrated this in their study at the Ochsenkopf tall tower in Germany, where they found that mesoscale flows, such as frontal passages, thermal circulation patterns but also variation in vertical mixing, have a strong influence on CO_2 levels. Their research highlighted that even minor deviations in CO_2 concentrations, if not properly accounted for, can lead to large biases in flux estimates, underlining the need for high-resolution modeling to accurately capture local variability.
In urban environments, WRF-GHG has demonstrated its effectiveness in accurately simulating and assessing greenhouse gas patterns. For instance, Park et al. (2018) acknowledged the value of WRF-GHG in their study conducted during the CalNex campaign in California, USA, where the model accurately simulated meteorological fields and diurnal CO_2 variations, providing valuable insights into regional-scale CO_2 transport, temporal variability, and budget in a complex urban setting. Also in the United States, Feng et al. (2016) compared WRF-GHG simulations with in situ CO_2 observations across Los Angeles, and concluded that while high-resolution transport modeling is essential, the detailed resolution of emission inventories plays an even more critical role in capturing the observed variability and accurately estimating urban emissions. Further, Zhao et al. (2019) utilized WRF-GHG combined with the differential column methodology (DCM) and a series of FTIR observations in Munich, Germany, to effectively estimate concentration enhancements attributable to city emissions and highlighted the model's capability in identifying and understanding major urban greenhouse gas sources.

During the past decade, many scientists have recognized the power of the WRF-GHG model in enhancing our understanding of the spatial and temporal variability of GHGs and the underlying processes driving these changes all over the globe. For instance, Liu et al. (2018) and Dong et al. (2021) employed WRF-GHG to refine their understanding of CO_2 fluxes and concentrations across China, making comparisons with satellite data and flask samples. Expanding this scope to a broader region, Ballav et al. (2020) used WRF-GHG to simulate CO_2 over a three-year period in Asia, comparing the results with data from nine

ground-based sites. Moreover, their analysis disentangled the contributions of different flux components—such as oceanic, biospheric, and fossil fuel sources—shedding light on the factors influencing observed variations in atmospheric CO_2.
A number of studies focused more specifically on the contributions of the biosphere and the role of meteorological processes. For example, Li et al. (2020) evaluated WRF-GHG against CO_2 fluxes and concentrations measured by two towers in northeast China, finding that while the model generally performed well, the respiration equation within VPRM could be improved. This study further underscored the importance of accounting for terrestrial signals, which can be as significant as anthropogenic contributions in regional CO_2 budgets. Hu et al. (2020) performed a similar analysis over the entire continental USA during the ACT-America campaign, where WRF-GHG successfully captured the spatiotemporal variation of CO_2 fluxes consistent with satellite-derived Solar-Induced Fluorescence (SIF) data. The model demonstrated its capability in capturing XCO_2 variability driven by synoptic weather systems and diurnal flux variations influenced by clouds and temperature changes, highlighting WRF-GHG's potential in investigating the interaction between land surface dynamics and atmospheric CO_2 variability. In a follow-up study, Hu et al. (2021) further investigated the link between CO_2 and cold fronts, highlighting the significance of respiration fluxes and the need for an improved representation of these processes within the VPRM model. With a focus on meteorological influences, Martin et al. (2019), assessed the impact of different anthropogenic emission inventories and weather conditions on CO_2 variability in Washington, D.C. This study identified two distinct scenarios: frontal passages that cause drastic shifts in meteorological fields and CO_2 concentrations, often leading to large model errors if not accurately captured, and periods of steady winds where CO_2 variation is minimal and largely determined by background values, resulting in generally lower model errors.

The success of WRF-GHG in CO_2 research can be largely attributed to its ability to simulate biogenic CO_2 fluxes alongside meteorological processes at high resolution, thanks to the integration of the VPRM model. This combination allows for a more accurate representation of the complex interactions between surface fluxes and atmospheric dynamics, which is why the model is often referred to as WRF-VPRM when focused exclusively on CO_2. While WRF-GHG's application in CO_2 studies has been extensive, its capabilities extend beyond CO_2. The model also supports the online calculation of biogenic CH_4 fluxes and the passive tracer transport of CH_4 and CO, although these features have been less frequently utilized. Nevertheless, recent studies are beginning to explore these capabilities, revealing the model's potential to advance our understanding of the spatial and temporal dynamics of other critical direct and indirect greenhouse gases, such as CH_4 and CO.
For CH_4, Beck et al. (2013) were among the first to leverage the model's capability for online calculation of wetland fluxes during the BARCA campaign in the Amazon. Their study underscored the critical role of accurately simulating convection processes and of the choice of wetland inundation maps for reliable CH_4 predictions. Similarly, Zhang et al. (2023) demonstrated WRF-GHG's utility in simulating the spatial and temporal distribution of CH_4 across China, using GOSAT and surface observations, although they did not use the online wetland emission model of Kaplan. Their findings highlighted the model's effectiveness, while noting that neglecting the OH sink might lead to an overestimation of XCH_4 during spring and

summer.
Further, Dekker et al. (2017) explored the potential to quantify CO emissions from Madrid by combining WRF-GHG simulations with MOPITT observations, while Borsdorff et al. (2019) analyzed CO enhancements over Iran, comparing WRF-GHG simulations with TROPOMI satellite data. They found a generally good agreement between the model and satellite observations, although discrepancies at city scales likely originated from inaccurate emission inventories. In another study, Dekker et al. (2019) investigated a significant pollution event in India in November 2017 using TROPOMI data, where WRF-GHG simulations highlighted the dominant role of meteorology over emission variations in driving the observed CO levels. Vellalassery et al. (2021) conducted a follow-up study on this topic.

Collectively, these studies underscore WRF-GHG's versatility and its ability in advancing our understanding of the dynamics of CO_2, CH_4, and CO across various spatial and temporal scales, regional settings and environments. Additionally, these research efforts play a crucial role in the ongoing evaluation and refinement of the model, enhancing its accuracy and relevance for future research.

1.6 Observatories in focus: Réunion Island and Xianghe

This thesis focuses on ground-based observations at two distinct locations: Réunion Island and Xianghe, as briefly mentioned in Sec. 1.3. These sites are highlighted on the global map in Fig. 1.14. Moreover, on Réunion Island, GHG measurements are conducted at two different sites: the capital city, Saint-Denis, and near the summit of Maïdo mountain.

The selection of these locations is primarily driven by the strong involvement of BIRA-IASB in both conducting and analyzing these measurements, ensuring easy access to the data and leveraging their extensive expertise in remote sensing retrieval processes. BIRA-IASB has been conducting FTIR observations on Réunion Island since 2002, initially on a campaign basis and later through the installation of a fixed instrument in Saint-Denis, followed by a similar setup at Maïdo. Both sites now operate automatically with remote control and are additionally equipped with in situ measurement instruments, in collaboration with local partners of the Observatoire de Physique de l'Atmosphère de La Réunion (OPAR) and the Laboratoire des Sciences du Climat et de l'Environnement (LSCE). Similarly, the Xianghe site in China, operated by the Institute of Atmospheric Physics, Chinese Academy of Science (IAP-CAS) since 1974, has benefited from a fruitful collaboration with BIRA-IASB, which led to the addition of an FTIR instrument in 2016. The longstanding and successful partnerships at both locations are invaluable, as local partners contribute their understanding of the instruments and surrounding environments, aiding in accurate data interpretation.
The FTIR observations at Saint-Denis and Xianghe are integrated into TCCON, therefore using the same retrieval strategies. The data from Maïdo on the other hand, contributes to both NDACC-IRWG (remote sensing) and ICOS (in situ).

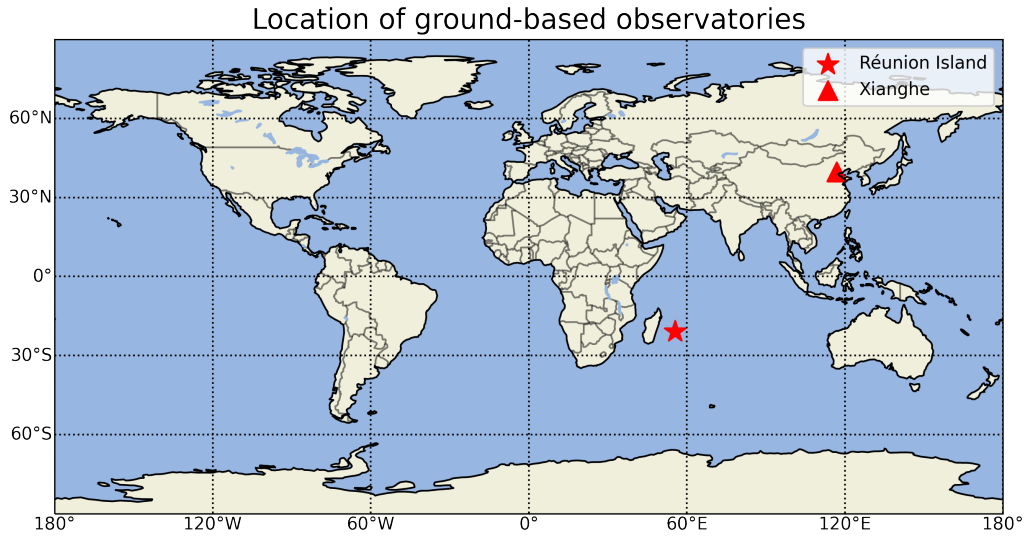

Figure 1.14: Global map highlighting the locations of ground-based observation sites analyzed in this study.

Both locations are particularly interesting to study, as they offer co-located near-surface and column measurements and are each characterized by distinct environmental processes.
Réunion Island, a French overseas department located in the Indian Ocean about 700 km east of Madagascar, is a remote and relatively isolated tropical island. Covering a small area of approximately 50 by 60 km, Réunion features a complex orography, with mountains rising up to 3,000 meters. The island itself has only minor emission sources, making it well-suited to represent background tracer concentrations in the Southern Hemisphere, a region that is notably underrepresented in global observing networks.
Xianghe, on the other hand, is a more recent site for greenhouse gas observations, located close to Beijing in a highly populated and industrialized region of China. Unlike Réunion, Xianghe is situated in a heavily polluted area, making it an ideal location to study the impacts of urbanization and industrialization on atmospheric composition. Ground-based GHG measurements are still relatively limited in China, particularly when compared to the extensive networks in the USA and Europe. This scarcity, combined with China's status as one of the world's largest emitters of greenhouse gases, highlights the importance of Xianghe as a critical site for understanding regional emissions and their global implications.
A more detailed description of the sites and their instrumentation is given further in this thesis.

Chapter 2

Objectives

In the context of climate change and the need to unravel local and regional greenhouse gas budgets, this work intends to provide deeper insights into atmospheric processes and the representativeness of specific sites by focusing on the variabilities of atmospheric greenhouse gases at Réunion Island and Xianghe. Specifically, this research will apply the WRF-GHG model to these locations for the first time, focusing on CO_2, CH_4 and CO simultaneously. By comparing the model results with co-located in situ and remote sensing observations, this study will also evaluate the model's ability in attributing changes in these GHG concentrations to anthropogenic and biogenic emission sources as well as meteorological processes. More precisely, my research aims to answer the following question:

How effective is the WRF-GHG model in evaluating the impact of anthropogenic and biogenic emission sources and sinks, and meteorological processes on the observed time series of CO_2, CH_4 and CO at Réunion Island and Xianghe?

To answer this question, the following specific objectives will be addressed:

1. To simulate the various time series of atmospheric CO_2, CH_4, and CO at Réunion Island and Xianghe over a period of at least one year using the WRF-GHG model in an appropriate configuration.

2. To compare the simulated time series with the observed in situ and remote sensing measurements and assess the model's performance in capturing temporal variations at Réunion Island and Xianghe.

3. To analyze the contributions of tagged tracers to distinguish between biogenic and anthropogenic sources and sinks, and assess the influence of both local and regional factors on the observed time series of atmospheric CO_2, CH_4, and CO at Réunion Island and Xianghe by comparing these contributions between in situ and remote sensing observations.

4. To investigate the specific meteorological processes that drive variability in atmospheric CO_2, CH_4, and CO observations at Réunion Island and Xianghe.

5. To assess the strengths and limitations of the WRF-GHG model and the input datasets in accurately simulating atmospheric CO_2, CH_4, and CO in the selected regions.

Chapter 3

Methodology

A substantial part of this research consists in simulating the observed time series using the WRF-GHG model. Sections 3.1 and 3.2 describe the model's components and input data. Further, Sect. 3.3 outlines the key steps and decisions required before running the model, followed by a brief overview of the practical execution in Sect. 3.4. The specific set-up of the model for the studies at Réunion Island and Xianghe will be provided in the respective chapters (Chapters 4 and 5). Lastly, Sect. 3.5 explains the methodology used to compare the simulated time series with the observations.

3.1 The WRF modeling system

As introduced in Sect. 1.5, WRF-GHG is integrated within the widely utilized WRF modeling system, a versatile numerical weather prediction (NWP) model designed for both research and operational applications. Over time, continuous contributions from a global community of users have allowed WRF to evolve into a comprehensive tool set for various Earth system prediction applications, built upon its core software. These applications include air chemistry (WRF-Chem), hydrology (WRF-Hydro), wildfires (WRF-Fire), hurricanes (HWRF), and urban climate (WRF-Urban) (Powers et al., 2017). In the following sections, we will first outline the key components of the base WRF system (Sect. 3.1.1), followed by a detailed discussion of the specific elements within WRF-Chem (Sect. 3.1.2) and finally, WRF-GHG (Sect. 3.1.3).

3.1.1 WRF

The Weather Research and Forecast Model (WRF) is a globally recognized atmospheric modeling tool, renowned for its versatility across a wide range of applications. Supported by the US National Center for Atmospheric Research (NCAR) and sustained by a large, active user community, WRF is well-documented and integrates the compressible, non-hydrostatic Euler equations.

These Euler equations, a set of partial differential equations rooted in the fundamental principles of fluid dynamics, i.e. conservation of mass, energy and momentum, describe the motion and evolution of the atmosphere from initial conditions. To solve these complex equations

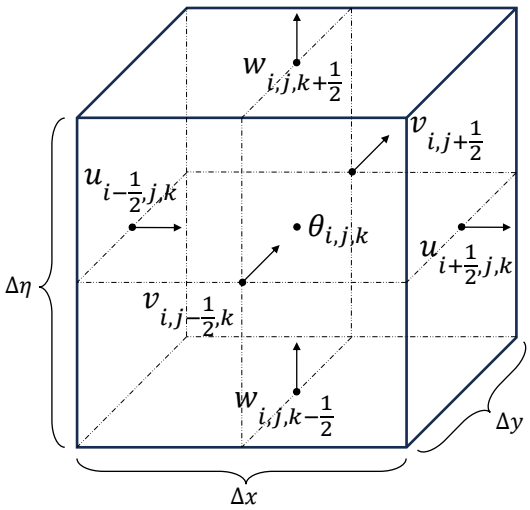

(a) Spatial grid in WRF: Arakawa C-grid.

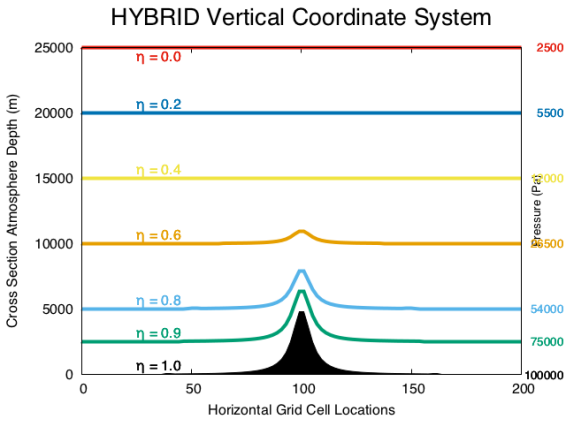

(b) Example of the hybrid vertical coordinate in WRF, for a model top at 25 km.

Figure 3.1: Illustration of the spatial discretization within WRF.

using computers, numerical approximations are applied. The model domain is discretized into a finite 3D grid or mesh, with time split into small intervals. Each grid cell represents a small volume of air, or air parcel, within the atmosphere.

WRF follows a *staggered Arakawa C-grid* for the spatial discretization, see Fig 3.1a where a model grid cell at index i,j,k is shown. The points where θ is located are referred to as mass points and are at the center of the cell. Almost all model variables are defined here, except for the geopotential which is computed on w points (vertical cell boundaries). The velocity vectors u, v, and w are staggered one half grid length from the thermodynamic variables: they are defined at the boundaries of the cell. The horizontal grid lengths Δx and Δy describe the horizontal resolution, while the vertical grid length $\Delta\eta$ represents the vertical resolution. Since model version V4, WRF uses a hybrid sigma-pressure vertical coordinate. This is a coordinate system that is terrain-following near the surface and becomes isobaric near the top, see Fig 3.1b.

Given the spherical shape of the Earth and the rectangular grid framework used in computer models, a map projection is necessary. WRF supports four different map projections and each one is recommended in a different region of the globe to minimize the distortion in the physical distances on the Earth's surface. The polar stereographic projection is best suited for high-latitude domains, while the Lambert conformal is recommended for mid-latitude domains (as was chosen for the Xianghe study, see Chapter 5). The Mercator projection on the other hand, is good for low-latitude domains (such as Réunion Island, see Chapter 4) and finally, the cylindrical equidistant projection should be used for global simulations.

Even though WRF supports global domains, it is however advised to use this option with

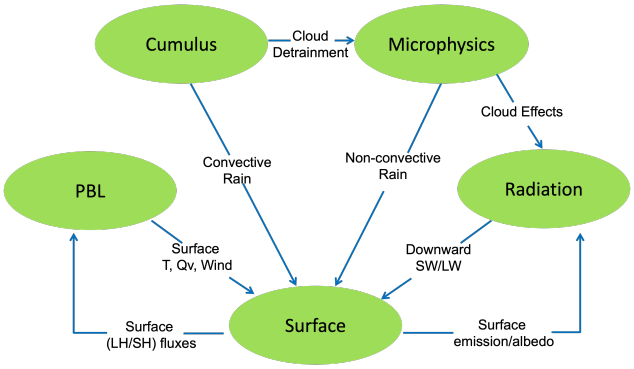

Figure 3.2: Overview of the physics schemes in WRF and their interactions. Illustration taken from the WRF Users Guide. For clarity, the following abbreviations are used in the figure: PBL (planetary boundary layer), T (temperature), Qv (specific humidity), LH (latent heat), SH (specific heat), SW (shortwave radiation), and LW (longwave radiation).

caution as it is not commonly used. The majority of applications apply limited area modeling, i.e. there is a focus on a specific geographic area, providing high-resolution predictions within that limited domain. In this case, lateral boundary conditions are required to describe the flow in and out of the model domain. This information is generally relying on global models with a coarser resolution. In the current work, the ERA5 and CAMS reanalysis data sets are used and will be described in Sect. 3.2.1.

WRF allows nesting of model domains to further increase the horizontal resolution over a specific region of interest. In a nesting configuration, multiple domains are simulated at the same time. A subdomain, or child domain, is completely surrounded by the parent domain and gets its lateral boundary conditions from its parent domain. Several parent-child domains can be included into the model simulation. Nesting can be either one-way or two-way. In a one-way nesting configuration the parent provides boundary data to the child, while in the two-way option, the child additionally feeds information back to the parent domain. This can also be referred to as *no feedback* vs *feedback*.

Finally, a variety of physics schemes is implemented within the WRF model to represent the several physical processes occurring in the atmosphere that cannot be explicitly resolved and must be parameterized. These subgrid-scale processes include radiation, cumulus parameterization, planetary boundary layer, land-surface processes and microphysics (Fig. 3.2).

Cumulus parameterization schemes describe convective clouds that are smaller than the model's grid size (subgrid-scale). Microphysics schemes resolve cloud and precipitation processes such as cloud formation, condensation, evaporation and rainfall. These cloud properties are passed on to the radiation scheme, which compute the longwave and shortwave radiation fluxes. The planetary boundary layer (PBL) schemes parameterize the turbulent mixing in the atmospheric boundary layer i.e. the lowest layer of the atmosphere which is directly influenced by the surface. They simulate the surface fluxes of heat, moisture and momentum and redistribute them by turbulent eddies. Finally, land-surface processes such as heat and moisture exchange coefficients and friction velocities are represented by surface layer schemes

and land surface model schemes. They take into account soil and vegetation properties.
For each of these processes, there is a variety of options available within WRF and it is up to the user to select the scheme that suits his specific region, grid size and research goal best. The options selected for the studies at Réunion Island and Xianghe are detailed in the respective chapters (Chapters 4 and 5).

3.1.2 WRF-Chem

WRF-Chem is the WRF model coupled online with chemistry: meteorology and chemistry are simulated at the same time. This extension of WRF includes the release, transformation and transport of atmospheric constituents, such as gases and aerosols and is a widely used tool in air quality studies worldwide. Depending on the chosen option, it may also include interactions of for example aerosols with radiation and microphysics processes. These chemistry options cover a variety of chemical mechanisms and modules to include for example aerosol processes at different levels of complexity. This model system is supported by NOAA/ESRL/GSL (National Oceanic and Atmospheric Administration / Earth Systems Resource Laboratories / Global Systems Laboratory).
The WRF-Chem model requires gridded emission data as additional input, which the user should prepare corresponding to his chosen option. An overview of the external data sets applied in this work is given in Sect. 3.2.3.

3.1.3 WRF-GHG

WRF-GHG, the greenhouse gas option of WRF-Chem, focuses on simulating the passive transport and mixing of CO_2, CH_4, and CO, making it an effective tool for studying these gases' behavior in the atmosphere with reduced computational demands.
A fundamental aspect of WRF-GHG is the implementation of the Vegetation Photosynthesis and Respiration Model (VPRM, Mahadevan et al. (2008)) for biogenic CO_2 fluxes as well as the online calculation of biogenic CH_4 fluxes by the Kaplan wetland inventory, Ridgwell soil uptake model and termite database of Sanderson (Kaplan, 2002; Ridgwell et al., 1999; Sanderson, 1996). A presentation of these components is given further below.

The simulation of gases in WRF-GHG is split into several tracers which correspond to several emission sources. The default configuration includes a background tracer, anthropogenic tracer, biomass burning tracer, biogenic tracer and ocean tracer (for CO_2 only). The background tracer describes the evolution of the initial and lateral boundary conditions over time. The sum of all these tracers represents the total concentration in the atmosphere and can be directly compared with measurements. It is however possible to adjust the included tracers by making some small adaptations to the model code and the corresponding emission input. This gives the user a large flexibility, leading to a variety of applications where this tool can be relevant.

Figure 3.3 shows the different elements that are part of the process of running WRF-GHG. The top of the flowchart (above the gray dashed line) indicates the steps that are part

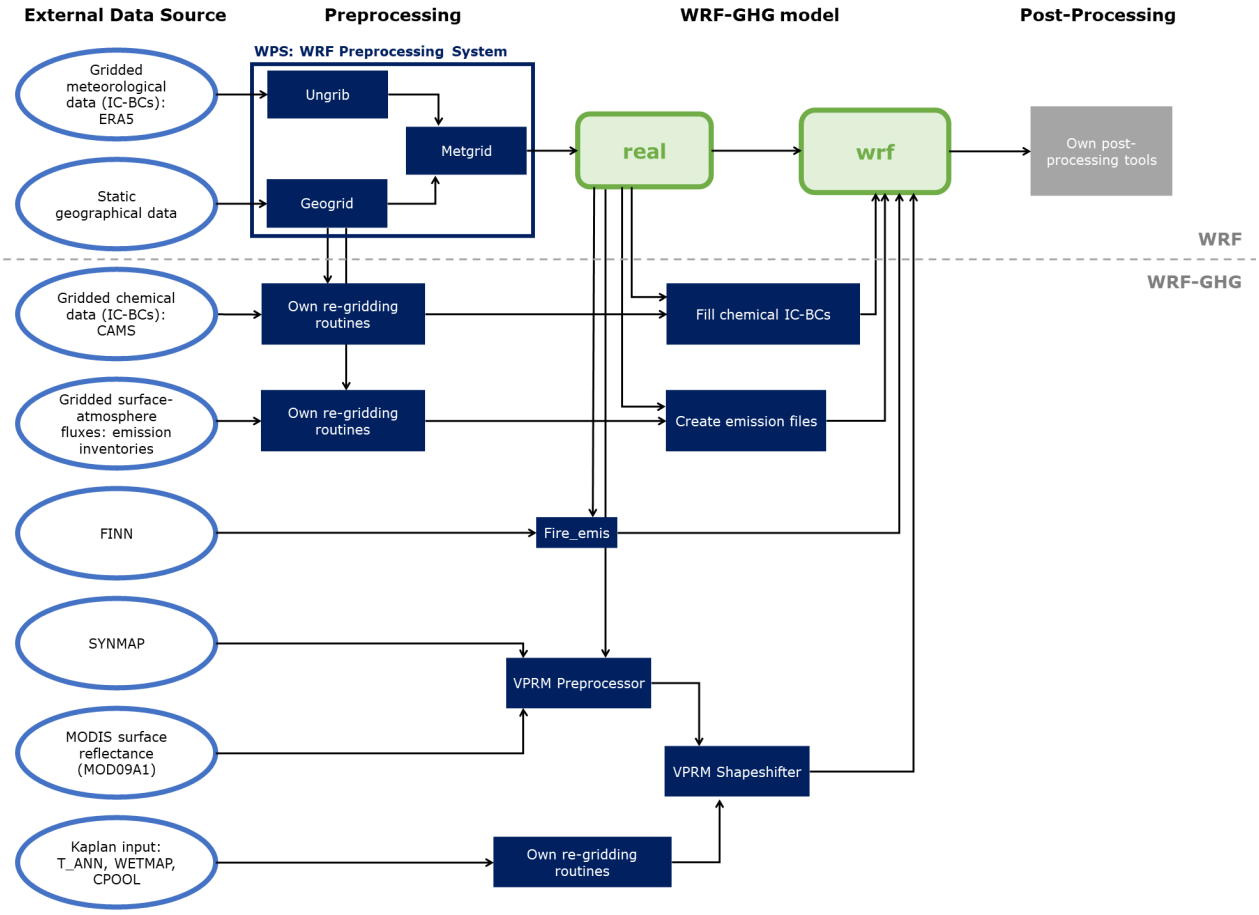

Figure 3.3: Flowchart of running WRF-GHG. Some of the essential components in the chart will be explained in the next sections.

of the base meteorological WRF model and is very well documented (WRF Users' Page: https://www2.mmm.ucar.edu/wrf/users/), while all items below represent additional steps specific to WRF-GHG.

Biogenic CO_2 fluxes

VPRM is a simple diagnostic model to calculate CO_2 exchange between the biosphere and the atmosphere using satellite indices (Mahadevan et al., 2008; Ahmadov et al., 2007). It is implemented in WRF-GHG in such a way that it uses the simultaneously computed 2m temperature and shortwave radiation to calculate the fluxes online. The biogenic CO_2 flux is represented by the Net Ecosystem Exchange (NEE) which in turn is the sum of the Gross Ecosystem Exchange (GEE) and Respiration (RES). Essentially, GEE describes the CO_2 uptake by photosynthesis and has a negative sign while RES is the CO_2 emission due to respiration processes and is positive.
The computation of this exchange is based on the satellite indices EVI (Enhanced Vegetation Index) and LSWI (Land Surface Water Index). They are derived from surface reflectance bands of the Moderate Resolution Imaging Spectroradiometer (MODIS) sensor onboard NASA's Aqua and Terra satellites. EVI is a good indicator of the vitality of vegetation and its greenness, and ranges from 0 (no vegetation) to 1 (very active vegetation). LSWI, on the other hand, represents the presence of moisture in the vegetation and soil and ranges from -1 (very dry) to 1 (very wet).
The main equations of the VPRM module in WRF-GHG are the following:

$$\begin{aligned} NEE &= GEE + RES \\ GEE &= -\lambda T_{scale} W_{scale} P_{scale} EVI \frac{SW}{1 + \frac{SW}{PAR_0}} \\ RES &= \alpha T_s + \beta. \end{aligned} \tag{3.1}$$

The factors of GEE are:

- λ: fixed parameter representing maximum quantum yield and empirical adjustments to the other parameters.
- T_{scale}: parameter that represents the sensitivity of photosynthesis to temperature. It is a function of the 2m temperature T and fixed literature values of T_{min}, T_{max} and T_{opt} which represent the optimal and limit temperatures for photosynthesis to occur. T_{scale} is calculated as
$$\frac{(T - T_{min})(T - T_{max})}{(T - T_{min})(T - T_{max}) - (T - T_{opt}^2)}.$$
The parameter is set to 0 when the temperature goes below T_{min} or above T_{max}.
- W_{scale}: parameter to include the effect of water stress on photosynthesis. It is a function of LSWI:
$$\frac{1 + LSWI}{1 + LSWI_{max}},$$
where $LSWI_{max}$ is the maximum value within the growing season per pixel.

- P_{scale}: parameter that describes the dependence of photosynthesis on leaf age. It uses the satellite indices EVI and LSWI to represent the leaf expansion and senescence phases. Generally P_{scale} is computed as $(1 + LSWI)/2$, except after the bud burst and before the senescence phases when the leaves are at their maximum expansion, then P_{scale} is set to 1. The transition between these phases is defined based on a threshold for EVI: $EVI_{min} + 0.55(EVI_{max} - EVI_{min})$.

- EVI: the Enhanced Vegetation Index representing vegetation health to describe the fraction of incident light absorbed by the photosynthetically active vegetation.

- SW: shortwave radiation as computed by WRF.

- PAR_0: empirically fixed parameter illustrating the half-saturation value.

The equation for RES is essentially made up by the parameters α, β and the surface temperature T_s. For the latter the model field for the 2m temperature T is used while the other parameters are empirically defined by comparing with flux tower data. As for the λ and PAR_0 parameters, default values for α and β over a couple of regions (USA, Europe, Tropics) are fixed within the model code and should be selected by the user. If alternative values are available, these should be manually included by the user.

Within WRF-GHG, the above equations are computed for 7 vegetation classes separately: evergreen trees, deciduous trees, mixed trees, shrubland, savanna, cropland and grassland. In fact there is an eighth category representing all barren, urban or snow-covered land surfaces where no vegetation is present and the biogenic CO_2 flux is set to 0. Then, for every grid cell, the weighted average of these values is taken using the fraction of every vegetation class in that cell. This information is taken from the high resolution global land cover product SYNMAP (Jung et al., 2006). The extraction of the vegetation indices from MODIS and regridding to the WRF model domain is done by two separate programs written in R and distributed by MPI-BGC: the *VPRM preprocessor* and the *VPRM shapeshifter* (see also Fig. 3.3). These tools also map the different SYNMAP vegetation classes to the 7 VPRM categories and regrid them to the WRF grid, and write all variable fields into NetCDF files which can be given as input to WRF-GHG.

To complete the description of how VPRM is implemented within WRF-GHG, it should be noted that some of the above parameters have slightly different calculations for specific vegetation types. As grassland and shrubland are xeric systems, i.e. they are better adapted to low water conditions, the W_{scale} parameter is calculated as

$$\frac{LSWI - LSWI_{min}}{LSWI_{max} - LSWI_{min}},$$

when $LSWI_{max} > 0$ and 0 otherwise. Similarly, $P_{scale} = 1$ for evergreen trees and $P_{scale} = (1 + LSWI)/2$ for savanna and grasslands, independent of the growing season.
Finally, remark that Eq. 3.1 differs slightly from Mahadevan et al. (2008) in that the Photosynthetically Active Radiation (PAR) is used instead of SW for the calculation of GEE.

However, they are closely related by $SW \sim 0.505 \cdot PAR$, so one only has to be careful when taking parameter values from literature to check which version of the equation is used and adjust the parameters accordingly.

Biogenic CH_4 fluxes

Within WRF-GHG, the online calculation of biogenic CH_4 is split into three parts: wetlands, termites, and soil uptake. In personal communication with other WRF-GHG users at MPI-BGC in Jena, it was advised not to use the soil uptake model due to detected irregularities, suggesting that modifications may be needed for proper implementation. Further, the wetland model by Kaplan (2002) requires additional external input and has only been employed in one study: Beck et al. (2013), who integrated it within WRF-GHG. Given that there are established offline inventories, such as the global WetCHARTs climatology (Bloom et al., 2017), which is widely used and deemed reliable, we opted to use this instead. Furthermore, for the regions we are focusing on, the contribution of wetland CH_4 emissions is not anticipated to be significant compared to other sources. Consequently, we have included emissions from the WetCHARTs climatology as a separate tracer and only the termite model will be explained below.

The computation of CH_4 emissions from termites follows Sanderson (1996). There, fluxes are described as the product of termite biomass (g m^{-2}) and CH_4 emission rates (μ g CH_4 / (g termite h^{-1})) per ecological region (or vegetation class). These values were determined by observations and given in Table 3 of Sanderson (1996) or Table 3.1 below. For every WRF grid, the value corresponding with the land use category that was determined during the initialization process is used for the termite flux. The distinction that Sanderson (1996) makes for the new world (America, Australia) and the old world (Europe, Asia, Africa) is applied by selecting the corresponding option in the model configuration file. These fluxes do not depend on any meteorological variable within WRF, only the land use category is used. This information is generally downloaded from the WPS (WRF Preprocessing System) geographical static data website, where two options are available: USGS 24-category or IGBP-Modified MODIS 20-category dataset. In the current work, the latter was used and the corresponding mapping and CH_4 emissions are given in Table 3.1.

WRF-GHG user guide

Following its integration into WRF-Chem in 2012, WRF-GHG lacks a dedicated user manual. The official documentation for WRF-Chem only briefly covers WRF-GHG due to the model's wide spectrum of options. In 2019, I had the opportunity to learn the fundamentals of running this model during a visit to the Max Planck Institute for Biogeochemistry (MPI-BGC) in Jena, Germany, and received valuable support from their scientists in the subsequent years. To share the insights gained during my PhD research with the broader modeling community, I wrote a general 'User Guide for WRF-GHG', which synthesizes essential information from the model's code, the WRF-Chem User's Guide, Emissions Guide, and the report by Beck

Ecological region of Sanderson (1996)	Biomass	Emissions old world	Emissions new world	IGBP-Modified MODIS 20-category Land Use Category
Tropical rain forest	11.0	6.16	5.64	Evergreen broadleaf forest
Raingreen forest	8.0	6.16	5.64	Evergreen needleleaf forest
Temperate forest	3.0	1.77	1.77	Deciduous broadleaf forest Deciduous needleleaf forest Mixed forests
Savannah/grassland (arid)	0.96	7.60	2.90	Savannas
Temperate grassland, prairie	5.2	1.77	1.77	Grasslands
Farmland, settlement	5.38	3.90	3.00	Croplands
Patchy wood, crop/grass	2.25	3.90	3.00	Cropland, Natural vegetation mosaic
Mediterranean tree/shrub	5.3	4.13	4.13	Closed Shrubland Open Shrubland
Dry highland shrub	2.7	4.13	4.13	Barren of Sparsely vegetated

Table 3.1: Mapping between ecological regions of Sanderson (1996) and WRF land use categories and corresponding biomass (g m^{-2}) and emission (μg CH_4 g $termite^{-1}h^{-1}$) values as implemented in WRF-GHG.

et al. (2011). This guide is publicly available through the BIRA-IASB data repository: https://doi.org/10.18758/Q6RAPNEU (Callewaert, 2024).

3.2 Model input data

This section outlines the external data sources utilized for the WRF-GHG simulations, presented sequentially as depicted in the flowchart in Fig. 3.3, from top to bottom.

3.2.1 Initial and lateral boundary conditions

As already briefly mentioned in Sect. 3.1.1, initial and lateral boundary conditions (IC-BCs) are required for limited area models to include information about the state of the atmosphere before the simulations start: the initial condition, and during the simulations over the rest of the globe (outside the model domain): the lateral boundary condition. The IC-BCs for WRF-GHG contain both meteorological fields and tracer fields and are coming from external data sets. This data should be processed into an appropriate input format and is then read by the model before starting the simulations.
The meteorological input data is handled by the WRF Preprocessing System (WPS), while it is up to the user to select the appropriate tools to handle the chemical input data, see Fig. 3.3. In the current work, this is done in Python using the Climate Data Operator (CDO) software (Schulzweida, 2020/2023). For the meteorological IC-BCs, ERA5 is used while for the tracers we apply the Copernicus Atmosphere Monitoring Service (CAMS) reanalysis, both provided by the European Center for Medium-Range Weather Forecasts (ECMWF). A brief description of each data set is given below.

ERA5

ERA5 is the global reanalysis data set of ECMWF providing estimates of a large number of atmospheric, ocean-wave and land-surface quantities. The reanalysis uses 4D-Var data assimilation based on the Integrated Forecast System (IFS) model CY41R2 to ensure consistency over a long period. Currently, hourly fields are available from 1940 up to the present. The hourly data for this study was retrieved through the C3S Climate Data Store (CDS, https://cds.climate.copernicus.eu/), both on single levels (for lower atmospheric and land surface quantities, GRIB1 format, Hersbach et al. (2023b)) and on pressure levels (for upper air fields, GRIB2 format, Hersbach et al. (2023a)). There are 137 vertical model levels up to 0.01 hPa following a hybrid pressure/sigma system. The native resolution of ERA5 is 31 km (or 0.28125°), however for convenience the data on CDS is regridded to a regular latitude-longitude grid of 0.25°.
The following surface level parameters are used: sea ice area fraction, sea surface temperature, volumetric soil water (layer 1-4), surface pressure, snow depth, mean sea level pressure, soil temperature (level 1-4), 10m u wind component, 10m v wind component, 2m temperature, 2m dewpoint temperature, land-sea mask and skin temperature.
At the model levels, the following parameters are used: geopotential, temperature, u wind component, v wind component, specific humidity and the logarithm of surface pressure.

CAMS reanalysis

The CAMS reanalysis is a global data set of atmospheric composition that is based on 4D-Var data assimilation and the IFS CY42R1 model of ECWMF with several updates to the aerosol and chemistry modules. In fact, there are two separate data sets: the EAC4 reanalysis with full chemistry and aerosols and the EGG4 greenhouse gas reanalysis focusing on the long-lived greenhouse gases CO_2 and CH_4 (Inness et al., 2019). They both cover the period 2003 until 2020 and the EAC4 reanalysis even extends to 2022. The sub-daily fields can be retrieved from the Atmosphere Data Store (ADS, https://ads.atmosphere.copernicus.eu/), but for this thesis we have used the GRIB2 data that was already available on the BIRA-IASB servers at a 3-hourly frequency for EGG4 and 6-hourly frequency of EAC4. The tracers are provided on 60 hybrid sigma/pressure levels up to 0.1 hPa with a horizontal resolution of approximately 80 km on a reduced Gaussian grid.
To drive our WRF-GHG simulations at the boundaries, we use the mass mixing ratio of CO from EAC4 while from EGG4 we take the mass mixing ratios of CO_2 and CH_4.

3.2.2 Static geographical data

The *geogrid* program of the WRF Preprocessing system (see Fig. 3.3) establishes the model domains and interpolates various terrestrial datasets to these domains. This time-invariant data includes for example soil and land use categories, terrain height, monthly vegetation fraction and albedo. Global datasets for these mandatory fields are downloaded from the WPS Geographical Static Data Downloads page at different resolutions:
https://www2.mmm.ucar.edu/wrf/users/download/get_sources_wps_geog.html .

3.2.3 Emission inventories

Most of the CO_2, CH_4, and CO emissions in WRF-GHG originate from external inventories, with the exception of the biogenic fluxes detailed earlier (Sect. 3.1.3). Users are responsible for sourcing and correctly managing this data to integrate it into the model simulations. A wide range of gridded emission datasets is available for this purpose, covering specific geographical regions or the entire globe, targeting individual species or multiple gases, focusing on various processes, and offering diverse spatial and temporal resolutions. Table 3.2 provides a brief overview of the anthropogenic emission inventories used in this thesis. Table 3.3 lists the datasets considered for ocean fluxes, biomass burning, and wetland emissions.

To correctly use these data sets as input into WRF-GHG, the user should process these emissions with a tool set of his own choice, as there is no single tool available for this purpose. This is a consequence of the large variety of options within WRF-Chem. More specifically, the emission data should be spatially regridded to the WRF model grid, converted to the expected unit (mol km^{-2} h^{-1}) and written into NetCDF files with appropriate dimensions, variables and attributes such that the model code can handle the incoming information. In this thesis, the processing was done in Python and using the CDO software for regridding.

Table 3.2: Summary of the anthropogenic emission inventory data sets used in this thesis with their main properties.

Abbreviation	Long name	Creator	Spatial coverage	Resolution	Temporal coverage	Frequency	Species	References
EDGAR v5.0	Emissions Database for Global Atmospheric Research	European Commission JRC[1]	Global	0.1°	1970 – 2015 GHG v6.0 to 2018, GHG v8.0 to 2020, AP v6.1 to 2018	Annual	CO_2, CH_4, CO, ⋯	Monforti-Ferrario et al. (2019)
CAMS-GLOB-ANT v5.3	Global Anthropogenic emission database of CAMS[2]	CAMS[2] CNRS[3] NOAA – ESRL[4]	Global	0.1°	2000 - 2023	Monthly, Yearly	CO_2, CH_4, CO, ⋯	Granier et al. (2019), Soulie et al. (2023)
ODIAC 2020b	Open-source Data Inventory for Anthropogenic CO_2	NIES[5]	Global	30 arcsec	2000 – 2019	Annual	CO_2	Oda and Maksyuto (2011) Oda et al. (2018) Oda and Maksyuto (2020)
FFDAS v2.2	Fossil Fuel Data Assimilation System	Dr. Peter Rayner (University of Melbourne) Dr. Kevin Robert Gurney (Northern Arizona University)	Global	0.1°	1997 - 2015	Hourly	CO_2	Asefi-Najafabady et al. (2014)
PKU-FUEL v2		PKU[6] LSCE[7]	Global	0.1°	1960 - 2014	Monthly	CO_2, CO, ⋯	Liu et al. (2015) Zhong et al. (2017) Wang et al. (2013)
REAS v3.2.1	Regional Emission inventory in Asia	NIES[5]	Asia	0.25°	1950 - 2015	Monthly	CO_2, CO, ⋯	Kurokawa and Ohara (2020)
MEIC-China v1.3	Multi-resolution Emission Inventory for China	Tsinghua University	Mainland China	0.25°	2008 - 2017	Monthly	CO_2, CO, ⋯	Li et al. (2017) Zheng et al. (2018)

[1]Joint Research Center
[2]Copernicus Atmosphere Monitoring Service
[3]Centre National de la Recherche Scientifique
[4]National Oceanic and Atmospheric Administration - Earth System Research Laboratories
[5]National Institute for Environmental Studies
[6]Peking University
[7]Laboratoire des Sciences du Climat et de l'Environnent

Table 3.3: Summary of the biogenic and biomass burning emission inventory data sets used in this thesis with their main properties.

Abbreviation	Long name	Creator	Spatial coverage	Resolution	Temporal coverage	Frequency	Species	References
	Global dataset of air-sea CO_2 fluxes based on SOCAT[1] and SOCCOM[2]	NOAA[3]	Global	1°	1982 - 2017	Monthly	CO_2	Bushinsky et al. (2019) Landschützer et al. (2019)
CT2019B	CarbonTracker	NOAA[3]	Global	1°	2000 - 2018	Monthly 3-hourly	CO_2	Jacobson et al. (2020)
GFAS	Global Fire Assimilation System	CAMS[4]	Global	0.1°	2003 - 2023	Daily	CO_2, CH_4, CO, ⋯	Kaiser et al. (2012)
FINN v1.5 / v2.5	Fire Inventory from NCAR[5]	NCAR[5]	Global	0.1° and 1 km	2002 – 2021	Daily	CO_2, CH_4, CO, ⋯	Wiedinmyer et al. (2006) Wiedinmyer et al. (2011) Wiedinmyer et al. (2023)
WetCHARTs v1.0	Global 0.5-deg Wetland Methane Emissions and Uncertainty	ORNL[6]	Global	0.5°	2015	Monthly	CH_4	Bloom et al. (2017)

[1]Surface Ocean CO_2 Atlas Database
[2]Southern Ocean Carbon and Climate Observations and Modeling
[3]National Oceanic and Atmospheric Administration
[4]Copernicus Atmosphere Monitoring Service
[5]National Center for Atmospheric Research
[6]Oak Ridge National Laboratory

Temporal profiles for anthropogenic emissions

In general, anthropogenic emissions from offline inventories are reported on an annual or monthly basis. In reality, the emission of species varies from day to day, and even from hour to hour. In the weekends, for example, there is usually less traffic than on weekdays, and some industrial activities might be reduced. The same holds for daytime hours versus nighttime hours. To cope with this, scientists have developed data sets of temporal profiles that can be multiplied with emissions at lower temporal frequency to make them more realistic. The idea behind this is that the more accurate the emissions are that are used as input for chemistry transport models, the more accurate the resulting simulated concentrations will be. In this thesis, I have explored three different data sets of temporal profiles, created by Guevara et al. (2021), Crippa et al. (2020a) and Nassar et al. (2013). Each data set will be briefly presented below.

Guevara et al. (2021) The Copernicus Atmosphere Monitoring Service TEMPOral profiles (CAMS-TEMPO) developed by Guevara et al. (2021) provide temporal profiles for a variety of chemical species (including CO_2, CH_4 and CO) at monthly, weekly, daily and hourly frequency. As the name of this data set suggests, it is following the spatial resolution (0.1°) and source sector classification from the CAMS global anthropogenic inventory (CAMS-GLOB-ANT). The definition of the profiles is based on international statistics and meteorological parameterizations. The temporal variation of emissions from the energy industry, residential combustion and road transportation is country- or even grid cell dependent, while other sectors show spatially constant monthly, weekly or daily variation. Some sectors, such as the energy industry, have different profiles for different pollutants. The monthly profiles are already applied to the CAMS-GLOB-ANT data set while the remaining weekly, daily and hourly profiles from 2000 up to 2020 are available to download through the Emissions of atmospheric Compounds and Compilation of Ancillary Data (ECCAD, eccad.aeris-data.fr) platform.

Crippa et al. (2020a) The high resolution temporal profiles of Crippa et al. (2020a) are developed in the context of the EDGAR inventory. A corresponding classification of over 20 source sectors is made, describing the monthly and hourly variation of these processes. These sector-specific profiles are also country-specific, taking into account different holidays and weekend definition, and can be applied to a wide set of pollutants. This extensive set of temporal profiles is available at figshare: https://doi.org/10.6084/m9.figshare.c.4780547.v1 (Crippa et al., 2020b).

Nassar et al. (2013) The Temporal Improvements for Modeling Emissions by Scaling, or TIMES, data set by Nassar et al. (2013) provides global profiles to temporally dissaggregate CO_2 emissions in weekly and diurnal fluxes. In contrast to the first two data sets as described above, the TIMES profiles are not sector-dependent and are available at a spatial resolution of 0.25°. The day-to-day and hour-to-hour variability is country-dependent. The scale factors can be downloaded at https://doi.org/10.15485/1463822 (Nassar, 2013).

Due to the correspondence between the data sets of temporal profiles and emissions, it is straightforward to use the temporal profiles of Guevara et al. (2021) together with the CAMS-GLOB-ANT emissions and those of Crippa et al. (2020a) with the EDGAR emissions. When only the total emissions are used in simulations, instead of those for each sector separately, or when there is no sector information available, the scaling factors by Nassar et al. (2013) are the easiest way to implement some temporal variation into the fluxes.
However, during the case study of Xianghe (Chapter 5), the need emerged to apply some temporal disaggregation to the sector-specific emissions of for example REAS, PKU-FUEL or MEIC-China. These inventories provide emissions in 4 or 5 broad sectors such as residential combustion, industrial processes, power plants, agriculture and transportation, which is much less than in CAMS-GLOB-ANT or EDGAR, where the classification contains at least 11 or 24 sectors, respectively. In order to apply the temporal factors of these sub-sectors to the broader ones, the following methodology was applied:

- Choose a set of temporal profiles to proceed with. For the Xianghe case study, I have chosen the EDGAR profiles (Crippa et al., 2020a).
- Create a mapping between the EDGAR sub-sectors and the more broader sectors of REAS, PKU-FUEL and MEIC-China. This is given in Table 3.4.
- Obtain temporal profiles for the broader sectors by weighing them with the EDGAR v6.0 emissions: for every broad sector, compute the hourly and daily variation in EDGAR v6.0 flux by multiplying the annual flux with the Crippa et al. (2020a) profiles for every sub-sector. Then, sum up all sub-sector fluxes following the mapping in Table 3.4 to get a total emission for every broad sector, but with a high temporal resolution. Then divide this sum by the total emission at low temporal resolution (annual or monthly) to retrieve the relative weight of every hour for each broad sector. These are then the temporal profiles for the broad sectors.
- Multiply the EDGAR-weighted profiles with the total flux for each of the broad sectors in the targeted inventory.

3.2.4 VPRM input: SYNMAP and MODIS surface reflectance

To enable the online calculation of biogenic CO_2 fluxes within WRF-GHG, external data is required as input: a land cover product and a surface reflectance satellite product, as outlined in Sect. 3.1.3. This work utilizes the SYNMAP land cover product from Jung et al. (2006) and the 8-day MODIS/Terra surface reflectance product (MOD09A1). The first of these two datasets is downloaded from a wepage (https://www.bgc-jena.mpg.de/4758306 /bsi_vprmpreproc) hosted by MPI-BGC that also serves as the main hub for accessing the *VPRM Preprocessor*, a tool written in R that is used to process both datasets. SYNMAP was created in 2005 as the 'best estimate' of the Global Land Cover Characterization Database (GLCC), Global Land Cover 2000 (GLC2000), and the MODIS land cover product, and covers the globe at a resolution of 1 km.
Further, the MODIS product MOD09A1 is publicly available at the download page of

EDGAR	REAS	PKU-FUEL	MEIC-China
Residential	Domestic	Residential and commercial	Residential
Combustion in manufacturing industry Production of foods Production of chemicals Production of iron and steel Production of non-ferrous metals Production of non-metallic minerals Production of pulp and paper Production and use of other products Application of solvents Non-energy use of fuels Solid waste disposal Waste water handling	Industry	Industry	Industry
Energy industry Fossil fuel fires Fuel production and transmission Oil refineries Transformation industry	Power plants (point and non-point)	Energy production	Power
Agriculture soils Enteric fermentation Manure management Agricultural waste burning		Agriculture	Agriculture
Road transport	Road transport	Transportation	Transportation
Non-road transport	Other transport		

Table 3.4: Mapping between emission sectors of EDGAR, REAS, PKU-FUEL and MEIC-China inventories in order to apply the temporal profiles of Crippa et al. (2020a).

NASA's Land Processes Distributed Active Archive Center (LP DAAC): https://e4ftl01.cr.usgs.gov/MOLT. It provides the global surface reflectance in seven spectral bands with a spatial resolution of 500 m, which is used to calculate the vegetation indices EVI and LSWI.

3.3 Model configuration

The configuration of the WRF-GHG model is a crucial step in ensuring that the simulation accurately represents the processes involved in greenhouse gas dynamics. This section outlines the key components of the model setup where choices need to be made to optimize its performance and ensure the relevance of the model output. These decisions include the configuration of the model domain, the choice of grid spacing and nesting options, as well as the selection of appropriate physics schemes, emission inventories, and specialized configurations such as the VPRM parameter optimization and tagged tracer adaptation. More details on the specific choices made for the two locations studied in the context of this thesis are given in the respective chapters (Ch. 4 and 5).

3.3.1 Model domain setup

For accurate simulations, it is essential to center the area of interest, which is a specific observatory in this case, within the model domain. Further, the extent of the domain must balance computational efficiency with the physical relevance of the simulation. While a larger domain increases computational costs, a smaller domain risks being overly influenced by boundary conditions, potentially undermining the benefits of high-resolution modeling. To avoid this, it is recommended to define a domain of at least 100×100 grid cells, ensuring that the lateral boundaries are sufficiently distant from the area of interest and strong forcings.
For simulations involving passive tracers, the domain should additionally include as much of the relevant emission sources as possible. This allows these emissions to be represented as specific tracers rather than being included in the background signal.
Grid spacing determines the model's resolution, requiring a careful balance between detail and computational resources. Changes in horizontal resolution impact not only atmospheric transport but also the representation of topography and surface fluxes. Higher resolutions generally improve both diurnal and day-to-day variability of atmospheric species, with significant benefits observed in mountainous regions due to more accurate orographic representation. However, to fully benefit from higher resolution, it is necessary that the resolution of the flux information corresponds with the model's spatial resolution.
Equally important is vertical resolution, with 40 to 60 vertical levels across the troposphere recommended to accurately resolve atmospheric processes, especially within the boundary layer and the free atmosphere. A model top pressure level of 50 hPa is typically sufficient to capture the necessary dynamics without imposing excessive computational demands.
Finally, nesting is employed to achieve finer resolution than what is provided by the global analysis data used at the lateral boundaries (in the current study, the IC-BCs fields have a resolution of approximately 25 km for meteorological fields and 80 km for tracers). This involves creating nested domains within the primary domain to refine the coarse input data. A nesting ratio of 3:1 or 5:1 is generally recommended to ensure that the central grid cells

of the child domain align with those of the parent domain, thereby maintaining accuracy. It is also important to position the nest boundaries well within the coarse domain, away from steep topography and the outer boundaries, to minimize potential boundary-related issues.

3.3.2 Simulation period selection

The selection of the simulation period is mainly determined by the availability of observational datasets for model evaluation and high-quality input data. It is essential to choose a period for which global meteorological and chemical analyses are available to drive the simulations, alongside up-to-date emission data, to ensure the accuracy of the model output. Since the current study aims at comparing model simulations with observational data, the chosen periods should additionally align with the observational time series and minimize any gaps in the data coverage.

3.3.3 Physics schemes options

As mentioned in Sect. 3.1, the WRF modeling system offers a wide variety of physical parameterization options. While certain combinations of physics schemes can produce notably different results, particularly for specific atmospheric processes or regions of interest, not all changes in parameterizations lead to significant impacts on the final results. Selecting appropriate physics schemes is an important step in configuring WRF-GHG, but testing every possible combination is neither feasible nor necessary for most studies. This is particularly relevant given that there is no universal set of physics options that performs best under all conditions - the capability of a particular combination depends on many factors such as domain size, geographical location, initialization data, and the specific atmospheric phenomena being studied. While all WRF options simulate the basic processes, making it unlikely to choose a completely "wrong" combination, certain schemes have been tested more extensively than others. Therefore, a practical approach is to focus initial sensitivity tests on well-established schemes, as supported by literature on similar WRF applications, and then evaluate if additional testing of alternative parameterizations is warranted for the specific research objectives.

3.3.4 Emission inventory selection

High-quality emission inventories are essential components for accurately simulating greenhouse gas concentrations, as the quality of the emission data directly influences the model's ability to reproduce observed GHG patterns. Ideally, these inventories include all emission processes and source sectors for each species at very high spatial and temporal resolutions. However, in practice, such precise data are often unavailable and are typically estimated using various approaches, as briefly discussed in Sect. 3.2.3. To achieve the most realistic simulation output, it is important to select inventories that offer the highest resolution (both spatial and temporal) and the most comprehensive coverage of source sectors, with data that aligns as closely as possible with the time period of the simulations.

3.3.5 VPRM parameter optimization

As described in Sect. 3.1.3, the online calculation of biogenic CO_2 fluxes based on VPRM requires a table of fixed values for four parameters (α, β, λ and PAR_0) over seven vegetation categories. Ideally, these parameters are tuned using flux tower data from the region of interest to best match the local conditions. In the absence of such data, it is recommended to use one of the three parameter tables that are provided within the model code for Europe, US and the tropics, or to use parameter values optimized for a similar region, as reported in the literature. The first option is available in the *namelist.input* configuration file while the latter requires adapting the model source code and recompiling.

3.3.6 Tagged tracer customization

WRF-GHG includes a default set of tracers that represent various sources, such as background concentrations from lateral boundary conditions, anthropogenic emissions, biogenic emissions, biomass burning, and oceanic sources. These tracer fields can be modified according to the study's objectives with minor adjustments to the model source code, followed by a recompilation. For instance, if the emission inventory provides sector-specific data, it might be beneficial to define additional tracers to track these sectors separately. This allows for a more detailed analysis of how different processes contribute to overall GHG concentrations. However, while defining additional tracers offers greater insight, it is important to consider the computational cost, as more tracers will increase the overall computation time.
For the simulations in this work, we modified the biogenic CH_4 tracers to save the three components (soil uptake, termite, and wetland emissions) in separate fields. This adjustment was made due to concerns about the quality of the soil uptake model, as discussed in Sect. 3.1.3. Additionally, for the case study on Réunion Island, the default tracers were used, while in the Xianghe domain, the anthropogenic tracer was divided into different source sectors, as will be explained in the respective chapters.

3.4 Running the model

Running the model executable (*wrf.exe*), which integrates the governing equations, is actually the final step in the modeling process, see also Fig. 3.3. Before reaching this stage, it is essential to have a properly configured *namelist.input* file and all the required input files, such as emissions and meteorological data, in the correct formats. The entire process of running WRF-GHG in the context of this thesis can be broadly divided into two main stages: preparing data on the BIRA-IASB servers and organizing all necessary input data on the High-Performance Computing (HPC) system, where the WRF-GHG model is ultimately run.
The preprocessing stage involves preparing the necessary external datasets for input into the model. This task is primarily managed on the BIRA-IASB compute servers using a set of Python scripts. Once the relevant intermediate files are ready, they are transferred to the HPC, where the WRF-GHG model runs. The HPC, a shared resource among the three institutes at the Space Pole (Royal Meteorological Institute of Belgium, Royal Observatory

of Belgium, and BIRA-IASB), is a powerful SGI Rackable Cluster with 2688 compute cores distributed across 112 Linux servers, each containing 24 cores. Designed for parallel computing, the HPC uses the PSPro batch scheduler to manage jobs, which are queued based on a complex formula considering factors such as the number of compute cores, duration, memory requirements, and the number of jobs already submitted.
The handling of input data on the HPC and the execution of WRF-GHG are managed by a series of Bash scripts. Once the model run is completed, the output files are copied back to the BIRA-IASB servers, as the HPC is not intended for long-term storage and does not offer backup services. A detailed step-by-step guide for this entire process is provided in appendix C.

3.5 Comparing model and observations

After generating the dataset of simulated concentration fields, the next step is to compare it with observations in a process known as *post-processing*. This involves reading the output files, extracting relevant data, performing additional calculations for accurate comparisons, and conducting data analysis. This is all done in Python. The following sections provide a detailed overview of the approach used to compare the model output with ground-based observations. It is crucial that the model output and greenhouse gas observations are co-located both temporally and spatially. Additionally, when comparing model profiles with remote sensing measurements, further calculations are required to account for the retrieval process, as explained in subsequent sections. The approach for comparing the model data with the measurements is outlined separately for in situ and FTIR remote sensing data in Sect. 3.5.1 and 3.5.2, respectively.

3.5.1 Comparing with in situ observations

Local ground-based observations usually have a high temporal frequency, going from every minute to every hour to everything in between. The model output is hourly and represents the status of the atmosphere at exactly that time step, not averaged. To compare the model with in situ observations, a time window should be selected over which the high-frequency measurements are averaged. With a large time window, possible measurement errors are weakened. However, a too large window might result in values that are not fully representing the specific time step anymore. A too small time window, on the other hand, might also result in representation errors due to the variability inherent to the in situ measurement of species close to the surface. It is important to find a good balance here, where a time window of 10 to 30 minutes is common.

For spatial co-location, generally the model grid cell covering the instrument is used. This is done by selecting the model cell of which the center coordinates (mass points θ) are closest to those of the measurement. In case of complex orography, such as for mountain sites, an adjacent grid cell might be more appropriate. This should be evaluated for every case separately.
Finally, the measurement and model should match vertically. There are several options

depending on the instrument setup. If the instrument is located close to the ground, the lowest model level is likely representative. However, Picarro gas analyzers are frequently installed at or near towers with varying sampling heights. In such situations it might be more appropriate to compare the observations with another model level, or to interpolate the model profile to the specific sampling altitude, depending on the model vertical resolution. This altitude can be expressed in meter above ground level (m.g.l.) or meter above sea level (m.s.l.), which additionally includes information on the surface altitude of the site (above sea level). Caused by horizontal discretization of the Earth's surface within the model, the surface altitude at the selected grid cell does not always match the real value. The discrepancy will be larger for regions with strong altitude differences and for low model resolutions. We can vertically interpolate the model profile to the instrument altitude m.g.l. or m.s.l., however both options will likely be different, depending on how accurate the model is representing the surface altitude. As the strongest concentration gradients are often found close to the surface, it is suggested to give priority to the altitude relative to the ground level, as opposed to sea level. As such, the impact of mixing processes in the lowest layer of the atmosphere on the measured concentrations will be better captured by the model value.

3.5.2 Comparing with remote sensing observations

As explained in Sect. 1.3.2, FTIR observations are the result of a retrieval method to extract information on the atmospheric composition in a column of air from a solar absorption spectrum. The outcome is influenced by instrument characteristics as well as retrieval technique choices (such as the a priori information). To take this into account, the Rodgers and Connor (2003) smoothing approach can be used when comparing FTIR data with other data sets. In the case of comparing with (high resolution) model data, it is common to assume that the model profile represents the true atmospheric profile, and that the smoothed model profile is then how it would be retrieved by the (lower vertical resolution) FTIR instrument. The general smoothing equation is given below. However, since the retrieval approach is slightly different for the FTIR observations associated with either TCCON or NDACC, some network-specific features are discussed further for the two networks separately.

The smoothing procedure is performed on all model-data pairs within a certain time frame (usually 30 min around the model hourly time step), after which the resulting *Xgas* values X_G are averaged to gain a unique model-data pair for every hour where FTIR observations are available. Spatially, the model profile directly above the grid cell of the instrument is used, similarly as for in situ measurements.

In general, the smoothed model profile of species G is calculated as:

$$\boldsymbol{\nu}_G^{smooth} = \boldsymbol{\nu}_G^{apriori} + \boldsymbol{A} \cdot (\boldsymbol{\nu}_G^{WRF} - \boldsymbol{\nu}_G^{apriori}), \tag{3.2}$$

where $\boldsymbol{\nu}_G^{apriori}$ is the a priori volume mixing ratio profile and $\boldsymbol{A}$ the averaging kernel matrix of the FTIR measurement, while $\boldsymbol{\nu}_G^{WRF}$ is the original model profile. The smoothed X_G is then computed using the smoothed profile and the profile of dry air. A mathematical description

of such computation is given in Appendix B.

In order for the data to fit in Eq. 3.2, the model profile needs to be regridded to the same vertical grid as the a priori profile and averaging kernel matrix (the 'FTIR grid'). A first obstacle is that usually WRF-GHG simulates the atmosphere up to 50 hPa, while the FTIR observations use solar radiation and thus cover the complete atmosphere of the Earth. To cope with this altitude difference, we extend the model profile above its upper limit with the a priori profile. Then, to regrid the extended profile to the FTIR grid with conservation of mass, the layer height weighted regridding algorithm of Langerock et al. (2015) is applied. This includes the calculation of a transformation matrix $\boldsymbol{D}$ that contains the fraction of how each layer of the model grid is covered by a FTIR grid layer. This matrix is then multiplied with the extended partial column profile: $\boldsymbol{PC}_G^{regrid} = \boldsymbol{D} \cdot \boldsymbol{PC}_G$. A partial column (mol m^{-2}) of species G represents the integrated amount of that species within a specific vertical section of an atmospheric column: it is the product of its volume mixing ratio in that section (mol mol^{-1}), the number density of dry air (mol m^{-3}) and its thickness (m).
Finally, to apply the smoothing equation 3.2, we divide this regridded partial column profile of G with the regridded partial column profile of dry air to retrieve the regridded volume mixing ratio profile of G:

$$\boldsymbol{\nu}_G^{regrid} = \frac{\boldsymbol{PC}_G^{regrid}}{\boldsymbol{PC}_{da}^{regrid}}.$$

Smoothing equation 3.2 can then be rewritten as:

$$\boldsymbol{\nu}_G^{smooth} = \boldsymbol{\nu}_G^{apriori} + \boldsymbol{A} \cdot (\boldsymbol{\nu}_G^{WRF,regrid} - \boldsymbol{\nu}_G^{apriori}), \tag{3.3}$$

TCCON

The smoothing equation for TCCON data looks a bit different than in Eq. 3.3 because the averaging kernel matrix is provided as a column averaging kernel vector $\boldsymbol{a}$. Instead of calculating a smoothed mixing ratio profile, a smoothed total column is calculated:

$$TC_G^{smooth} = TC_G^{apriori} + \boldsymbol{a} \cdot \left(\boldsymbol{PC}_G^{WRF,regrid} - \boldsymbol{PC}_G^{apriori} \right), \tag{3.4}$$

where the regridded partial column profile of WRF-GHG is computed as described above and in Appendix B. For the smoothed X_G, the smoothed total column TC_G^{smooth} has to be divided by the total column of dry air TC_{da}. Here we can choose to use the atmospheric profiles of pressure, temperature and water vapour from the TCCON retrieval or from the WRF-GHG simulations. As both sources are already included in Eq. 3.4, it is most appropriate to use a combination and calculate the smoothed X_G as:

$$X_G^{smooth} = \frac{TC_G^{apriori}}{TC_{da}^{TCCON}} + \boldsymbol{a} \cdot \left(\frac{\boldsymbol{PC}_G^{WRF,regrid}}{TC_{da}^{WRF,regrid}} - \frac{\boldsymbol{PC}_G^{apriori}}{TC_{da}^{TCCON}} \right). \tag{3.5}$$

An alternative is to not use the model dry air partial column at all, but only the model's volume mixing ratio profile and use the TCCON a priori information in every term:

$$X_G^{smooth} = \frac{1}{TC_{da}^{TCCON}} \left(TC_G^{apriori} + \boldsymbol{a} \cdot \left(\boldsymbol{\nu}_G^{WRF,regrid} \boldsymbol{PC}_{da}^{TCCON} - \boldsymbol{PC}_G^{apriori} \right) \right). \tag{3.6}$$

As mentioned above, we can take into account the altitude difference between the WRF-GHG simulations and the FTIR observations by extending the WRF-GHG data above the model limit to the top of the atmosphere. There is an alternative where the FTIR X_G is scaled to be representative for the atmospheric column from surface up to 50 hPa. Both methods are an option, but we must be consistent and manipulate both data sets (model and observations) in a comparable way.
When choosing to scale the X_G up to 50 hPa, the smoothed X_G from WRF-GHG is calculated as in Eq. 3.5 or 3.6 where the sum is taken over those layers i below 50 hPa. The TCCON retrieval provides only information on the total column, so the data of the a priori profile is used to compute the column below the model limit: a scaling factor is calculated that represents the fraction of the total column up to 50 hPa to the total column based on the same fractions in the a priori profile. By multiplying this factor with the retrieved total column, a column representative for the lowest part of the troposphere (up to 50 hPa) is then calculated.
The alternative is to use the original FTIR data, representing the full atmospheric column, and to manipulate the WRF-GHG data. Then, the procedure is as described above in Eq.3.5 or 3.6 where the sum is taken over all layers i.

NDACC

The NDACC retrieval results in mixing ratio profiles and an associated averaging kernel matrix, so Eq. 3.3 can be applied directly. The smoothed X_G then follows by multiplication with the dry air partial column profile. Here, we can choose to use either the information from the model or from the NDACC a priori:

$$X_G^{smooth} = \frac{TC_G^{smooth}}{TC_{da}^{NDACC}} = \frac{\sum_i \nu_G^{smooth} PC_{da,i}^{NDACC}}{\sum_i PC_{da,i}^{NDACC}}, \tag{3.7}$$

or

$$X_G^{smooth} = \frac{TC_G^{smooth}}{TC_{da}^{WRF,regrid}} = \frac{\sum_i \nu_G^{smooth} PC_{da,i}^{WRF,regrid}}{\sum_i PC_{da,i}^{WRF,regrid}}, \tag{3.8}$$

As explained for the TCCON data, we can compare NDACC with WRF-GHG by truncating the observed X_G values to 50 hPa or by extending the model data above this value. The truncated NDACC X_G is easily calculated from the retrieved profile and taking the sum of only those layers below 50 hPa (see Eq. B.4). Similarly the smoothed WRF-GHG X_G is calculated from Eq. 3.7 or 3.8 and taking the sum over the layers i below 50 hPa.
For the second option the sum is taken over all layers when computing both observed and simulated X_G.

Chapter 4

Atmospheric GHG patterns in a remote tropical environment: a WRF-GHG study at Réunion Island

This chapter focuses on the in situ and column observations of CO_2, CH_4 and CO at Réunion Island. The observations from the two sites on the French Island (Saint-Denis and Maïdo) are simulated with the WRF-GHG model. The model performance is assessed and the main source sectors and meteorological parameters that influence the observed time series are discussed. In June 2022, this chapter was published in the peer-reviewed journal Atmospheric Chemistry & Physics and is available online:

Callewaert, S., Brioude, J., Langerock, B., Duflot, V., Fonteyn, D., Müller, J.-F., Metzger, J.-M., Hermans, C., Kumps, N., Ramonet, M., Lopez, M., Mahieu, E., and De Mazière, M.: Analysis of CO_2, CH_4, and CO Surface and Column Concentrations Observed at Réunion Island by Assessing WRF-Chem Simulations, Atmospheric Chemistry and Physics, 22, 7763–7792, doi: 10.5194/acp-22-7763-2022, 2022

Atmos. Chem. Phys., 22, 7763–7792, 2022
https://doi.org/10.5194/acp-22-7763-2022

Atmospheric Chemistry and Physics
Open Access
EGU

Analysis of CO_2, CH_4, and CO surface and column concentrations observed at Réunion Island by assessing WRF-Chem simulations

Sieglinde Callewaert[1], Jérôme Brioude[2], Bavo Langerock[1], Valentin Duflot[2], Dominique Fonteyn[1], Jean-François Müller[1], Jean-Marc Metzger[3], Christian Hermans[1], Nicolas Kumps[1], Michel Ramonet[4], Morgan Lopez[4], Emmanuel Mahieu[5], and Martine De Mazière[1]

[1]Division of Sources and Sinks of Atmospheric Constituents: Infrared observations, Royal Belgian Institute for Space Aeronomy (BIRA-IASB), Brussels, Belgium
[2]Laboratoire de l'Atmosphère et des Cyclones (LACy), UMR 8105, Saint-Denis, Réunion Island, France
[3]UAR 3365 – OSU Réunion, Université de La Réunion, Saint-Denis, Réunion Island, France
[4]Laboratoire des Sciences du Climat et de l'Environnement (LSCE), IPSL, UMR 8212 (CEA, CNRS, UVSQ), Gif-sur-Yvette, France
[5]UR SPHERES, Department of Astrophysics, Geophysics and Oceanography, University of Liège, Liège, Belgium

Correspondence: Sieglinde Callewaert (sieglinde.callewaert@aeronomie.be)

Received: 9 February 2022 – Discussion started: 18 February 2022
Revised: 20 May 2022 – Accepted: 25 May 2022 – Published: 15 June 2022

Abstract. Réunion Island is situated in the Indian Ocean and holds one of the very few atmospheric observatories in the tropical Southern Hemisphere. Moreover, it hosts experiments providing both ground-based surface and column observations of CO_2, CH_4, and CO atmospheric concentrations. This work presents a comprehensive study of these observations made in the capital Saint-Denis and at the high-altitude Maïdo Observatory. We used simulations of the Weather Research and Forecasting model coupled with Chemistry (WRF-Chem), in its passive tracer option (WRF-GHG), to gain more insight to the factors that determine the observed concentrations. Additionally, this study provides an evaluation of the WRF-GHG performance in a region of the globe where it has not yet been applied.

A comparison of the basic meteorological fields near the surface and along atmospheric profiles showed that WRF-GHG has decent skill in reproducing these meteorological measurements, especially temperature. Furthermore, a distinct diurnal CO_2 cycle with values up to 450 ppm was found near the surface in Saint-Denis, driven by local anthropogenic emissions, boundary layer dynamics, and accumulation due to low wind speed at night. Due to an overestimation of local wind speed, WRF-GHG underestimates this nocturnal buildup. At Maïdo, a similar diurnal cycle is found but with much smaller amplitude. There, surface CO_2 is essentially driven by the surrounding vegetation. The hourly column-averaged mole fractions of CO_2 (XCO_2) of WRF-GHG and the corresponding TCCON observations were highly correlated with a Pearson correlation coefficient of 0.90. These observations represent different air masses to those near the surface; they are influenced by processes from Madagascar, Africa, and further away. The model shows contributions from fires during the Southern Hemisphere biomass burning season but also biogenic enhancements associated with the dry season. Due to a seasonal bias in the boundary conditions, WRF-GHG fails to accurately reproduce the CH_4 observations at Réunion Island. Furthermore, local anthropogenic fluxes are the largest source influencing the surface CH_4 observations. However, these are likely overestimated. Furthermore, WRF-GHG is capable of simulating CO levels on Réunion Island with a high precision. As to the observed CO column (XCO), we confirmed that biomass burning plumes from Africa and elsewhere are important for explaining the observed variability. The in situ observations at the Maïdo Observatory can characterize both anthropogenic signals from the coastal regions

and biomass burning enhancements from afar. Finally, we found that a high model resolution of 2 km is needed to accurately represent the surface observations. At Maïdo an even higher resolution might be needed because of the complex topography and local wind patterns. To simulate the column Fourier transform infrared (FTIR) observations on the other hand, a model resolution of 50 km might already be sufficient.

1 Introduction

Major greenhouse gases such as carbon dioxide (CO_2) and methane (CH_4) have a direct impact on the radiative forcing of the atmosphere. They are the main drivers of climate change, since their global mean concentrations have increased over the industrial era by about 47 % and 156 %, for CO_2 and CH_4, respectively, as a result of human activities (IPCC, 2021). Carbon monoxide (CO), on the other hand, is not a greenhouse gas but indirectly affects the lifetime of CH_4 in the atmosphere through its competing reaction with OH. Additionally, it plays a major role in air pollution as it participates in the formation of tropospheric ozone and urban smog.

The importance of these gases, hereafter all referred to as greenhouse gases (GHGs), has led to the establishment of global observation networks to monitor their trends and variability. Ground-based remote sensing networks such as the Network for the Detection of Atmospheric Composition Change (NDACC) and the Total Carbon Column Observing Network (TCCON) are known for their long time series of accurate column observations (De Mazière et al., 2018; Wunch et al., 2011). The Fourier transform infrared (FTIR) spectrometer observations carried out in these networks use direct sunlight to measure the absorption of atmospheric trace gases along the line of sight and provide precise information on the total column abundance or vertical profile of GHGs and other species. They are used by scientists worldwide to detect changes in the atmospheric composition, to improve our understanding of the carbon cycle, or to provide validation for space-based measurements. Recently, these kinds of observations from mobile low-cost FTIR spectrometers within the Collaborative Carbon Column Observing Network (COCCON) have been used to constrain fluxes in urban regions (Hase et al., 2015; Vogel et al., 2019; Makarova et al., 2021). In addition to FTIR observations, surface in situ observations of these gases are carried out to better constrain sources and sinks on an even smaller scale. Both observation types contain valuable information on the emissions and transport of these species and are complementary.

Réunion Island (55° E, 21° S) is a French island in the Indian Ocean, situated about 550 km east of Madagascar. It hosts one of the very few atmospheric observatories in the tropical Southern Hemisphere, which provides both ground-based in situ and FTIR observations of GHGs, contributing to the Integrated Carbon Observation System (ICOS) and NDACC and TCCON, respectively. GHG observations at Réunion Island are made at two sites, i.e., in the capital Saint-Denis and at the high-altitude Maïdo Observatory (Baray et al., 2013). Several studies have already investigated the factors influencing the observations at Réunion Island. Zhou et al. (2018) analyzed the trends and seasonal cycles of CH_4 and CO by comparing the ground-based remote sensing and in situ observations. They noticed a distinct seasonal cycle in the column-averaged dry air mole fractions of CO (XCO), with peak values between September and November, linked to the biomass burning season in Africa and South America, which confirmed the earlier work from Duflot et al. (2010). Furthermore, backward trajectory simulations revealed different origins of air masses observed at Réunion Island near the surface and higher up, resulting in surface CO concentrations that are systematically lower than XCO. Near the surface, air masses generally originate in the Indian Ocean, while those higher up come from Africa and South America. The ability to detect biomass burning plumes at Réunion Island was also reported by Vigouroux et al. (2012). The available XCO_2 time series has, however, not yet been investigated. Additionally, the Maïdo Observatory hosts a wide range of instruments, of which the measurements have already been used by a variety of scientists to characterize the processes that occur at this particular location (Guilpart et al., 2017; Foucart et al., 2018; Duflot et al., 2019; Verreyken et al., 2021). However, the in situ observations at the Maïdo Observatory of the longer-lived species, CO_2 and CH_4, have not yet been studied in detail, and this applies also to the available surface measurements at Saint-Denis.

Therefore, the aim of the current work is to make a comprehensive description and analysis of in situ and column observations of CO_2, CH_4, and CO at Réunion Island, both at Saint-Denis and Maïdo. To gain more insight into the factors that influence the observed concentrations, we will rely on the simulations of the widely used Weather Research and Forecasting model coupled with chemistry (WRF-Chem; Skamarock et al., 2021) in its passive tracer option called WRF-GHG (Beck et al., 2013). This regional atmospheric model simulates 4D fields of CO_2, CH_4, and CO, resulting from their sources, sinks, and transport in the troposphere, without interaction with other species, while accounting for the meteorology. The model makes it possible to separate each chemical compound into several tracers representing the contributions of different emissions sources within the model domain, such as anthropogenic, biogenic, biomass burning, and oceanic. Moreover, it supports the online calculation of

biogenic CO_2 fluxes following the Vegetation Photosynthesis and Respiration Model (VPRM; Mahadevan et al., 2008). Thus far, applications of WRF-GHG have mainly focused on CO_2 to study city emissions (Pillai et al., 2016; Feng et al., 2016; Park et al., 2018; Zhao et al., 2019) or to evaluate the VPRM model (Ahmadov et al., 2007; Jamroensan, 2013; Dayalu et al., 2018; Hu et al., 2020; Park et al., 2020). It has also been used in combination with in situ and column observations, flux towers, and satellite measurements to better understand the carbon cycle (Pillai et al., 2010, 2012; Liu et al., 2018; Li et al., 2020). The model has shown to be an excellent tool for studying regional carbon budgets and is therefore very well suited to our needs. Few studies have used WRF-GHG to simulate CH_4 and CO, and these studies focused on explaining enhancements identified by satellite instruments (Beck et al., 2013; Dekker et al., 2017; Tsivlidou, 2018; Borsdorff et al., 2019; Dekker et al., 2019; Verkaik, 2019). Hence, this work additionally aims at evaluating the model performance for these species in a region where it has not yet been applied. This might potentially draw attention to shortcomings in the model, thus allowing and motivating the model community to improve it.

This paper focuses on the factors that influence the observed GHG concentrations and their variations at Saint-Denis and the Maïdo Observatory. In particular, it addresses the following questions: (1) to what extent are the observations influenced by local and nearby sources and sinks or long-range transport of emitted gases? (2) What are the different contributions (of anthropogenic, biogenic, biomass burning, and ocean fluxes) to the observed concentrations, both at the surface and in the total column? (3) How accurate is WRF-GHG in simulating the different observation types of the three gases (CO_2, CH_4, and CO) in the Southern Indian Ocean region, in particular at Saint-Denis and at the Maïdo Observatory? What are its strengths and weaknesses?

The structure of this document is as follows. Section 2 describes the location of the observation sites at Réunion Island, the general transport patterns, the GHG-measuring instruments, and the data sets used in this study. Details on the model setup and input inventories are described in Sect. 3. Section 4 constitutes the main part of this work. First, the model performance is evaluated with regard to meteorological fields, both at the surface and higher up, in Sect. 4.1. The model assessment and data analysis at Saint-Denis and Maïdo are discussed in Sect. 4.2 and 4.3, respectively. Finally, the impact of model resolution is discussed in Sect. 5, and conclusions are drawn in Sect. 6.

2 Observations at Réunion Island

The data used in this study come from two observation sites on Réunion Island, namely Saint-Denis (referred to as SDe from now on; 20.9014° S, 55.4848° E; 85 m a.s.l. or meters above sea level), which is the capital city and is situated close to the northern coast, and the Maïdo Observatory (referred to as MA from now on; 21.0796° S, 55.3841° E; 2155 m a.s.l.), which is close to the top of a mountain ridge on the northwestern side of the island. Currently, each site is equipped with a Fourier transform infrared (FTIR) spectroscopy instrument and an in situ cavity ring-down spectroscopy (CRDS) analyzer, both of which are described more in detail below. These instruments measure the column-averaged dry air mole fractions and local near-surface mole fractions, respectively. The locations of both sites on the island are shown in Fig. 1.

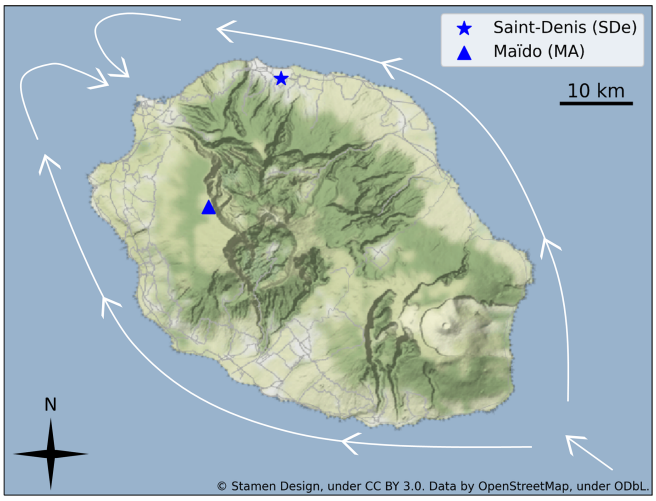

Figure 1. Map of Réunion Island, indicating the location of the two measurement sites: Saint-Denis (star) and Maïdo (triangle). The white arrows roughly illustrate the local wind patterns, which are generated by the trade winds and the orography of the island.

2.1 Climate and transport patterns

The atmospheric transport around Réunion Island is controlled by the position of the Intertropical Convergence Zone (ITCZ) and the south Hadley cell (Baldy et al., 1996; Foucart et al., 2018). During a large part of the year, a strong subtropical high induces steady southeasterly trade winds near the surface and westerlies aloft. Hence, the air above Réunion Island is characterized by a wind (and temperature) inversion causing generally clear skies which are common during the dry season (Baldy et al., 1996; Lesouëf et al., 2011; Baray et al., 2013). Typically, this (colder) dry season lasts from May to November (Foucart et al., 2018). In austral summer (January to March) the ITCZ moves south, sometimes reaching Réunion Island. This results in weaker trade winds and often heavy rains, resulting in the (warmer) wet season in those months (Baldy et al., 1996; Foucart et al., 2018).

With its high altitudes (up to 3000 m a.s.l.), Réunion Island represents a sudden obstacle for the stable southeasterly trade winds. In combination with the inversion layer, this causes a blocking on the windward side and wind flow splitting (and

accelerating) around the island to form counter-flowing vortices on the northwestern (lee) side (Lesouëf et al., 2011). This is illustrated by the white arrows in Fig. 1. Moreover, the split flow is under the influence of thermally driven circulations (so-called trade breathing); nighttime downslope and land breezes push the trade wind offshore, whereas daytime upslope and sea breezes allow the wind to pass over coastal areas (Lesouëf et al., 2011, 2013). These circulations are the dominant (daily) wind pattern on the northwestern side of Réunion Island (where MA is situated), which is sheltered from the trade winds (Lesouëf et al., 2011; Baray et al., 2013; Guilpart et al., 2017; Verreyken et al., 2021).

2.2 Saint-Denis

Saint-Denis is the capital of Réunion Island, located on the coast in the northern part of the island. As of 2018, there were 309 635 inhabitants in the metropolitan area of Saint-Denis, with a population density of about 1100 km^{-2}. The city lies on a slope between the ocean and the nature reserve of La Roche Écrite (ultimately reaching a height of 2276 m).

The observations at SDe are made on top of a building at the University of Réunion Island (85 m a.s.l.). In situ mole fractions of CO_2 and CH_4 have been measured by a CRDS analyzer (Picarro G1301) since August 2010, in collaboration with the Laboratoire de l'Atmosphère et des Cyclones (LACy), the Observatoire des Sciences de l'Univers de la Réunion (OSU-R), and the Laboratoire des Sciences du Climat et de l'Environnement (LSCE). The measurements are available with a time frequency of 1 min, and the uncertainties on the measured mole fractions are about 0.1 ppm (parts per million) and 2 ppb (parts per billion), for CO_2 and CH_4, respectively.

In September 2011, the Royal Belgian Institute for Space Aeronomy (BIRA-IASB) installed a high-resolution Bruker IFS 125HR FTIR at SDe, next to the Picarro analyzer. This instrument is primarily dedicated to measuring the near-infrared (NIR; 4000–16 000 cm^{-1}) spectra and contributes to TCCON (Wunch et al., 2011). The solar spectra are used to retrieve the total column-averaged dry air mole fractions of CO_2, CH_4, and CO (De Mazière et al., 2017). The standard TCCON retrieval algorithm, called GGG2014, applies a profile scaling, therefore deriving information on the total column only and not on the vertical profile. TCCON measurements have been calibrated to World Meteorological Organization (WMO) standards, so it is assumed that there are no systematic biases compared to in situ measurements (Wunch et al., 2010). More detail on both instruments can be found in Zhou et al. (2018).

2.3 Maïdo

The Maïdo Observatory (2155 m a.s.l.) is located close to the summit of a mountain with the same name, which has an altitude of about 2200 m.a.s.l. and is situated in the western part of the island. The observatory is devoted to long-term atmospheric monitoring in the tropical region of the Southern Hemisphere and houses a variety of atmospheric measurement instruments such as lidar systems, spectroradiometers, and in situ gas and aerosol analyzers (Baray et al., 2013). To the west of MA is a gentle slope reaching the coastal areas and the ocean, while the summit lies to the east of the site, followed by a cliff leading to the caldera of Cirque de Mafate. The area around MA is covered by mountain shrubs and heathlands (Duflot et al., 2019).

The mole fractions of all three gases (CO_2, CH_4, and CO) have been collected by a CRDS analyzer (Picarro G2401) at MA since December 2014 and were certified as ICOS atmospheric data in late 2019 (De Mazière et al., 2021). The measurements are available at a time resolution of 1 min, and the uncertainties are about 50, 1, and 2 ppb for CO_2, CH_4, and CO, respectively.

In March 2013, BIRA-IASB started operating a second Bruker IFS 125HR FTIR spectrometer, in addition to the one at SDe, for observing the solar spectra in the mid-infrared (MIR) range from 600 to 4500 cm^{-1} (Baray et al., 2013). These FTIR measurements are affiliated with NDACC. Gas mole fractions of CH_4 and CO are retrieved from the FTIR solar spectra by the SFIT4 algorithm, which is based on the optimal estimation method of Rodgers (2000). More information about the specific methods used can be found in Zhou et al. (2018). The final data consist of the retrieved vertical profiles, expressed as volume mixing ratio (VMR) profiles on a vertical altitude grid.

2.4 Meteorological measurements

The quality of the WRF-GHG simulations is evaluated against meteorological fields that are being measured in parallel at the two observation sites. More specifically, there are in situ measurements of 2 m temperature and 10 m wind direction and wind speed. These fields are measured by the Vaisala Weather Transmitter (model WXT510 at SDe and model WXT520 at MA) every 3 s.

Additionally, we will compare the WRF-GHG output with vertical profiles from operational daily meteorological Meteomodem M10 radiosonde launches performed by Météo-France at 12:00 UTC at Roland Garros Airport (4 km away from SDe). The Meteomodem M10 radiosondes provide measurements of temperature, pressure, and relative humidity with respect to water and zonal and meridional winds. A detailed description of this sensor can be found in Dupont et al. (2020).

3 WRF-GHG model

WRF-GHG is an abbreviation for the Weather Research and Forecast model coupled with Chemistry (WRF-Chem) in its passive tracer option (Skamarock et al., 2021; Beck et al., 2011). WRF-Chem simulates the emission, transport, mix-

ing, and chemical transformation of trace gases and aerosols simultaneously with the meteorology. In WRF-GHG, only CO_2, CO, and CH_4 are transported, and there are no chemical reactions simulated. Separate tracers for each compound represent the contribution from the fluxes within the model domains (d01–d03) from the following different categories: anthropogenic, biomass burning, biogenic (for CO_2 and CH_4 (termites)), ocean (for CO_2), and wetlands (for CH_4). Additionally, there is a so-called background tracer which represents the contribution of the initial and lateral boundary conditions. The sum of all tracers for a species is equal to the total modeled mole fractions. In this study, WRF-Chem version 4.1.5 is used.

In total, two time periods have been simulated, i.e., from 1 August 2015 until 1 May 2016 and from 1 July 2016 until 15 July 2017. These periods have been selected because then quite complete data sets are available from all considered instruments. The first 14 d in each period are regarded as the spin-up period and are not used in the model–data comparisons. The model provides 3D fields of CO_2, CH_4, CO, and meteorological fields every hour.

3.1 Emissions and initial and boundary conditions

An overview of the data that are used as input to the WRF-GHG model are given in Table 1 and described hereafter. The hourly meteorological initial and lateral boundary conditions (IC-BCs) are obtained from the European Centre for Medium-Range Weather Forecasts (ECMWF) global ERA5 reanalysis data set ($0.25° \times 0.25°$; Hersbach et al., 2018a, b), while the chemical IC-BCs are imported from the CAMS global reanalysis for greenhouse gases (EGG4, for CO_2 and CH_4) and reactive gases (EAC4, for CO; Inness et al., 2019). The data for CO_2 and CH_4 are available every 3 h, while data are available for CO every 6 h. These fields from the Copernicus Atmosphere Monitoring Service (CAMS) reanalysis are used to drive the background tracers. The IC-BCs of the tracers corresponding with the contribution from surface fluxes are set to zero.

The anthropogenic emissions for CH_4 and CO are taken from the Emission Database for Global Atmospheric Research (EDGAR). For CH_4, we have used the v5.0 Global Greenhouse Gas Emissions product (Crippa et al., 2019b), while for CO, the EDGAR v5.0 Global Air Pollutant Emissions product (Crippa et al., 2019a) was used. Furthermore, we performed simulations over a short period of a few days to test alternative inventories for anthropogenic CO_2 and CO fluxes. We concluded that the Open-Data Inventory for Anthropogenic Carbon dioxide (ODIAC2020; Oda and Maksyuto, 2015, 2011; Oda et al., 2018) was more representative for the anthropogenic CO_2 emissions, probably due to its much higher spatial resolution (1 km) compared to EDGAR (0.1°).

Similarly, we use a CO surface emission inventory at a resolution of 500 m, based on the posterior estimates of a mesoscale inverse model (Jérôme Brioude, personal communication, 2020), but only in the innermost domain d03. The atmospheric transport of the inverse model was calculated using the FLEXPART (FLEXible PARTicle dispersion model) Lagrangian dispersion model (Verreyken et al., 2019) coupled with the Meso-NH mesoscale model (Lac et al., 2018) at a resolution of 500 m and 60 vertical levels. FLEXPART-Meso-NH was run backward in time to calculate the source–receptor relationships between MA and the surface sources from the CO measurements at MA, from 4 April to 3 May 2019, during the BIO-MAIDO (Bio-physico-chemistry of tropical clouds at Maïdo, Réunion Island) campaign (Dominutti et al., 2022). The ODIAC CO_2 emission inventory was used a priori to benefit from its native spatial resolution of major urban areas. A scaling factor, based on the ratio between the mean CO enhancement above background and mean CO_2 enhancement above background, was applied on the CO_2 fluxes to obtain a priori surface CO fluxes. A temporal resolution of 1 h was used for the observed and simulated CO mixing ratios at MA. A lognormal distribution was assumed for the observation and surface flux errors (Brioude et al., 2012, 2013). Such an assumption better matches the CO distribution in the atmosphere and prevents the inversion from calculating negative fluxes.

The anthropogenic fluxes used within WRF-GHG are combined with a temporal emission factor from Nassar et al. (2013). Note that these factors are representative for CO_2 and might be less accurate for CO and CH_4.

Daily biomass burning emissions for all three gases are obtained from the Fire INventory from NCAR (FINN v1.5; Wiedinmyer et al., 2011). The biogenic CH_4 flux from wetlands is obtained from the WetCHARTs v1.0 ensemble (Bloom et al., 2017), while the biogenic CO_2 flux from oceans is taken from the observation-based global monthly gridded sea surface pCO_2 climatology by Landschützer et al. (2017), which also provides air–sea CO_2 fluxes. Finally, the biogenic CO_2 flux from the vegetation is simulated online using the VPRM model (Mahadevan et al., 2008; Ahmadov et al., 2007). This model uses the 2 m temperature and downward shortwave radiation calculated by WRF-GHG in combination with surface reflectance data from the Moderate Resolution Imaging Spectroradiometer (MODIS). Furthermore, it uses the global SYNMAP land cover data of 1 km resolution by Jung et al. (2006). Additionally, the VPRM requires a set of four model parameters for each vegetation class, dependent on the region of interest. Ideally, these parameters are optimized using a network of eddy flux towers. Since this is not available at Réunion Island, we use the set of parameters optimized by Botía et al. (2021), based on measurements from nine sites in the Amazon region in Brazil, created in the context of the Large Scale Biosphere–Atmosphere Experiment (LBA-ECO). Exact parameter values are given in Table A1 of Appendix A.

Table 1. Overview of data sets used as input for the WRF-GHG simulations.

	Species	Source	Time and spatial resolution
Initial and lateral boundary conditions	CO_2, CH_4 CO	CAMS reanalysis for greenhouse gases CAMS reanalysis for reactive gases	3 h, 0.75° 6 h, 0.75°
Anthropogenic flux (multiplied with temporal factors of Nassar et al., 2013)	CO_2 CH_4 CO	ODIAC2020 EDGAR v5.0 Global Greenhouse Emissions EDGAR v5.0 Global Air Pollutant Emissions (d01, d02) Jérôme Brioude (personal communication, 2020), (d03)	Monthly, 1 km (land), 1° (ocean) Yearly, 0.1° Yearly, 0.1° Yearly, 500 m
Biomass burning flux	CO_2, CH_4, CO	FINN v1.5	Daily, 1 km
Biogenic flux	CO_2 CH_4	Online (VPRM) Online, WetCHARTs v1.0	Hourly, model resolution Monthly, 0.5°
Ocean flux	CO_2	Observation-based global monthly gridded sea surface pCO_2 climatology	Monthly, 1°

3.2 Settings

To achieve a high-resolution model grid over Réunion Island, a configuration of three nested domains was established, going from a larger domain with a lower resolution to a smaller domain with a higher resolution. The domains are shown in Fig. 2. Their respective resolutions are 50, 10, and 2 km. The innermost domain, d03, covers Réunion Island and the two measurement sites completely. WRF-GHG uses a hybrid vertical coordinate, which is a coordinate that is terrain following near the ground and becomes isobaric higher up. In all our domains, the model has 60 vertical levels extending from the surface up to 50 hPa.

The following physical parameterization options are used: the Morrison two-moment scheme (Morrison et al., 2009) for microphysics, the Rapid Radiative Transfer Model for general circulation models (RRTMG) shortwave and longwave schemes (Iacono et al., 2008). The Eta similarity scheme (Janjić, 1994) for surface layer processes and the Unified Noah LSM (land surface model; Tewari et al., 2004) for the land surface. To choose between the diverse parameterization schemes for cumulus parameterization and planetary boundary layer (PBL) physics, several model test runs were made for a short simulation period of a couple of days and compared with the observed meteorology. As a result, the University of Washington turbulence kinetic energy (TKE) boundary layer scheme (Bretherton and Park, 2009) for PBL physics and the Grell–Freitas ensemble scheme (Grell and Freitas, 2014) for cumulus parameterization, but only in the largest domain (d01), were chosen for this study.

3.3 Data handling

The various observation types are dealt with in different ways for comparison with the model.

The surface observations (both meteorological fields and GHGs) are averaged over a period of 30 min around the hourly model time step. At SDe, we compare these data with the lowermost level of the model grid cell, whose center is closest to the location of the instrument. Because of the complex topography, the cell covering MA is less representative for the observatory, as its center is located behind the summit, in the caldera of Cirque de Mafate below. Model–data comparisons of the surrounding cells showed that the cell to the west of MA is more representative. Therefore, this alternative model grid cell, of which the center is only 1.3 km away from the observatory, is used in the analysis.

In order to compare similar quantities, the total column-averaged dry air mole fractions from TCCON and NDACC are truncated to the same atmospheric column that is simulated by WRF-GHG, e.g., from surface up to 50 hPa. This is needed because the FTIR data represent the total atmospheric column, whereas the WRF-GHG upper limit lies at around 21 km.

As NDACC additionally provides volume mixing ratio profiles, the column-averaged mole fractions are recalculated by taking only those layers below the model upper limit. For TCCON, only information on the total column is retrieved. Therefore, we multiply the TCCON data with a factor representing the ratio between the column-averaged mole fraction of the smaller column (up to 50 hPa) to that of the total column. This ratio is calculated from the a priori information. In the rest of this paper, all dry air column-averaged mole fractions (so-called Xgas) mentioned refer to this reduced atmospheric column only (surface up to 50 hPa). Due to the specific profile of the respective gases in the atmosphere, this scaling is more significant for XCH_4 than it is for XCO or XCO_2; the values generally increase after scaling

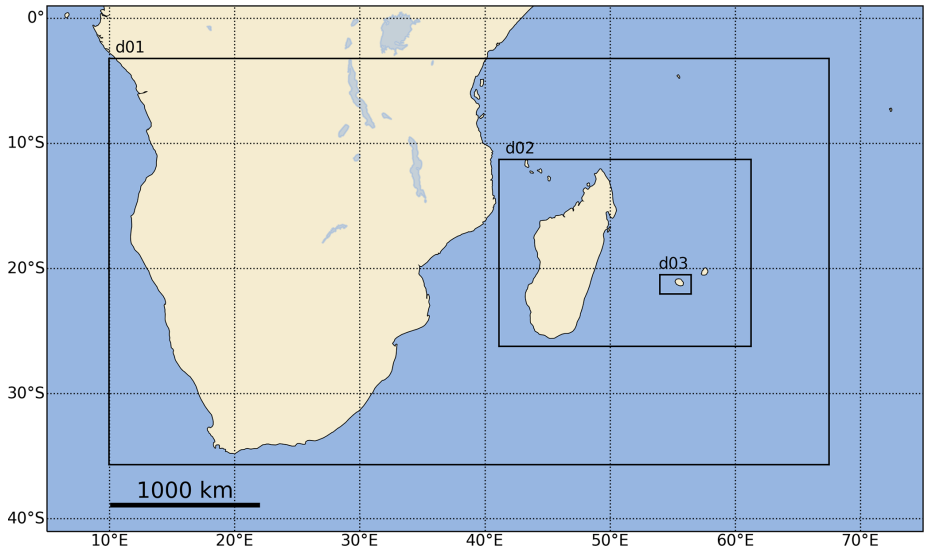

Figure 2. Location of the WRF-GHG domains, with horizontal resolutions of 50 km (d01), 10 km (d02), and 2 km (d03). All domains have 60 (hybrid) vertical levels extending from the surface up to 50 hPa.

by about 27–35 ppb for XCH_4, 3 ppb for XCO, and 0.25 ppm for XCO_2.

To compare with the hourly WRF-GHG outputs, the scaled mole fractions are averaged over a period of 30 min around the model time step. Furthermore, a smoothing is applied to the WRF-GHG profiles, according to Rodgers and Connor (2003). Because of the different characteristics of the TCCON and NDACC observing systems, this smoothing procedure is slightly different at the two sites. Technical details on how the smoothed dry air column-averaged mole fractions of WRF-GHG are calculated at SDe and MA can be found in Appendix B.

Table 2. Overview of the meteorological evaluation of the surface measurements at the two sites. The root mean square error (RMSE), mean bias error (MBE), and Pearson correlation coefficient (CORR) are shown.

	2 m temperature (C)		10 m wind direction (°)		10 m wind speed ($m\,s^{-1}$)	
	SDe	MA	SDe	MA	SDe	MA
RMSE	1.33	1.94	52.33	66.80	4.29	2.93
MBE	0.74	−0.35	–	–	3.83	1.59
CORR	0.93	0.83	0.72	0.76	0.73	0.27

4 Results

4.1 Meteorological evaluation

4.1.1 Surface measurements

To assess the general model performance, the hourly model output of d03 near the surface is compared with local measurements of 2 m temperature and 10 m wind direction and speed at both sites. Table 2 gives the root mean square error (RMSE), mean bias error (MBE), and Pearson correlation coefficient (CORR) of the model–data comparison over the complete time series (13 583 paired data points at SDe; 14 031 at MA).

The 2 m temperature is well simulated by WRF-GHG at both sites with very high correlation coefficients of 0.93 at SDe and 0.83 at MA and RMSE between 1 and 2 °C (1.33 at SDe, 1.94 at MA). Figure 3a–b compare the median diurnal cycle at both sites, which is very well reproduced by the model. Overall, higher temperatures are measured at SDe compared to MA because of the large difference in altitude between the sites (85 m a.s.l. compared to 2155 m a.s.l.).

The wind roses in Fig. 4 show the most-occurring 10 m wind directions and their corresponding wind speed. The 10 m wind direction of WRF-GHG correlates well with the measurements at both sites (correlation coefficients of 0.72 and 0.76). There is a larger error of the wind direction at MA (RMSE of 66.80°) compared to SDe (RMSE of 52.33°). At SDe, the wind is mainly from the east or southeast (trade winds); however, for calmer wind speeds ($< 2\,m\,s^{-1}$), the wind can also come from the south(west). WRF-GHG captures the dominant southeastern winds but does not simulate winds from the south. It highly overestimates the wind speed, with a mean bias error of $3.83\,m\,s^{-1}$ and a RMSE of $4.29\,m\,s^{-1}$. There is a clear diurnal cycle of the wind speed at SDe, shown in Fig. 3c, with stronger winds during the day and calmer conditions at night. As WRF-GHG follows the observed pattern, the correlation coefficient is still quite high (0.73). The overestimation might be caused

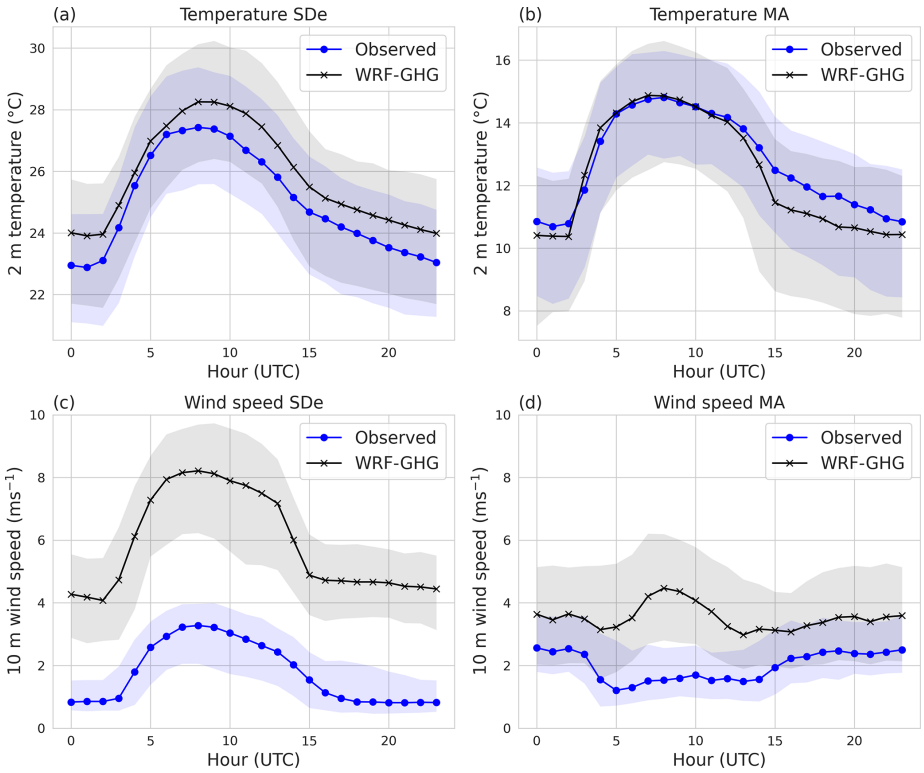

Figure 3. **(a–b)** Diurnal cycle of the 2 m temperature and **(c–d)** 10 m wind speed at both SDe and MA. The blue and black lines show the median values for every hour of the measurements and simulations, respectively. The shaded blue and gray areas indicate the corresponding interquartile ranges of the measurements and simulations, respectively. Hours are given in UTC (local time at Réunion Island is UTC+4). Note that the temperature plots have different y axes.

by an underestimation of the surface roughness of the city within WRF-GHG. Besides the unified Noah land surface model (see Sect. 3.2), no additional urban surface model was included in the simulations. Other studies using the WRF model often show wind speed overestimation above urban areas (Feng et al., 2016; Barlage et al., 2016; Zhang et al., 2009; Kim et al., 2013). Additionally, there is a large gradient in the surface wind speed near SDe caused by the presence of the strong trade winds. Therefore, an insufficient high model resolution might also be the cause for the wind speed overestimation.

At MA, on the other hand, the most common wind direction is east with some occurrences of westerly winds. This points to the typical thermally induced circulations during the day, whereby wind is driven from the coast upwards and sometimes reaches MA (Duflot et al., 2019). The prominent east winds illustrate the presence of overflowing trade winds. The simulated winds from WRF-GHG are mainly from the east, indicating that the larger errors at MA might be linked to the missing westerly wind components. This is likely due to the complex topography around the Maïdo Observatory and the model resolution (of 2 km), which might be insufficient for resolving these very local wind dynamics.

As to the wind speed at MA, the bias and RMSE are smaller (1.59 and 2.93 m s^{-1}, respectively) than at SDe, but the model is still overestimating the wind speed. Moreover, the correlation is very low at this site. The daily 10 m wind speed cycle at MA is less distinct than at SDe; however, at night the wind is more often faster (> 2 m s^{-1}) than during the day. This could be linked to the local wind dynamics around MA, where calmer upslope winds from the west often reach MA during the day, while at night the observatory is generally in the free troposphere under the influence of the faster trade winds (Guilpart et al., 2017).

4.1.2 Radiosonde profile measurements

Daily radiosonde profiles of air temperature, wind direction, wind speed, and relative humidity are compared with the model data to assess the accuracy of WRF-GHG on all levels of the troposphere. The profiles were matched as follows: for every data point measured by the radiosonde, the grid cell corresponding to its coordinate is selected. Next, the model profile (consisting of the meteorological field in the complete vertical column above the selected grid cell) is interpolated to the altitude of the measurement. This interpolated value is then paired with the value of the measurement. This results in a paired model–data profile for the four variables once every

day. An example of such a paired profile on 5 July 2016 is shown in Fig. 5. For every paired profile, the RMSE, MBE, and CORR statistics are calculated. This is done for a total of 267 d in the year 2016.

For the temperature, correlation coefficients are very high on all days (median is 0.99). Moreover, the RMSE values are quite small on most days (median is 1.07 °C), indicating that WRF-GHG can simulate the temperature in the troposphere quite accurately.

There is a good correlation for the wind direction and speed profiles as well. Half of the days in 2016 have a correlation coefficient higher than 0.87 for wind direction and 0.83 for wind speed. When calculating the RMSE of wind direction along the daily profiles, we find a median of 48.18°, while the median RMSE of the wind speed is 3.87 m s^{-1}. On most days, WRF-GHG is slightly underestimating the wind speed (median bias error is -1 m s^{-1}), which is in contrast with the overestimation found at the surface sites.

The profiles of relative humidity are analyzed up to an altitude of 15 km because the measurements are less accurate higher up. WRF-GHG correlates well with these profiles, with a correlation coefficient higher than 0.87 on 75 % of the days in 2016. The median RMSE on the daily profiles of relative humidity is only 11.6 %, showing a decent model performance.

Overall, we can conclude that the simulations of basic meteorological parameters are quite accurate along vertical profiles, where near the surface wind speed and direction agree less well with the observations.

4.2 GHG data at Saint-Denis

At SDe, the in situ surface mole fractions of CO_2 and CH_4 are measured together with the TCCON column-averaged dry air mole fractions of CO_2, CH_4, and CO. The comparison with the WRF-GHG simulations will be described in detail below, for each species and measurement type separately. The full time series of the observed and modeled data can be found in Appendix C. An overview of the statistics of the comparisons is given in Table 3.

4.2.1 Surface CO_2

The model–data comparison of the surface data shows a moderate correlation coefficient of 0.62 together with a relative large error of 9.17 ppm and a model underestimation of 5.39 ppm. The scatterplot in Fig. 6a indicates that these discrepancies arise from a model underestimation of the higher CO_2 mole fractions. The lower CO_2 concentrations are, in general, much better reproduced.

The CO_2 measurements at SDe show a clear diurnal cycle (see Fig. 7a), with lower values during the day and higher values during the night. The diurnal cycle of WRF-GHG reproduces this pattern but with much lower nighttime concentrations, leading to the moderate correlation found in Table 3.

Table 3. Overview of the WRF-GHG performance for hourly in situ and column observations of GHG at Réunion Island. The comparison with the column observations is based on the smoothed model profiles. There are no in situ CO data available at SDe (Saint-Denis) and no XCO_2 data at MA (Maïdo).

	SDe			MA		
	(X)CO_2 (ppm)	(X)CH_4 (ppb)	(X)CO (ppb)	(X)CO_2 (ppm)	(X)CH_4 (ppb)	(X)CO (ppb)
In situ						
RMSE	9.17	18.51	–	1.95	19.33	10.99
MBE	−5.39	9.04	–	−0.15	14.09	5.51
CORR	0.62	0.35	–	0.75	0.30	0.83
FTIR						
RMSE	0.75	10.26	8.08	–	10.80	7.37
MBE	−0.37	5.69	5.07	–	−5.65	1.81
CORR	0.90	0.31	0.89	–	0.37	0.90

As shown in the diurnal cycle in Fig. 7b, the main contributors to the total CO_2 signal in WRF-GHG, in addition to the background signal, are the anthropogenic and biogenic tracers. They correspond with anthropogenic and biogenic fluxes within the model domains (d01–d03) and show similar diurnal patterns with maxima at night and minima during the day. The influence of biomass burning or ocean fluxes is negligible at SDe.

In urban areas, anthropogenic pollution is generally trapped in and around the city, creating a so-called urban CO_2 dome (Idso et al., 2002). The strength of this dome is primarily dependent on the local emissions and variations in the boundary layer. In calm weather, near-surface air temperature inversions at night trap anthropogenic pollution near the ground in the shallow nocturnal boundary layer, leading to strongly enhanced CO_2 mixing ratios. During the day, solar radiation causes convective mixing of the air, creating a deep planetary boundary layer (PBL). The near-surface CO_2 concentrations are then diluted by this thorough mixing of air, and the urban dome extends to greater heights.

However, wind speed and direction can alter the strength of this urban CO_2 enhancement; at higher wind speeds (from 2 m s^{-1}), ventilation processes prevent strong CO_2 accumulation, while winds from rural areas could bring pristine air to the city (Idso et al., 2002; Rice and Bostrom, 2011; Massen and Beck, 2011; García et al., 2012; Xueref-Remy et al., 2018).

Within WRF-GHG, the main contributors to the simulated CO_2 in the grid cells around SDe are anthropogenic and peak during the day. The biogenic CO_2 flux at the grid cell of SDe is zero because the corresponding VPRM vegetation class is 100 % barren, urban, and built-up. Thus, the model assumes that there is no vegetation within the city. Given that Saint-Denis is the capital city of Réunion Island and has plenty of anthropogenic activities, the impact of local vegetation is probably very small, and these WRF-GHG fluxes appear re-

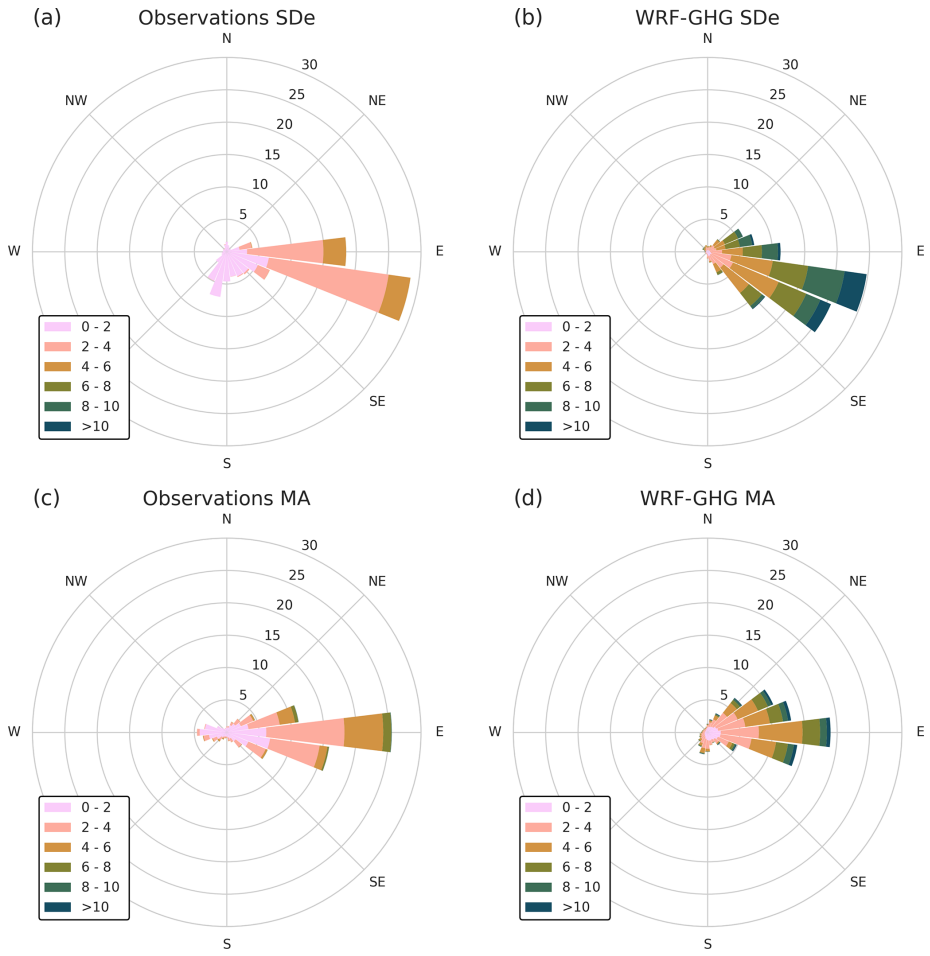

Figure 4. Wind rose from observations and WRF-GHG simulations at SDe **(a–b)** and at MA **(c–d)**. The colors indicate the associated wind speed (in m s^{-1}), while the lengths of the bars show the frequency of any wind direction binned by 15°, given in percentage.

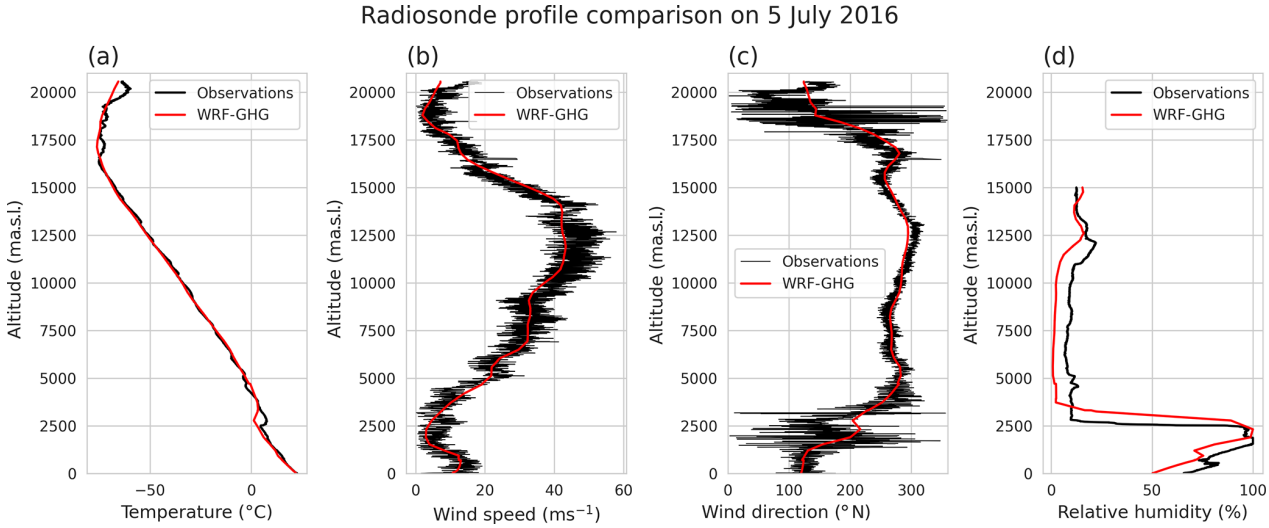

Figure 5. Example of the radiosonde data at Roland Garros Airport on 5 July 2016, compared with the model for **(a)** temperature, **(b)** wind speed, **(c)** wind direction, and **(d)** relative humidity. The black line represents the measured values. The red line is the corresponding WRF-GHG data.

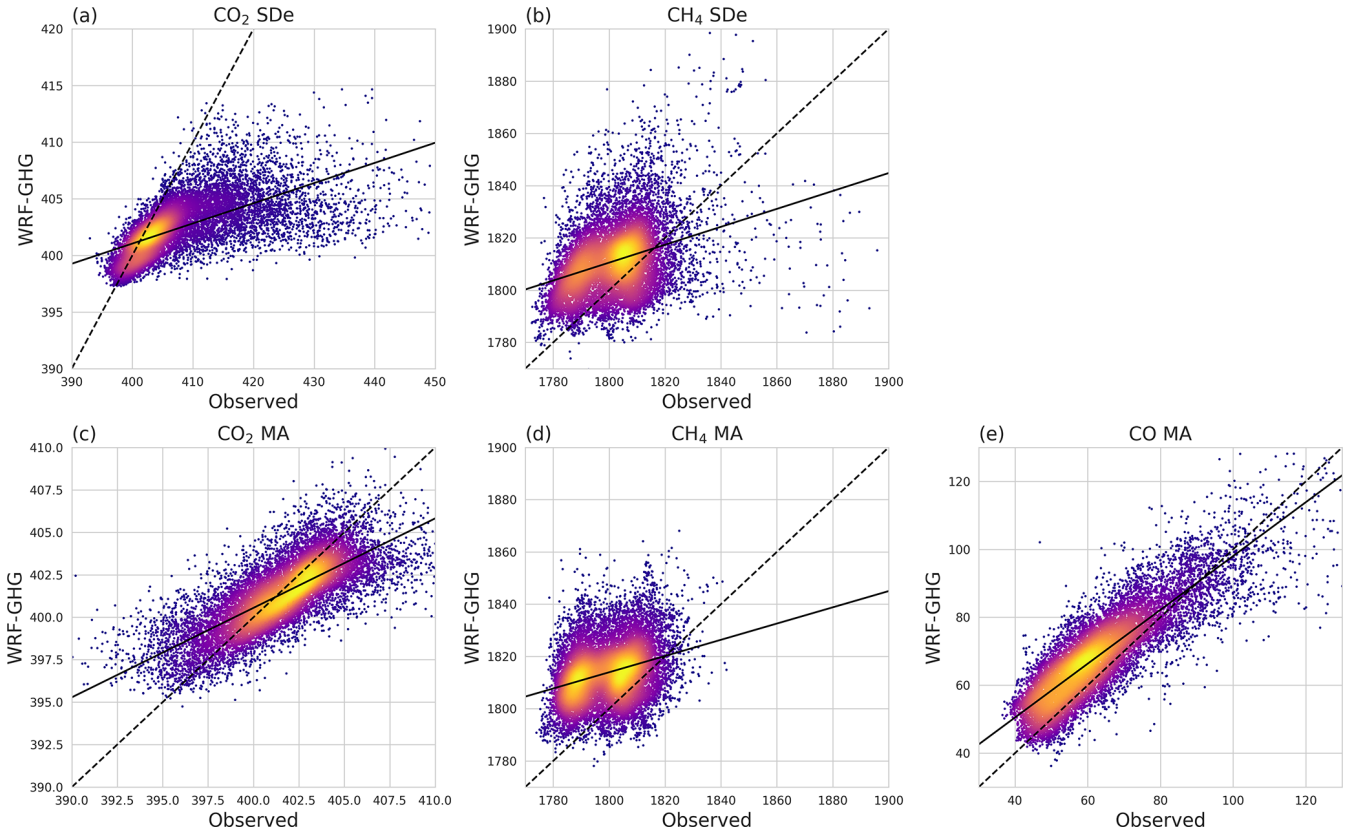

Figure 6. Scatterplot of hourly observed and modeled in situ greenhouse gases at SDe **(a, b)** and MA **(c, d, e)**. The colors indicate the point density.

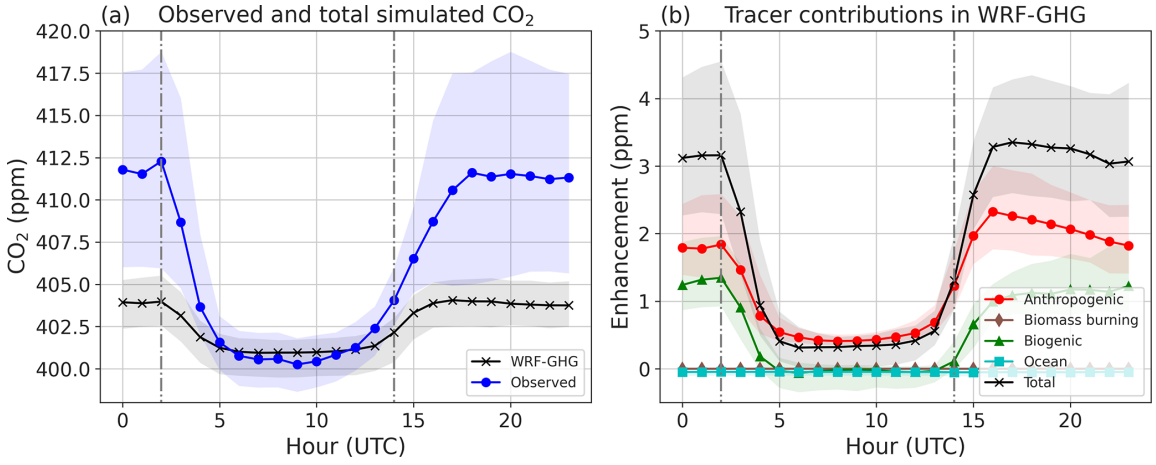

Figure 7. Diurnal cycle of **(a)** in situ CO_2 at SDe **(b)** and model tracer contributions. The black line in panel **(a)** represents the median hourly concentrations of WRF-GHG, while the blue line represents the observed values. The shaded areas cover the interquartile ranges. The gray dotted vertical lines at 02:00 and 14:00 UTC indicate the approximate times of sunrise and sunset. The colored lines in panel **(b)** represent the different tracer deviations from the background concentration in WRF-GHG, including anthropogenic (red), biogenic (green), ocean (cyan), and biomass burning (brown) tracers. The black line is the sum of all tracers, except the background.

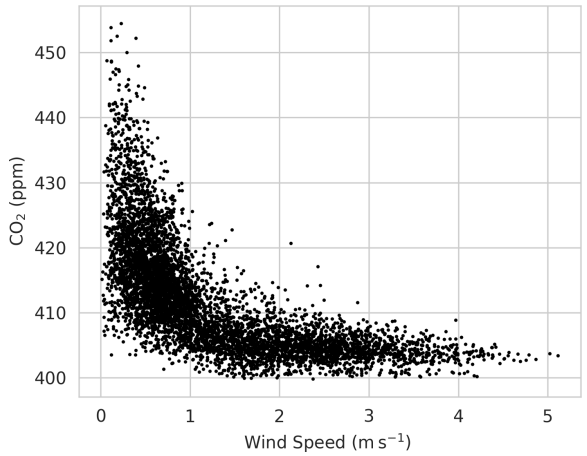

Figure 8. Scatterplot of nighttime wind speed at SDe against hourly observed in situ CO_2. Nighttime hours are defined as those between 14:00 and 02:00 UTC.

alistic. The nighttime peak of CO_2 mixing ratios is therefore attributed to PBL dynamics and regional transport.

Figure 7a shows that the observed interquartile range at night is wide, indicating a large variability in the CO_2 accumulation. We find a negative correlation between 10 m wind speed and in situ CO_2 concentrations at night for the observations at SDe (see Fig. 8). At low wind speeds, a large variability in CO_2 mixing ratios is observed from 400 up to 450 ppm. For wind speeds above $2\,m\,s^{-1}$, on the other hand, values higher than 410 ppm are rarely found, which indicates that ventilation processes take place. At the same time, there is a large overestimation of the wind speed within WRF-GHG (Sect. 4.1.1; Table 2). At night, 91.7 % of the simulated hours has a wind speed of more than $2\,m\,s^{-1}$, compared to only 23.2 % of the nocturnal observations, leading to a wind speed MBE of $3.23\,m\,s^{-1}$ at night. Note that the mean wind speed at night within WRF-GHG is $4.4\,m\,s^{-1}$ (see also Fig. 3c), while the nighttime CO_2 concentration in WRF-GHG is on average 403.8 ppm (see also Fig. 7a). Looking at Fig. 8, these values follow the pattern as found in the observations, where a nocturnal wind speed of more than $4\,m\,s^{-1}$ corresponds with CO_2 mole fractions of about 403–404 ppm. Therefore the model is likely underestimating the in situ CO_2 observations at SDe because of an overestimation of the surface wind speed.

Furthermore, we examine the relation of nighttime CO_2 concentrations and 10 m wind direction at SDe. Figure 9a shows that the dominant observed wind direction at night is easterly–southeasterly (ESE), followed by southerly (S). The ESE winds generally correspond with higher wind speeds ($> 2\,m\,s^{-1}$) and lower CO_2 concentrations (generally below 410 ppm), whereas observations with southerly winds generally coincide with very low wind speeds and CO_2 accumulation (Fig. 9a and b). The region in the ESE of SDe is a rural area dominated by agricultural activities. Therefore, these stronger ESE winds would generally bring air with a lower CO_2 content to SDe. WRF-GHG, on the other hand, overestimates the wind speed and almost consistently simulates ESE winds and lower CO_2 concentrations (Fig. 9c and d). As such, the model–data mismatch is likely caused by a combination of both wind speed overestimation in WRF-GHG and discrepancies as to the wind direction, which are interrelated.

4.2.2 XCO_2

A higher correlation coefficient of 0.90 is found when comparing the daytime hourly averaged TCCON XCO_2 data with the smoothed XCO_2 from WRF-GHG (see Table 3). Moreover, the RMSE along the time series is 0.75 ppm, and there is a model underestimation of 0.37 ppm. The hourly relative model–data errors are below 0.5 % (Fig. 10). This is, however, slightly larger than the TCCON standard deviation of the hourly averages, which is around 0.1 %.

WRF-GHG provides a separation into different tracer contributions, which are shown in Fig. 11. Monthly averages of these contributions for XCO_2 show a large (positive) biogenic enhancement in the months from August to December. The biogenic tracer in WRF-GHG is driven by the online biogenic CO_2 fluxes calculated through the VPRM module as the sum of the gross ecosystem exchange (GEE) and respiration (Mahadevan et al., 2008). A positive biogenic tracer suggests that the respiration accumulates more CO_2 than the ecosystem can capture during the day by photosynthesis. Indeed, in the Southern Hemisphere, the dry season is generally from May until November, leading to a decrease in GEE in some ecosystems (Quansah et al., 2015; Räsänen et al., 2017). Moreover, this carbon source was higher in 2016 because of a strong El Niño–Southern Oscillation (ENSO) event, leading to higher temperatures and less precipitation in the tropics (Yue et al., 2017).

The anthropogenic enhancement is relatively constant throughout the year. There is also a small biomass burning component modeled in XCO_2 in the months from August to December, which corresponds to the biomass burning (BB) season. During these months, frequent fires occur in southern Africa and South America. Duflot et al. (2010) showed that these polluted air masses can be transported to Réunion Island and detected by FTIR observations, such as XCO. Note that the XCO_2 enhancements due to biomass burning coincides with the biogenic enhancements because, especially in the tropics, the occurrence and duration of the BB season are linked to the dry season (Giglio et al., 2006).

A recent study using a COCCON spectrometer at Gobabeb in Namibia showed that the African biosphere can impact the observed XCO_2 signal there due to medium- and long-range transport (Frey et al., 2021). More specifically, they demonstrated that the carbon sink of the African biosphere during austral summer can be observed in their XCO_2 measurements, while it is not (or to a lesser extent) visible in

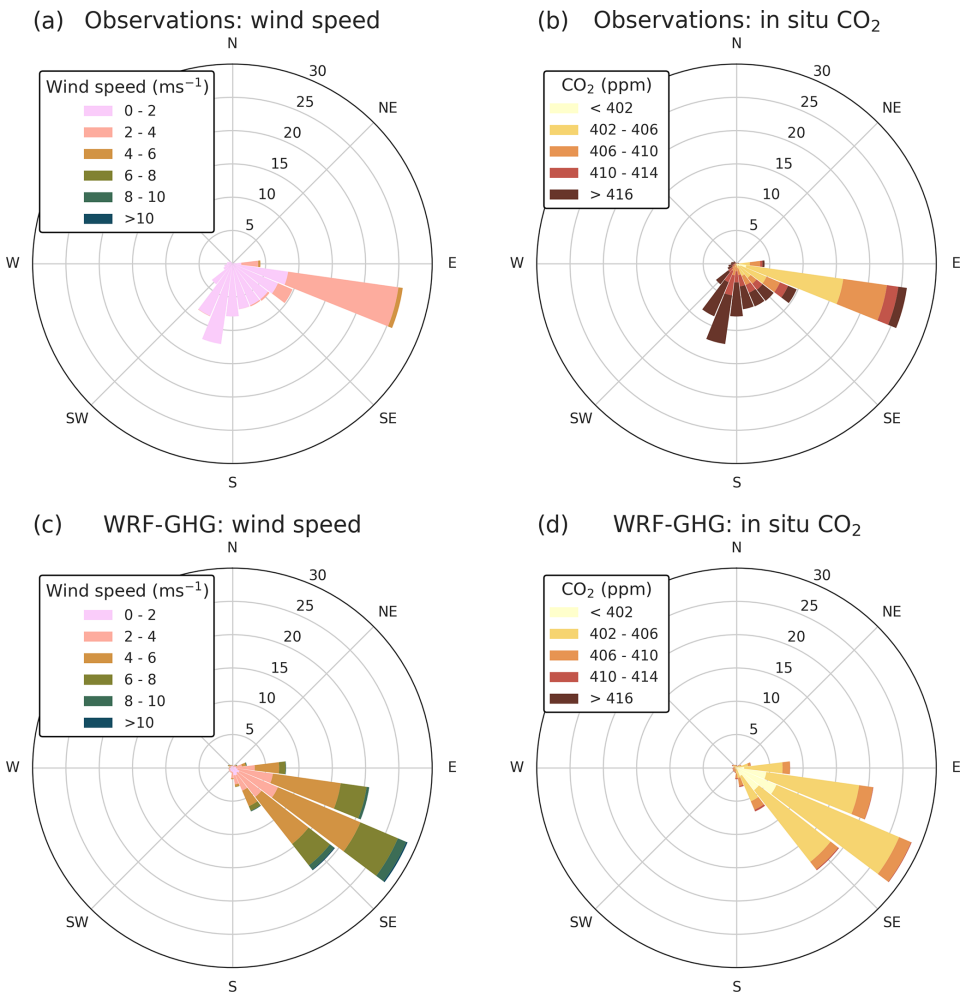

Figure 9. Wind rose of hourly nighttime data at SDe, where the night is defined between 14:00 and 02:00 UTC. Panels **(a)** and **(b)** show the distribution of the observed wind speed per wind direction and near-surface CO_2 concentration per wind direction, respectively. Panels **(c)** and **(d)** show the same for WRF-GHG simulated data. The lengths of the bars show the frequency of occurrence in percentage.

the time series at Réunion Island. Backward trajectories for 1 specific day in February 2017 revealed that this contrast comes from the sampling of different air masses. This might suggest that the influence of fluxes from the African continent on the air above Réunion Island is seasonally dependent, with a high impact during the dry season and a lower impact during wet season. Backward trajectory simulations over a longer time period performed by Zhou et al. (2018) might suggest this as well; however, more research is needed to prove this statement.

As expected, the column observations of CO_2 are determined by different processes than the in situ CO_2 concentrations. Where the variation in XCO_2 is mainly driven by fluxes on the African continent, the surface CO_2 mole fractions are heavily influenced by local sources and PBL dynamics. This also agrees with the trajectory calculations by Zhou et al. (2018), showing that surface air mainly originates in the Indian Ocean, while free tropospheric air is mainly coming from Africa and South America.

4.2.3 Surface CH_4

The model–data comparison for CH_4 at SDe (Table 3) shows only a weak correlation (0.35) between modeled CH_4 and observations at SDe. WRF-GHG shows an overestimation of about 9 ppb. Figure 6b and d show two apparent distributions in the scatterplot. This is linked with the seasonal cycle of CH_4, where observations show minimum values in December–February and maximum values in August–September. The errors between the observations and WRF-GHG are not constant over time. In Fig. 12, a seasonal bias is found, with larger errors between December and February, which is austral summer. This is a known weakness in the CAMS reanalysis, used as boundary information, as pointed out in the most recent validation report by Ramonet et al. (2020).

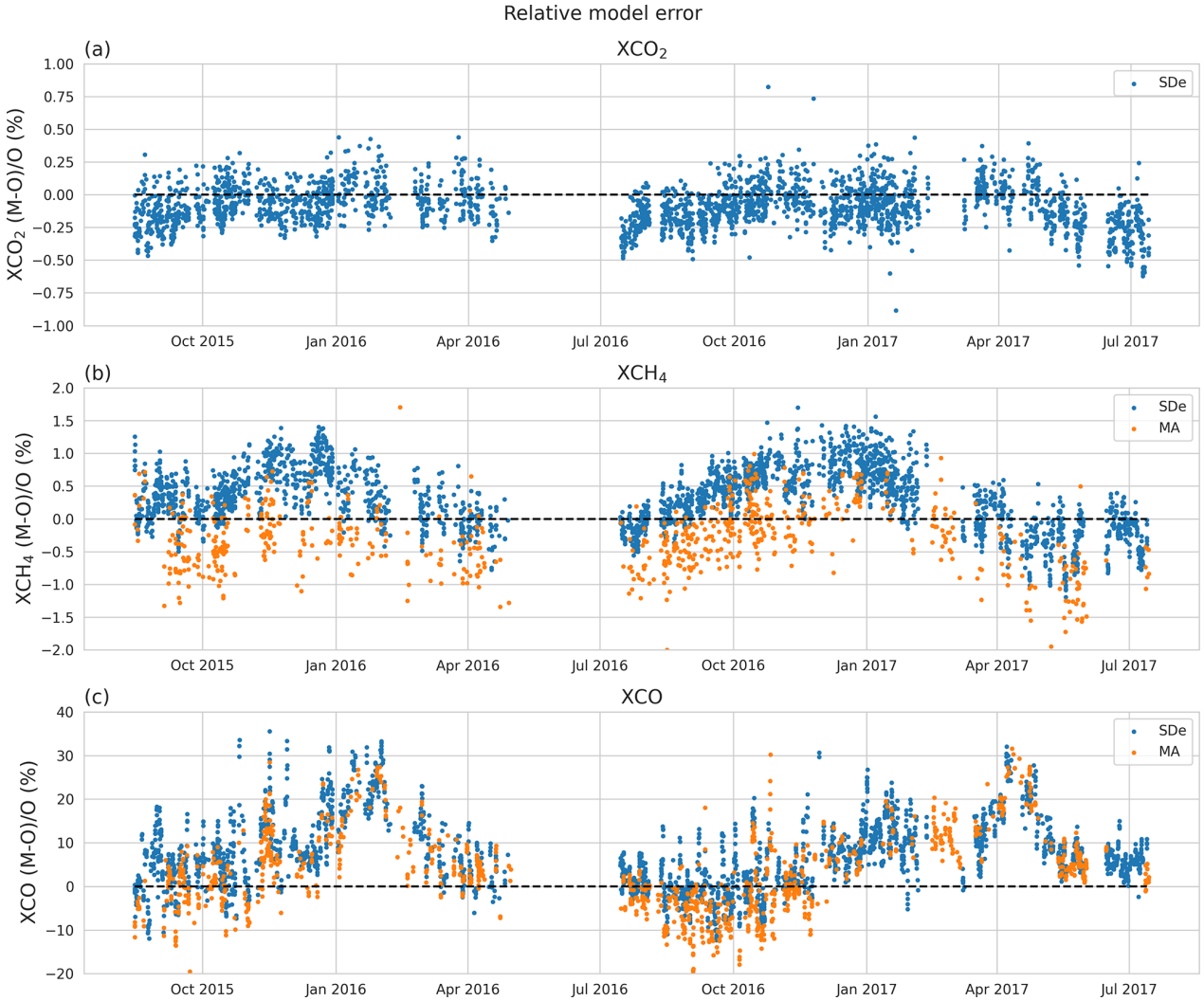

Figure 10. Relative percentage differences between hourly (smoothed) WRF-GHG and FTIR observations of XCO_2, XCO, and XCH_4. The blue dots represent the data at SDe (WRF–TCCON), while the orange data are from MA (WRF–NDACC).

> For all observations CH_4 shows a seasonality in the relative difference between observations and CAMS simulations, which is increasing in the Southern Hemisphere after 2008. … The seasonal dependence, which needs to be investigated in more detail, may be related to the representation of OH in the model, or/and to errors in the seasonal cycle of surface emissions (mainly from agriculture and wetlands). (Ramonet et al., 2020)

This demonstrates the importance of accurate lateral boundary conditions for simulating long-lived tracers with regional models such as WRF-GHG.

The diurnal cycle of the CH_4 tracer contributions in Fig. 13 shows that the modeled CH_4 consists almost entirely of the background signal and an anthropogenic enhancement, whereby both factors can add to the model–data mismatch.

The diurnal cycle is less pronounced in the observations (not shown). Nighttime values are on average only slightly larger than during the day, with a mean difference of only 3.09 ppb ($\sigma^2 = 6.35$), indicating that a nocturnal accumulation as identified for CO_2 in Saint-Denis is less evident for CH_4. Moreover, the overestimation of the daily amplitude in WRF-GHG suggests an overestimation of the local anthropogenic CH_4 fluxes from EDGAR.

In contrast to CO_2, the CH_4 mole fractions near the surface are less impacted by PBL dynamics and more by the background concentration.

4.2.4 XCH_4

Incorrect boundary values and hence background concentrations have an impact on all CH_4 simulations at Réunion Island. Therefore, the statistics for the column-averaged mole fraction of XCH_4 at SDe (part of TCCON) are worse than

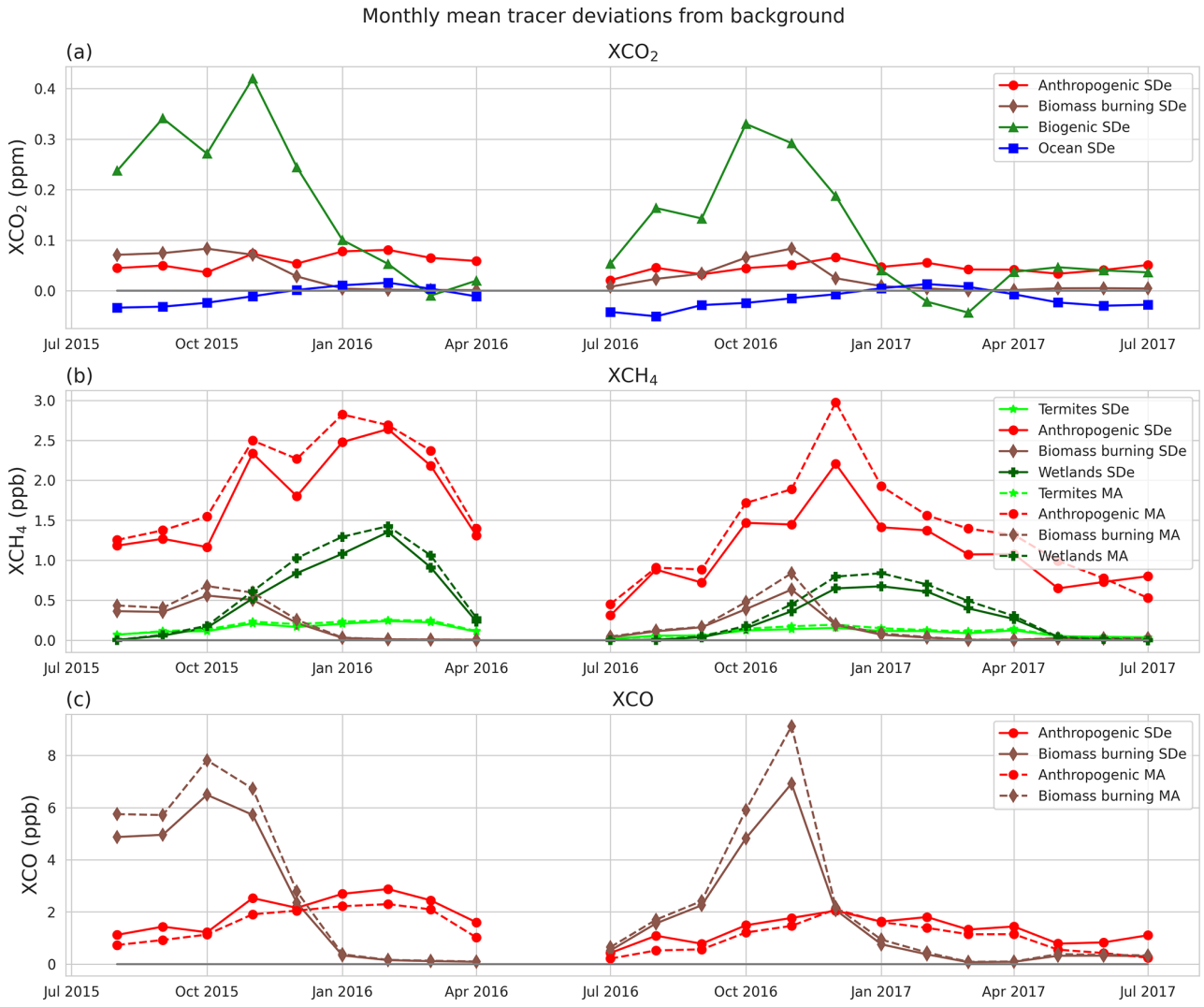

Figure 11. Monthly mean tracer contributions to the column-averaged mole fractions of **(a)** CO_2, **(b)** CO, and **(c)** CH_4. The different colors represent different tracers, i.e., anthropogenic (red), biogenic (green), ocean (blue), wetlands (dark green), termites (light green), or biomass burning (brown). The solid lines are the mean monthly contributions at SDe, while the dashed lines are for MA.

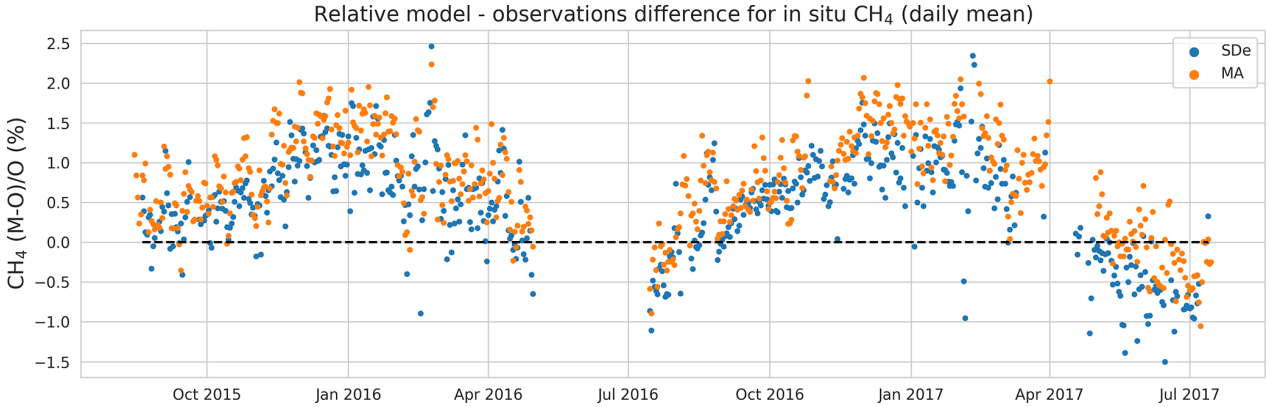

Figure 12. Time series of daily mean relative percentage differences between model and in situ observations of CH_4 at SDe (orange) and MA (blue). The black dashed line indicates zero difference.

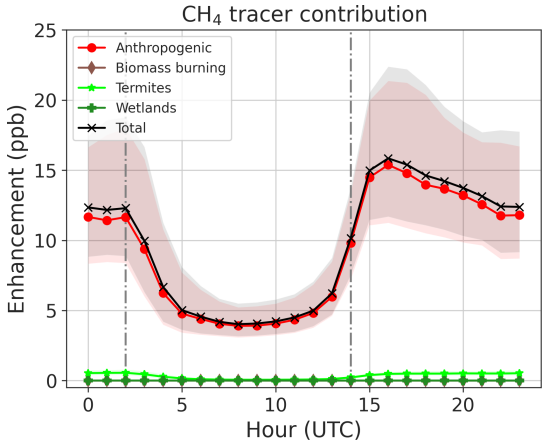

Figure 13. Diurnal cycle of in situ CH_4 tracer contributions of WRF-GHG at SDe. The black crosses represent the median hourly enhancements above the background for the sum of all tracers. The separate tracer contributions are given in red (anthropogenic), dark green (wetlands), light green (termites), or brown (biomass burning). The shaded areas cover the interquartile ranges. The gray dotted vertical lines at 02:00 and 14:00 UTC indicate the approximate times of sunrise and sunset.

for CO_2. A weak correlation is found (0.31; Table 3), and the model overestimates TCCON XCH_4 by 5.69 ppb, which is slightly less than the bias with respect to in situ data (Sect. 4.2.3).

Figure 10c shows the relative differences between WRF-GHG and observational data, which have the same seasonal pattern as for the in situ comparisons (Fig. 12) caused by the reported seasonal bias for CH_4 in the CAMS reanalysis data. The relative differences are below 2 %, but due to this seasonality in the errors, very little correlation is found.

Even though the model fails at reproducing the measured time series, it is still interesting to examine the different modeled tracer contributions to XCH_4 (Fig. 11b). The tracers contribute only a few ppb to the total signal, with the anthropogenic being dominant throughout the year. Furthermore, small peaks in biomass burning enhancements are found during the BB season, as for the other species. The biogenic tracers for CH_4 in WRF-GHG are generated by emissions from termites and wetlands. The termite signal is, however, very small and thus not relevant for this region. The signal from wetlands is larger, especially in austral summer. This roughly coincides with the rain season, causing a greater wetland extent (Lunt et al., 2019).

In the same way as for CO_2, the surface CH_4 mole fractions at SDe are influenced by local sources at Réunion Island, while fluxes from Africa and Madagascar are detected in the column observations because of the different air masses they sample.

4.2.5 XCO

At SDe, CO is only available as a column-averaged mole fraction (part of TCCON). As seen in Table 3, a very high correlation (0.89) is found for the hourly averaged paired data. WRF-GHG slightly overestimates the observed XCO (MBE of 5.07 ppb). Figure 10c shows that the relative error between WRF-GHG and the XCO observations from TCCON is often below 20 % but not constant because larger errors up to 30 % are found from January until May.

As for the other species, large contributions of BB emissions are found in the months from August to December (Fig. 11c). Duflot et al. (2010) showed that XCO values during the BB season can reach up to twice the CO background concentration from other months. The rather limited BB enhancement found in WRF-GHG suggests that a substantial XCO increase in the BB season is already included in the background tracer. This suggests that fires outside of the large domain can also be detected at Réunion Island, such as those from South America, which would confirm the findings of Duflot et al. (2010). The anthropogenic contribution is more constant throughout the year, and it is the dominant contribution outside BB season. However, it remains rather small compared to the background, which appears to be the main driver behind the simulated XCO values at Réunion Island.

The larger model overestimations in January 2016 and April 2017 are thus likely linked to the background tracer, which is based on the CAMS global reanalysis for reactive gases. The corresponding CAMS validation report (Errera et al., 2021) mentions no known biases but shows similar relative errors in those months in the Southern Hemisphere and in particular at MA (visible in Errera et al., 2021; see their Fig. S6 on p. 10). Again this demonstrates the importance of accurate boundary conditions for simulating XCO in this region but additionally points to the large influence of remote regions (outside domain d01) on the observed XCO time series at Réunion Island.

4.3 GHG data at Maïdo

At MA, the surface mole fractions of all three gases (CO_2, CH_4, and CO) are measured together with the column-averaged mole fractions of CH_4 and CO that are part of NDACC. The results of each species are given in the sections below. Again, the full time series of the observed and modeled data can be found in Appendix C, and statistical metrics of the model–data comparison are shown in Table 3. Note that all statistical analyses of in situ observations at MA are performed on the complete data set. Studies at other high-altitude stations often filter only those measurements which are representative for the free troposphere (Sepúlveda et al., 2014). However, analyses comparing only day- or nighttime data at MA showed no significant differences in the results.

4.3.1 Surface CO_2

At MA, the in situ CO_2 observations by the Picarro instrument are well reproduced by WRF-GHG, resulting in a correlation coefficient of 0.75 and a very small MBE of −0.15 ppm (see Table 3). As at SDe, the diurnal CO_2 cycle at MA shows a daytime minimum and a nighttime maximum (see Fig. 14a); however, the amplitude is much smaller. This pattern is caught by WRF-GHG, although the amplitude is slightly underestimated. During the day, WRF-GHG shows a small overestimation of the CO_2 measurements of about 0.9 ppm, while at night a slight underestimation (about 0.4 ppm) is found. As seen on Fig. 14b, the modeled diurnal variation is almost entirely produced by the biogenic tracer, indicating that the biogenic flux calculated by VPRM might be the reason for the model–observation discrepancies. The VPRM parameters used in the model are based on model tests in the Amazon region.

Foucart et al. (2018) showed that, due to surface radiative cooling, the observatory is primarily situated in the free troposphere at night. The air at MA is then disconnected from local pollution sources, and air from remote regions can be sampled. Indeed, no anthropogenic contribution is detected during the nighttime. However, the observed and simulated diurnal cycle of CO_2 (Fig. 14a and b) shows that nighttime measurements at MA are still influenced by the respiration of the local vegetation.

The anthropogenic contribution at MA is very minor in WRF-GHG, which is expected because of the remote location of the observatory. A very small enhancement is identified during the day. Since the local grid cell used for the model comparison does not include any anthropogenic flux, this enhancement is advected from elsewhere. It has been shown that orographic lifting can bring polluted air from coastal areas in the west towards MA during the day (Foucart et al., 2018; Duflot et al., 2019). Despite the fact that these westerly winds during the day were not reproduced by WRF-GHG (see Sect. 4.1.1), a daytime anthropogenic enhancement is found in the simulations. The model components representing biomass burning and ocean fluxes at MA are negligible.

So, according to WRF-GHG, the main contribution (above the background) to the CO_2 signal at MA is coming from the local vegetation and its photosynthesis and respiration, leading to a distinct diurnal cycle. The importance of the surrounding biosphere for the surface observations at MA was also found by Verreyken et al. (2021), for volatile organic compounds. Even though the diurnal cycles of CO_2 at SDe and MA display similar patterns of minima during the day and maxima at night, they are caused by entirely different mechanisms.

4.3.2 Surface CH_4

Because of the importance of accurate background concentrations, the model performance at simulating in situ CH_4 concentrations at MA is very similar compared to SDe as the correlation is low (0.30) and the model overestimates the observations by circa 19 ppb. The modeled signal consists almost entirely out of the anthropogenic tracer (in addition to the background signal; see Fig. 15a). Since the errors at MA follow the same pattern (Fig. 12) as at SDe, and because inaccurate background information affects all CH_4 simulations, the seasonal bias in the CAMS reanalysis is also the cause for the weak model performance at MA. The errors at MA are larger than those at SDe, likely due to the relatively low resolution of the EDGAR inventory (0.1°) used for anthropogenic CH_4 emissions, leading to horizontal dilution, where the concentration difference between high-emission areas and their surroundings becomes smaller, leading to an overestimation of the emissions in the low-emission areas. In contrast with the model results, no diurnal cycle could be detected in the observations (not shown).

4.3.3 XCH_4

The model–data comparison for the NDACC data shows a very weak correlation (0.37) and a model underestimation of NDACC XCH_4 (−5.65 ppb). This MBE has an opposite sign compared to TCCON CH_4. Zhou et al. (2018) showed that NDACC XCH_4 is generally about 10 ppb lower than TCCON XCH_4 at Réunion Island due to their difference in vertical sensitivity. This pattern in the bias is the same as the one found by Ramonet et al. (2020) in comparisons of the CAMS reanalysis with NDACC and TCCON XCH_4. Again, a seasonal pattern is found in the relative differences (Fig. 10b), which are caused by the reported bias for CH_4 in the CAMS reanalysis data.

The tracer contributions to the XCH_4 signal at MA in WRF-GHG are very similar to those at SDe, with seasonal enhancements from biomass burning and wetlands from Africa alongside a more constant anthropogenic part (Fig. 11b). Note that the contributions at MA seem to be slightly larger than those at SDe. This is because the atmospheric column above the high-altitude station of MA is smaller than the one above SDe and because the enhancements are transported from Africa and Madagascar by the westerlies higher up in the troposphere. The relative contributions averaged over the column are then higher at MA than at SDe.

4.3.4 Surface CO

WRF-GHG captures the in situ surface CO time series at MA quite well, and there is a high correlation of 0.83 (Table 3; Fig. 6e). The RMSE is about 11 ppb, and there is a small model overestimation of 5.51 ppb. During the day, a small anthropogenic enhancement is found (see Fig. 15b), as for

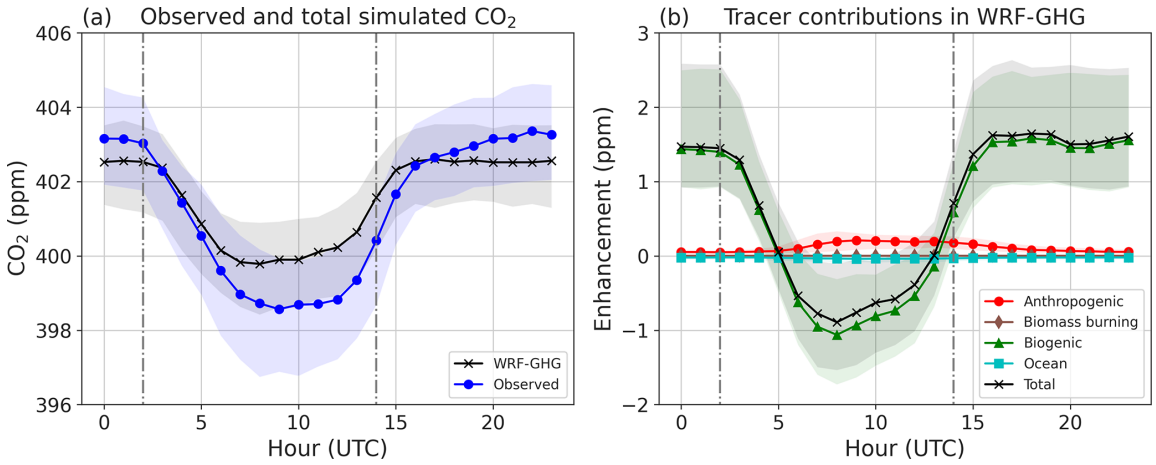

Figure 14. Same as Fig. 7 but for Maïdo.

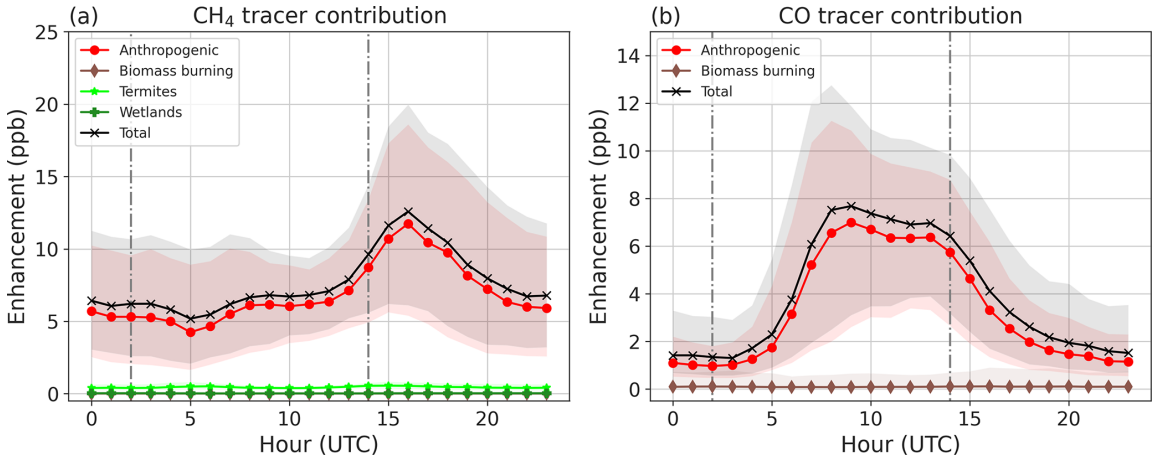

Figure 15. Diurnal cycle of tracer contributions for **(a)** CH_4 and **(b)** CO in situ surface concentration at MA.

CO_2. As already noticed, thermal contrasts make air masses from the coastal areas arise during the day along the mountain slope before reaching the Maïdo Observatory. This air contains anthropogenic pollution. At the observatory itself, no anthropogenic CO fluxes are implemented, so the model is representing this daytime advection to some extent.

Another contributor is the BB signal from August to December. The contribution is not very visible in the diurnal cycle due to its seasonal nature, but daily enhancements of up to 40 ppb are simulated by WRF-GHG. BB contributions from the African continent and Madagascar are highest during the night, when MA is generally located in the free troposphere and transport from distant regions is detected (Baray et al., 2013).

4.3.5 XCO

A very high correlation (0.90) is found for the hourly averaged paired column data of NDACC and WRF-GHG (Table 3). In general, WRF-GHG slightly overestimates the observed XCO (MBE of 1.81 ppb). Note that the errors are larger (the overestimation is larger) for the TCCON data compared to the NDACC data (also Fig. 10b). This is probably linked to biases between the TCCON and NDACC data sets. Zhou et al. (2019) showed that there is a bias of 2.5 % between TCCON XCO and NDACC XCO at Réunion Island due to differences in the retrieval algorithm and data corrections.

As for XCH_4, the average monthly tracer contributions of XCO at MA are very similar as those at SDe (Fig. 11b), with large contributions of BB emissions in the months August to December. Because of the unique location of MA, both the in situ observations and the column-averaged XCO are sensitive to these large seasonal events.

5 Model resolution

The above analysis was done using the WRF-GHG simulations from the innermost domain d03 (Fig. 2), which has a

horizontal resolution of 2×2 km. As surface in situ observations are heavily influenced by local fluxes and dynamics, this high resolution is necessary to represent these measurements accurately, especially in regions with complex topography. As the ground-based remote sensing FTIR observations sample a much larger volume of air, a lower model resolution is likely sufficient to catch the fluxes and processes that influence them. Therefore, the model–data comparison for domains d01 and d02, with a horizontal resolution of 50 and 10 km, respectively, is given in this section. Table 4 gives the statistical metrics for the FTIR observations at both sites, for all model domains.

The results are very similar among the different model resolutions, indicating that even a horizontal resolution of 50 km (as in d01) could be sufficient to simulate the FTIR observations at Réunion Island. In addition to the larger sampling volume, this can be explained by the fact that the most important contributions to the column are coming from remote areas such as Africa and Madagascar, situated in d01 and d02. The added value of high-resolution transport in d03 is negligible for the FTIR observations.

6 Conclusions

We studied the variability in CO_2, CH_4, and CO surface and column observations at Réunion Island and evaluated the possible factors influencing their observed mole fractions. This was achieved by comparing the available data sets with simulations of the WRF-GHG model over two periods between 2015 and 2017, totaling 20 months. The model performance was first evaluated for basic meteorological fields both near the surface and along atmospheric profiles. WRF-GHG shows good skill in reproducing these measurements, especially temperature. However, the local wind speed in Saint-Denis is overestimated by almost 4 m s^{-1}, and also at Maïdo, there are some discrepancies in the wind speed and direction, which are likely linked to the complex topography and the model resolution of 2 km not being sufficient to represent the very local dynamical processes.

Nevertheless, the results enable us to answer the scientific questions posed in the introduction.

1. *To what extent are the observations influenced by local and nearby sources and sinks or long-range transport of emitted gases?*
   At both Saint-Denis and Maïdo, the in situ observations are heavily influenced by local and nearby sources and sinks, especially for CO_2. However, the in situ observations at Maïdo can detect both signals from the coastal regions and from afar at night, when the observatory is located in the boundary layer and the free troposphere, respectively. On the other hand, the column-averaged mole fractions describe different air masses to those near the surface and are not or only very slightly influenced by local activities. As shown by previous studies and confirmed here, these measurements at Réunion Island are influenced by processes from distant areas such as Africa and Madagascar. This is further evidenced by the fact that a model resolution of 50 km appears to be sufficient to simulate these observations.

2. *What are the different tracer contributions to the observed concentrations, both at the surface and in the total column?*
   The surface CO_2 mole fractions in Saint-Denis follow a distinct diurnal cycle, with values up to 450 ppm at night, driven by local anthropogenic emissions, planetary boundary layer dynamics, and accumulation due to low wind speeds. Additionally, the signal includes respiration from vegetation that is carried by eastern winds from more rural regions. At the Maïdo Observatory, on the other hand, a similar diurnal cycle of CO_2 is found but with much smaller amplitude. There, the surface CO_2 mole fractions are essentially driven by the surrounding vegetation that take up CO_2 during the day and release CO_2 during the night through respiration. The different model tracers of XCO_2 show contributions from fire emissions during the biomass burning season but also positive biogenic enhancements associated with the dry season. For CH_4, tracer contributions reveal that the emission sources within the model domain have only a minimal effect on the overall signal. Besides the background, local anthropogenic fluxes are the major source influencing the in situ CH_4 observations at Réunion Island. However, the comparisons between the model fields and observations at Saint-Denis show that the anthropogenic emissions from EDGAR are likely largely overestimated; this is even more evidenced at Maïdo. Some (minor) impacts from Africa and Madagascar can be seen in the XCH_4 observations, with fire plumes during the biomass burning season and wetland emissions during the rainy season. For XCO, the importance of biomass burning plumes from Africa and elsewhere for the observed variability is confirmed. These plumes can also be detected by the in situ observations at Maïdo at night, while local anthropogenic signals are the main influence during the day.

3. *How accurate is WRF-GHG in simulating the different observation types of the three gases (CO_2, CH_4, and CO) in the Southern Indian Ocean region, in particular at Saint-Denis and at the Maïdo Observatory? What are its strengths and weaknesses?*
   In general, WRF-GHG shows great skill in simulating the different in situ surface and column observations of GHG. The simulations of XCO_2 and XCO show a high correlation with the TCCON data, with coefficients of 0.9 and 0.89, respectively. Similarly, a Pearson correlation coefficient of 0.9 and low errors are found between the model and NDACC XCO time series. Furthermore, WRF-GHG is able to adequately reproduce

Table 4. Overview of WRF-GHG performance of simulating hourly FTIR observations of GHG at Réunion Island, for all model domains. Comparison with the column observations is done using the smoothed model profiles.

	SDe									MA					
	XCO_2 (ppm)			XCH_4 (ppb)			XCO (ppb)			XCH_4 (ppb)			XCO (ppb)		
	d01	d02	d03	d01	d02	d03	d01	d02	d03	d01	d02	d03	d01	d02	d03
RMSE	0.66	1.26	0.75	12.45	11.89	10.26	8.05	8.01	8.08	10.55	11.03	10.80	7.64	7.24	7.37
MBE	0.12	−0.24	−0.37	8.69	6.89	5.69	5.06	5.02	5.07	−5.22	−6.00	−5.65	1.92	1.46	1.81
CORR	0.90	0.75	0.90	0.27	0.34	0.31	0.88	0.89	0.89	0.36	0.37	0.37	0.89	0.89	0.89

the in situ CO observations at Maïdo, and consequently, to some extent, the anabatic winds that are typical for the northwestern part of the island, despite the differences in modeled and observed wind directions. The high model resolution of 2 km is needed to accurately represent local fluxes and small-scale processes that affect the in situ observations. However, because of the complex topography and the unique local wind patterns, an even higher resolution might be needed to simulate more precisely the observations at Maïdo. In addition, certain model flaws were discovered in this study. Due to an overestimation of local wind speeds in the capital, WRF-GHG underestimates the nocturnal CO_2 buildup, leading to a correlation coefficient of only 0.62 between the model and surface CO_2 measurements at Saint-Denis. Furthermore, we found a small model underestimation of the amplitude of the diurnal cycle of surface CO_2 at Maïdo, which might indicate that the VPRM parameters could be improved for this region. Finally, WRF-GHG fails to accurately reproduce the different CH_4 observations at Réunion Island due to a seasonal bias in the background arising from the CAMS reanalysis.

This study showed an application of the WRF-GHG model in a region of the globe where it had not yet been run before. It demonstrated that WRF-GHG had great skill in simulating the meteorological fields and different in situ surface and column observations of GHG. However, the results are highly dependent on accurate boundary conditions and the availability of high-resolution emission inventories.

Appendix A: VPRM parameters

As mentioned in Sect. 3.1, this study uses the VPRM parameter set that was optimized by Botía et al. (2021) for the Amazon region in Brazil. Table A1 gives the exact values for every vegetation class.

Appendix B: Smoothing model data

A smoothing correction is applied when comparing the model data with the TCCON and NDACC data. Retrieved column-averaged mole fractions are affected by the observing system characteristics, and therefore, Rodgers and Connor (2003) suggest taking into account the a priori information and averaging kernels of the retrieval when calculating the Xgas of the model. The different steps undertaken to calculate this are explained hereafter for TCCON and NDACC separately.

Generally, the smoothed Xgas from WRF-GHG is calculated as follows:

$$X_{\mathrm{gas,s}} = \frac{\mathrm{TC}_{\mathrm{s}}^{\mathrm{gas}}}{\mathrm{TC}_{\mathrm{air}}} = \frac{\sum_i \mathrm{PC}_{\mathrm{s}}^{\mathrm{gas},i}}{\mathrm{TC}_{\mathrm{air}}} = \frac{\sum_i x_{\mathrm{s}}^{i} \mathrm{PC}_{\mathrm{air}}^{i}}{\mathrm{TC}_{\mathrm{air}}}, \quad \text{(B1)}$$

where $\mathrm{PC}_{\mathrm{air}}^{i}$ is the partial column number density of dry air in layer i, and x_{s}^{i} is the volume mixing ratio with respect to dry air in layer i of the smoothed model profile. In the following, all parameters indicating a volume mixing ratio or column number density are also with respect to dry air; however, for brevity, it will not be specified any more.

B1 TCCON

Equation (B1) requires a smoothed vertical profile (x_{s}^{i}). Since TCCON does not provide profile retrievals, we cannot calculate this. Instead, we use the following smoothing equation for TCCON:

$$X_{\mathrm{gas,s}} = \frac{\mathrm{TC}_{\mathrm{apriori}}^{\mathrm{gas}}}{\mathrm{TC}_{\mathrm{TCCON}}} + \boldsymbol{a} \cdot \left(\frac{\mathrm{PC}_{\mathrm{WRF,regrid}}^{\mathrm{gas}}}{\mathrm{TC}_{\mathrm{WRF,regrid}}} - \frac{\mathrm{PC}_{\mathrm{apriori}}^{\mathrm{gas}}}{\mathrm{TC}_{\mathrm{TCCON}}} \right), \quad \text{(B2)}$$

where $\mathrm{TC}_{\mathrm{TCCON}}$ is the total column (number density) of dry air from TCCON (for an atmospheric column up to 50 hPa). Similarly, $\mathrm{TC}_{\mathrm{apriori}}^{\mathrm{gas}}$ is the total column of the a priori mole fraction from TCCON calculated as the sum of the partial columns $\mathrm{PC}_{\mathrm{apriori}}^{\mathrm{gas},i}$ over those layers i that are below 50 hPa. Furthermore, $\boldsymbol{a}$ is the vector with the column averaging kernels of TCCON.

The regridded partial column profile of WRF-GHG ($\mathrm{PC}_{\mathrm{WRF,regrid}}^{\mathrm{gas}}$) and the total column of dry air from WRF ($\mathrm{TC}_{\mathrm{WRF,regrid}}$) are calculated in a few steps which are explained below. By including the total column of dry air from WRF in Eq. (B2), we want to eliminate potential differences in air between TCCON and the model. As such, the priority

Table A1. VPRM parameters used within WRF-GHG.

	Evergreen forest	Deciduous forest	Mixed forest	Shrubs	Savanna	Crops	Grasses
PAR_0	993.9	324.0	206.0	303.0	6860.7	2329.0	15475.5
λ	0.1096	0.1729	0.2555	0.0874	0.0277	0.0417	0.0568
α	0.2114	0.3258	0.3422	0.0239	−0.2535	−0.0814	−0.3122
β	1.8187	0.0	0.0	0.0	7.1125	3.6716	7.3377

is given to the volume mixing ratio profiles (instead of the calculation of dry air). The steps we take are as follows:

1. Extend the WRF-GHG atmospheric profiles (gas mole fraction, pressure, temperature, and water vapor) above the model limit (50 hPa) using information of the TCCON a priori profiles.

2. Calculate the dry air partial column in layer i using the ideal gas law as follows:

$$\mathrm{PC}^i_{\mathrm{air}} = \frac{P^i}{RT^i}\frac{\tau^i}{1+1.6075q^i},$$

with P as atmospheric pressure, T as air temperature, R as the ideal gas constant, q as the mass mixing ratio of water vapor, and τ as the layer thickness.

3. Calculate the gas number density partial columns as $\mathrm{PC}^i_{\mathrm{gas}} = x^i_{\mathrm{gas}}\mathrm{PC}^i_{\mathrm{air}}$, with x^i_{gas} as the gas mole fraction in layer i.

4. Regrid these partial column profiles to the full TCCON grid using a transformation matrix $\mathbf{D}$, as in Langerock et al. (2015), as follows:

$$\mathrm{PC}^{\mathrm{gas}}_{\mathrm{WRF,regrid}} = \mathbf{D}\cdot\mathrm{PC}_{\mathrm{gas}},$$

and

$$\mathrm{PC}_{\mathrm{WRF,regrid}} = \mathbf{D}\cdot\mathrm{PC}_{\mathrm{air}}.$$

5. Finish with $\mathrm{TC}_{\mathrm{WRF,regrid}} = \sum_i \mathrm{PC}^i_{\mathrm{WRF,regrid}}$, where the sum is taken over all layers i below 50 hPa.

B2 NDACC

The smoothed X_{gas} from WRF-GHG at MA is calculated slightly differently to at SDe, as, for NDACC, the volume mixing ratio profiles are provided. The smoothing equation can be written as follows:

$$\boldsymbol{x}_{\mathrm{gas,s}} = \boldsymbol{x}^{\mathrm{gas}}_{\mathrm{apriori}} + \mathbf{A}\cdot\left(\boldsymbol{x}^{\mathrm{gas}}_{\mathrm{WRF,regrid}} - \boldsymbol{x}^{\mathrm{gas}}_{\mathrm{apriori}}\right), \tag{B3}$$

where $\boldsymbol{x}^{\mathrm{gas}}_{\mathrm{apriori}}$ is the volume mixing ratio (VMR) a priori profile from NDACC, and $\mathbf{A}$ is the NDACC VMR averaging kernel matrix. Similar to that for TCCON, a few steps need to be taken to make the WRF-GHG data fit in Eq. (B3). Steps 1–4, as described above, should be followed but by using NDACC information instead of TCCON (a priori VMR profile, temperature, and water vapor profiles; vertical grid). Then the regridded VMR profile from WRF-GHG is calculated as $\boldsymbol{x}^{\mathrm{gas}}_{\mathrm{WRF,regrid}} = \frac{\mathrm{PC}^{\mathrm{gas}}_{\mathrm{WRF,regrid}}}{\mathrm{PC}_{\mathrm{WRF,regrid}}}$. Finally, the smoothed dry air mole fraction at MA is given by the following:

$$X_{\mathrm{gas,s}} = \frac{\sum_i x^i_{\mathrm{gas,s}}\mathrm{PC}^i_{\mathrm{WRF,regrid}}}{\sum_i \mathrm{PC}^i_{\mathrm{WRF,regrid}}},$$

where the sum is taken over all layers i below 50 hPa.

Appendix C: Time series

The full time series of both the observed and modeled concentrations at SDe and MA are given in the figures hereafter. Figures C1 and C2 show the time series of the in situ data at SDe and MA, respectively. Similarly, Figs. C3 and C4 show the comparison of the FTIR data at SDe (TCCON) and MA (NDACC).

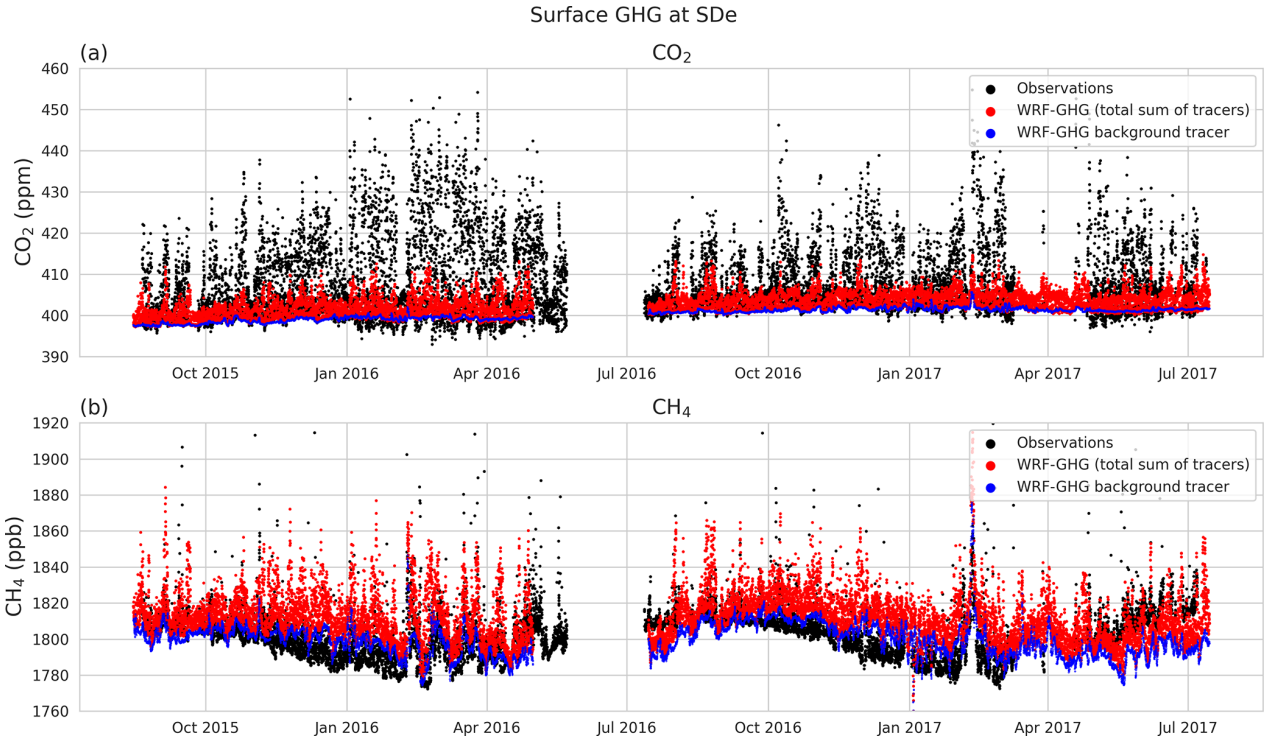

Figure C1. Time series of all observed (black) and modeled (red) in situ concentrations at SDe of **(a)** CO_2 and **(b)** CH_4. The blue dots represent the modeled background tracer.

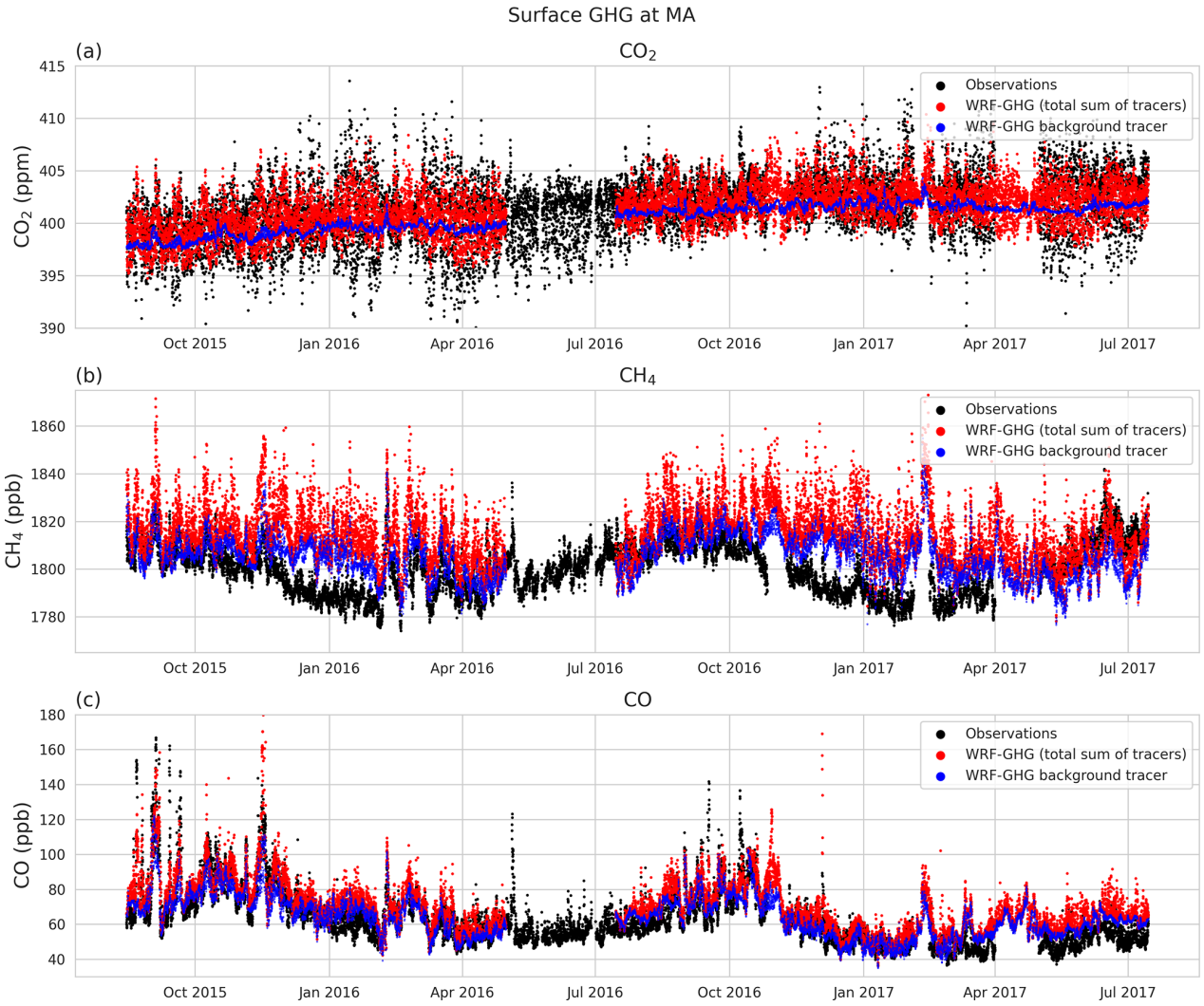

Figure C2. Time series of all observed (black) and modeled (red) in situ concentrations at MA of **(a)** CO_2, **(b)** CH_4, and **(c)** CO. The blue dots represent the modeled background tracer.

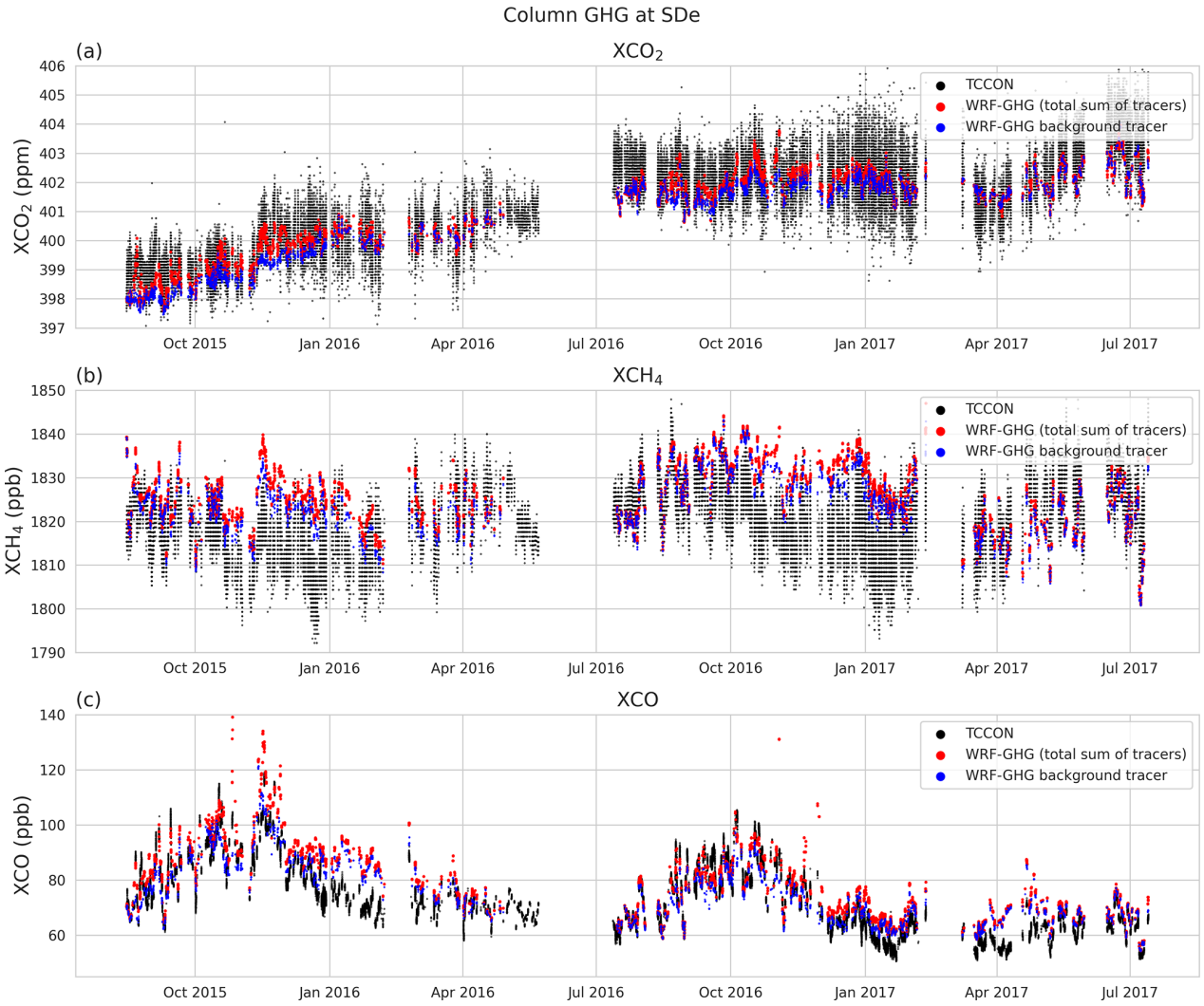

Figure C3. Time series of all observed (black) and modeled (red) column concentrations at SDe of **(a)** CO_2, **(b)** CH_4, and **(c)** CO. The blue dots represent the modeled background tracer. The modeled data are hourly and smoothed. The observed data are scaled to the atmospheric column until 50 hPa, and all available measurements are shown.

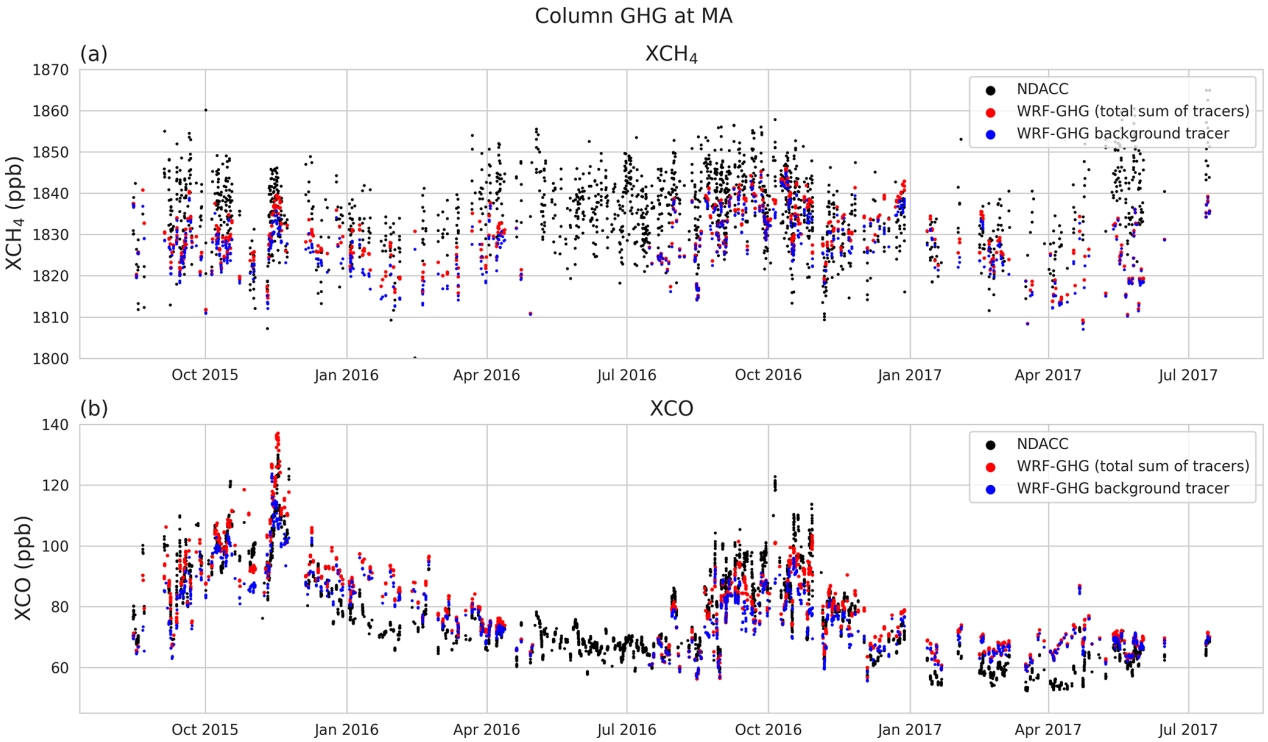

Figure C4. Time series of all observed (black) and modeled (red) column concentrations at MA of **(a)** CH_4 and **(b)** CO. The blue dots represent the modeled background tracer. The modeled data are hourly and smoothed. The observed data are scaled to atmospheric column until 50 hPa, and all available measurements are shown.

Code and data availability. The data used in this publication were obtained from Martine De Mazière, as part of the Network for the Detection of Atmospheric Composition Change (NDACC), and are available through the NDACC website https://www-air.larc.nasa.gov/missions/ndacc/data.html?station=la.reunion.maido/hdf/ftir/ (De Mazière, 2019). The TCCON data were obtained from the TCCON Data Archive hosted by CaltechDATA at https://doi.org/10.14291/TCCON.GGG2014.REUNION01.R1 (De Mazière et al., 2017). The ICOS data used for this study are hosted on the Carbon Portal at https://doi.org/10.18160/Z7WE-5XHP (De Mazière et al., 2021). The ERA5 and CAMS reanalysis data set (https://doi.org/10.24381/cds.adbb2d47, Hersbach et al., 2018a; https://doi.org/10.24381/cds.bd0915c6, Hersbach et al., 2018b), used as input for the WRF-GHG simulations, was downloaded from the Copernicus Climate Change Service (C3S) Climate Data Store (2021). The WRF-Chem model code is distributed by NCAR (https://doi.org/10.5065/D6MK6B4K, NCAR, 2020).

Author contributions. SC set up the model simulations, did the analysis, and wrote the paper. JB provided the anthropogenic CO fluxes at Réunion Island and its description. VD provided the meteorological radiosonde profiles. BL provided expertise on the FTIR data and model comparison techniques. DF assisted in setting up the model and, together with JFM, helped with correctly interpreting the results. JMM, CH, NK, MR, and ML provided the FTIR and in situ measurements on Réunion Island. EM and MDM provided general guidance and support during the analysis and revised and edited the paper. All authors reviewed and commented on the paper.

Competing interests. The contact author has declared that neither they nor their co-authors have any competing interests.

Disclaimer. The results contain modified Copernicus Atmosphere Monitoring Service information 2020–2021. Neither the European Commission nor ECMWF is responsible for any use that may be made of the Copernicus information or data it contains.

Publisher's note: Copernicus Publications remains neutral with regard to jurisdictional claims in published maps and institutional affiliations.

Acknowledgements. We acknowledge the providers of the observational data sets.

The authors also acknowledge the European Communities, the Région Réunion Island, CNRS, and Université de la Réunion Island, for their support and contribution in the construction phase of the research infrastructure OPAR (Observatoire de Physique de l'Atmosphère à La Réunion). OPAR is presently funded by CNRS (INSU), Météo-France, and Université de La Réunion and managed by OSU-R (Observatoire des Sciences de l'Univers à La Réunion, UAR 3365). OPAR is supported by the French research infrastructure ACTRIS-FR (Aerosols, Clouds, and Trace gases Research InfraStructure – France).

We thank Christophe Gerbig, Roberto Kretschmer, and Thomas Koch (MPI BGC), for their work on the VPRM preprocessor and support on installing the software at the BIRA-IASB servers. The authors also wish to thank Julia Marshall (DLR) and Michael Gałkowski (MPI BGC), for their guidance in running the WRF-GHG model and interpreting its results. Additionally, we thank the broader WRF-GHG community, for the regular exchange of expertise. Finally, we thank Mahesh Kumar Sha (BIRA-IASB) and Minqiang Zhou (IAP, CAS), for the helpful discussions on the interpretation of the data.

Financial support. This research has been supported by the Belgian Federal Government through the tax exemption law for promoting scientific research (Art. 275/3 of CIR92).

Review statement. This paper was edited by Christoph Gerbig and reviewed by two anonymous referees.

References

Ahmadov, R., Gerbig, C., Kretschmer, R., Koerner, S., Neininger, B., Dolman, A. J., and Sarrat, C.: Mesoscale covariance of transport and CO_2 fluxes: Evidence from observations and simulations using the WRF-VPRM coupled atmosphere-biosphere model, J. Geophys. Res.-Atmos., 112, D22107, https://doi.org/10.1029/2007JD008552, 2007.

Baldy, S., Ancellet, G., Bessafi, M., Badr, A., and Luk, D. L. S.: Field observations of the vertical distribution of tropospheric ozone at the island of Reunion (southern tropics), J. Geophys. Res.-Atmos., 101, 23835–23849, https://doi.org/10.1029/95JD02929, 1996.

Baray, J.-L., Courcoux, Y., Keckhut, P., Portafaix, T., Tulet, P., Cammas, J.-P., Hauchecorne, A., Godin Beekmann, S., De Mazière, M., Hermans, C., Desmet, F., Sellegri, K., Colomb, A., Ramonet, M., Sciare, J., Vuillemin, C., Hoareau, C., Dionisi, D., Duflot, V., Vérèmes, H., Porteneuve, J., Gabarrot, F., Gaudo, T., Metzger, J.-M., Payen, G., Leclair de Bellevue, J., Barthe, C., Posny, F., Ricaud, P., Abchiche, A., and Delmas, R.: Maïdo observatory: a new high-altitude station facility at Reunion Island (21° S, 55° E) for long-term atmospheric remote sensing and in situ measurements, Atmos. Meas. Tech., 6, 2865–2877, https://doi.org/10.5194/amt-6-2865-2013, 2013.

Barlage, M., Miao, S., and Chen, F.: Impact of physics parameterizations on high-resolution weather prediction over two Chinese megacities, J. Geophys. Res.-Atmos., 121, 4487–4498, https://doi.org/10.1002/2015JD024450, 2016.

Beck, V., Koch, T., Kretschmer, R., Ahmadov, R., Gerbig, C., Marshall, J., Pillai, D., and Heimann, M.: The WRF Greenhouse Gas Model (WRF-GHG), Technical Report No. 25, techreport 25, Max Planck Institute for Biogeochemistry, https://www.bgc-jena.mpg.de/bgc-systems/pmwiki2/uploads/Download/Wrf-ghg/WRF-GHG_Techn_Report.pdf (last access: 27 September 2018), 2011.

Beck, V., Gerbig, C., Koch, T., Bela, M. M., Longo, K. M., Freitas, S. R., Kaplan, J. O., Prigent, C., Bergamaschi, P., and Heimann, M.: WRF-Chem simulations in the Amazon region during wet and dry season transitions: evaluation of methane models and wetland inundation maps, Atmos. Chem. Phys., 13, 7961–7982, https://doi.org/10.5194/acp-13-7961-2013, 2013.

Bloom, A. A., Bowman, K. W., Lee, M., Turner, A. J., Schroeder, R., Worden, J. R., Weidner, R., McDonald, K. C., and Jacob, D. J.: A global wetland methane emissions and uncertainty dataset for atmospheric chemical transport models (WetCHARTs version 1.0), Geosci. Model Dev., 10, 2141–2156, https://doi.org/10.5194/gmd-10-2141-2017, 2017.

Borsdorff, T., aan de Brugh, J., Pandey, S., Hasekamp, O., Aben, I., Houweling, S., and Landgraf, J.: Carbon monoxide air pollution on sub-city scales and along arterial roads detected by the Tropospheric Monitoring Instrument, Atmos. Chem. Phys., 19, 3579–3588, https://doi.org/10.5194/acp-19-3579-2019, 2019.

Botía, S., Komiya, S., Marshall, J., Koch, T., Gałkowski, M., Lavric, J., Gomes-Alves, E., Walter, D., Fisch, G., Pinho, D. M., Nelson, B. W., Martins, G., Luijkx, I. T., Koren, G., Florentie, L., Carioca de Araújo, A., Sá, M., Andreae, M. O., Heimann, M., Peters, W., and Gerbig, C.: The CO_2 record at the Amazon Tall Tower Observatory: A new opportunity to study processes on seasonal and inter-annual scales, Glob. Change Biol., 28, 588–611, https://doi.org/10.1111/gcb.15905, 2021.

Bretherton, C. S. and Park, S.: A New Moist Turbulence Parameterization in the Community Atmosphere Model, J. Climate, 22, 3422–3448, https://doi.org/10.1175/2008JCLI2556.1, 2009.

Brioude, J., Petron, G., Frost, G., Ahmadov, R., M. Angevine, W., Hsie, E.-Y., Kim, S.-W., Lee, S.-H., McKeen, S., Trainer, M., Fehsenfeld, F., Holloway, J., Peischl, J., B. Ryerson, T., and Gurney, K.: A new inversion method to calculate emission inventories without a prior at mesoscale: Application to the anthropogenic CO_2 emission from Houston, Texas, J. Geophys. Res., 117, D05312, https://doi.org/10.1029/2011JD016918, 2012.

Brioude, J., Angevine, W. M., Ahmadov, R., Kim, S.-W., Evan, S., McKeen, S. A., Hsie, E.-Y., Frost, G. J., Neuman, J. A., Pollack, I. B., Peischl, J., Ryerson, T. B., Holloway, J., Brown, S. S., Nowak, J. B., Roberts, J. M., Wofsy, S. C., Santoni, G. W., Oda, T., and Trainer, M.: Top-down estimate of surface flux in the Los Angeles Basin using a mesoscale inverse modeling technique: assessing anthropogenic emissions of CO, NO_x and CO_2 and their impacts, Atmos. Chem. Phys., 13, 3661–3677, https://doi.org/10.5194/acp-13-3661-2013, 2013.

Crippa, M., Guizzardi, D., Muntean, M., and Schaaf, E.: EDGAR v5.0 Global Air Pollutant Emissions, European Commission, Joint Research Centre (JRC) [data set], http://data.europa.eu/89h/377801af-b094-4943-8fdc-f79a7c0c2d19 (last access: 2 April 2020), 2019a.

Crippa, M., Guizzardi, D., Muntean, M., Schaaf, E., Lo Vullo, E., Solazzo, E., Monforti-Ferrario, F., Olivier, J., and Vignati, E.: EDGAR v5.0 Greenhouse Gas Emissions, European Commission, Joint Research Centre (JRC) [data set], http://data.europa.eu/89h/488dc3de-f072-4810-ab83-47185158ce2a (last access: 7 April 2021), 2019b.

Dayalu, A., Munger, J. W., Wang, Y., Wofsy, S. C., Zhao, Y., Nehrkorn, T., Nielsen, C., McElroy, M. B., and Chang, R.: Carbon dioxide emissions in Northern China based on atmospheric observations from 2005 to 2009, Atmos. Chem. Phys. Discuss. [preprint], https://doi.org/10.5194/acp-2018-632, 2018.

Dekker, I. N., Houweling, S., Aben, I., Röckmann, T., Krol, M., Martínez-Alonso, S., Deeter, M. N., and Worden, H. M.: Quantification of CO emissions from the city of Madrid using MOPITT satellite retrievals and WRF simulations, Atmos. Chem. Phys., 17, 14675–14694, https://doi.org/10.5194/acp-17-14675-2017, 2017.

Dekker, I. N., Houweling, S., Pandey, S., Krol, M., Röckmann, T., Borsdorff, T., Landgraf, J., and Aben, I.: What caused the extreme CO concentrations during the 2017 high-pollution episode in India?, Atmos. Chem. Phys., 19, 3433–3445, https://doi.org/10.5194/acp-19-3433-2019, 2019.

De Mazière, M.: M. De Mazière (IASB-BIRA) – Bruker 125HR installed in March 2013 for NDACC measurements, NDACC [data set], https://www-air.larc.nasa.gov/missions/ndacc/data.html?station=la.reunion.maido/hdf/ftir/, last access: 7 May 2019.

De Mazière, M., Sha, M. K., Desmet, F., Hermans, C., Scolas, F., Kumps, N., Metzger, J.-M., Duflot, V., and Cammas, J.-P.: TCCON data from Réunion Island (RE), Release GGG2014.R1 (Version R1), CaltechDATA [data set], https://doi.org/10.14291/TCCON.GGG2014.REUNION01.R1, 2017.

De Mazière, M., Thompson, A. M., Kurylo, M. J., Wild, J. D., Bernhard, G., Blumenstock, T., Braathen, G. O., Hannigan, J. W., Lambert, J.-C., Leblanc, T., McGee, T. J., Nedoluha, G., Petropavlovskikh, I., Seckmeyer, G., Simon, P. C., Steinbrecht, W., and Strahan, S. E.: The Network for the Detection of Atmospheric Composition Change (NDACC): history, status and perspectives, Atmos. Chem. Phys., 18, 4935–4964, https://doi.org/10.5194/acp-18-4935-2018, 2018.

De Mazière, M., Sha, M. K., Ramonet, M., and ICOS RI: ICOS Atmosphere Level 2 data, La Réunion, release 2021-1 (Version 1.0). ICOS ERIC – Carbon Portal [data set], https://doi.org/10.18160/Z7WE-5XHP, 2021.

Dominutti, P. A., Renard, P., Vaïtilingom, M., Bianco, A., Baray, J.-L., Borbon, A., Bourianne, T., Burnet, F., Colomb, A., Delort, A.-M., Duflot, V., Houdier, S., Jaffrezo, J.-L., Joly, M., Leremboure, M., Metzger, J.-M., Pichon, J.-M., Ribeiro, M., Rocco, M., Tulet, P., Vella, A., Leriche, M., and Deguillaume, L.: Insights into tropical cloud chemistry in Réunion (Indian Ocean): results from the BIO-MAÏDO campaign, Atmos. Chem. Phys., 22, 505–533, https://doi.org/10.5194/acp-22-505-2022, 2022.

Duflot, V., Dils, B., Baray, J. L., De Mazière, M., Attié, J. L., Vanhaelewyn, G., Senten, C., Vigouroux, C., Clain, G., and Delmas, R.: Analysis of the origin of the distribution of CO in the subtropical southern Indian Ocean in 2007, J. Geophys. Res.-Atmos., 115, D22106, https://doi.org/10.1029/2010JD013994, 2010.

Duflot, V., Tulet, P., Flores, O., Barthe, C., Colomb, A., Deguillaume, L., Vaïtilingom, M., Perring, A., Huffman, A., Hernandez, M. T., Sellegri, K., Robinson, E., O'Connor, D. J., Gomez, O. M., Burnet, F., Bourrianne, T., Strasberg, D., Rocco, M., Bertram, A. K., Chazette, P., Totems, J., Fournel, J., Stamenoff, P., Metzger, J.-M., Chabasset, M., Rousseau, C., Bourrianne, E., Sancelme, M., Delort, A.-M., Wegener, R. E., Chou, C., and Elizondo, P.: Preliminary results from the FARCE 2015 campaign: multidisciplinary study of the forest–gas–aerosol–cloud system on the tropical island of La Réunion, Atmos. Chem. Phys., 19, 10591–10618, https://doi.org/10.5194/acp-19-10591-2019, 2019.

Dupont, J.-C., Haeffelin, M., Badosa, J., Clain, G., Raux, C., and Vignelles, D.: Characterization and Corrections of Relative Humidity Measurement from Meteomodem M10 Radiosondes at Midlatitude Stations, J. Atmos. Ocean. Tech., 37, 857–871, https://doi.org/10.1175/JTECH-D-18-0205.1, 2020.

Errera, Q., Bennouna, Y., Schulz, M., Eskes, H., Basart, S., Benedictow, A., Blechschmidt, A.-M., Chabrillat, S., Clark, H., Cuevas, E., Flentje, H., Hansen, K., U. Im, J. K., Langerock, B., Petersen, K., Richter, A., Sudarchikova, N., Thouret, V., Wagner, A., Wang, Y., Warneke, T., and Zerefos, C.: Validation report of the CAMS global Reanalysis of aerosols and reactive gases, years 2003–2020, Tech. rep., Copernicus Atmosphere Monitoring Service (CAMS), https://doi.org/10.24380/8gf9-k005, 2021.

Feng, S., Lauvaux, T., Newman, S., Rao, P., Ahmadov, R., Deng, A., Díaz-Isaac, L. I., Duren, R. M., Fischer, M. L., Gerbig, C., Gurney, K. R., Huang, J., Jeong, S., Li, Z., Miller, C. E., O'Keeffe, D., Patarasuk, R., Sander, S. P., Song, Y., Wong, K. W., and Yung, Y. L.: Los Angeles megacity: a high-resolution land–atmosphere modelling system for urban CO_2 emissions, Atmos. Chem. Phys., 16, 9019–9045, https://doi.org/10.5194/acp-16-9019-2016, 2016.

Foucart, B., Sellegri, K., Tulet, P., Rose, C., Metzger, J.-M., and Picard, D.: High occurrence of new particle formation events at the Maïdo high-altitude observatory (2150 m), Réunion (Indian Ocean), Atmos. Chem. Phys., 18, 9243–9261, https://doi.org/10.5194/acp-18-9243-2018, 2018.

Frey, M. M., Hase, F., Blumenstock, T., Dubravica, D., Groß, J., Göttsche, F., Handjaba, M., Amadhila, P., Mushi, R., Morino, I., Shiomi, K., Sha, M. K., de Mazière, M., and Pollard, D. F.: Long-term column-averaged greenhouse gas observations using a COCCON spectrometer at the high-surface-albedo site in Gobabeb, Namibia, Atmos. Meas. Tech., 14, 5887–5911, https://doi.org/10.5194/amt-14-5887-2021, 2021.

García, M. Á., Sánchez, M. L., and Pérez, I. A.: Differences between carbon dioxide levels over suburban and rural sites in Northern Spain, Environm. Sci. Pollut. R., 19, 432–439, https://doi.org/10.1007/s11356-011-0575-4, 2012.

Giglio, L., Csiszar, I., and Justice, C. O.: Global distribution and seasonality of active fires as observed with the Terra and Aqua Moderate Resolution Imaging Spectroradiometer (MODIS) sensors, J. Geophys. Res.-Biogeo., 111, G02016, https://doi.org/10.1029/2005JG000142, 2006.

Grell, G. A. and Freitas, S. R.: A scale and aerosol aware stochastic convective parameterization for weather and air quality modeling, Atmos. Chem. Phys., 14, 5233–5250, https://doi.org/10.5194/acp-14-5233-2014, 2014.

Guilpart, E., Vimeux, F., Evan, S., Brioude, J., Metzger, J.-M., Barthe, C., Risi, C., and Cattani, O.: The isotopic composition of near-surface water vapor at the Maïdo observatory (Reunion Island, southwestern Indian Ocean) doc-

uments the controls of the humidity of the subtropical troposphere, J. Geophys. Res.-Atmos., 122, 9628–9650, https://doi.org/10.1002/2017JD026791, 2017.

Hase, F., Frey, M., Blumenstock, T., Groß, J., Kiel, M., Kohlhepp, R., Mengistu Tsidu, G., Schäfer, K., Sha, M. K., and Orphal, J.: Application of portable FTIR spectrometers for detecting greenhouse gas emissions of the major city Berlin, Atmos. Meas. Tech., 8, 3059–3068, https://doi.org/10.5194/amt-8-3059-2015, 2015.

Hersbach, H., Bell, B., Berrisford, P., Biavati, G., Horányi, A., Muñoz Sabater, J., Nicolas, J., Peubey, C., Radu, R., Rozum, I., Schepers, D., Simmons, A., Soci, C., Dee, D., and Thépaut, J.-N.: ERA5 hourly data on single levels from 1979 to present, Copernicus Climate Change Service (C3S) Climate Data Store (CDS) [data set], https://doi.org/10.24381/cds.adbb2d47, 2018a.

Hersbach, H., Bell, B., Berrisford, P., Biavati, G., Horányi, A., Muñoz Sabater, J., Nicolas, J., Peubey, C., Radu, R., Rozum, I., Schepers, D., Simmons, A., Soci, C., Dee, D., and Thépaut, J.-N.: ERA5 hourly data on pressure levels from 1979 to present, Copernicus Climate Change Service (C3S) Climate Data Store (CDS) [data set], https://doi.org/10.24381/cds.bd0915c6, 2018b.

Hu, X.-M., Crowell, S., Wang, Q., Zhang, Y., Davis, K. J., Xue, M., Xiao, X., Moore, B., Wu, X., Choi, Y., and DiGangi, J. P.: Dynamical Downscaling of CO_2 in 2016 Over the Contiguous United States Using WRF-VPRM, a Weather-Biosphere-Online-Coupled Model, J. Adv. Model. Earth Syst., 12, e2019MS001875, https://doi.org/10.1029/2019MS001875, 2020.

Iacono, M. J., Delamere, J. S., Mlawer, E. J., Shephard, M. W., Clough, S. A., and Collins, W. D.: Radiative forcing by long-lived greenhouse gases: Calculations with the AER radiative transfer models, J. Geophys. Res.-Atmos., 113, D13103, https://doi.org/10.1029/2008JD009944, 2008.

Idso, S. B., Idso, C. D., and Balling, R. C.: Seasonal and diurnal variations of near-surface atmospheric CO_2 concentration within a residential sector of the urban CO_2 dome of Phoenix, AZ, USA, Atmos. Environ., 36, 1655–1660, https://doi.org/10.1016/S1352-2310(02)00159-0, 2002.

Inness, A., Ades, M., Agustí-Panareda, A., Barré, J., Benedictow, A., Blechschmidt, A.-M., Dominguez, J. J., Engelen, R., Eskes, H., Flemming, J., Huijnen, V., Jones, L., Kipling, Z., Massart, S., Parrington, M., Peuch, V.-H., Razinger, M., Remy, S., Schulz, M., and Suttie, M.: The CAMS reanalysis of atmospheric composition, Atmos. Chem. Phys., 19, 3515–3556, https://doi.org/10.5194/acp-19-3515-2019, 2019.

IPCC: Summary for Policymakers, in: Climate Change 2021: The Physical Science Basis. Contribution of Working Group I to the Sixth Assessment Report of the Intergovernmental Panel on Climate Change, edited by: Masson-Delmotte, V., Zhai, P., Pirani, A., Connors, S. L., Péan, C., Berger, S., Caud, N., Chen, Y., Goldfarb, L., Gomis, M. I., Huang, M., Leitzell, K., Lonnoy, E., Matthews, J. B. R., Maycock, T. K., Waterfield, T., Yelekçi, O., Yu, R., and Zhou, B., Cambridge University Press, Cambridge, United Kingdom and New York, NY, USA, 3–32, https://doi.org/10.1017/9781009157896.001, 2021.

Jamroensan, A.: Improving bottom-up and top-down estimates of carbon fluxes in the Midwestern USA, PhD thesis, University of Iowa, https://doi.org/10.17077/etd.99sd8cdc, 2013.

Janjić, Z. I.: The Step-Mountain Eta Coordinate Model: Further Developments of the Convection, Viscous Sublayer, and Turbulence Closure Schemes, Mon. Weather Rev., 122, 927–945, https://doi.org/10.1175/1520-0493(1994)122<0927:TSMECM>2.0.CO;2, 1994.

Jung, M., Henkel, K., Herold, M., and Churkina, G.: Exploiting synergies of global land cover products for carbon cycle modeling, Remote Sens. Environ., 101, 534–553, https://doi.org/10.1016/j.rse.2006.01.020, 2006.

Kim, Y., Sartelet, K., Raut, J.-C., and Chazette, P.: Evaluation of the Weather Research and Forecast/Urban Model Over Greater Paris, Bound.-Lay. Meteorol., 149, 1573–1472, https://doi.org/10.1007/s10546-013-9838-6, 2013.

Lac, C., Chaboureau, J.-P., Masson, V., Pinty, J.-P., Tulet, P., Escobar, J., Leriche, M., Barthe, C., Aouizerats, B., Augros, C., Aumond, P., Auguste, F., Bechtold, P., Berthet, S., Bielli, S., Bosseur, F., Caumont, O., Cohard, J.-M., Colin, J., Couvreux, F., Cuxart, J., Delautier, G., Dauhut, T., Ducrocq, V., Filippi, J.-B., Gazen, D., Geoffroy, O., Gheusi, F., Honnert, R., Lafore, J.-P., Lebeaupin Brossier, C., Libois, Q., Lunet, T., Mari, C., Maric, T., Mascart, P., Mogé, M., Molinié, G., Nuissier, O., Pantillon, F., Peyrillé, P., Pergaud, J., Perraud, E., Pianezze, J., Redelsperger, J.-L., Ricard, D., Richard, E., Riette, S., Rodier, Q., Schoetter, R., Seyfried, L., Stein, J., Suhre, K., Taufour, M., Thouron, O., Turner, S., Verrelle, A., Vié, B., Visentin, F., Vionnet, V., and Wautelet, P.: Overview of the Meso-NH model version 5.4 and its applications, Geosci. Model Dev., 11, 1929–1969, https://doi.org/10.5194/gmd-11-1929-2018, 2018.

Landschützer, P., Gruber, N., and Bakker, D. C. E.: An observation-based global monthly gridded sea surface pCO_2 product from 1982 onward and its monthly climatology (NCEI Accession 0160558), NOAA National Centers for Environmental Information [data set], https://doi.org/10.7289/v5z899n6, 2017.

Langerock, B., De Mazière, M., Hendrick, F., Vigouroux, C., Desmet, F., Dils, B., and Niemeijer, S.: Description of algorithms for co-locating and comparing gridded model data with remote-sensing observations, Geosci. Model Dev., 8, 911–921, https://doi.org/10.5194/gmd-8-911-2015, 2015.

Lesouëf, D., Gheusi, F., Delmas, R., and Escobar, J.: Numerical simulations of local circulations and pollution transport over Reunion Island, Ann. Geophys., 29, 53–69, https://doi.org/10.5194/angeo-29-53-2011, 2011.

Lesouëf, D., Gheusi, F., Chazette, P., Delmas, R., and Sanak, J.: Low Tropospheric Layers Over Reunion Island in Lidar-Derived Observations and a High-Resolution Model, Bound.-Lay. Meteorol., 149, 425–453, https://doi.org/10.1007/s10546-013-9851-9, 2013.

Li, X., Hu, X.-M., Cai, C., Jia, Q., Zhang, Y., Liu, J., Xue, M., Xu, J., Wen, R., and Crowell, S. M. R.: Terrestrial CO_2 Fluxes, Concentrations, Sources and Budget in Northeast China: Observational and Modeling Studies, J. Geophys. Res.-Atmos., 125, e2019JD031686, https://doi.org/10.1029/2019JD031686, 2020.

Liu, Y., Yue, T., Zhang, L., Zhao, N., Zhao, M., and Liu, Y.: Simulation and analysis of XCO_2 in North China based on high accuracy surface modeling, Environ. Sci. Pollut. R., 25, 27378–27392, https://doi.org/10.1007/s11356-018-2683-x, 2018.

Lunt, M. F., Palmer, P. I., Feng, L., Taylor, C. M., Boesch, H., and Parker, R. J.: An increase in methane emissions from tropical Africa between 2010 and 2016 inferred

from satellite data, Atmos. Chem. Phys., 19, 14721–14740, https://doi.org/10.5194/acp-19-14721-2019, 2019.

Mahadevan, P., Wofsy, S. C., Matross, D. M., Xiao, X., Dunn, A. L., Lin, J. C., Gerbig, C., Munger, J. W., Chow, V. Y., and Gottlieb, E. W.: A satellite-based biosphere parameterization for net ecosystem CO_2 exchange: Vegetation Photosynthesis and Respiration Model (VPRM), Global Biogeochem. Cy., 22, GB2005, https://doi.org/10.1029/2006GB002735, 2008.

Makarova, M. V., Alberti, C., Ionov, D. V., Hase, F., Foka, S. C., Blumenstock, T., Warneke, T., Virolainen, Y. A., Kostsov, V. S., Frey, M., Poberovskii, A. V., Timofeyev, Y. M., Paramonova, N. N., Volkova, K. A., Zaitsev, N. A., Biryukov, E. Y., Osipov, S. I., Makarov, B. K., Polyakov, A. V., Ivakhov, V. M., Imhasin, H. Kh., and Mikhailov, E. F.: Emission Monitoring Mobile Experiment (EMME): an overview and first results of the St. Petersburg megacity campaign 2019, Atmos. Meas. Tech., 14, 1047–1073, https://doi.org/10.5194/amt-14-1047-2021, 2021.

Massen, F. and Beck, E.-G.: Accurate Estimation of CO_2 Background Level from Near Ground Measurements at Non-Mixed Environments, Springer Berlin Heidelberg, Berlin, Heidelberg, https://doi.org/10.1007/978-3-642-14776-0_31, 2011.

Morrison, H., Thompson, G., and Tatarskii, V.: Impact of Cloud Microphysics on the Development of Trailing Stratiform Precipitation in a Simulated Squall Line: Comparison of One- and Two-Moment Schemes, Mon. Weather Rev., 137, 991–1007, https://doi.org/10.1175/2008MWR2556.1, 2009.

Nassar, R., Napier-Linton, L., Gurney, K. R., Andres, R. J., Oda, T., Vogel, F. R., and Deng, F.: Improving the temporal and spatial distribution of CO_2 emissions from global fossil fuel emission data sets, J. Geophys. Res.-Atmos., 118, 917–933, https://doi.org/10.1029/2012JD018196, 2013.

National Center for Atmospheric Research (NCAR): Weather Research and Forecasting Model Version 4.1.5, NCAR [code], https://doi.org/10.5065/D6MK6B4K, 2020.

Oda, T. and Maksyutov, S.: A very high-resolution (1 km × 1 km) global fossil fuel CO_2 emission inventory derived using a point source database and satellite observations of nighttime lights, Atmos. Chem. Phys., 11, 543–556, https://doi.org/10.5194/acp-11-543-2011, 2011.

Oda, T. and Maksyuto, S.: ODIAC Fossil Fuel CO_2 Emissions Dataset (ODIAC2020), Center for Global Environmental Research, National Institute for Environmental Studies [data set], https://doi.org/10.17595/20170411.001, 2015.

Oda, T., Maksyutov, S., and Andres, R. J.: The Open-source Data Inventory for Anthropogenic CO_2, version 2016 (ODIAC2016): a global monthly fossil fuel CO_2 gridded emissions data product for tracer transport simulations and surface flux inversions, Earth Syst. Sci. Data, 10, 87–107, https://doi.org/10.5194/essd-10-87-2018, 2018.

Park, C., Gerbig, C., Newman, S., Ahmadov, R., Feng, S., Gurney, K. R., Carmichael, G. R., Park, S.-Y., Lee, H.-W., Goulden, M., Stutz, J., Peischl, J., and Ryerson, T.: CO_2 Transport, Variability, and Budget over the Southern California Air Basin Using the High-Resolution WRF-VPRM Model during the CalNex 2010 Campaign, J. Appl. Meteorol. Clim., 57, 1337–1352, https://doi.org/10.1175/JAMC-D-17-0358.1, 2018.

Park, C., Park, S.-Y., Gurney, K. R., Gerbig, C., DiGangi, J. P., Choi, Y., and Lee, H. W.: Numerical simulation of atmospheric CO_2 concentration and flux over the Korean Peninsula using WRF-VPRM model during Korus-AQ 2016 campaign, PLoS ONE, 15, 1–21, https://doi.org/10.1371/journal.pone.0228106, 2020.

Pillai, D., Gerbig, C., Marshall, J., Ahmadov, R., Kretschmer, R., Koch, T., and Karstens, U.: High resolution modeling of CO_2 over Europe: implications for representation errors of satellite retrievals, Atmos. Chem. Phys., 10, 83–94, https://doi.org/10.5194/acp-10-83-2010, 2010.

Pillai, D., Gerbig, C., Kretschmer, R., Beck, V., Karstens, U., Neininger, B., and Heimann, M.: Comparing Lagrangian and Eulerian models for CO_2 transport – a step towards Bayesian inverse modeling using WRF/STILT-VPRM, Atmos. Chem. Phys., 12, 8979–8991, https://doi.org/10.5194/acp-12-8979-2012, 2012.

Pillai, D., Buchwitz, M., Gerbig, C., Koch, T., Reuter, M., Bovensmann, H., Marshall, J., and Burrows, J. P.: Tracking city CO_2 emissions from space using a high-resolution inverse modelling approach: a case study for Berlin, Germany, Atmos. Chem. Phys., 16, 9591–9610, https://doi.org/10.5194/acp-16-9591-2016, 2016.

Quansah, E., Mauder, M., Balogun, A. A., Amekudzi, L. K., Hingerl, L., Bliefernicht, J., and Kunstmann, H.: Carbon dioxide fluxes from contrasting ecosystems in the Sudanian Savanna in West Africa, Carbon Balance and Management, 10, 1 , https://doi.org/10.1186/s13021-014-0011-4, 2015.

Ramonet, M., Langerock, B., Warneke, T., and Eskes, H. J.: Validation report of the CAMS greenhouse gas global reanalysis, years 2003–2016, Copernicus Atmosphere Monitoring Service (CAMS) report, https://doi.org/10.24380/y034-7672, 2020.

Räsänen, M., Aurela, M., Vakkari, V., Beukes, J. P., Tuovinen, J.-P., Van Zyl, P. G., Josipovic, M., Venter, A. D., Jaars, K., Siebert, S. J., Laurila, T., Rinne, J., and Laakso, L.: Carbon balance of a grazed savanna grassland ecosystem in South Africa, Biogeosciences, 14, 1039–1054, https://doi.org/10.5194/bg-14-1039-2017, 2017.

Rice, A. and Bostrom, G.: Measurements of carbon dioxide in an Oregon metropolitan region, Atmos. Environ., 45, 1138–1144, https://doi.org/10.1016/j.atmosenv.2010.11.026, 2011.

Rodgers, C. D.: Inverse Methods for Atmospheric Sounding, World Scientific, https://doi.org/10.1142/3171, 2000.

Rodgers, C. D. and Connor, B. J.: Intercomparison of remote sounding instruments, J. Geophys. Res.-Atmos., 108, 4116, https://doi.org/10.1029/2002JD002299, 2003.

Sepúlveda, E., Schneider, M., Hase, F., Barthlott, S., Dubravica, D., García, O. E., Gomez-Pelaez, A., González, Y., Guerra, J. C., Gisi, M., Kohlhepp, R., Dohe, S., Blumenstock, T., Strong, K., Weaver, D., Palm, M., Sadeghi, A., Deutscher, N. M., Warneke, T., Notholt, J., Jones, N., Griffith, D. W. T., Smale, D., Brailsford, G. W., Robinson, J., Meinhardt, F., Steinbacher, M., Aalto, T., and Worthy, D.: Tropospheric CH_4 signals as observed by NDACC FTIR at globally distributed sites and comparison to GAW surface in situ measurements, Atmos. Meas. Tech., 7, 2337–2360, https://doi.org/10.5194/amt-7-2337-2014, 2014.

Skamarock, W. C., Klemp, J. B., Dudhia, J., Gill, D. O., Liu, Z., Berner, J., Wang, W., Powers, J. G., Duda, M. G., Barker, D., and Huang, X.-Y.: A Description of the Advanced Research WRF Model Version 4.3, Tech. rep., No. NCAR/TN-556+STR, NCAR/UCAR, https://doi.org/10.5065/1dfh-6p97, 2021.

Tewari, M., Chen, F., Wang, W., Dudhia, J., Lemone, M. A., and Mitchell, K. E.: Implementation and verification of the unified

Noah land-surface model in the WRF model, American Meteorological Society, Seattle, WA, US, in: 20th Conference on Weather Analysis and Forecasting/16th Conference on Numerical Weather Prediction, 14 January 2004, Seattle, WA, USA, http://n2t.net/ark:/85065/d7fb523p (last access: 21 April 2020), 2004.

Tsivlidou, M.: TROPOMI and WRF comparison for understanding South Sudan wetland emissions, MA thesis, Utrecht University, https://studenttheses.uu.nl/handle/20.500.12932/31525 (last access: 4 September 2019), 2018.

Verkaik, J.: Evaluation of Colombian methane emissions combining WRF-Chem and TROPOMI, Master's thesis, University of Wageningen, https://edepot.wur.nl/496227 (last access: 11 August 2020), 2019.

Verreyken, B., Brioude, J., and Evan, S.: Development of turbulent scheme in the FLEXPART-AROME v1.2.1 Lagrangian particle dispersion model, Geosci. Model Dev., 12, 4245–4259, https://doi.org/10.5194/gmd-12-4245-2019, 2019.

Verreyken, B., Amelynck, C., Schoon, N., Müller, J.-F., Brioude, J., Kumps, N., Hermans, C., Metzger, J.-M., Colomb, A., and Stavrakou, T.: Measurement report: Source apportionment of volatile organic compounds at the remote high-altitude Maïdo observatory, Atmos. Chem. Phys., 21, 12965–12988, https://doi.org/10.5194/acp-21-12965-2021, 2021.

Vigouroux, C., Stavrakou, T., Whaley, C., Dils, B., Duflot, V., Hermans, C., Kumps, N., Metzger, J.-M., Scolas, F., Vanhaelewyn, G., Müller, J.-F., Jones, D. B. A., Li, Q., and De Mazière, M.: FTIR time-series of biomass burning products (HCN, C_2H_6, C_2H_2, CH_3OH, and HCOOH) at Reunion Island (21° S, 55° E) and comparisons with model data, Atmos. Chem. Phys., 12, 10367–10385, https://doi.org/10.5194/acp-12-10367-2012, 2012.

Vogel, F. R., Frey, M., Staufer, J., Hase, F., Broquet, G., Xueref-Remy, I., Chevallier, F., Ciais, P., Sha, M. K., Chelin, P., Jeseck, P., Janssen, C., Té, Y., Groß, J., Blumenstock, T., Tu, Q., and Orphal, J.: XCO_2 in an emission hot-spot region: the COCCON Paris campaign 2015, Atmos. Chem. Phys., 19, 3271–3285, https://doi.org/10.5194/acp-19-3271-2019, 2019.

Wiedinmyer, C., Akagi, S. K., Yokelson, R. J., Emmons, L. K., Al-Saadi, J. A., Orlando, J. J., and Soja, A. J.: The Fire INventory from NCAR (FINN): a high resolution global model to estimate the emissions from open burning, Geosci. Model Dev., 4, 625–641, https://doi.org/10.5194/gmd-4-625-2011, 2011.

Wunch, D., Toon, G. C., Wennberg, P. O., Wofsy, S. C., Stephens, B. B., Fischer, M. L., Uchino, O., Abshire, J. B., Bernath, P., Biraud, S. C., Blavier, J.-F. L., Boone, C., Bowman, K. P., Browell, E. V., Campos, T., Connor, B. J., Daube, B. C., Deutscher, N. M., Diao, M., Elkins, J. W., Gerbig, C., Gottlieb, E., Griffith, D. W. T., Hurst, D. F., Jiménez, R., Keppel-Aleks, G., Kort, E. A., Macatangay, R., Machida, T., Matsueda, H., Moore, F., Morino, I., Park, S., Robinson, J., Roehl, C. M., Sawa, Y., Sherlock, V., Sweeney, C., Tanaka, T., and Zondlo, M. A.: Calibration of the Total Carbon Column Observing Network using aircraft profile data, Atmos. Meas. Tech., 3, 1351–1362, https://doi.org/10.5194/amt-3-1351-2010, 2010.

Wunch, D., Toon, G. C., Blavier, J.-F. L., Washenfelder, R. A., Notholt, J., Connor, B. J., Griffith, D. W. T., Sherlock, V., and Wennberg, P. O.: The Total Carbon Column Observing Network, Philos. T. Roy. Soc. A, 369, 2087–2112, https://doi.org/10.1098/rsta.2010.0240, 2011.

Xueref-Remy, I., Dieudonné, E., Vuillemin, C., Lopez, M., Lac, C., Schmidt, M., Delmotte, M., Chevallier, F., Ravetta, F., Perrussel, O., Ciais, P., Bréon, F.-M., Broquet, G., Ramonet, M., Spain, T. G., and Ampe, C.: Diurnal, synoptic and seasonal variability of atmospheric CO_2 in the Paris megacity area, Atmos. Chem. Phys., 18, 3335–3362, https://doi.org/10.5194/acp-18-3335-2018, 2018.

Yue, C., Ciais, P., Bastos, A., Chevallier, F., Yin, Y., Rödenbeck, C., and Park, T.: Vegetation greenness and land carbon-flux anomalies associated with climate variations: a focus on the year 2015, Atmos. Chem. Phys., 17, 13903–13919, https://doi.org/10.5194/acp-17-13903-2017, 2017.

Zhang, Y., Dubey, M. K., Olsen, S. C., Zheng, J., and Zhang, R.: Comparisons of WRF/Chem simulations in Mexico City with ground-based RAMA measurements during the 2006-MILAGRO, Atmos. Chem. Phys., 9, 3777–3798, https://doi.org/10.5194/acp-9-3777-2009, 2009.

Zhao, X., Marshall, J., Hachinger, S., Gerbig, C., Frey, M., Hase, F., and Chen, J.: Analysis of total column CO_2 and CH_4 measurements in Berlin with WRF-GHG, Atmos. Chem. Phys., 19, 11279–11302, https://doi.org/10.5194/acp-19-11279-2019, 2019.

Zhou, M., Langerock, B., Vigouroux, C., Sha, M. K., Ramonet, M., Delmotte, M., Mahieu, E., Bader, W., Hermans, C., Kumps, N., Metzger, J.-M., Duflot, V., Wang, Z., Palm, M., and De Mazière, M.: Atmospheric CO and CH_4 time series and seasonal variations on Reunion Island from ground-based in situ and FTIR (NDACC and TCCON) measurements, Atmos. Chem. Phys., 18, 13881–13901, https://doi.org/10.5194/acp-18-13881-2018, 2018.

Zhou, M., Langerock, B., Vigouroux, C., Sha, M. K., Hermans, C., Metzger, J.-M., Chen, H., Ramonet, M., Kivi, R., Heikkinen, P., Smale, D., Pollard, D. F., Jones, N., Velazco, V. A., García, O. E., Schneider, M., Palm, M., Warneke, T., and De Mazière, M.: TCCON and NDACC X_{CO} measurements: difference, discussion and application, Atmos. Meas. Tech., 12, 5979–5995, https://doi.org/10.5194/amt-12-5979-2019, 2019.

Chapter 5

Explaining GHG variability in northeast China: a WRF-GHG study at Xianghe

This chapter examines the in situ and column observations of CO_2, CH_4, and CO at the Xianghe site near Beijing, China. The WRF-GHG model is used to simulate the observed time series, assessing the model's accuracy at this location. It also investigates the primary source sectors and meteorological processes influencing the observed variabilities, and attempts to explain discrepancies between the model and observed data.
The manuscript discussing the results for CH_4 was submitted to the peer-reviewed journal Atmospheric Chemistry & Physics in October 2024 and is currently under review. The first section of this chapter consists of this preprint, which is also available online at the EGUsphere platform:

Callewaert, S., Zhou, M., Langerock, B., Wang, P., Wang, T., Mahieu, E., and De Mazière, M.: A WRF-Chem Study of the Greenhouse Gas Column and in Situ Surface Concentrations Observed at Xianghe, China. Part 1: Methane (CH_4), EGUsphere, pp. 1–39, doi: 10.5194/egusphere-2024-3228, 2024

The results for CO_2 and CO will be published in a follow-up article and are given in the second part of this chapter.

5.1 Analysis of CH_4 time series

https://doi.org/10.5194/egusphere-2024-3228
Preprint. Discussion started: 29 October 2024

A WRF-Chem study of the greenhouse gas column and in situ surface concentrations observed at Xianghe, China. Part 1: Methane (CH_4)

Sieglinde Callewaert[1,3], Minqiang Zhou[1,2], Bavo Langerock[1], Pucai Wang[2], Ting Wang[2], Emmanuel Mahieu[3], and Martine De Mazière[1]

[1]Royal Belgian Institute for Spacy Aeronomy (BIRA-IASB), Brussels, Belgium
[2]CNRC & LAGEO, Institute of Atmospheric Physics, Chinese Academy of Sciences, Beijing, China
[3]UR SPHERES, Department of Astrophysics, Geophysics and Oceanography, University of Liège, Liège, Belgium

Correspondence: Sieglinde Callewaert (sieglinde.callewaert@aeronomie.be), Minqiang Zhou (minqiang.zhou@aeronomie.be)

Abstract. This study is the first of two companion papers which investigate the temporal variability of CO_2, CH_4 and additionally CO concentrations measured at the Xianghe observation site near Beijing in China using the Weather Research and Forecast model coupled with Chemistry (WRF-Chem), aiming to understand the contributions from different emission sectors and the influence of meteorological processes. Simulations of the in situ (PICARRO) and remote sensing (TCCON-affiliated) measurements are produced by the model's greenhouse gas option, called WRF-GHG, from September 2018 until September 2019. The present study discusses the results for CH_4. The model shows good performance, after correcting for biases in boundary conditions, achieving correlation coefficients up to 0.66 for near-surface concentrations and 0.65 for column-averaged data. The simulations use separate tracers for different source sectors and revealed that energy, residential heating, waste management and agriculture are the primary contributors to the CH_4 concentrations, with the energy sector having a greater impact on column measurements than surface concentrations. Monthly variability is linked to both emission patterns and meteorological influences, with advection of either clean or polluted air masses from the North China Plain playing a significant role. The diurnal variation of the in situ concentrations due to planetary boundary layer dynamics is quite well captured by WRF-GHG. Despite capturing the key variability of the CH_4 observations, the model displays a seasonal bias, likely originating from an incorrect seasonality in the emissions from agricultural and/or waste management activities. Our findings highlight the value of WRF-GHG to interpret both surface and column observations at Xianghe, offering source sector attribution and insights in the link with local and large-scale winds based on the simultaneously computed meteorological fields. However, they also highlight the need to improve the knowledge on the seasonal CH_4 cycle in northern China to obtain more accurate emission data and boundary conditions for high-resolution modeling.

1 Introduction

Carbon dioxide (CO_2) and methane (CH_4) are the most important anthropogenic greenhouse gases (GHG), contributing to climate change. Driven by human activities, the atmospheric burden of both species has been increasing over the last 200 years

https://doi.org/10.5194/egusphere-2024-3228
Preprint. Discussion started: 29 October 2024

to unprecedented levels (Masson-Delmotte et al., 2021). Moreover, CH_4 has a 28 times larger global warming potential than CO_2 over a period of 100 year and a 10 times shorter atmospheric lifetime. Controlling CH_4 emissions is therefore a priority to mitigate climate change in the near future (Saunois et al., 2020).

Because of rapid industrialization in the past decades and its heavy dependence on coal, China is the world's largest emitter of CO_2 and CH_4 (Friedlingstein et al., 2022; Worden et al., 2022). The main anthropogenic CO_2 sources in China are industry, power generation, residential and commercial activities and transportation (Zhao et al., 2012), while sectors such as coal mining, livestock, rice paddies, landfills and wastewater management are the largest contributors to the CH_4 emissions in China (Chen et al., 2022). China has pledged to reach its carbon peak by 2030 and neutrality by 2060. To help battle climate change and reach these goals, it is essential to have accurate observations of the GHG concentrations. Not only does atmospheric monitoring aid in revealing sources and sinks and controlling the impact of mitigation measures, but by studying temporal variations a better understanding of the carbon cycle and its interactions with the atmosphere can be achieved.

Since 2018, both ground-based in situ and remote sensing observations of GHGs have been deployed at the Xianghe observatory, which is located about 50 km southwest of Beijing. Its location in the center of the Beijing-Tianjin-Hebei (BTH) megalopolis makes it an interesting site to study the properties and variability of GHGs in a polluted area. The remote sensing observations are made by a Fourier Transform Infrared (FTIR) spectrometer and are part of the international Total Column Carbon Observing Network (TCCON), while the in situ concentrations are measured by a PICARRO cavity ring-down spectroscopy (CRDS) analyzer that samples air from a tower at an altitude of 60 m above the ground.

Our work aims to perform a comprehensive analysis of both in situ and column observations of CO_2, CH_4 and additionally CO at Xianghe to gain a better understanding of the causes of the observed temporal variabilities and complement previous studies. The present article is the first of two companion papers where the focus of the current work lies on the CH_4 observations. A second paper (in preparation) will cover the analysis for CO_2 and CO.

Some first insights in the observed CH_4 time series at Xianghe were made by Yang et al. (2020) and Ji et al. (2020). They found that the seasonal cycle of XCH_4 is different compared to those at other TCCON sites at similar latitude, with larger concentrations in summer and autumn and lower values in spring. Furthermore, the column observations of CO_2, CH_4 and CO show a large day-to-day variability and are correlated with each other. Yang et al. (2020) showed that the high values are related to both local pollution and pollution originating from the south, while low concentrations are corresponding with clean airmasses from more remote regions in the north.

To achieve our goal, we will simulate the time series at a high spatial resolution with the WRF-Chem model for greenhouse gases (WRF-GHG). This widely used regional atmospheric transport model simulates the 3-D concentrations together with meteorological fields without chemical interactions, which is generally a valid assumption regarding the regional domain and the relatively long atmospheric lifetimes of the target species ($\sim$ 100 yrs for CO_2, $\sim$ 10 yrs for CH_4 and several weeks for CO)(Dekker et al., 2017). Nevertheless, both CH_4 and CO are prone to chemical reactions in the atmosphere, making this assumption a simplification of actual conditions, which should be taken into account when analyzing the results. WRF-GHG has already shown to be a useful tool to study CO_2 fluxes and variability in China (Dayalu et al., 2018; Liu et al., 2018; Li et al., 2020; Dong et al., 2021). However, and to our best knowledge, applications to CH_4 or CO observations in China have

https://doi.org/10.5194/egusphere-2024-3228
Preprint. Discussion started: 29 October 2024

not been reported yet. Elsewhere, this model was successfully used to analyze comparable observations (Zhao et al., 2019; Hu et al., 2020; Park et al., 2020; Callewaert et al., 2022). Therefore, this study will additionally assess the model's capability of simulating these time series in north China and highlight its strengths and weaknesses in this region.

This work is structured as follows: in Sect. 2 the Xianghe site and its observations are described, together with the XCH_4 product of TROPOMI (the TROPOspheric Monitoring Instrument onboard Sentinel-5P), which will give additional insight into the results. Further, an overview of the WRF-GHG model system is given and the approach used to compare the model simulations with the different measurements. Section 3 presents the results and discussion: the main model performance is evaluated in Sect.3.1, followed by an analysis of the contributions from different source sectors to the CH_4 observations at Xianghe in Sect.3.2. Section 3.3 explores potential causes of the observed seasonal bias in the model simulations, while Sect. 3.4 examines the key meteorological processes influencing CH_4 variability. Further, a comparison with TROPOMI XCH_4 is conducted in Sect. 3.5 to investigate the potential overestimation of emissions from a coal mine source near Tangshan. Finally, Sect.4 summarizes the key findings and conclusions for CH_4.

2 Data, models and methods

2.1 Xianghe site

The observation site is situated in Xianghe county (39.7536° N, 116.96155° E; 30 m a.s.l.), a suburban area in the Beijing-Tianjin-Hebei (BTH) region in north China. The center of Xianghe is about 2 km to the east of the site, while the metropolitan cities of Beijing and Tianjin are located about 50 km to the northwest and 70 km to the south-southeast, respectively (see Fig. 1b). Cropland and irrigated cropland are the predominant kind of vegetation in the area. The East Asian Monsoon, which causes hot, humid summers with plenty of precipitation and cold, dry winters, determines the climate.

Since 1974, atmospheric observations are made at the Xianghe observatory by the Institute of Atmospheric Physics (IAP), Chinese Academy of Sciences (CAS). In June 2016 a FTIR spectroscopy instrument (Bruker IFS 125HR) was installed on the roof of the observatory, two years later, a solar tracker was added to the setup and continuous measurements are made from June 2018 onwards. This ground-based remote sensing instrument measures spectra in the infrared and is affiliated with TCCON (Wunch et al., 2011; Zhou et al., 2022), providing total column-averaged dry air mole fractions (denoted as Xgas) of CO_2, CH_4 and CO. In the current study, the GGG2020 data version (Laughner et al., 2024) is used. Depending on the weather and measurement status, observations occur every 5-20 min. TCCON measurements are performed under clear sky conditions only. The measurement uncertainty is about 6 ppb for XCH_4. Further details about the instrument and retrieval methodology can be found in Yang et al. (2020).

Additionally, in situ mole fractions of CO_2 and CH_4 are measured by a PICARRO cavity ring-down spectroscopy G2301 analyzer since June 2018. The instrument samples air from an inlet fixed at 60 m above the ground on a tower. More detail about the measurement setup is given in Yang et al. (2021). The measurement uncertainty is 1 ppb for CH_4.

https://doi.org/10.5194/egusphere-2024-3228
Preprint. Discussion started: 29 October 2024

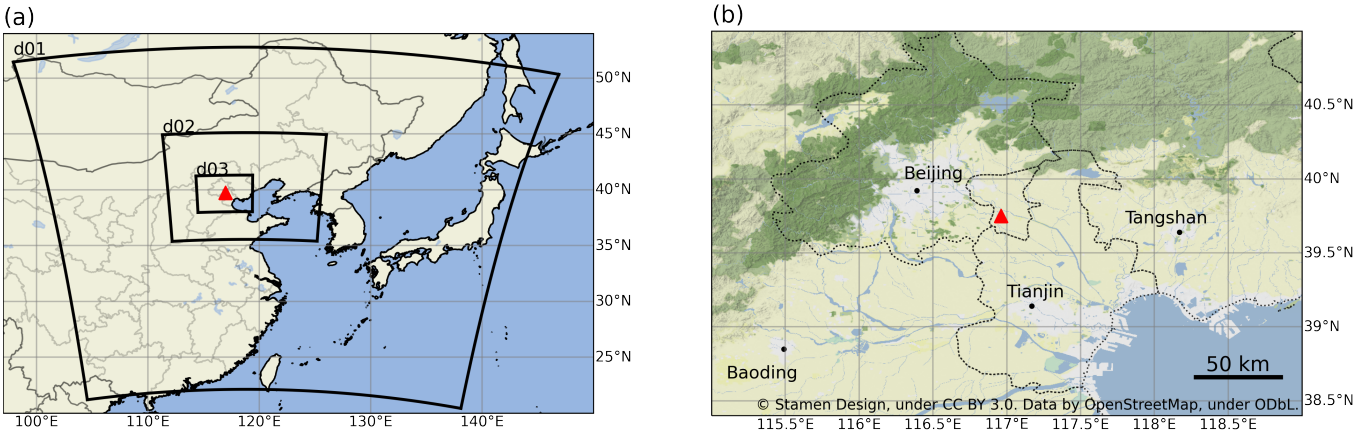

Figure 1. (a) Location of the WRF-GHG domains, with horizontal resolutions of 27 km (d01), 9 km (d02) and 3 km (d03). All domains have 60 (hybrid) vertical levels extending from the surface up to 50 hPa. (b) Terrain map including the largest cities in the region of Xianghe, roughly corresponding to d03. The location of the Xianghe site is indicated by the red triangle in both maps.

2.2 TROPOMI

The TROPOMI instrument on board the Sentinel-5 Precursor (S5P) satellite is observing the Earth on a polar sun-synchronous orbit. With a daily global coverage, it measures solar backscatter in the near and shortwave infrared absorption bands of which column-average mixing ratios of CH_4 can be retrieved. In the current study, the bias-corrected reprocessed L2 RemoTec-S5P XCH_4 product from SRON (ESA, 2021) was used, where a quality filter of 1.0 was applied. This L2 product was evaluated at Xianghe by Yang et al. (2020) and Tian et al. (2022): they found a small negative bias of -0.6% and -0.39% with TCCON XCH_4, respectively. These values are well within the mission requirements of 1.5 % and therefore indicate a good quality of TROPOMI XCH_4 in this part of China.

2.3 WRF-GHG modelling system

We use the Weather Research and Forecasting model coupled with Chemistry version 4.1.5 (WRF-Chem, Grell et al. (2005); Skamarock et al. (2019); Fast et al. (2006)) in its greenhouse gas option, called WRF-GHG (Beck et al., 2011). WRF-GHG is a Eulerian atmospheric transport model that simulates the 3-D concentration of trace gases at every time step simultaneously with meteorological fields, neglecting chemical reactions. The model configuration consists of three nested domains with increasing resolution in a Lambert Conformal projection (see Fig. 1a). The parent domain (d01) has 134 by 130 grid cells of 27×27 km^2 and covers a large part of China, Mongolia, North and South Korea and Japan. The second domain (d02), which has 133 by 121 grid cells of 9×9 km^2, mainly covers north China. Finally, the innermost domain (d03) has a resolution of 3×3 km^2 over 145 by 124 grid cells and almost completely covers BTH. There are 60 vertical levels between the surface and 50 hPa. A set of physical parameterization schemes was chosen (see Table 1) after performing several sensitivity tests which are detailed in Appendix A. Given the wide range of global anthropogenic emission datasets available and the significance of these fluxes

https://doi.org/10.5194/egusphere-2024-3228
Preprint. Discussion started: 29 October 2024

Physics	Scheme name	Option
Microphysics	Morrison 2-moment	10
Longwave radiation	RRTMG	4
Shortwave radiation	RRTMG	4
Planetary boundary layer	Mellor-Yamada-Janjic	2
Surface layer	Eta similarity	2
Cumulus	Grell 3D Ensemble	5
Land surface	Unified Noah Land Surface Model	2

Table 1. Overview of physical parameterization options used for WRF-GHG simulations.

to simulate accurate concentrations in regions with large anthropogenic activity such as BTH, several anthropogenic emission inventories were also included in these sensitivity tests.

2.3.1 Input data and parameterization

The model was driven by the hourly European Centre for Medium-Range Weather Forecasts (ECMWF) global ERA5 reanalysis data set (0.25° × 0.25°, Hersbach et al. (2023a, b)) for meteorological fields. The concentration fields for CO_2 and CH_4 are initialized by the 3-hourly Copernicus Atmosphere Monitoring Service (CAMS) global reanalysis for greenhouse gases (EGG4), while the 6-hourly reactive gases product is used for CO (EAC4, Inness et al. (2019)). These CAMS reanalysis data sets are also used at the model domain boundaries to represent influences coming from outside the parent domain (d01). The evolution of these initial and lateral boundary conditions inside the domain over time is stored in a separate tracer, the so-called background tracer. Similarly, the evolution of concentrations caused by emissions within the boundaries of d01 is saved in different tracers, dependent on their source sector. The sum of all tracers, including the background, gives the total simulated concentrations which can be compared to the observations.

The simulations are re-initialized with the ECMWF ERA5 data every 30 h, starting at 18:00 UTC the previous day with a 6 h spin-up period, as done in other WRF-GHG modelling studies (Feng et al., 2016; Park et al., 2018; Pillai et al., 2011). Every day at 00:00 UTC, the tracer fields from the previous run are copied to the new simulation to ensure continuous transport of the concentrations.

We conducted sensitivity tests to identify a set of physical parameterization schemes and anthropogenic fluxes that provide appropriate simulations for all three species (CH_4, CO_2, and CO) across the different observation methods (in situ and remote sensing). The details of these tests are provided in Appendix A. Our findings indicate that the anthropogenic fluxes from CAMS-GLOB-ANT v5.3 (Granier et al., 2019; Soulie et al., 2023) for CO_2 and CH_4, and from REAS v3.2.1 (Regional Emission Inventory in Asia, Kurokawa and Ohara (2020)) for CO offer the best alignment with the Xianghe observations. We released all fluxes in the lowest model layer near the surface and multiplied them with temporal factors of CAMS-TEMPO (Guevara et al., 2021) to account for hourly and daily variation. Remark that both chosen anthropogenic inventories additionally provide sector-specific information. To include this information in our simulations, different sectors are linked to separate tracers. The

https://doi.org/10.5194/egusphere-2024-3228
Preprint. Discussion started: 29 October 2024

This study	CAMS-GLOB-ANT (for CO_2 and CH_4)	REAS (for CO)
Energy	Power generation (ene)	Power plants point
	Fugitives (fef)	Power plants non-point
	Oil refineries and transformation sector (ref)	
Industry	Industrial processes (ind)	Industry
Transport	Road transportation (tro)	Road transport
	Off Road transportation (tnr)	Other transport
	Ships (shp)	
Residential & Waste	Residential, commercial and other combustion (res)	Domestic
	Solid waste and waste water (swd)	
Agriculture	Agriculture soils (ags)	
	Agricultural waste burning (awb)	
	Agriculture livestock (agl)	

Table 2. Overview of mapping between the five broad sectors used in this study (first column) and the emission sectors provided by CAMS-GLOB-ANT v5.3 (second column) and REAS v3.2.1 (third column).

11 sectors from CAMS-GLOB-ANT were aggregated into five broad sectors to make the model simulations computationally less expensive. A similar aggregation was performed on the REAS sectors. The mapping is given in Table 2. This will allow us to track the respective contributions to the total simulated concentrations of the following source categories: energy, industry, transportation, residential & waste and agriculture. More detail about what is included in every sub-sector can be found in the documentation of the respective data set.

Further, biomass burning emissions are coming from the Fire INventory from NCAR (FINN v2.5, Wiedinmyer et al. (2011)) for all species. The observation-based global pCO_2 climatology from Landschützer et al. (2017) is used to represent the ocean-atmosphere exchange of CO_2, while the CH_4 fuxes from wetlands are taken from the WetCHARTS v1.0 climatology (Bloom et al., 2017). Finally, WRF-GHG calculates the biogenic CO_2 fluxes online based on the Vegetation Photosynthesis and Respiration Model (VPRM, Mahadevan et al. (2008); Ahmadov et al. (2007)). It uses its own calculated 2 m temperature and downward shortwave radiation together with surface reflectance data from the Moderate Resolution Imaging Spectroradiameter (MODIS) onboard the Aqua and Terra satellites. The extra required parameters for VPRM are taken from Li et al. (2020).

2.4 Comparing observations with WRF-GHG simulations

2.4.1 Xianghe in situ observations

The WRF-GHG model cell which covers the location of the instrument is selected to compare with the in situ observations. Because the concentrations are measured at an altitude of 60 m.a.g.l., this WRF-GHG profile is interpolated to that altitude,

https://doi.org/10.5194/egusphere-2024-3228
Preprint. Discussion started: 29 October 2024

using the model surface as ground level. Finally, the observations are averaged over a period of 30 minutes around the hourly model output.

2.4.2 Xianghe TCCON remote sensing observations

The same model cell as for the in situ observations is used to compare with the column observations. The five TCCON observations that are closest in time with the WRF-GHG output, but deviate no more than 15 minutes, are averaged and used for the comparison. The model profile is extended above 50 hPa with the TCCON a priori profile and then smoothed by using the averaging kernels in order to account for the instrument and retrieval characteristics (Rodgers and Connor, 2003). Note that an alternative approach would be to extend the model profiles with the CAMS reanalysis that is used as initial and lateral boundary conditions. However, the accuracy issues with CAMS CH_4 data in the stratosphere are well-documented (Ramonet et al., 2021; Agustí-Panareda et al., 2023), and would introduce known biases into our study. Moreover the optimized a priori profiles of the TCCON GGG2020 data show improved accuracy in the stratosphere (Laughner et al., 2023), supporting our decision to utilize this data for extending the model profiles.

2.4.3 TROPOMI observations

To compare the spatial XCH_4 distribution of TROPOMI with those of WRF-GHG, the model profiles are extended above 50 hPa with the TROPOMI a priori column number density profiles of CH_4 and dry air (mol m^{-2}) to ensure that both products in the comparison cover the same altitude range. Since a typical CH_4 profile shows a sharp decrease in the upper layers of the atmosphere, this part has a non-negligible impact on the column-averaged mole fraction. Further, the extended WRF-GHG CH_4 profiles are smoothed with the TROPOMI column averaging kernels and a priori profiles following Apituley et al. (2023). The column number density profiles of CH_4 and dry air are calculated from the hourly 3-D WRF-GHG output as follows:

$$\rho_i^{CH_4} = \nu_i^{CH_4} \rho_i^{da}, \text{ with } \rho_i^{da} = \frac{P_i}{RT_i} \frac{1}{1 + 1.6075 q_i} \tau_i. \quad (1)$$

In the above equation $\nu_i^{CH_4}$ is the CH_4 dry air volume mixing ratio (ppb) and ρ_i^{da} the dry air column number density in WRF-GHG layer i. The dry air column number density ρ_i^{da} is calculated according to the ideal gas law, where P_i, T_i and q_i are the air pressure (Pa), temperature (K) and water vapour mixing ratio with respect to dry air (kg kg^{-1}), respectively. The thickness of layer i (m) is represented by τ_i. Finally, R is the ideal gas constant 8.3145 J K^{-1} mol^{-1}. Note that 1.6075 is the ratio of the molar mass of dry air with respect to the molar mass of water to convert wet air to dry air.

TROPOMI has an equator crossing time of around 13:30 local solar time, so we compute the equivalent simulated XCH_4 by taking the average over 12h-15h LT. Note that we use the model simulations from the d02 domain (which has a horizontal resolution of 9×9 km^2) for this analysis, instead of d03 as for the comparisons with Xianghe observations, since a larger spatial extent is advantageous for a statistically effective comparison with TROPOMI.

Using the HARP toolset (part of the Atmospheric Toolbox, https://atmospherictoolbox.org/) for TROPOMI and the CDO software (Schulzweida, 2020) for WRF-GHG, both XCH_4 products are then binned to a common spatial grid to enable a quantitative analysis: we have chosen a regular latitude-longitude grid with a horizontal resolution of 0.05°.

https://doi.org/10.5194/egusphere-2024-3228
Preprint. Discussion started: 29 October 2024

3 Results and discussion

3.1 Overall model performance

With the model settings as elaborated in Sect. 2.3, WRF-GHG was run from 15 August 2018 to 1 September 2019. However, the first two weeks were regarded as a spin-up phase, so the analysis is made on one full year of data: from 1 September 2018 until 1 September 2019. This conservative spin-up period is implemented to ensure thorough mixing of the tracers within the domain. The complete data set can be accessed on https://doi.org/10.18758/P34WJEW2 (Callewaert, 2023).

An overview of the simulated and observed time series of the CH_4 concentrations at Xianghe is shown in Fig. 2, together with the model error. For the column observations, the model shows a mean underestimation of -3.03 ppb, with a moderate correlation of 0.56 (Table 3). At the surface level, the data were divided into afternoon (13:00–18:00 LT) and nighttime (03:00–08:00 LT) periods for statistical analysis, as models generally perform better in simulating concentrations during the afternoon when the lower atmosphere is better mixed. The definition of these time periods is based on the daily maximum and minimum values, as will be discussed later in Sect. 3.4.2. Indeed, the correlation is higher during the afternoon (0.66) compared to nighttime (0.42), with mean bias errors of 14.22 ppb and 12.68 ppb, respectively (see Table 3). Additionally, significantly larger errors were found at night, indicating greater challenges for the model in accurately capturing nighttime values compared to afternoon.

The moderate correlation coefficients are likely due to a seasonality in the bias: WRF-GHG is underestimating the CH_4 data at Xianghe in summer and autumn (June - November) and slightly overestimating them in winter (January - March), which is especially visible for the column data in Fig. 2c.

	insitu CH_4 (afternoon)	insitu CH_4 (night)	XCH_4
BIAS	14.22	12.68	-3.03
RMSE	159.74	334.06	23.96
CORR	0.66	0.42	0.56

Table 3. Statistics of the model-data comparison of the ground-based CH_4 observations at the Xianghe site from 1 September 2018 until 1 September 2019. We present the mean bias error (BIAS), root mean square error (RMSE) and Pearson correlation coefficient (CORR). The mean bias error and root mean square error are given in ppb. For in situ observations, the data is split in afternoon (13-18 LT) and night (3-8 LT) hours.

Possible sources of this bias are inaccuracies in the background values, misrepresentation of CH_4 sources and sinks within WRF-GHG, or a combination of these factors. Given CH_4's long atmospheric lifetime, background values significantly contribute to the total simulated signal, as also illustrated by the mean values for the background and total simulated tracer in the top of Table 4. We therefore start by further examining the global CAMS reanalysis which is used to represent the inflow and outflow at the model domain boundaries. In the CAMS validation report by Ramonet et al. (2021), a similar seasonal bias between CAMS CH_4 and TCCON is found. To explore this pattern in more detail and include Xianghe in the analysis, we

https://doi.org/10.5194/egusphere-2024-3228
Preprint. Discussion started: 29 October 2024

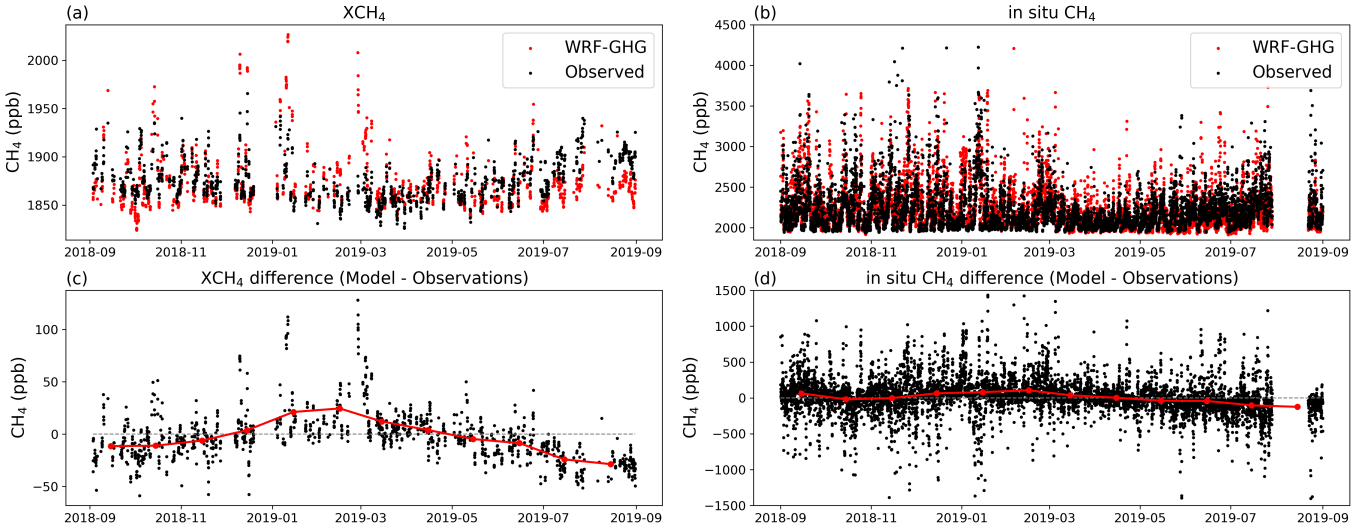

Figure 2. Time series of the observed (black) and simulated (red) (a) XCH_4 and (b) insitu CH_4 concentrations at the Xianghe site. Panels (c) and (d) show the differences between WRF-GHG simulations and observations for XCH_4 and in situ CH_4, respectively. Data points are hourly. The red points in (c) and (d) represent the monthly mean differences.

	XCH_4 (ppb)				in situ CH_4 (ppb)			
	Q1	median	mean	Q3	Q1	median	mean	Q3
Total	1900.74	1916.18	1927.36	1942.42	2028.75	2132.50	2212.50	2302.58
Background	1885.79	1890.75	1891.34	1896.57	1912.83	1927.69	1925.37	1938.20
Biomass burning	0.00	0.00	0.00	0.00	0.00	0.00	0.00	0.00
Energy	2.61	11.13	19.04	28.90	12.03	49.67	105.88	135.21
Residential (& waste)	2.65	5.86	8.17	10.72	31.24	65.49	94.33	122.11
Industry	0.07	0.17	0.21	0.30	0.77	1.63	2.29	2.99
Transportation	0.06	0.12	0.15	0.20	0.66	1.40	2.00	2.58
Agriculture	2.00	4.75	7.56	9.49	24.95	51.77	76.08	97.30
Wetlands	0.02	0.12	0.56	0.62	0.09	0.66	4.17	3.91
Termites	0.17	0.29	0.34	0.46	1.13	2.02	2.37	3.17
Total tracers	9.86	24.76	36.02	51.21	102.75	209.15	287.13	377.48

Table 4. Statistics of the total simulated CH_4 concentrations and the different tracer contributions over the complete simulation period. Q1 and Q3 represent the first and third quartile, respectively, between which 50 % of the data fall.

reproduce their calculations for several TCCON sites at similar latitudes (Karlsruhe (49.1° N), Orleans (48.0° N), Garmisch (47.5° N), Park Falls (45.9° N), Rikubetsu (43.5° N), Lamont (36.6° N), Tsukuba (36.0° N), Edwards (35.0° N), Pasadena (34.1° N), Saga (33.2° N), and Hefei (31.9° N)) for the period of interest, as shown in Fig. 3. Indeed, we find a seasonal

https://doi.org/10.5194/egusphere-2024-3228
Preprint. Discussion started: 29 October 2024

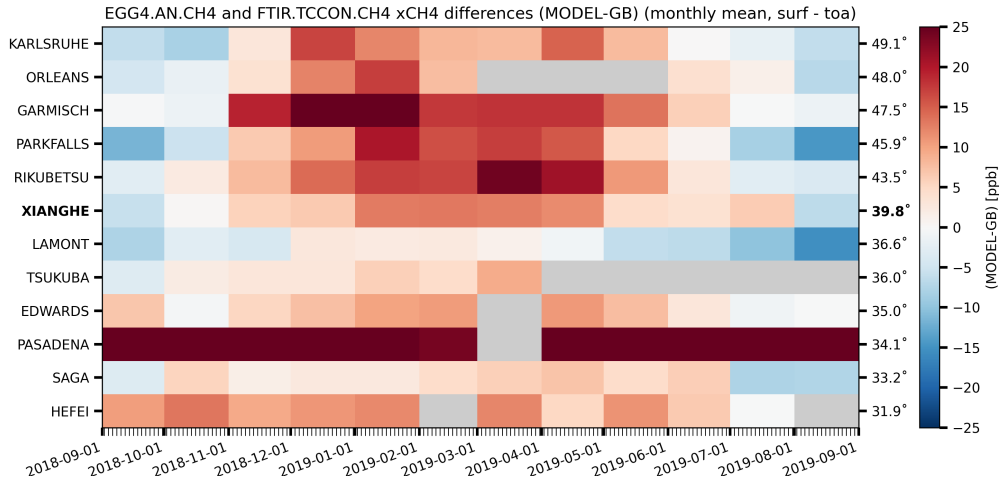

Figure 3. Monthly mean difference (in ppb) between CAMS reanalysis model and TCCON XCH_4 between 30 - 50° N over the simulation period of this study.

bias where CAMS is overestimating TCCON XCH_4 from December until May and showing a small underestimation in the rest of the period. The bias at Xianghe ranges from 13.17 ppb in February 2019 to -6.56 ppb in August 2019 (monthly mean differences). The monthly mean bias of WRF on the other hand, ranges between 24.49 ppb in February 2019 and -28.70 ppb in August 2019 and shows a significantly larger amplitude than the CAMS bias. Moreover, the same seasonal pattern is found in the time series of the differences for the in situ data (Fig. 2d). Ramonet et al. (2021) assume the seasonal bias within CAMS is related to an inaccurate representation of the seasonal cycle of surface emissions and/or the OH sink. Similarly, the remaining WRF-GHG bias likely arises from errors in the seasonality of the CH_4 emissions and/or neglecting the reaction of CH_4 with OH. This will be further investigated in Sect. 3.3.

In the rest of this work, we have applied a bias correction to the WRF-GHG simulations by subtracting the monthly mean difference between CAMS and TCCON XCH_4, averaged over all sites (except Pasadena due to outlier behavior) between 30 - 50° N, from the background tracer. The updated statistical metrics are given in Table 5. The correlation coefficient for the column data slightly improves to 0.65, where for the surface concentrations the bias correction has only a negligible impact on the model-data comparison. The remaining monthly mean bias for XCH_4 (in situ CH_4) ranges between 13.04 ppb (95.20 ppb) in February 2019 and -25.70 ppb (-121.25 ppb) in August 2019, which is still larger than the measurement uncertainty of 6 ppb (1 ppb).

3.2 Sector contributions to observed concentrations

All fluxes that are included in WRF-GHG are tracked in separate tracers, as explained in Sect. 2.3. This allows us to disentangle the total simulated concentrations into the different tracer contributions and evaluate the influence of different source sectors on the observations at Xianghe, as well as their respective importance. An overview of the monthly mean values is shown in

https://doi.org/10.5194/egusphere-2024-3228
Preprint. Discussion started: 29 October 2024

	insitu CH_4 (afternoon)	insitu CH_4 (night)	XCH_4
BIAS	8.43	6.88	-8.10
RMSE	158.29	333.22	22.35
CORR	0.66	0.43	0.67

Table 5. Same as Table 3 but with bias corrected model values.

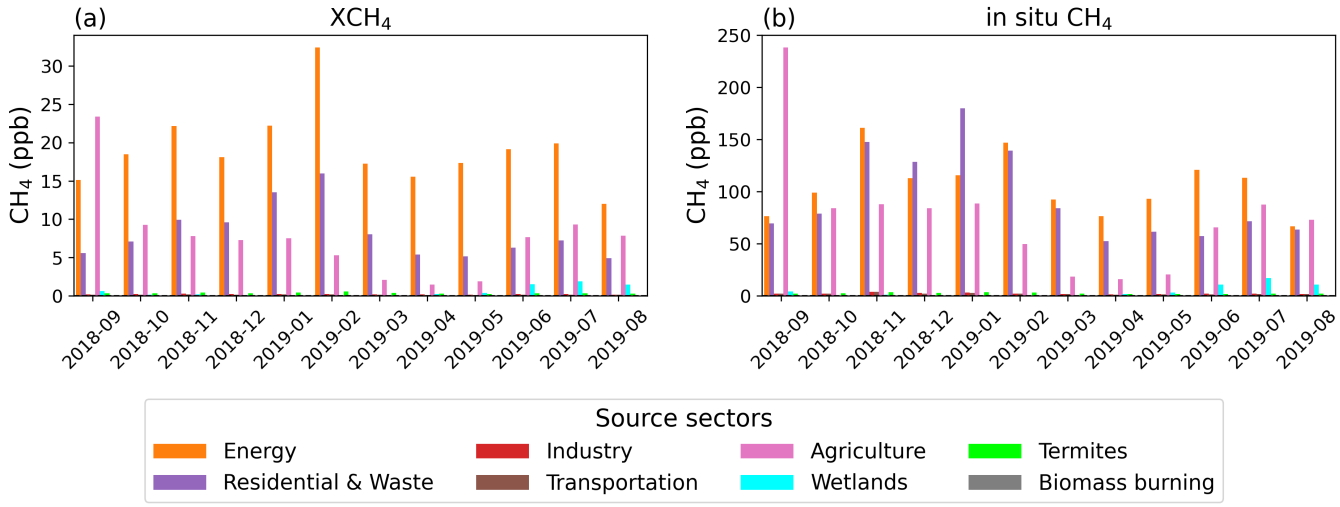

Figure 4. Monthly mean tracer contributions above the background for (a) XCH_4 and (b) in situ CH_4 simulated concentrations at Xianghe.

Fig. 4, while additionally the median and interquartile range of the complete period are given in Table 4. Note that all simulated hours were used for this analysis, not just the ones coinciding with observations.

For CH_4, the simulated signal at Xianghe is mainly determined by three sectors: energy, residential & waste (which combines both residential heating and waste management sectors) and agriculture. They respectively contribute with a median enhancement of 11.13 ppb, 5.86 ppb and 4.75 ppb above the background for the columns and 49.67 ppb, 65.49 ppb and 51.77 ppb near the surface (see Table 4). Furthermore there is a small contribution from wetlands in summer, peaking in July with a median tracer contribution of 1.49 ppb for the columns and 10.65 ppb near the surface. Other sectors such as industry, transportation, termites and biomass burning seem to be irrelevant at Xianghe. Overall, the total tracer enhancement is about ten times larger for the in situ concentrations compared to the column-averaged values.

The fact that the dominant source sectors (agriculture, residential heating, waste management and energy (which is mainly coal mining in this case)) are not known for releasing CH_4 at elevated altitudes, supports our choice to implement the emissions only in the lowest model layer.

Futhermore, remark that for the in situ concentrations, the three dominant sectors are roughly equally important, while for

https://doi.org/10.5194/egusphere-2024-3228
Preprint. Discussion started: 29 October 2024

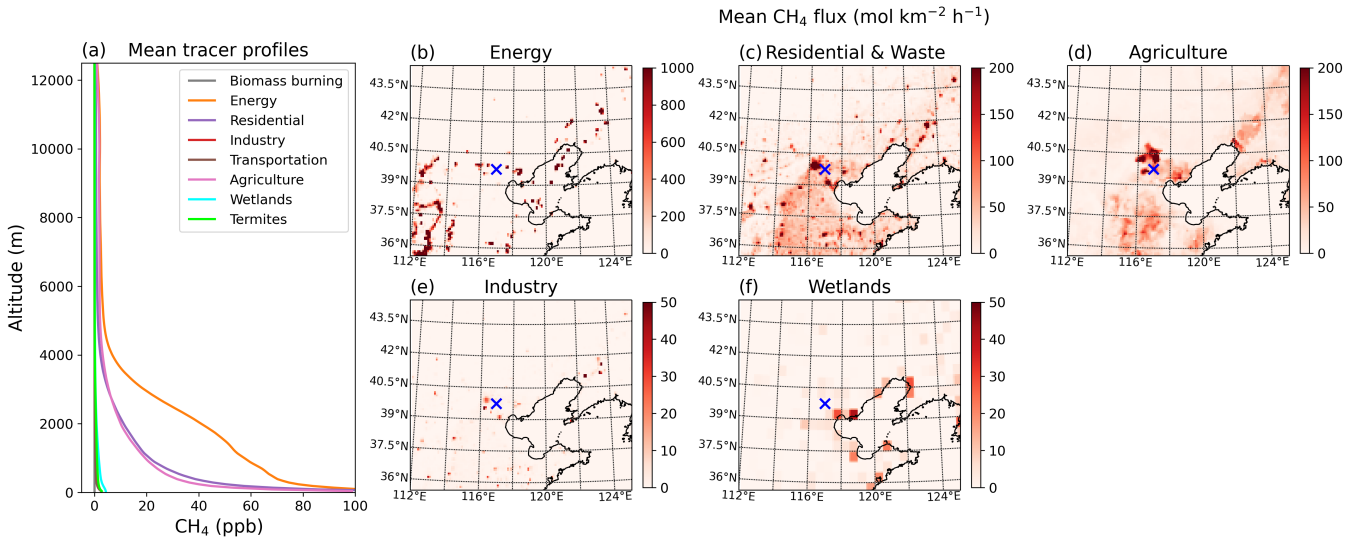

Figure 5. (a) Mean vertical profile of the tracer fields in WRF-GHG for CH_4 at Xianghe. All simulated hours were used for this plot. (b-f) Maps of the mean CH_4 flux (mol km^{-2} h^{-1}) in WRF-GHG domain d02 during the entire simulation period for the most important sectors. Remark that different sectors have different ranges in the colorbar. The lcoation of the Xianghe site is indicated by the blue cross.

the column concentrations we find a larger impact of the energy sources: the relative mean enhancement of the energy tracer is 52.87% for the column concentrations, while it is only 36.88% for the surface concentrations. When looking at the mean vertical profiles of the different tracer contributions above Xianghe (Fig. 5a) we see that the contributions from the energy sector are generally found at a higher altitude compared to other sectors. High concentrations near the surface are associated with emission sources nearby, while those aloft are likely caused by long-distance pollutant transport in the free troposphere. Therefore, we assume that this difference between column and surface energy contribution is because the strongest energy sources are situated in Shanxi (the largest coal producing province in China), which is much further away from Xianghe than for example the strongest residential (mainly Beijing and Tianjin) and agricultural sources, see Fig. 5b-d.

In Fig. 4, we further observe a larger residential signal in winter, where the median tracer contribution peaks with 13.43 ppb in February for the columns and with 132.75 ppb in January, near the surface. Meanwhile, the influence from agriculture reaches its maximum in September (monthly median values of 14.46 ppb for XCH_4 and 196.07 ppb for in situ CH_4) and its minimum in March-April (monthly median values of 0.89 ppb for XCH_4 and 11.49 ppb for in situ CH_4). This corresponds with the seasonal pattern of emissions within CAMS-GLOB-ANT.

3.3 Seasonal CH_4 bias

In Sect. 3.1, we identified a seasonal bias in the CH_4 simulations (WRF-GHG underestimates CH_4 in summer and autumn, overestimates in winter) that could not be fully explained by a similar bias in the background data, indicating a potential bias in the seasonality of the emission data and/or a consequence of ignoring the OH sink. In this section, we first investigate the

https://doi.org/10.5194/egusphere-2024-3228
Preprint. Discussion started: 29 October 2024

primary emission sectors that may have contributed to this seasonal bias. One of the major sources of CH_4 at Xianghe is the energy sector (see Sect. 3.2), primarily through fugitive emissions from the extraction, processing, storage, and transport of coal, oil, and natural gas. These emissions are not expected to exhibit significant monthly variation. Indeed, the energy emissions in the CAMS-GLOB-ANT inventory are relatively stable throughout the year: they show a coefficient of variation (CV, calculated as the ratio of the standard deviation to the mean) of only 0.42% for the monthly averaged values across the model domain. As a result, our focus will be on the following emission categories: agriculture, residential & waste, and wetlands.

- Agriculture. As presented in Table 2, the agricultural sector is comprised of three subsectors: soils (this is mainly rice cultivation), agricultural waste burning, and livestock (manure management and enteric fermentation). In China, rice cultivation plays a vital role but is predominantly concentrated in regions south of 35°N. In CAMS-GLOB-ANT, the most important agriculture subsector in the region of the Xianghe site is livestock. According to the emission inventory, livestock emissions in the wide region around Xianghe peak in September and reach their lowest levels in March and April. Unfortunately, the source of these monthly variations in CH_4 emissions within the inventory is unclear, as the accompanying data set of temporal factors, CAMS-GLOB-TEMPO (Guevara et al., 2021), references constant factors for CH_4 emissions from agricultural sources. Previous research by Maasakkers et al. (2016) suggests that emissions from manure management often correlate with air temperature, with higher emissions during warmer months (May to September in this case) and lower emissions during colder months (December to February). If the true seasonality of agricultural emissions around Xianghe is indeed temperature-driven, this implies that the current inventory underestimates emissions during spring and summer (May to August) and overestimates them in winter, as it shows a peak only in September and a minimum in spring (March-April) rather than in winter. This discrepancy in the seasonality of emissions could explain the seasonal bias observed in our CH_4 simulations, pointing to inaccuracies in the representation of agricultural emissions.

- Residential & waste. This sector represents emissions from residential, commercial and other combustion sources together with CH_4 emissions from solid waste and waste water treatment. In CAMS-GLOB-ANT, the waste sector is the most important one in the Xianghe region and assumed to be relatively constant throughout the year: monthly total CH_4 emissions between 38-41 °N and 115-119 °E range between 0.0408 Tg and 0.0452 Tg. In summer, total residential combustion emissions in the region can be as low as 0.0039 Tg per month, while in winter, they are almost of the same size as the waste emissions: 0.0357 Tg. So the seasonality of the residential & waste sector is coming from the residential part, peaking in winter. However, Hu et al. (2023) showed that CH_4 emissions from waste treatment often follow the seasonality of air temperature. Even though this study is based on observations in the Hangzhou megacity, their results could possibly be representative for the BTH region as well. This would mean that the waste emissions are underestimated in summer and/or overestimated in winter, which would match the current model-observation mismatch for CH_4.

- Wetlands. Within the WRF-GHG simulations, wetlands only show minor contributions to the surface and column data, and only in summer. Emissions are taken from the WetCHARTs v1.0 ensemble data set. In the BTH area, the main

https://doi.org/10.5194/egusphere-2024-3228
Preprint. Discussion started: 29 October 2024

wetland areas are located close to the Bohai Sea (see Fig. 5f). However, according to WetCHARTs, these emissions are relatively small compared to those from wetlands more in the south of China. In an evaluation of the WetCHARTs ensemble against GOSAT observations by Parker et al. (2020), a general underestimation of the seasonal amplitude in China was found. Furthermore, Chen et al. (2022) showed increased posterior wetlands emissions compared to the a priori values when inferring yearly CH_4 emissions over China using TROPOMI satellite observations. This could point to an underestimation of the wetland emissions in the current study, and therefore an underestimation of CH_4 in summer.

The observed seasonal error pattern between the WRF-GHG CH_4 simulations and the Xianghe observations may be due to one or more of the reasons previously mentioned. To gain a spatial perspective on this seasonal bias, we compared the WRF-GHG XCH_4 field with TROPOMI observations. Figure 6 shows the seasonal mean XCH_4 from both WRF-GHG and TROPOMI, as well as their normalized difference over the broader Xianghe region. To highlight seasonal variations, we subtracted the mean difference between WRF-GHG and TROPOMI over the entire simulation period (also shown in Fig. 12d) from the seasonal means, resulting in a 'normalized difference.' Overall, we find a mean bias error between WRF-GHG and TROPOMI of -10.55 ppb (or -0.56% [(TROPOMI - WRF-GHG)/WRF-GHG]), consistent with previous studies. (Yang et al., 2020; Tian et al., 2022; Sha et al., 2021).

The analysis reveals a model underestimation in summer (JJA) and an overestimation in winter (DJF), see Fig. 6. The biases are smaller in spring and autumn. However, we cannot identify a distinct spatial pattern throughout the seasons that could point to errors within a specific source sector. Figure 6 shows differences on a large spatial scale, suggesting that for example the underestimation by WRF-GHG is linked to emission sources that are widespread in the region. Since the North China Plain is a livestock-dominated region with strong urbanization and industrial activities, this implies that the fluxes of either agriculture (livestock), waste treatment, or both, rather than the fluxes from wetlands, are underestimated in summer in CAMS-GLOB-ANT. Given the lack of a clear outcome from our analysis, it is likely a combination of factors.

Finally, we used backward simulations with the FLEXible PARTicle dispersion model (FLEXPART) v10.4 (Pisso et al., 2019) to evaluate the impact of the OH sink on CH_4 concentrations at Xianghe. Details of the model configuration are provided in Appendix B. By comparing simulations that include or exclude the chemical reaction with OH, we estimated its influence. The results indicate a more pronounced difference in summer than in winter, with mean relative backward sensitivity differences of about 0.04%, 0.005%, 0.05%, and 0.2% in October 2018, January 2019, April 2019, and July 2019, respectively, over the entire footprint. Considering the size of CH_4 emissions within the WRF-GHG domain (Table 4), the contribution of the ignored OH reaction to the CH_4 mole fraction is around 0.11 ppb in winter and 4.4 ppb in summer, which remains small compared to the measurement uncertainties (1 ppb for in situ data and 6 ppb for TCCON) and the magnitude of the observed bias. Moreover, the higher impact in summer should theoretically cause a model overestimation during this season if the OH sink is ignored. However, since the observed seasonal bias shows a different trend, it is unlikely to be driven by CH_4 chemistry.

Therefore, our analysis highlights an urgent need for further research into the seasonality of CH_4 emissions in northern China.

https://doi.org/10.5194/egusphere-2024-3228
Preprint. Discussion started: 29 October 2024

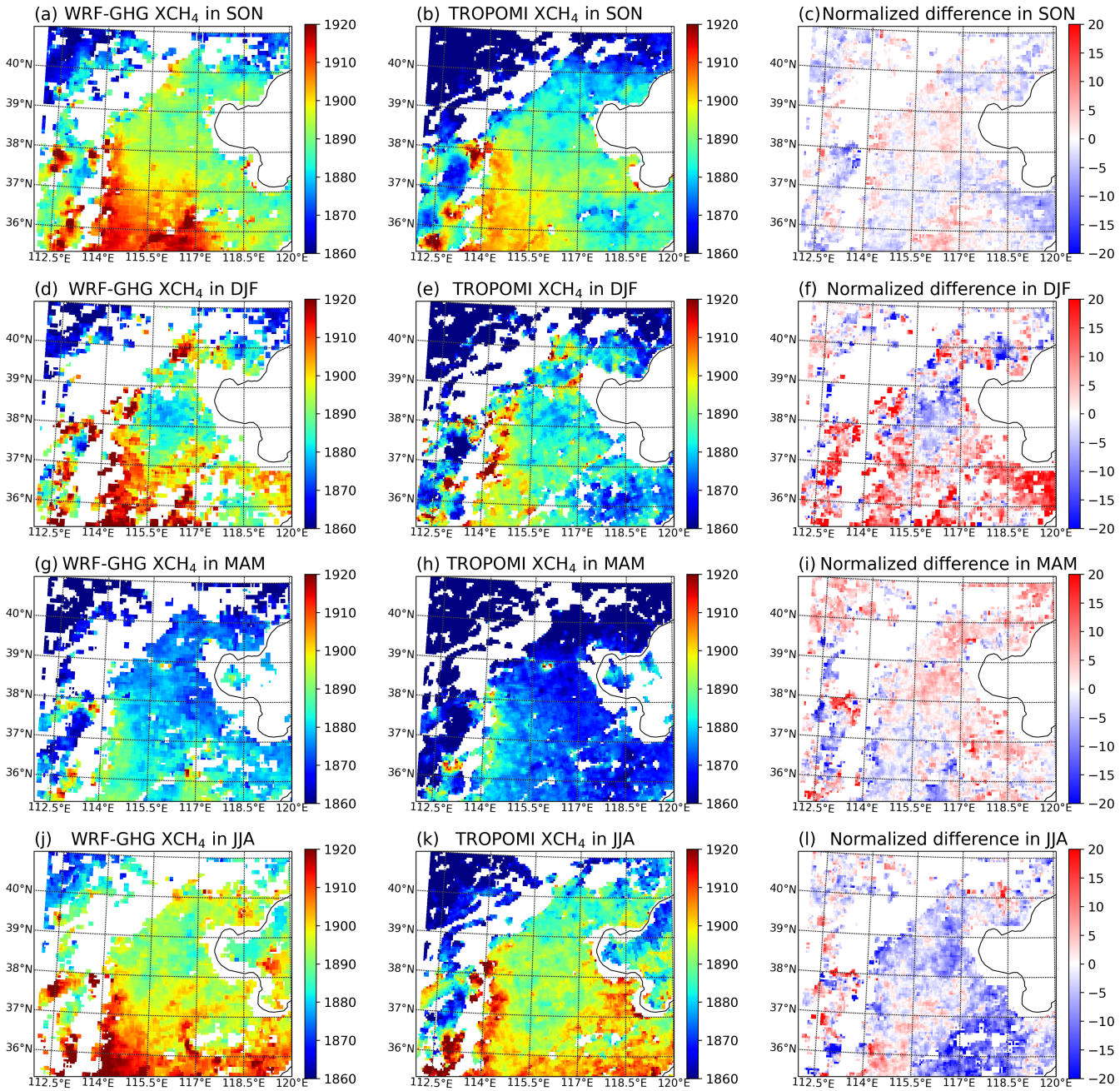

Figure 6. Seasonal mean XCH_4 (ppb) over the domain d02 (provinces of Beijing, Tianjin, Hebei, Shanxi and part of Shandong) as simulated by WRF-GHG (first column) and observed by TROPOMI (second column), as well as the normalized difference between them (WRF-GHG - TROPOMI, in ppb). Normalized difference indicates that the mean difference over the entire simulation period is subtracted from the seasonal means. The seasons are defined as (a,b,c) SON: September - November (autumn), (d,e,f) DJF: December - February (winter), (g,h,i) MAM: March - April (spring) and (j,k,l) JJA: June - August (summer). White pixels indicate that there are no observations available during the entire period.

https://doi.org/10.5194/egusphere-2024-3228
Preprint. Discussion started: 29 October 2024

3.4 Impact of meteorology on variability of concentrations

In Sect. 3.2, we showed how emissions from different sources affect the CH_4 observations at Xianghe. In the current section we want to focus on the meteorological factors that influence the temporal variability of the time series. More specifically we will discuss the impact of large-scale phenomena, the planetary boundary layer and local winds.

3.4.1 Synoptic scale winds

Because FTIR observations generally have a large area of representativeness (generally a few 100 km), column concentrations are relatively insensitive to local fluxes and vertical mixing, while they are strongly influenced by large-scale patterns (Keppel-Aleks et al., 2011). We use the winds at 800 hPa to represent horizontal transport in the free troposphere, as this altitude is generally above the planetary boundary layer height. More specifically, we looked at the daily mean column concentrations above the background for every wind direction to see if a clear relationship could be found. This is shown in Fig. 7.

Remark that only southwest (SW) and northwest (NW) wind segments are given because southeast and northeast winds occur only seldom at 800 hPa: only on 2 and 13 days out of 231, respectively. We find that in general, larger enhancements are found when winds blow from the SW wind segment (median tracer contribution of 57.79 ppb) compared to the NW segment (median tracer contribution of 7.33 ppb). To quantify the difference, we conducted a non-parametric Mann-Whitney U test on the two categories, which yielded p-values well below 0.05 (see Fig. 7, in the title), indicating that the differences are statistically significant. Higher concentrations coincide with 800 hPa winds coming from the SW while NW winds correspond with lower concentrations. Yang et al. (2020) already showed that the day-to-day variation of the column observations of CH_4, CO_2 and CO are highly intercorrelated, and that clean days are linked with air from the north, while polluted days are linked with air from the south, which is confirmed here by the WRF-GHG simulations. Air masses from the north have been moving over rather remote and clean areas such as Inner Mongolia, Mongolia and Russia. Meanwhile, southerly air is linked with the highly populated North China Plain (NCP), where many anthropogenic emission sources are located.

The influence of polluted air from the southwest is visible in the surface concentrations as well, as we find a high correlation coefficient of 0.79 between the daily mean column and surface tracer enhancements. This indicates that both surface and column CH_4 concentrations are affected by synoptic-scale winds, which advect either clean or polluted air masses to Xianghe.

Furthermore, the levels of pollution in these air masses can vary significantly from month to month due to changing meteorological conditions. For instance, during the winter months, weather conditions are generally more favorable to the accumulation of pollutants, leading to higher pollution levels (Li et al., 2022). This can intensify both local pollution plumes and those transported by southwestern winds. This phenomenon likely explains why despite relatively constant emissions throughout the year, we observe a significant month-to-month variability in the energy tracer contributions (see Fig. 4). More specifically, we find a CV of 26.53% for the column and 26.65% for the surface tracers. These findings suggest that tracer concentrations at Xianghe result from a complex interplay of emissions, wind direction, and weather patterns both near and far.

https://doi.org/10.5194/egusphere-2024-3228
Preprint. Discussion started: 29 October 2024

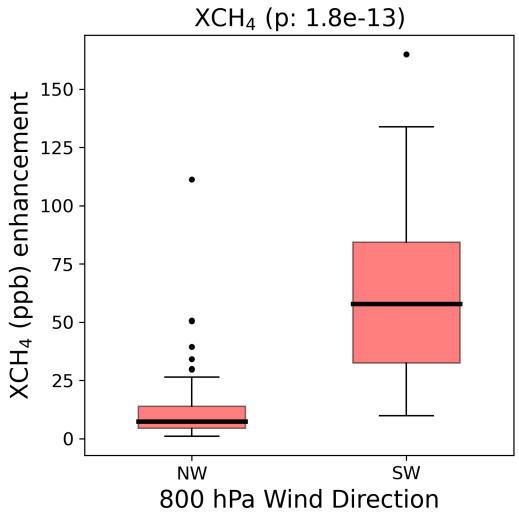

Figure 7. The distribution of the daily mean simulated column tracers above the background per 800 hPa wind direction category and species. NW is for winds with an angle of 292.5 to 337.5 ° from north, while SW represents the angles between 202.5 and 247.5°. There are 72 days with NW winds and 33 days with SW winds. The colored boxes indicate the range between the first and third quartile, while the thick solid line is the median. Outliers (values that are 1.5 times the interquartile range above (below) the third (first) quartile) are shown by black dots.

3.4.2 Planetary boundary layer dynamics

The planetary boundary layer (PBL) is the lowermost layer of the atmosphere which is in direct contact with the Earth's surface. The characteristics of this layer vary throughout the day. During the day, under influence of solar radiation, turbulent motions cause strong vertical mixing of the air within the PBL. These processes allow gases to be dispersed and transported upwards, which generally leads to reduced concentrations near the surface. At night, radiational cooling of the surface creates a temperature inversion close to the ground. This causes the nocturnal PBL to be stable and more shallow, trapping pollutants near the surface and as such increasing their local concentrations.

Figure 8 shows the diurnal variation of the PBL height as simulated by WRF-GHG and the CH_4 concentrations near the surface (both simulated and observed). Indeed, the height of the PBL in WRF-GHG is largest in the afternoon when solar radiation is strongest, reaching its peak at 15:00 (local time). This corresponds with the lowest simulated surface concentrations (Fig. 8b), where we find median (and interquartile) values of 2039.77 (1977.74 - 2158.28) ppb. Right after sunset, the height of the PBL drops to its lowest value ($\approx$ 50 m - 430 m in WRF-GHG), after which it persists during the course of the night, until sunrise. This period corresponds with slightly increasing CH_4 concentrations as emissions near the surface accumulate within this stable shallow layer. Hence, the highest concentrations are found in the early morning: at 8:00 with 2239.75 (2079.29 - 2484.04) ppb. As the PBL height starts to rise at 8:00 due to turbulent mixing, CH_4 start to drop in WRF-GHG, creating a diurnal cycle.

Note that WRF-GHG is quite capable at simulating this diurnal variation of CH_4 in situ observations. The observations show

https://doi.org/10.5194/egusphere-2024-3228
Preprint. Discussion started: 29 October 2024

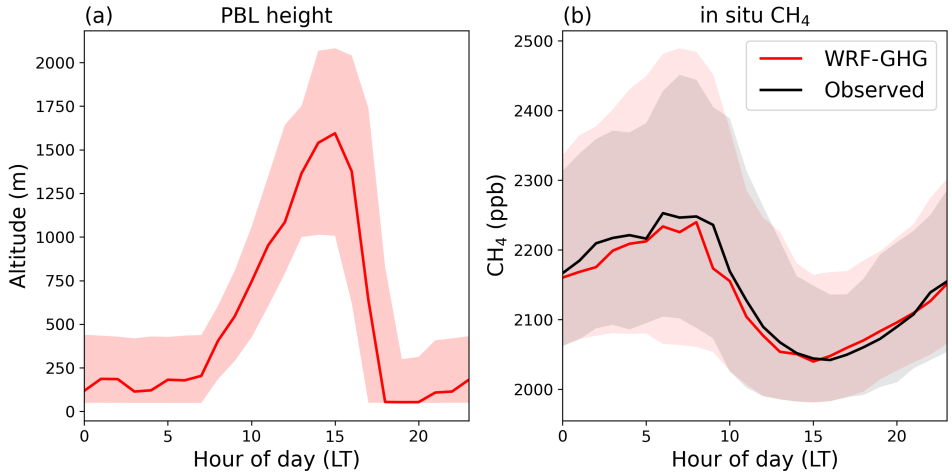

Figure 8. Hourly median and interquartile range of the (a) simulated planetary boundary layer height, and (b) observed and simulated surface CH_4 concentration at Xianghe.

minimal concentrations at 16:00 with a median (and interquartile) value of 2041.94 (1981.54 – 2135.88) ppb, which are well captured by WRF-GHG, even though one hour earlier. The peak CH_4 concentrations however, are observed at 6:00 with a median (and interquartile) value of 2252.71 (2104.36 – 2451.01) ppb, portraying a small model underestimation of about 13 ppb. Together, this leads to a small underestimation of the CH_4 diurnal amplitude in WRF-GHG of 10.79 ppb.

We have shown that these PBL dynamics are very important for the variability of the surface concentrations, however they are irrelevant for the column concentrations, as the latter are much less affected by vertical transport (Wunch et al., 2011). Indeed, the WRF-GHG simulated column concentrations don't exhibit a clear diurnal cycle, suggesting that this aspect is well captured by the model. It is however difficult to validate this using observations, as FTIR measurements are only possible during periods of sunlight.

3.4.3 Local emissions

Regional emissions are influencing both column and in situ concentrations at Xianghe, as elaborated in Sect. 3.4.1. However, emission sources nearby could also have an impact on these values, especially for the in situ observations as they sample the local air. To analyze which nearby sources influence the Xianghe measurements, we look for correlations between the 10m wind speed and direction and the simulated concentrations. Figure 9 reveals the mean WRF-GHG tracer contribution per wind direction and speed for CH_4. To eliminate the influence of polluted plumes from further away, we select only those days on which the mean daily XCO enhancement is smaller than 45 ppb. We use XCO as a tracer for polluted events as it is the species with the shortest atmospheric lifetime. Furthermore, we compute the mean concentrations separately for day and night to avoid the effects of the PBL. The night hours are defined as those with the peak concentrations, i.e., between 3h and 8h LT, while the day represents those hours with highest atmospheric mixing and lowest concentrations, i.e., between 13h and 18h. During

https://doi.org/10.5194/egusphere-2024-3228
Preprint. Discussion started: 29 October 2024

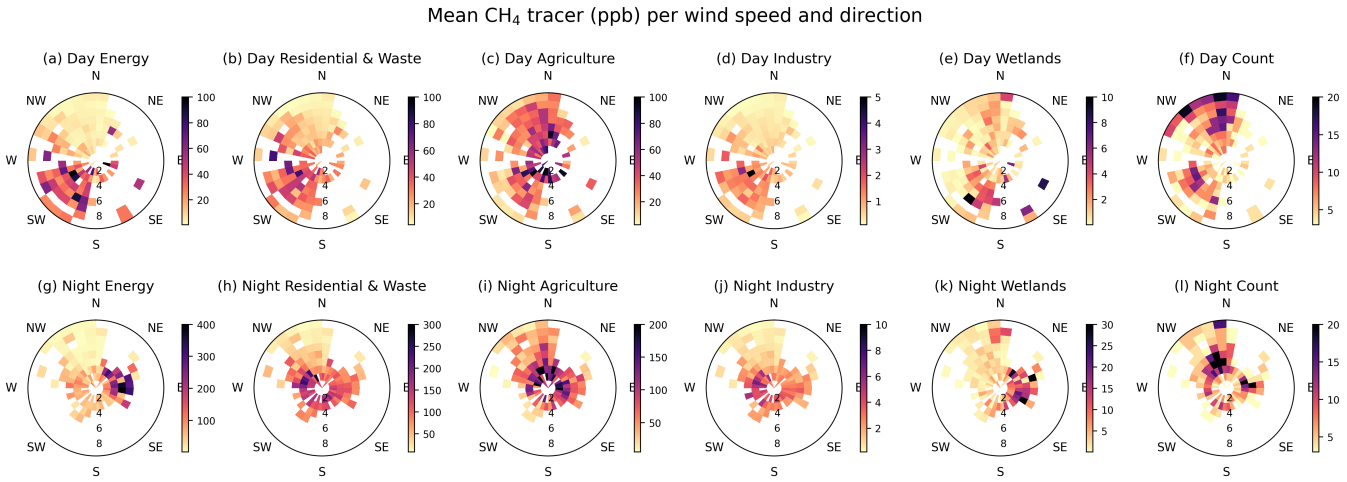

Figure 9. Mean CH_4 simulated tracer concentrations (indicated by colour scale, in ppb) binned per wind speed and direction for the main sectors (a) energy, (b) residential & waste, (c) agriculture, (d) industry and (f) wetlands on days without strong regional pollution. The first row represents afternoon hours (13h - 18h LT), while the second row represents nighttime hours (3h - 8h LT). Data is binned per 1 m s^{-1} and 11.25° wind direction. (f) Count of data points in each bin. Only bins with at least 3 points are included in the figure. Remark that the panels have different colour scales.

the day most winds are coming from the north and southwest, while at night the most frequent wind directions near the surface are north and east. Higher wind speeds are found during the day than at night. The northern winds typically have the lowest tracer contributions since there are fewer emission sources in this direction, with the exception of agriculture (see Fig. 10). In general, we see that wind directions with the largest enhancements correspond with the largest sources nearby (Fig. 9-10): east and west for energy, all but north for residential, all directions for agriculture, southwest for industry and southeast for wetlands. The highest values overall (> 400 ppb) are found for the energy tracer at night and they are coming from the east, where some very large CH_4 point sources are located that correspond to coal mine emissions nearby the city of Tangshan (see Fig. 10a). However, when looking closer at the CH_4 time series (not shown) we see that WRF-GHG is often overestimating the Xianghe in situ CH_4 observations at times where the model shows a large energy contribution. This is also visible in Fig. 11. This makes us to believe that these coal mine emissions might be overestimated in CAMS-GLOB-ANT. In the next section we further investigate this hypothesis by comparing WRF-GHG concentration fields with TROPOMI observations.

3.5 Source assessment near Tangshan

By comparing the yearly TROPOMI XCH_4 with WRF-GHG XCH_4, we want to assess if the CH_4 emissions from coal mines around Tangshan are indeed overestimated in CAMS-GLOB-ANT or not. Figure 12 shows the maps of the mean XCH_4 during the entire simulation period: September 2018 until September 2019. The yearly mean total CH_4 fluxes from CAMS-GLOB-ANT in the WRF-GHG d02 is also given, as well as the difference between WRF-GHG and TROPOMI. By taking the average

https://doi.org/10.5194/egusphere-2024-3228
Preprint. Discussion started: 29 October 2024

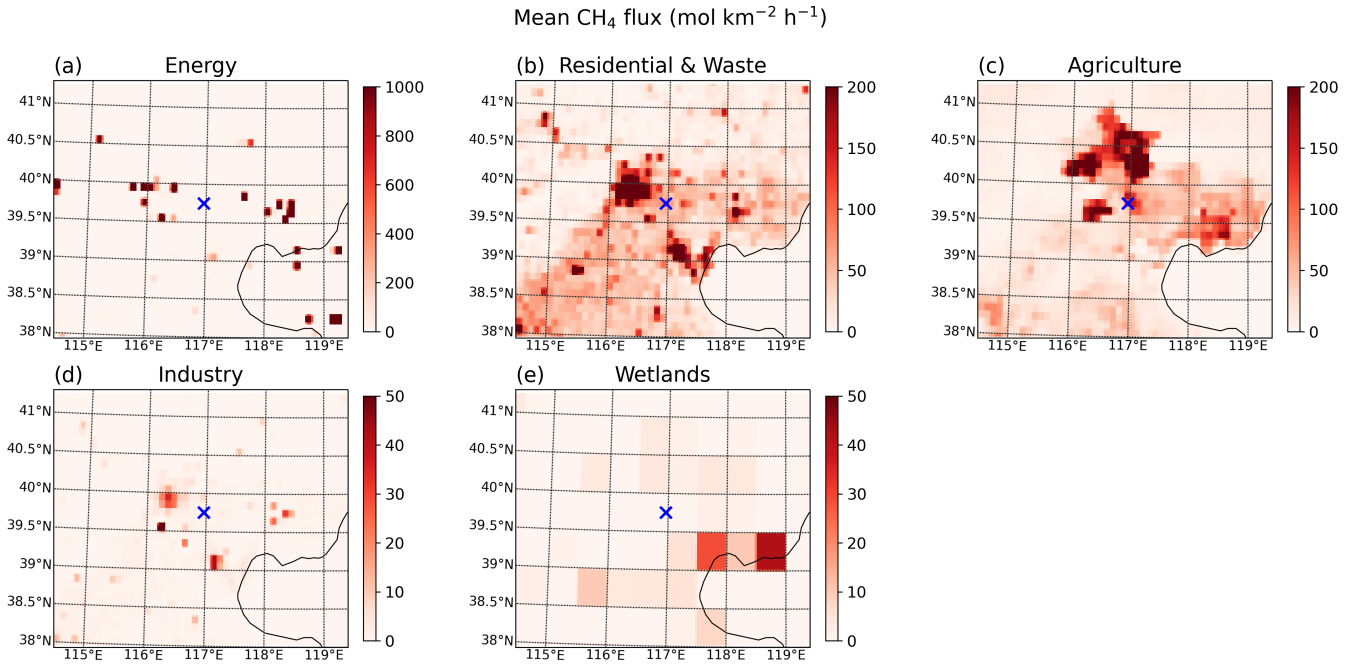

Figure 10. Map of the mean CH_4 flux (mol km^{-2} h^{-1}) in WRF-GHG domain d03 during the entire simulation period from September 2018 until September 2019, for the most important sectors. Remark that the panels have different colour scales. The location of the Xianghe site is indicated by a blue cross.

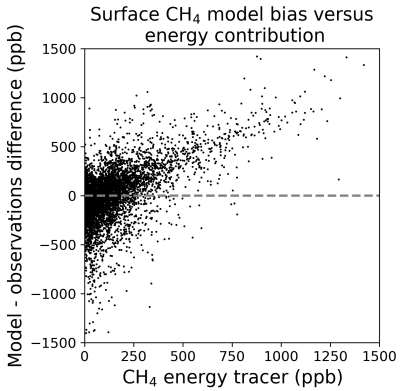

Figure 11. Correlation between energy tracer contribution to simulated CH_4 surface concentrations and differences between total simulated and observed surface concentrations. For this plot, the data was not filtered on day, night or polluted/clean days.

https://doi.org/10.5194/egusphere-2024-3228
Preprint. Discussion started: 29 October 2024

over the complete simulation period we minimize the influence of meteorological patterns on the XCH_4 concentration and expose the main emission sources.

When comparing the WRF-GHG input fluxes in Fig. 12a with the resulting XCH_4 concentration field in Fig. 12b, we indeed find a strong agreement. The largest sources are found to the west of 114°E, which correspond to the extensive coal mining activities in Shanxi. In the same locations on the XCH_4 map of WRF-GHG we find the highest concentration values of the region. Unfortunately due to the mountainous terrain, TROPOMI observations are sparse in this area. Other sources, such as a hotspot around 36.25°N, 116.75°E and the slightly smaller emissions around Beijing (40°N, 116.3°E) and Tangshan (39.6°N, 118.4°E) correspond with elevated XCH_4 values. This suggests that yearly averaged XCH_4 maps can indeed reveal the strongest emission sources. It should be noted however, that the CH_4 sources around Beijing and Tangshan are approximately three times smaller than those in Shanxi (west of 114°E) and are barely strong enough to cause significant enhancements in the yearly XCH_4 maps. Our analysis indicates that point sources should emit at least around 0.1 Tg per year to be clearly distinguishable on annual XCH_4 maps, taken into account the noise of the observations. The region below 37°N shows high simulated XCH_4 values as well, however they do not directly correspond to strong sources in the inventory. This can likely be explained by the presence of the Taihang mountains on the west which lead to poor dispersion conditions (Fu et al., 2014). Therefore the larger concentrations in this area are likely more determined by the topography and associated meteorological conditions than by surface fluxes.

We observe slightly elevated XCH_4 values near the coal mines of Tangshan in both the WRF-GHG (1888.39 ppb compared to 1883.12 ppb in the surrounding area) and TROPOMI (1879.01 ppb vs 1876.64 ppb) maps. The surrounding area is defined between 39.3-40 °N and 117.8-118.8 °E as there are no major CH_4 sources located therein, while the coal mine sources are concentrated in the area between 39.45-39.8 °N and 118.15-118.6 °E. Although these differences are minor, the enhancement in WRF-GHG is somewhat greater than in TROPOMI. More specific, the mean difference between WRF-GHG and TROPOMI is 8.87 ppb around Tangshan, while it is 11.85 ppb near the emission sources, suggesting that the model overestimation is more pronounced over the coal mines of Tangshan compared to the surrounding area. This difference is statistically significant with a p-value of 7e-10, according to a one-sample t-test. This analysis suggests that these emission sources are indeed overestimated in CAMS-GLOB-ANT, occasionally leading to an overestimation of the energy tracer at Xianghe.

Note that the XCH_4 maps in Fig. 12 suggest that it is very likely that the CH_4 hotspot around 36.25°N, 116.75°E is overestimated as well, as the very strong XCH_4 enhancement in WRF-GHG is absent in the TROPOMI map.

4 Conclusions

We have used the WRF-Chem model in its greenhouse gas option WRF-GHG to simulate surface concentrations and column abundances of CO_2, CH_4 and CO observed at the Xianghe site in China, aiming to improve our understanding of the variabilities in the measured time series. Since June 2018, column-averaged concentrations are measured with a FTIR spectrometer that is part of TCCON, while near-surface concentrations of CO_2 and CH_4 are measured with a PICARRO CRDS analyzer at an altitude of 60 m.a.g.l. We computed 3-D concentration fields from September 2018 until September 2019 in

https://doi.org/10.5194/egusphere-2024-3228
Preprint. Discussion started: 29 October 2024

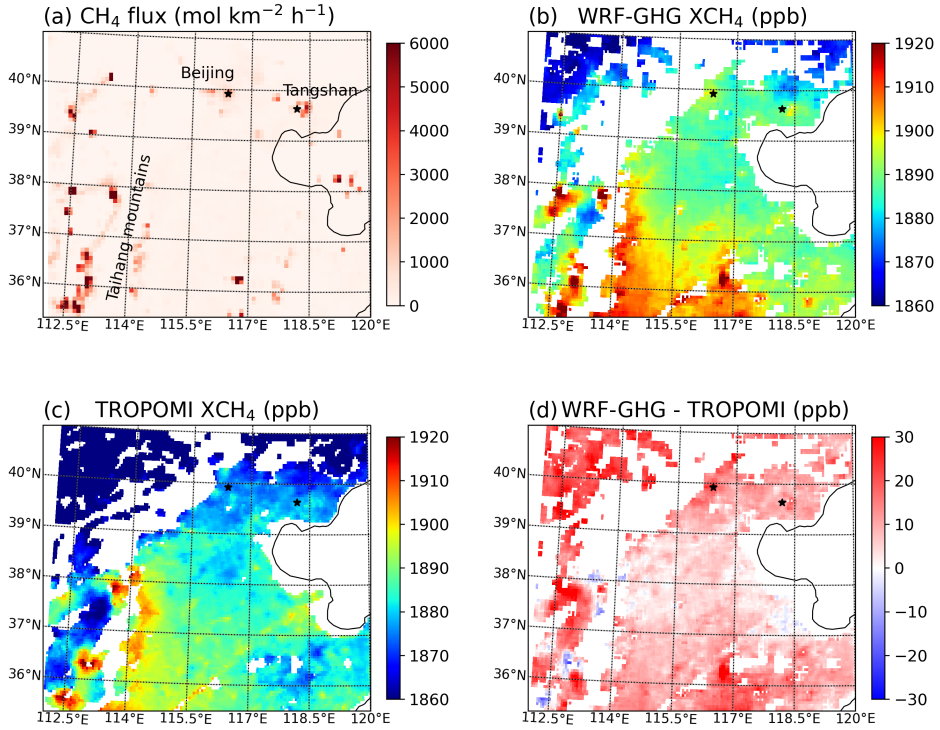

Figure 12. (a) The CH_4 flux from all sectors in CAMS-GLOB-ANT averaged from September 2018 until September 2019 and regridded to WRF-GHG grid d02 (9 km resolution). Mean XCH_4 over the same period as (b) simulated by WRF-GHG and (c) observed by TROPOMI (both regridded to 0.05 °). (d) Mean difference between WRF-GHG and TROPOMI XCH_4 over the entire simulation period.

three nested domains covering a large part of China. The ground-based observations are compared with simulations from the innermost domain, centered on the Beijing-Tianjin-Hebei region, with a horizontal resolution of 3×3 km^2. We employed the CAMS-GLOB-ANT v5.3 inventory for anthropogenic emissions of CO_2 and CH_4, and the REAS v3.2.1 dataset for CO. To disentangle the total simulated signal into the various source sectors, including a wide range of both natural and anthropogenic sources, they were simulated as separate tracers. This study is the first part of the analysis, focusing on CH_4.

In general, the model demonstrated moderate performance, with a correlation coefficient of 0.66 for near-surface CH_4 concentrations in the afternoon and 0.56 for column-averaged concentrations. After adjusting for the observed seasonal bias coming from the boundary conditions (CAMS reanalyses), the performance improved, as indicated by an increase in the correlation coefficient to 0.67 with the TCCON time series.

The simulated CH_4 concentrations is predominantly influenced by emissions from three main human activity sectors: energy, residential & waste, and agriculture. The energy sector has a more significant impact on column abundances (accounting for 52.9% of the total enhancement) compared to surface concentrations (36.9%), reflecting differences in the sensitivity of remote sensing and in situ measurements to sources at large distances, such as Shanxi province. For the in situ concentrations, the three emission sectors are equally important.

https://doi.org/10.5194/egusphere-2024-3228
Preprint. Discussion started: 29 October 2024

Monthly variability in the contributions from each tracer is found to align broadly with expected emission patterns: the residential tracer is higher in winter, while the agricultural tracer peaks in late summer (September). This month-to-month variation is further influenced by meteorological conditions such as horizontal advection and atmospheric stability, which is especially visible in the energy tracer where corresponding emissions remain relatively constant throughout the year, while the contributions from this tracer show notable variations.

The model simulations confirm the importance of large-scale wind patterns, with air masses from the southwest transporting higher CH_4 concentrations to the Xianghe site compared to those from the northwest (median tracer contributions of 57.8 ppb vs. 7.3 ppb, respectively). During southwest wind regimes, pollution from the densely populated North China Plain reaches the Xianghe site. While large-scale air masses influence the variability of both measurement types, smaller-scale factors such as planetary boundary layer dynamics and local wind patterns, also play a significant role for the near-surface concentrations. WRF-GHG effectively captures the diurnal variability driven by these boundary layer dynamics, with CH_4 surface concentrations reaching their lowest levels in the afternoon (16:00 LT) and peaking around sunrise (6:00 LT), leading to a diurnal amplitude of almost 200 ppb.

Despite correcting for the bias in boundary conditions, a residual seasonal bias remained in the model, likely due to inaccuracies in emission estimates from agricultural (livestock) and waste management activities. Furthermore, comparisons between simulated and observed CH_4 concentrations near the surface, along with TROPOMI XCH_4 data, indicate an overestimation of coal mine emissions near Tangshan in the emission inventory of CAMS-GLOB-ANT. However, due to the averaging effect in the column measurements and the relatively low emission strength, this source is just at the threshold of being distinguishable in the XCH_4 enhancements.

In summary, the WRF-GHG model successfully captures key aspects of CH_4 variability at the Xianghe site for both remote sensing and in situ observations. The model simulations also provide valuable insights into the relative contributions of different source sectors and the influence of meteorological processes on CH_4 concentrations.

However, the observed discrepancies, particularly the seasonal bias and overestimated emissions from certain sources, underscore the need for improved emission inventories in this region of China, especially for agricultural, waste management, and coal mining activities. Future research should aim to enhance our understanding of the monthly variations of CH_4 in northern China, which is crucial for providing more accurate boundary conditions and emission flux information to high-resolution modeling studies like the present work. By addressing these challenges, we can further refine our understanding of CH_4 sources and their impacts on regional air quality, ultimately contributing to more effective greenhouse gas mitigation strategies.

Code and data availability. The ERA5 and CAMS reanalysis data set (Hersbach et al., 2023a, b), used as input for the WRF-GHG simulations, was downloaded from the Copernicus Climate Change Service (C3S) Climate Data Store (2022). The CAMS-GLOB-ANT v5.3 emissions (Granier et al., 2019; Soulie et al., 2023) and temporal profiles CAMS-GLOB-TEMPO v3.1 (Guevara et al., 2021) are archived and distributed through the Emissions of atmospheric Compounds and Compilation of Ancillary Data (ECCAD) platform. The REAS emission inventory is publicly available at https://www.nies.go.jp/REAS/ (Kurokawa and Ohara, 2020). The WRF-Chem model code is distributed by

https://doi.org/10.5194/egusphere-2024-3228
Preprint. Discussion started: 29 October 2024

Test	PBL	Surface Layer	Radiation
BASE	YSU scheme (option 1)	Revised MM5 scheme (option 1)	RRTM and Dudhia (option 1)
A	YSU scheme (option 1)	Revised MM5 scheme (option 1)	RRTMG (option 4)
B	MYJ scheme (option 2)	Eta similarity scheme (option 2)	RRTMG (option 4)
C	MYNN3 scheme (option 6)	Eta similarity scheme (option 2)	RRTMG (option 4)
D	MYNN3 scheme (option 6)	Revised MM5 scheme (option 1)	RRTMG (option 4)

Table A1. Overview of sensitivity tests on different physical parameterization options. They are a combination of three different PBL schemes: Yonsei University (Hong et al., 2006), Mellor-Yamada-Janjic (Janjić, 1994) and Mellor-Yamada-Nakanishi Niino Level 3 (Nakanishi and Niino, 2006, 2009; Olson et al., 2019); two surface layer schemes: Revised MM5 (Jiménez et al., 2012) and Eta similarity (Janjić, 1994); and two radiation schemes: RRTMG Longwave and Shortwave schemes (Iacono et al., 2008) versus RRTM Longwave and Dudhia Shortwave schemes (Dudhia, 1989; Mlawer et al., 1997).

NCAR (https://doi.org/10.5065/D6MK6B4K, NCAR, 2020). The WRF-GHG simulation output created in the context of this study can be accessed on https://doi.org/10.18758/P34WJEW2 (Callewaert, 2023). The TCCON data were obtained from the TCCON Data Archive hosted by CaltechDATA at https://tccondata.org (Zhou et al., 2022), while the surface observations at Xianghe were received through private communication with the co-authors. TROPOMI Level 2 Methane Total Column data are publicly available online at https://doi.org/10.5270/S5P-3lcdqiv and the Copernicus Open Access Hub.

Appendix A: WRF-GHG sensitivity tests

Sensitivity tests were carried out to identify a model configuration that matches the observations (of CO_2, Ch_4 and CO) well. We have tested several physical parameterization schemes and anthropogenic fluxes because these elements are essential to accurately simulate tracer concentrations. The initial set of physical parameterization schemes (BASE) was taken from Li et al. (2020) and Dong et al. (2021) as they have shown good model performance for simulating CO_2 concentrations in China. Four alternative combinations (A-D) were created by changing the schemes for the longwave and shortwave radiation, planetary boundary layer (PBL) and surface layer physics, leading to 5 different model configurations in total (see Table A1). Remark that there are several more physical parameterization schemes that could have been included in these tests. Nevertheless, a full sensitivity analysis is outside the scope of this study. Thus, we restricted our tests to the most frequently used schemes in the literature and chose the combination that produced satisfactory model simulations without additional optimization.

Further, the following anthropogenic flux inventories were tested: EDGAR GHG v6.0 (for CO_2 and CH_4, Ferrario et al. (2021)), EDGAR Air Pollutants v5.0 (for CO, Crippa et al. (2019)), CAMS-GLOB-ANT v5.3 (for CO_2, CH_4 and CO, Granier et al. (2019); Soulie et al. (2023)), PKU v2 (for CO_2 and CO, Wang et al. (2013); Zhong et al. (2017)), REAS v3.2.1 (for CO_2 and CO, Kurokawa and Ohara (2020)), MEICv3.1 (for CO_2 and CO, http://www.meicmodel.org/), ODIAC2020b (for CO_2, Oda and Maksyuto (2011, 2020); Oda et al. (2018)) and FFDAS v2.2 (for CO_2, Asefi-Najafabady et al. (2014)). Monthly fluxes are disaggregated into hourly fluxes using the temporal factors of Crippa et al. (2020), Guevara et al. (2021) and Nassar

https://doi.org/10.5194/egusphere-2024-3228
Preprint. Discussion started: 29 October 2024

et al. (2013). The model code was adapted to include these different anthropogenic emission inventories in separate tracers. As such, one simulation is sufficient to compare the effect of all inventories.

The five simulations, representing different combinations of physical parameterization schemes and anthropogenic fluxes, were run over three periods of about 2 weeks spread over the year: 1-17 October 2018, 1-17 February 2019 and 10-25 June 2019. The first 48h were regarded as spin-up and are not taken into account in the analysis.

For each time series the root mean square error (RMSE), mean bias error (BIAS) and Pearson correlation coefficient (CORR) were calculated. In order to find the most suitable combination of physical parameterization schemes and anthropogenic emission inventory for all observations at Xianghe, a combined skill score (S) was computed as follows, based on Gbode et al. (2019):

$$S = (1 - RMSE_{norm}) + (1 - |BIAS_{norm}|) + CORR_{norm}, \tag{A1}$$

where $X_{norm} = \frac{X_i - X_{min}}{X_{max} - X_{min}}$ is the normalized statistical metric. As such, the combination with the highest S will overall have the lowest RMSE, lowest absolute BIAS and highest CORR. Exact values of the statistical metrics and combined skill scores for every sensitivity test can be found below in Tables A2, A3, A4, A5 and A6 for the time series of in situ CO_2, in situ CH_4, XCO_2, XCH_4 and XCO, respectively.

Unfortunately, there is not one combination of physical parameterization schemes and anthropogenic flux inventories that yields optimal scores for all species (CO_2, CH_4 and CO) across various observation types (surface and column). To identify the most appropriate model configuration for simulating all observations at the Xianghe site, it is necessary that the chosen physical parameterization schemes (denoted as test A - D, BASE) show satisfactory skill scores across all five time series. Moreover, the choice of anthropogenic flux inventory, although potentially varying among species, should yield reasonable score values for all observation types of the same species. Therefore, the final combination was determined through the following logical process, where preference was given to the surface data (as it is assumed that the physical schemes will have the highest impact on these simulations):

- We reject the combination with the worst retults: for each statistical metric, we calculate a threshold derived from the mean (μ) and standard deviation (σ) of all occurring values. Combinations in which one or more of the metrics exceed or fall below these thresholds are excluded from the selection process. Specifically, these combinations must conform to the following set of equations:

$$\begin{aligned} &\text{CORR} \geq \mu_{\text{CORR}} - \sigma_{\text{CORR}}, \\ &|\text{BIAS}| \leq \mu_{|\text{BIAS}|} + \sigma_{|\text{BIAS}|}, \\ &\text{RMSE} \leq \mu_{\text{RMSE}} + \sigma_{\text{RMSE}} \end{aligned} \tag{A2}$$

  The combinations that are discarded after this step are indicated with an asterisk (*) behind the inventories name in the tables below.

https://doi.org/10.5194/egusphere-2024-3228
Preprint. Discussion started: 29 October 2024

- For CO_2 and CH_4, discard the combinations that are only present in the table of either the surface or either the column data in order to keep only those that are performing good enough on both time series. The combinations that are discarded after this step are highlighted in italic in the tables below.

- From what is left, we see that only combinations with test A, B or C should be considered as those with test D and BASE settings have been discarded for CH_4. The choice of physical parameterization option should be the same for all species. When sorting the remaining combinations for CO_2 and CO based on S (from the in situ time series for CO_2), we find that options with test B and C are superior to those with test A. Finally, a choice has to be made between options with test B and options with test C.

- For both test B and C, we take the emission inventory which has the highest S, for CO_2 and CH_4 based on the in situ time series and for CO based on the column. This leads to the following options:

  - Test B: CAMS-GLOB-ANT for CH_4 and CO_2; REAS for CO
  - Test C: CAMS-GLOB-ANT for CH_4, REAS for CO_2 and PKU for CO

- The final choice between these two options is rather arbitrary since certain combinations yield slightly improved results for one time series but perform less favorably for another, and vice versa. In our study we have chose the combinations with test B.

This approach leads to the settings of test B, together with CAMS-GLOB-ANT v5.3 fluxes for CO_2 and CH_4 and REAS v3.2.1 (Regional Emission Inventory in Asia) fluxes for CO.

Appendix B: FLEXPART simulations

The FLEXPART v10.4 model (Pisso et al., 2019) is applied to quantitatively estimate the OH impact on the WRF-GHG CH_4 simulation at Xianghe. Table B1 lists the main settings of the FLEXPART model. CH_4 particles are released using the FLEXPART backward mode at Xianghe site with and without OH reaction. We release the CH_4 particles between 00:00-01:00 and 12:00-13:00 (LT) every day in Oct 2018, Jan 2019, Apr 2019 and July 2019. The release height is set to 0-100 m a.g.l., since the OH reaction will have a higher impact near the surface where the wind is weaker than at higher altitudes. The backward running duration is set to 3 days, and the backward sensitivities are extending outside of the WRF-GHG d01 boundary. As an example, Fig. B1 shows the spatial distribution of CH_4 backward sensitivities for a release at 12:00-13:00 LT on 30 January 2019 including the OH reaction, and Fig. B2 shows the corresponding relative difference in the CH_4 backward sensitivities between the simulations with and without OH reaction. Note that FLEXPART v10.4 includes a monthly OH climatology based on GEOS-Chem simulations (Pisso et al., 2019).

https://doi.org/10.5194/egusphere-2024-3228
Preprint. Discussion started: 29 October 2024

Test	Flux	CORR	BIAS	RMSE	S
B	*PKU*	*0.67*	*-1.62*	*16.09*	*2.91*
B	**CAMS**	**0.63**	**-0.12**	**17.50**	**2.81**
B	EDGAR	0.63	0.92	17.87	2.72
C	*PKU*	*0.64*	*-3.96*	*16.91*	*2.65*
C	**REAS**	**0.61**	**-1.19**	**18.88**	**2.58**
A	*PKU*	*0.63*	*-4.51*	*17.16*	*2.57*
BASE	*PKU*	*0.61*	*-3.51*	*17.65*	*2.53*
D	*PKU*	*0.62*	*-4.84*	*17.38*	*2.52*
C	FFDAS	0.58	-0.92	19.12	2.50
C	CAMS	0.59	-2.77	18.06	2.49
C	EDGAR	0.58	-1.71	18.53	2.47
D	FFDAS	0.58	-1.69	19.19	2.44
B	REAS	0.58	1.44	20.14	2.41
B	FFDAS	0.60	2.97	20.19	2.41
A	CAMS	0.58	-3.46	18.26	2.40
A	EDGAR	0.57	-2.46	18.58	2.40
A	FFDAS	0.56	-1.36	19.76	2.35
C	MEIC	0.63	5.15	20.68	2.34
D	CAMS	0.57	-3.74	18.90	2.30
D	EDGAR	0.55	-2.73	19.32	2.29
BASE	REAS	0.55	-0.29	22.00	2.27
A	REAS	0.55	-1.33	21.49	2.25
A	*MEIC*	*0.59*	*4.60*	*21.84*	*2.20*
D	MEIC	0.58	4.02	21.86	2.19
D	REAS	0.54	-1.33	22.02	2.19
BASE	FFDAS *	0.51	0.11	21.66	2.17
BASE	CAMS *	0.52	-2.21	20.93	2.13
BASE	EDGAR *	0.51	-1.11	21.72	2.09
B	MEIC *	0.64	9.16	22.95	2.07
BASE	MEIC *	0.57	5.94	23.34	1.99
D	ODIAC *	0.52	3.63	22.57	1.96
C	ODIAC *	0.53	5.04	22.80	1.91
A	ODIAC *	0.49	4.56	24.46	1.69
B	ODIAC *	0.54	8.63	24.91	1.63
BASE	ODIAC *	0.47	5.81	25.67	1.51

Table A2. Statistical metrics for sensitivity tests, in situ CO_2 data at Xianghe. Unit of BIAS and RMSE is ppm. Rows where the inventory name if followed by an asterisk (∗) indicate those where one or more statistical metrics surpass the thresholds defined in Eq. A2. Rows in italic represent combinations that are rejected due to the XCO_2 value falling outside the thresholds. The bold lines represent the final two options as determined by the methodology outlined in Appendix A.

https://doi.org/10.5194/egusphere-2024-3228
Preprint. Discussion started: 29 October 2024

Test	Flux	CORR	BIAS	RMSE	S
C	**CAMS**	**0.52**	**2.19**	**206.50**	**2.81**
C	EDGAR	0.52	19.09	208.24	2.67
BASE	*CAMS*	*0.48*	*3.26*	*213.26*	*2.47*
A	*CAMS*	*0.45*	*-7.09*	*210.84*	*2.31*
BASE	*EDGAR*	*0.48*	*22.33*	*216.09*	*2.28*
A	EDGAR	0.46	12.50	213.59	2.27
B	**CAMS**	**0.50**	**31.39**	**228.56**	**2.17**
B	EDGAR *	0.51	52.53	237.75	1.87
D	EDGAR *	0.41	8.83	237.26	1.70
D	CAMS *	0.39	-9.19	237.31	1.60

Table A3. Same as Table A2 but for in situ CH_4. Unit of BIAS and RMSE is ppb.

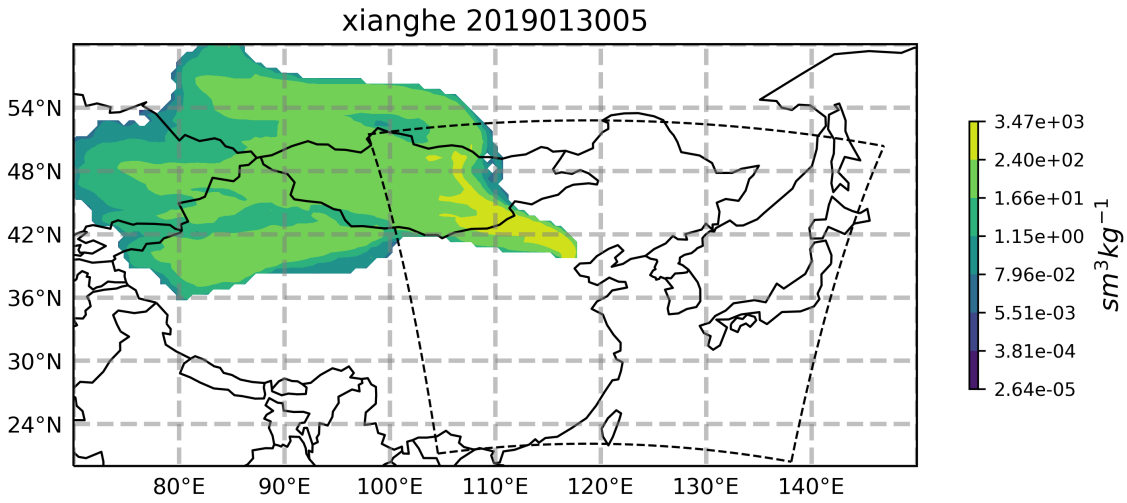

Figure B1. The spatial distribution of CH_4 backward sensitivities (in sm^3kg^{-1}) for a release at 12:00-13:00 LT (which is 04:00-05:00 UTC as indicated in the title) on 30 January 2019 from the FLEXPART simulation including the OH reaction. The location of WRF-GHG d01 is indicated by the dashed line.

Author contributions. SC made the model simulations and performed the formal analysis, investigation and visualization. The research was conceptualized by SC, MDM and EM and supervised by MDM and EM. MZ, TW and PW have provided the observational in situ data at Xianghe. BL supported with computing tools to correctly compare the model with TCCON and TROPOMI data. MZ designed and performed the FLEXPART simulations. SC prepared the initial draft of this manuscript while it was reviewed and edited by MZ, BL, TW, MDM, EM and PW.

https://doi.org/10.5194/egusphere-2024-3228
Preprint. Discussion started: 29 October 2024

Test	Flux	CORR	BIAS	RMSE	S
D	MEIC	0.77	0.62	1.52	2.87
C	MEIC	0.76	0.62	1.54	2.83
BASE	MEIC *	0.66	0.95	1.95	1.86
D	*ODIAC*	*0.78*	*-1.27*	*2.28*	*1.86*
C	*ODIAC*	*0.79*	*-1.32*	*2.29*	*1.85*
A	MEIC *	0.62	0.97	2.03	1.62
D	FFDAS	0.80	-1.60	2.43	1.58
C	FFDAS	0.80	-1.62	2.45	1.55
BASE	*ODIAC*	*0.75*	*-1.36*	*2.47*	*1.54*
D	EDGAR	0.79	-1.59	2.45	1.54
A	*ODIAC*	*0.74*	*-1.30*	*2.50*	*1.49*
B	*ODIAC*	*0.72*	*-1.23*	*2.53*	*1.47*
C	EDGAR	0.77	-1.57	2.49	1.45
D	CAMS	0.79	-1.70	2.52	1.38
B	EDGAR	0.76	-1.54	2.55	1.38
B	FFDAS	0.75	-1.52	2.58	1.33
C	**REAS**	**0.80**	**-1.81**	**2.56**	**1.33**
BASE	*FFDAS*	*0.77*	*-1.65*	*2.58*	*1.32*
D	REAS	0.79	-1.80	2.56	1.32
BASE	*EDGAR*	*0.77*	*-1.64*	*2.59*	*1.31*
C	CAMS	0.77	-1.68	2.57	1.30
A	FFDAS	0.76	-1.62	2.60	1.28
B	**CAMS**	**0.75**	**-1.64**	**2.63**	**1.22**
BASE	*CAMS*	*0.76*	*-1.74*	*2.66*	*1.15*
D	PKU *	0.80	-1.98	2.67	1.13
C	PKU *	0.80	-2.00	2.67	1.13
B	REAS	0.75	-1.71	2.69	1.10
A	EDGAR	0.72	-1.54	2.71	1.09
BASE	REAS	0.76	-1.85	2.73	1.03
A	CAMS	0.72	-1.65	2.76	0.98
A	REAS	0.75	-1.84	2.75	0.97
B	MEIC *	0.55	1.25	2.30	0.95
B	PKU *	0.76	-1.91	2.77	0.94
BASE	PKU *	0.77	-2.02	2.81	0.87
A	PKU *	0.76	-2.00	2.82	0.84

Table A4. Same as Table A2 but for XCO_2.

https://doi.org/10.5194/egusphere-2024-3228
Preprint. Discussion started: 29 October 2024

Test	Flux	CORR	BIAS	RMSE	S
B	**CAMS**	**0.69**	**-0.79**	**20.53**	**2.94**
B	*EDGAR*	*0.69*	*0.65*	*20.94*	*2.62*
C	EDGAR	0.67	-0.96	21.24	1.73
D	*EDGAR*	*0.66*	*-0.80*	*21.45*	*1.47*
C	**CAMS**	**0.67**	**-2.16**	**21.31**	**1.12**
A	EDGAR	0.65	-1.17	21.72	0.86
BASE	EDGAR *	0.65	-1.66	21.76	0.59
D	CAMS *	0.65	-2.09	21.75	0.55
A	CAMS *	0.65	-2.75	21.45	0.37
BASE	CAMS *	0.65	-3.03	21.42	0.34

Table A5. Same as Table A2 but for XCH_4. Unit of BIAS and RMSE is ppb.

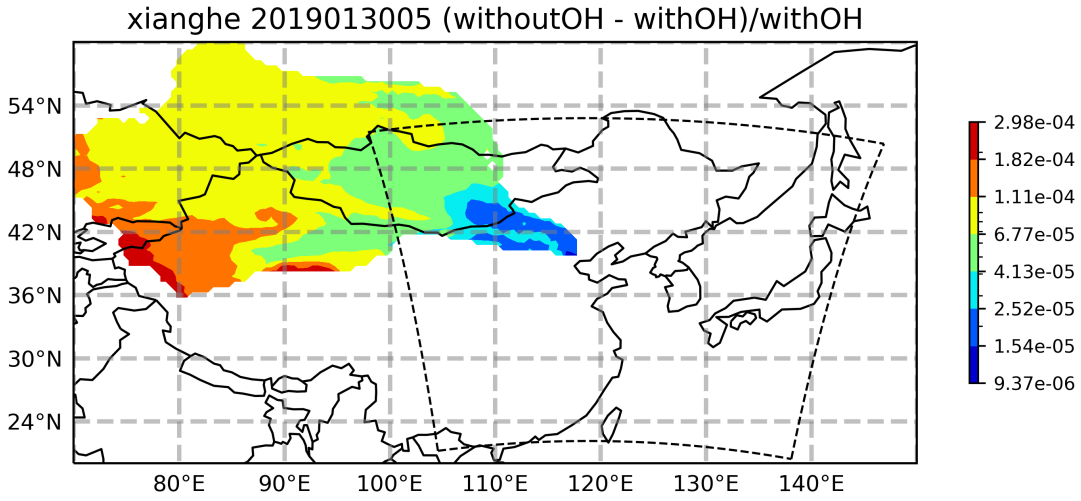

Figure B2. Relative difference in the CH_4 backward sensitivities between simulations with and without OH reaction. The location of WRF-GHG d01 is indicated by the dashed line.

Competing interests. The contact authors have declared that neither they nor their co-authors have any competing interests.

Disclaimer. The results contain modified Copernicus Climate Change Service information 2022. Neither the European Commission nor ECMWF is responsible for any use that may be made of the Copernicus information or data it contains.

https://doi.org/10.5194/egusphere-2024-3228
Preprint. Discussion started: 29 October 2024

Test	Flux	CORR	BIAS	RMSE	S
B	**REAS**	**0.78**	**-3.99**	**30.25**	**2.96**
B	PKU	0.78	-5.38	30.32	2.94
D	REAS	0.76	-5.32	31.54	2.83
BASE	REAS	0.77	-7.12	31.39	2.81
C	**PKU**	**0.76**	**-6.88**	**31.73**	**2.79**
D	PKU	0.76	-6.82	31.75	2.79
C	REAS	0.75	-5.53	32.00	2.79
BASE	PKU	0.77	-7.85	31.74	2.77
A	REAS	0.75	-7.15	32.35	2.72
A	PKU	0.75	-7.51	32.67	2.71
B	CAMS	0.68	-24.21	43.48	1.70
BASE	CAMS	0.66	-25.16	44.35	1.61
D	CAMS	0.64	-24.34	44.34	1.57
BASE	EDGAR *	0.52	3.27	57.84	1.45
A	CAMS	0.59	-23.19	44.78	1.44
C	CAMS	0.60	-23.77	45.07	1.43
B	EDGAR *	0.53	5.90	59.57	1.34
A	EDGAR *	0.50	6.27	62.83	1.16
D	MEIC *	0.65	-37.13	49.72	1.05
C	MEIC *	0.61	-37.10	50.26	0.94
B	MEIC *	0.53	-30.94	47.80	0.93
C	EDGAR *	0.46	8.30	67.22	0.87
D	EDGAR *	0.47	8.66	68.01	0.86
BASE	MEIC *	0.55	-34.80	49.89	0.82
A	MEIC *	0.52	-34.49	50.35	0.72

Table A6. Same as Table A2 but for XCO. Unit of BIAS and RMSE is ppb.

https://doi.org/10.5194/egusphere-2024-3228
Preprint. Discussion started: 29 October 2024

Parameter	Settings
Release location	$\pm 0.1^\circ$ around Xianghe site
Release height	0 - 100 m.a.g.l
Release time	00:00-01:00 and 12:00-13:00 (LT) every day in Oct 2018, Jan 2019, Apr 2019 and July 2019
Number of backward running days	3
Number of releasing particles	20 000
OH reaction	On and off
Meteorological data	NCEP CFSv2 with $0.5^\circ \times 0.5^\circ$ horizontal resolution and 64 vertical levels (Saha et al., 2014)

Table B1. The main settings of FLEXPART model run with a CH_4 tracer

Acknowledgements. We would like to thank all staff at the Xianghe site for operating the FTIR and PICARRO measurements. This work is supported by the National Natural Science Foundation of China (No. 42205140; 41975035). Emmanuel Mahieu is a senior research associate with the F.R.S.-FNRS. The authors acknowledge all providers of observational data and emission inventories. We thank the IT team at BIRA-IASB for their support on data storage and HPC maintenance. Christophe Gerbig, Roberto Kretschmer, and Thomas Koch (MPI BGC) are thanked for distributing the VPRM preprocessor code. Finally, we are grateful for fruitful discussions with Jean-François Müller (BIRA-IASB) and Bernard Heinesch (ULiège).

https://doi.org/10.5194/egusphere-2024-3228
Preprint. Discussion started: 29 October 2024

References

TROPOMI Level 2 Methane Total Column Products. Version 02, https://doi.org/10.5270/S5P-3lcdqiv, 2021.

Agustí-Panareda, A., Barré, J., Massart, S., Inness, A., Aben, I., Ades, M., Baier, B. C., Balsamo, G., Borsdorff, T., Bousserez, N., Boussetta, S., Buchwitz, M., Cantarello, L., Crevoisier, C., Engelen, R., Eskes, H., Flemming, J., Garrigues, S., Hasekamp, O., Huijnen, V., Jones, L., Kipling, Z., Langerock, B., McNorton, J., Meilhac, N., Noël, S., Parrington, M., Peuch, V.-H., Ramonet, M., Razinger, M., Reuter, M., Ribas, R., Suttie, M., Sweeney, C., Tarniewicz, J., and Wu, L.: Technical Note: The CAMS Greenhouse Gas Reanalysis from 2003 to 2020, Atmospheric Chemistry and Physics, 23, 3829–3859, https://doi.org/10.5194/acp-23-3829-2023, 2023.

Ahmadov, R., Gerbig, C., Kretschmer, R., Koerner, S., Neininger, B., Dolman, A. J., and Sarrat, C.: Mesoscale Covariance of Transport and CO2 Fluxes: Evidence from Observations and Simulations Using the WRF-VPRM Coupled Atmosphere-Biosphere Model, Journal of Geophysical Research: Atmospheres, 112, https://doi.org/10.1029/2007JD008552, 2007.

Apituley, A., Pedergnana, M., Sneep, M., Veefkind, P. J., Loyola, D., Hasekamp, O., Lorente Delgado, A., and Borsdorff, T.: Sentinel-5 precursor/TROPOMI Level 2 Product User Manual Methane, Tech. rep., SRON/KNMI, ref: SRON-S5P-LEV2-MA-001, issue: 2.6.0, 2023.

Asefi-Najafabady, S., Rayner, P. J., Gurney, K. R., McRobert, A., Song, Y., Coltin, K., Huang, J., Elvidge, C., and Baugh, K.: A Multiyear, Global Gridded Fossil Fuel CO $_2$ Emission Data Product: Evaluation and Analysis of Results: GLOBAL FOSSIL FUEL CO2 EMISSIONS, Journal of Geophysical Research: Atmospheres, 119, 10,213–10,231, https://doi.org/10.1002/2013JD021296, 2014.

Beck, V., Koch, T., Kretschmer, R., Marshall, J., Ahmadov, R., Gerbig, C., Pillai, D., and Heimann, M.: The WRF Greenhouse Gas Model (WRF-GHG), 2011.

Bloom, A., Bowman, K., Lee, M., Turner, A., Schroeder, R., Worden, J., Weidner, R., McDonal, K., and Jacob, D.: CMS: Global 0.5-Deg Wetland Methane Emissions and Uncertainty (WetCHARTs v1.0), https://doi.org/10.3334/ORNLDAAC/1502, 2017.

Callewaert, S.: WRF-Chem Simulations of CO2, CH4 and CO around Xianghe, China, https://doi.org/10.18758/P34WJEW2, 2023.

Callewaert, S., Brioude, J., Langerock, B., Duflot, V., Fonteyn, D., Müller, J.-F. c., Metzger, J.-M., Hermans, C., Kumps, N., Ramonet, M., Lopez, M., Mahieu, E., and De Mazière, M.: Analysis of CO_2, CH_4, and CO Surface and Column Concentrations Observed at Réunion Island by Assessing WRF-Chem Simulations, Atmospheric Chemistry and Physics, 22, 7763–7792, https://doi.org/10.5194/acp-22-7763-2022, 2022.

Chen, Z., Jacob, D. J., Nesser, H., Sulprizio, M. P., Lorente, A., Varon, D. J., Lu, X., Shen, L., Qu, Z., Penn, E., and Yu, X.: Methane Emissions from China: A High-Resolution Inversion of TROPOMI Satellite Observations, Atmospheric Chemistry and Physics, 22, 10 809–10 826, https://doi.org/10.5194/acp-22-10809-2022, 2022.

Crippa, M., Guizzardi, D., Muntean, M., and Schaaf, E.: EDGAR v5.0 Global Air Pollutant Emissions., http://data.europa.eu/89h/377801af-b094-4943-8fdc-f79a7c0c2d19, 2019.

Crippa, M., Solazzo, E., Huang, G., Guizzardi, D., Koffi, E., Muntean, M., Schieberle, C., Friedrich, R., and Janssens-Maenhout, G.: High Resolution Temporal Profiles in the Emissions Database for Global Atmospheric Research, Scientific Data, 7, 121, https://doi.org/10.1038/s41597-020-0462-2, 2020.

Dayalu, A., Munger, J. W., Wofsy, S. C., Wang, Y., Nehrkorn, T., Zhao, Y., McElroy, M. B., Nielsen, C. P., and Luus, K.: Assessing Biotic Contributions to CO_2 Fluxes in Northern China Using the Vegetation, Photosynthesis and Respiration Model (VPRM-CHINA) and Observations from 2005 to 2009, Biogeosciences, 15, 6713–6729, https://doi.org/10.5194/bg-15-6713-2018, 2018.

https://doi.org/10.5194/egusphere-2024-3228
Preprint. Discussion started: 29 October 2024

Dekker, I. N., Houweling, S., Aben, I., Röckmann, T., Krol, M., Martínez-Alonso, S., Deeter, M. N., and Worden, H. M.: Quantification of CO Emissions from the City of Madrid Using MOPITT Satellite Retrievals and WRF Simulations, Atmospheric Chemistry and Physics, 17, 14 675–14 694, https://doi.org/10.5194/acp-17-14675-2017, 2017.

Dong, X., Yue, M., Jiang, Y., Hu, X.-M., Ma, Q., Pu, J., and Zhou, G.: Analysis of CO_2 Spatio-Temporal Variations in China Using a Weather–Biosphere Online Coupled Model, Atmospheric Chemistry and Physics, 21, 7217–7233, https://doi.org/10.5194/acp-21-7217-2021, 2021.

Dudhia, J.: Numerical Study of Convection Observed during the Winter Monsoon Experiment Using a Mesoscale Two-Dimensional Model, Journal of the Atmospheric Sciences, 46, 3077–3107, https://doi.org/10.1175/1520-0469(1989)046<3077:NSOCOD>2.0.CO;2, 1989.

Fast, J. D., Gustafson Jr., W. I., Easter, R. C., Zaveri, R. A., Barnard, J. C., Chapman, E. G., Grell, G. A., and Peckham, S. E.: Evolution of Ozone, Particulates, and Aerosol Direct Radiative Forcing in the Vicinity of Houston Using a Fully Coupled Meteorology-Chemistry-Aerosol Model, Journal of Geophysical Research: Atmospheres, 111, https://doi.org/10.1029/2005JD006721, 2006.

Feng, S., Lauvaux, T., Newman, S., Rao, P., Ahmadov, R., Deng, A., Díaz-Isaac, L. I., Duren, R. M., Fischer, M. L., Gerbig, C., Gurney, K. R., Huang, J., Jeong, S., Li, Z., Miller, C. E., O'Keeffe, D., Patarasuk, R., Sander, S. P., Song, Y., Wong, K. W., and Yung, Y. L.: Los Angeles Megacity: A High-Resolution Land–Atmosphere Modelling System for Urban CO_2 Emissions, Atmospheric Chemistry and Physics, 16, 9019–9045, https://doi.org/10.5194/acp-16-9019-2016, 2016.

Ferrario, F. M., Crippa, M., Guizzardi, D., Muntean, M., Schaaf, E., Vullo, E. L., Solazzo, E., Olivier, J., and Vignati, E.: EDGAR v6.0 Greenhouse Gas Emissions, http://data.europa.eu/89h/97a67d67-c62e-4826-b873-9d972c4f670b, 2021.

Friedlingstein, P., O'Sullivan, M., Jones, M. W., Andrew, R. M., Gregor, L., Hauck, J., Le Quéré, C., Luijkx, I. T., Olsen, A., Peters, G. P., Peters, W., Pongratz, J., Schwingshackl, C., Sitch, S., Canadell, J. G., Ciais, P., Jackson, R. B., Alin, S. R., Alkama, R., Arneth, A., Arora, V. K., Bates, N. R., Becker, M., Bellouin, N., Bittig, H. C., Bopp, L., Chevallier, F., Chini, L. P., Cronin, M., Evans, W., Falk, S., Feely, R. A., Gasser, T., Gehlen, M., Gkritzalis, T., Gloege, L., Grassi, G., Gruber, N., Gürses, O., Harris, I., Hefner, M., Houghton, R. A., Hurtt, G. C., Iida, Y., Ilyina, T., Jain, A. K., Jersild, A., Kadono, K., Kato, E., Kennedy, D., Klein Goldewijk, K., Knauer, J., Korsbakken, J. I., Landschützer, P., Lefèvre, N., Lindsay, K., Liu, J., Liu, Z., Marland, G., Mayot, N., McGrath, M. J., Metzl, N., Monacci, N. M., Munro, D. R., Nakaoka, S.-I., Niwa, Y., O'Brien, K., Ono, T., Palmer, P. I., Pan, N., Pierrot, D., Pocock, K., Poulter, B., Resplandy, L., Robertson, E., Rödenbeck, C., Rodriguez, C., Rosan, T. M., Schwinger, J., Séférian, R., Shutler, J. D., Skjelvan, I., Steinhoff, T., Sun, Q., Sutton, A. J., Sweeney, C., Takao, S., Tanhua, T., Tans, P. P., Tian, X., Tian, H., Tilbrook, B., Tsujino, H., Tubiello, F., van der Wer, G. R., Walker, A. P., Wanninkhof, R., Whitehead, C., Willstrand Wranne, A., Wright, R., Yuan, W., Yue, C., Yue, X., Zaehle, S., Zeng, J., and Zheng, B.: Global Carbon Budget 2022, Earth System Science Data, 14, 4811–4900, https://doi.org/10.5194/essd-14-4811-2022, 2022.

Fu, G. Q., Xu, W. Y., Yang, R. F., Li, J. B., and Zhao, C. S.: The Distribution and Trends of Fog and Haze in the North China Plain over the Past 30 Years, Atmospheric Chemistry and Physics, 14, 11 949–11 958, https://doi.org/10.5194/acp-14-11949-2014, 2014.

Gbode, I. E., Dudhia, J., Ogunjobi, K. O., and Ajayi, V. O.: Sensitivity of Different Physics Schemes in the WRF Model during a West African Monsoon Regime, Theoretical and Applied Climatology, 136, 733–751, https://doi.org/10.1007/s00704-018-2538-x, 2019.

Granier, C., Darras, S., Denier van der Gon, H., Doubalova, J., Elguindi, N., Galle, B., Gauss, M., Guevara, M., Jalkanen, J.-P., Kuenen, J., Liousse, C., Quack, B., Simpson, D., and Sindelarova, K.: The Copernicus Atmosphere Monitoring Service Global and Regional Emissions (April 2019 Version), https://doi.org/10.24380/D0BN-KX16, 2019.

Grell, G. A., Peckham, S. E., Schmitz, R., McKeen, S. A., Frost, G., Skamarock, W. C., and Eder, B.: Fully Coupled "Online" Chemistry within the WRF Model, Atmospheric Environment, 39, 6957–6975, https://doi.org/10.1016/j.atmosenv.2005.04.027, 2005.

https://doi.org/10.5194/egusphere-2024-3228
Preprint. Discussion started: 29 October 2024

Guevara, M., Jorba, O., Tena, C., Denier van der Gon, H., Kuenen, J., Elguindi, N., Darras, S., Granier, C., and Pérez García-Pando, C.: Copernicus Atmosphere Monitoring Service TEMPOral Profiles (CAMS-TEMPO): Global and European Emission Temporal Profile Maps for Atmospheric Chemistry Modelling, Earth System Science Data, 13, 367–404, https://doi.org/10.5194/essd-13-367-2021, 2021.

Hersbach, H., Bell, B., Berrisford, P., Biavati, G., Horányi, A., Munoz Sabater, J., Nicolas, J., Peubey, C., Radu, R., Rozum, I., Schepers, D., Simmons, A., Soci, C., Dee, D., and Thépaut, J.-N.: ERA5 Hourly Data on Pressure Levels from 1940 to Present., https://doi.org/10.24381/cds.bd0915c6, 2023a.

Hersbach, H., Bell, B., Berrisford, P., Biavati, G., Horányi, A., Munoz Sabater, J., Nicolas, J., Peubey, C., Radu, R., Rozum, I., Schepers, D., Simmons, A., Soci, C., Dee, D., and Thépaut, J.-N.: ERA5 Hourly Data on Single Levels from 1940 to Present., https://doi.org/10.24381/cds.adbb2d47, 2023b.

Hong, S.-Y., Noh, Y., and Dudhia, J.: A New Vertical Diffusion Package with an Explicit Treatment of Entrainment Processes, Monthly Weather Review, 134, 2318–2341, https://doi.org/10.1175/MWR3199.1, 2006.

Hu, C., Zhang, J., Qi, B., Du, R., Xu, X., Xiong, H., Liu, H., Ai, X., Peng, Y., and Xiao, W.: Global Warming Will Largely Increase Waste Treatment CH_4 Emissions in Chinese Megacities: Insight from the First City-Scale CH_4 Concentration Observation Network in Hangzhou, China, Atmospheric Chemistry and Physics, 23, 4501–4520, https://doi.org/10.5194/acp-23-4501-2023, 2023.

Hu, X.-M., Crowell, S., Wang, Q., Zhang, Y., Davis, K. J., Xue, M., Xiao, X., Moore, B., Wu, X., Choi, Y., and DiGangi, J. P.: Dynamical Downscaling of CO2 in 2016 Over the Contiguous United States Using WRF-VPRM, a Weather-Biosphere-Online-Coupled Model, Journal of Advances in Modeling Earth Systems, 12, e2019MS001 875, https://doi.org/10.1029/2019MS001875, 2020.

Iacono, M. J., Delamere, J. S., Mlawer, E. J., Shephard, M. W., Clough, S. A., and Collins, W. D.: Radiative Forcing by Long-Lived Greenhouse Gases: Calculations with the AER Radiative Transfer Models, Journal of Geophysical Research: Atmospheres, 113, https://doi.org/10.1029/2008JD009944, 2008.

Inness, A., Ades, M., Agustí-Panareda, A., Barré, J., Benedictow, A., Blechschmidt, A.-M., Dominguez, J. J., Engelen, R., Eskes, H., Flemming, J., Huijnen, V., Jones, L., Kipling, Z., Massart, S., Parrington, M., Peuch, V.-H., Razinger, M., Remy, S., Schulz, M., and Suttie, M.: The CAMS Reanalysis of Atmospheric Composition, Atmospheric Chemistry and Physics, 19, 3515–3556, https://doi.org/10.5194/acp-19-3515-2019, 2019.

Janjić, Z. s. I.: The Step-Mountain Eta Coordinate Model: Further Developments of the Convection, Viscous Sublayer, and Turbulence Closure Schemes, Monthly Weather Review, 122, 927–945, https://doi.org/10.1175/1520-0493(1994)122<0927:TSMECM>2.0.CO;2, 1994.

Ji, D., Zhou, M., Wang, P., Yang, Y., Wang, T., Sun, X., Hermans, C., Yao, B., and Wang, G.: Deriving Temporal and Vertical Distributions of Methane in Xianghe Using Ground-based Fourier Transform Infrared and Gas-analyzer Measurements, Advances in Atmospheric Sciences, 37, 597–607, https://doi.org/10.1007/s00376-020-9233-4, 2020.

Jiménez, P. A., Dudhia, J., González-Rouco, J. F., Navarro, J., Montávez, J. P., and García-Bustamante, E.: A Revised Scheme for the WRF Surface Layer Formulation, Monthly Weather Review, 140, 898–918, https://doi.org/10.1175/MWR-D-11-00056.1, 2012.

Keppel-Aleks, G., Wennberg, P. O., and Schneider, T.: Sources of Variations in Total Column Carbon Dioxide, Atmospheric Chemistry and Physics, 11, 3581–3593, https://doi.org/10.5194/acp-11-3581-2011, 2011.

Kurokawa, J. and Ohara, T.: Long-Term Historical Trends in Air Pollutant Emissions in Asia: Regional Emission Inventory in ASia (REAS) Version 3, Atmospheric Chemistry and Physics, 20, 12 761–12 793, https://doi.org/10.5194/acp-20-12761-2020, 2020.

Landschützer, P., Gruber, N., and Bakker, D. C. E.: An Observation-Based Global Monthly Gridded Sea Surface pCO_2 Product from 1982 Onward and Its Monthly Climatology (NCEI Accession 0160558). NOAA National Centers for Environmental Information., https://doi.org/10.7289/v5z899n6, 2017.

https://doi.org/10.5194/egusphere-2024-3228
Preprint. Discussion started: 29 October 2024

Laughner, J. L., Roche, S., Kiel, M., Toon, G. C., Wunch, D., Baier, B. C., Biraud, S., Chen, H., Kivi, R., Laemmel, T., McKain, K., Quéhé, P.-Y., Rousogenous, C., Stephens, B. B., Walker, K., and Wennberg, P. O.: A New Algorithm to Generate a Priori Trace Gas Profiles for the GGG2020 Retrieval Algorithm, Atmospheric Measurement Techniques, 16, 1121–1146, https://doi.org/10.5194/amt-16-1121-2023, 2023.

Laughner, J. L., Toon, G. C., Mendonca, J., Petri, C., Roche, S., Wunch, D., Blavier, J.-F., Griffith, D. W. T., Heikkinen, P., Keeling, R. F., Kiel, M., Kivi, R., Roehl, C. M., Stephens, B. B., Baier, B. C., Chen, H., Choi, Y., Deutscher, N. M., DiGangi, J. P., Gross, J., Herkommer, B., Jeseck, P., Laemmel, T., Lan, X., McGee, E., McKain, K., Miller, J., Morino, I., Notholt, J., Ohyama, H., Pollard, D. F., Rettinger, M., Riris, H., Rousogenous, C., Sha, M. K., Shiomi, K., Strong, K., Sussmann, R., Té, Y., Velazco, V. A., Wofsy, S. C., Zhou, M., and Wennberg, P. O.: The Total Carbon Column Observing Network's GGG2020 data version, Earth System Science Data, 16, 2197–2260, https://doi.org/10.5194/essd-16-2197-2024, publisher: Copernicus GmbH, 2024.

Li, J., Hao, X., Liao, H., Wang, Y., Cai, W., Li, K., Yue, X., Yang, Y., Chen, H., Mao, Y., Fu, Y., Chen, L., and Zhu, J.: Winter Particulate Pollution Severity in North China Driven by Atmospheric Teleconnections, Nature Geoscience, 15, 349–355, https://doi.org/10.1038/s41561-022-00933-2, 2022.

Li, X., Hu, X.-M., Cai, C., Jia, Q., Zhang, Y., Liu, J., Xue, M., Xu, J., Wen, R., and Crowell, S. M. R.: Terrestrial CO2 Fluxes, Concentrations, Sources and Budget in Northeast China: Observational and Modeling Studies, Journal of Geophysical Research: Atmospheres, 125, e2019JD031 686, https://doi.org/10.1029/2019JD031686, 2020.

Liu, Y., Yue, T., Zhang, L., Zhao, N., Zhao, M., and Liu, Y.: Simulation and Analysis of XCO2 in North China Based on High Accuracy Surface Modeling, Environmental Science and Pollution Research International, 25, 27 378–27 392, https://doi.org/10.1007/s11356-018-2683-x, 2018.

Maasakkers, J. D., Jacob, D. J., Sulprizio, M. P., Turner, A. J., Weitz, M., Wirth, T., Hight, C., DeFigueiredo, M., Desai, M., Schmeltz, R., Hockstad, L., Bloom, A. A., Bowman, K. W., Jeong, S., and Fischer, M. L.: Gridded National Inventory of U.S. Methane Emissions, Environmental Science & Technology, 50, 13 123–13 133, https://doi.org/10.1021/acs.est.6b02878, 2016.

Mahadevan, P., Wofsy, S. C., Matross, D. M., Xiao, X., Dunn, A. L., Lin, J. C., Gerbig, C., Munger, J. W., Chow, V. Y., and Gottlieb, E. W.: A Satellite-Based Biosphere Parameterization for Net Ecosystem CO2 Exchange: Vegetation Photosynthesis and Respiration Model (VPRM), Global Biogeochemical Cycles, 22, https://doi.org/10.1029/2006GB002735, 2008.

Masson-Delmotte, V., Zhai, P., Pirani, A., Connors, S. L., Péan, C., Berger, S., Caud, N., Chen, Y., Goldfarb, L., Gomis, M. I., Huang, M., Leitzell, K., Lonnoy, E., Matthews, J. B. R., Maycock, T. K., Waterfield, T., Yelek¸ci, O., Yu, R., and Zhou (eds.), a. B.: IPCC, 2021: Climate Change 2021: The Physical Science Basis. Contribution of Working Group I to the Sixth Assessment Report of the Intergovernmental Panel on Climate Change, 2021.

Mlawer, E. J., Taubman, S. J., Brown, P. D., Iacono, M. J., and Clough, S. A.: Radiative Transfer for Inhomogeneous Atmospheres: RRTM, a Validated Correlated-k Model for the Longwave, Journal of Geophysical Research: Atmospheres, 102, 16 663–16 682, https://doi.org/10.1029/97JD00237, 1997.

Nakanishi, M. and Niino, H.: An Improved Mellor–Yamada Level-3 Model: Its Numerical Stability and Application to a Regional Prediction of Advection Fog, Boundary-Layer Meteorology, 119, 397–407, https://doi.org/10.1007/s10546-005-9030-8, 2006.

Nakanishi, M. and Niino, H.: Development of an Improved Turbulence Closure Model for the Atmospheric Boundary Layer, Journal of the Meteorological Society of Japan. Ser. II, 87, 895–912, https://doi.org/10.2151/jmsj.87.895, 2009.

https://doi.org/10.5194/egusphere-2024-3228
Preprint. Discussion started: 29 October 2024

Nassar, R., Napier-Linton, L., Gurney, K. R., Andres, R. J., Oda, T., Vogel, F. R., and Deng, F.: Improving the Temporal and Spatial Distribution of CO2 Emissions from Global Fossil Fuel Emission Data Sets, Journal of Geophysical Research: Atmospheres, 118, 917–933, https://doi.org/10.1029/2012JD018196, 2013.

Oda, T. and Maksyuto, S.: A Very High-Resolution (1 Km×1 Km) Global Fossil Fuel CO_2 Emission Inventory Derived Using a Point Source Database and Satellite Observations of Nighttime Lights, Atmospheric Chemistry and Physics, 11, 543–556, https://doi.org/10.5194/acp-11-543-2011, 2011.

Oda, T. and Maksyuto, S.: ODIAC Fossil Fuel CO_2 Emissions Dataset (ODIAC2020b), Center for Global Environmental Research, National Institute for Environmental Studies, https://doi.org/10.17595/20170411.001, 2020.

Oda, T., Maksyuto, S., and Andres, R. J.: The Open-source Data Inventory for Anthropogenic CO_2, Version 2016 (ODIAC2016): A Global Monthly Fossil Fuel CO_2 Gridded Emissions Data Product for Tracer Transport Simulations and Surface Flux Inversions, Earth System Science Data, 10, 87–107, https://doi.org/10.5194/essd-10-87-2018, 2018.

Olson, J. B., Kenyon, J. S., family=Angevine, given=Wayne. A., g.-i., Brown, J. M., Pagowski, M., and Su˘ selj, K.: A Description of the MYNN-EDMF Scheme and the Coupling to Other Components in WRF–ARW, https://doi.org/10.25923/n9wm-be49, 2019.

Park, C., Gerbig, C., Newman, S., Ahmadov, R., Feng, S., Gurney, K. R., Carmichael, G. R., Park, S.-Y., Lee, H.-W., Goulden, M., Stutz, J., Peischl, J., and Ryerson, T.: CO2 Transport, Variability, and Budget over the Southern California Air Basin Using the High-Resolution WRF-VPRM Model during the CalNex 2010 Campaign, Journal of Applied Meteorology and Climatology, 57, 1337–1352, https://doi.org/10.1175/JAMC-D-17-0358.1, 2018.

Park, C., Park, S.-Y., Gurney, K. R., Gerbig, C., DiGangi, J. P., Choi, Y., and Lee, H. W.: Numerical Simulation of Atmospheric CO2 Concentration and Flux over the Korean Peninsula Using WRF-VPRM Model during Korus-AQ 2016 Campaign, PLOS ONE, 15, e0228 106, https://doi.org/10.1371/journal.pone.0228106, 2020.

Parker, R. J., Wilson, C., Bloom, A. A., Comyn-Platt, E., Hayman, G., McNorton, J., Boesch, H., and Chipperfield, M. P.: Exploring Constraints on a Wetland Methane Emission Ensemble (WetCHARTs) Using GOSAT Observations, Biogeosciences, 17, 5669–5691, https://doi.org/10.5194/bg-17-5669-2020, 2020.

Pillai, D., Gerbig, C., Ahmadov, R., Rödenbeck, C., Kretschmer, R., Koch, T., Thompson, R., Neininger, B., and Lavrié, J. V.: High-resolution simulations of atmospheric CO₂ over complex terrain – representing the Ochsenkopf mountain tall tower, Atmospheric Chemistry and Physics, 11, 7445–7464, https://doi.org/10.5194/acp-11-7445-2011, 2011.

Pisso, I., Sollum, E., Grythe, H., Kristiansen, N. I., Cassiani, M., Eckhardt, S., Arnold, D., Morton, D., Thompson, R. L., Groot Zwaaftink, C. D., Evangeliou, N., Sodemann, H., Haimberger, L., Henne, S., Brunner, D., Burkhart, J. F., Fouilloux, A., Brioude, J., Philipp, A., Seibert, P., and Stohl, A.: The Lagrangian Particle Dispersion Model FLEXPART Version 10.4, Geoscientific Model Development, 12, 4955–4997, https://doi.org/10.5194/gmd-12-4955-2019, 2019.

Ramonet, M., Langerock, B., Warneke, T., and Eskes, H.: Validation Report of the CAMS Greenhouse Gas Global Reanalysis, Years 2003-2020, Tech. rep., KNMI, https://doi.org/10.24380/438C-4597, 2021.

Rodgers, C. D. and Connor, B. J.: Intercomparison of Remote Sounding Instruments, Journal of Geophysical Research: Atmospheres, 108, n/a–n/a, https://doi.org/10.1029/2002JD002299, 2003.

Saha, S., Moorthi, S., Wu, X., Wang, J., Nadiga, S., Tripp, P., Behringer, D., Hou, Y.-T., Chuang, H.-y., Iredell, M., Ek, M., Meng, J., Yang, R., Mendez, M. P., van den Dool, H., Zhang, Q., Wang, W., Chen, M., and Becker, E.: The NCEP Climate Forecast System Version 2, https://doi.org/10.1175/JCLI-D-12-00823.1, 2014.

https://doi.org/10.5194/egusphere-2024-3228
Preprint. Discussion started: 29 October 2024

Saunois, M., Stavert, A. R., Poulter, B., Bousquet, P., Canadell, J. G., Jackson, R. B., Raymond, P. A., Dlugokencky, E. J., Houweling, S., Patra, P. K., Ciais, P., Arora, V. K., Bastviken, D., Bergamaschi, P., Blake, D. R., Brailsford, G., Bruhwiler, L., Carlson, K. M., Carrol, M., Castaldi, S., Chandra, N., Crevoisier, C., Crill, P. M., Covey, K., Curry, C. L., Etiope, G., Frankenberg, C., Gedney, N., Hegglin, M. I., Höglund-Isaksson, L., Hugelius, G., Ishizawa, M., Ito, A., Janssens-Maenhout, G., Jensen, K. M., Joos, F., Kleinen, T., Krummel, P. B., Langenfelds, R. L., Laruelle, G. G., Liu, L., Machida, T., Maksyutov, S., McDonald, K. C., McNorton, J., Miller, P. A., Melton, J. R., Morino, I., Müller, J., Murguia-Flores, F., Naik, V., Niwa, Y., Noce, S., O'Doherty, S., Parker, R. J., Peng, C., Peng, S., Peters, G. P., Prigent, C., Prinn, R., Ramonet, M., Regnier, P., Riley, W. J., Rosentreter, J. A., Segers, A., Simpson, I. J., Shi, H., Smith, S. J., Steele, L. P., Thornton, B. F., Tian, H., Tohjima, Y., Tubiello, F. N., Tsuruta, A., Viovy, N., Voulgarakis, A., Weber, T. S., van Weele, M., van der Werf, G. R., Weiss, R. F., Worthy, D., Wunch, D., Yin, Y., Yoshida, Y., Zhang, W., Zhang, Z., Zhao, Y., Zheng, B., Zhu, Q., Zhu, Q., and Zhuang, Q.: The Global Methane Budget 2000–2017, Earth System Science Data, 12, 1561–1623, https://doi.org/10.5194/essd-12-1561-2020, 2020.

Schulzweida, U.: Climate Data Operators (CDO) User Guide, 10.5281/zenodo.10020800, 2020.

Sha, M. K., Langerock, B., Blavier, J.-F. L., Blumenstock, T., Borsdorff, T., Buschmann, M., Dehn, A., De Mazière, M., Deutscher, N. M., Feist, D. G., García, O. E., Griffith, D. W. T., Grutter, M., Hannigan, J. W., Hase, F., Heikkinen, P., Hermans, C., Iraci, L. T., Jeseck, P., Jones, N., Kivi, R., Kumps, N., Landgraf, J., Lorente, A., Mahieu, E., Makarova, M. V., Mellqvist, J., Metzger, J.-M., Morino, I., Nagahama, T., Notholt, J., Ohyama, H., Ortega, I., Palm, M., Petri, C., Pollard, D. F., Rettinger, M., Robinson, J., Roche, S., Roehl, C. M., Röhling, A. N., Rousogenous, C., Schneider, M., Shiomi, K., Smale, D., Stremme, W., Strong, K., Sussmann, R., Té, Y., Uchino, O., Velazco, V. A., Vigouroux, C., Vrekoussis, M., Wang, P., Warneke, T., Wizenberg, T., Wunch, D., Yamanouchi, S., Yang, Y., and Zhou, M.: Validation of methane and carbon monoxide from Sentinel-5 Precursor using TCCON and NDACC-IRWG stations, Atmospheric Measurement Techniques, 14, 6249–6304, https://doi.org/10.5194/amt-14-6249-2021, publisher: Copernicus GmbH, 2021.

Skamarock, C., Klemp, B., Dudhia, J., Gill, O., Liu, Z., Berner, J., Wang, W., Powers, G., Duda, G., Barker, D., and Huang, X.-y.: A Description of the Advanced Research WRF Model Version 4.1, Tech. rep., National Center for Atmospheric Research, https://doi.org/10.5065/1dfh-6p97, 2019.

Soulie, A., Granier, C., Darras, S., Zilbermann, N., Doumbia, T., Guevara, M., Jalkanen, J.-P., Keita, S., Liousse, C., Crippa, M., Guizzardi, D., Hoesly, R., and Smith, S.: Global Anthropogenic Emissions (CAMS-GLOB-ANT) for the Copernicus Atmosphere Monitoring Service Simulations of Air Quality Forecasts and Reanalyses, Earth System Science Data Discussions, pp. 1–45, https://doi.org/10.5194/essd-2023-306, 2023.

Tian, Y., Hong, X., Shan, C., Sun, Y., Wang, W., Zhou, M., Wang, P., Lin, P., and Liu, C.: Investigating the Performance of Carbon Monoxide and Methane Observations from Sentinel-5 Precursor in China, Remote Sensing, 14, 6045, https://doi.org/10.3390/rs14236045, 2022.

Wang, R., Tao, S., Ciais, P., Shen, H. Z., Huang, Y., Chen, H., Shen, G. F., Wang, B., Li, W., Zhang, Y. Y., Lu, Y., Zhu, D., Chen, Y. C., Liu, X. P., Wang, W. T., Wang, X. L., Liu, W. X., Li, B. G., and Piao, S. L.: High-Resolution Mapping of Combustion Processes and Implications for CO_2 Emissions, Atmospheric Chemistry and Physics, 13, 5189–5203, https://doi.org/10.5194/acp-13-5189-2013, 2013.

Wiedinmyer, C., Akagi, S. K., Yokelson, R. J., Emmons, L. K., Al-Saadi, J. A., Orlando, J. J., and Soja, A. J.: The Fire INventory from NCAR (FINN): A High Resolution Global Model to Estimate the Emissions from Open Burning, Geosci. Model Dev., https://doi.org/10.5194/gmd-4-625-2011, 2011.

Worden, J. R., Cusworth, D. H., Qu, Z., Yin, Y., Zhang, Y., Bloom, A. A., Ma, S., Byrne, B. K., Scarpelli, T., Maasakkers, J. D., Crisp, D., Duren, R., and Jacob, D. J.: The 2019 Methane Budget and Uncertainties at 1° Resolution and Each Country through Bayesian

https://doi.org/10.5194/egusphere-2024-3228
Preprint. Discussion started: 29 October 2024

Integration Of GOSAT Total Column Methane Data and a Priori Inventory Estimates, Atmospheric Chemistry and Physics, 22, 6811–6841, https://doi.org/10.5194/acp-22-6811-2022, 2022.

Wunch, D., Toon, G. C., Blavier, J.-F. c. L., Washenfelder, R. A., Notholt, J., Connor, B. J., Griffith, D. W. T., Sherlock, V., and Wennberg, P. O.: The Total Carbon Column Observing Network, Philosophical Transactions of the Royal Society A: Mathematical, Physical and Engineering Sciences, 369, 2087–2112, https://doi.org/10.1098/rsta.2010.0240, 2011.

Yang, Y., Zhou, M., Langerock, B., Sha, M. K., Hermans, C., Wang, T., Ji, D., Vigouroux, C., Kumps, N., Wang, G., De Mazière, M., and Wang, P.: New Ground-Based Fourier-transform near-Infrared Solar Absorption Measurements of XCO_2, XCH_4 and XCO at Xianghe, China, Earth System Science Data, 12, 1679–1696, https://doi.org/10.5194/essd-12-1679-2020, 2020.

Yang, Y., Zhou, M., Wang, T., Yao, B., Han, P., Ji, D., Zhou, W., Sun, Y., Wang, G., and Wang, P.: Spatial and Temporal Variations of CO_2 Mole Fractions Observed at Beijing, Xianghe, and Xinglong in North China, Atmospheric Chemistry and Physics, 21, 11 741–11 757, https://doi.org/10.5194/acp-21-11741-2021, 2021.

Zhao, X., Marshall, J., Hachinger, S., Gerbig, C., Frey, M., Hase, F., and Chen, J.: Analysis of Total Column CO_2 and CH_4 Measurements in Berlin with WRF-GHG, Atmospheric Chemistry and Physics, 19, 11 279–11 302, https://doi.org/10.5194/acp-19-11279-2019, 2019.

Zhao, Y., Nielsen, C. P., and McElroy, M. B.: China's CO2 Emissions Estimated from the Bottom up: Recent Trends, Spatial Distributions, and Quantification of Uncertainties, Atmospheric Environment, 59, 214–223, https://doi.org/10.1016/j.atmosenv.2012.05.027, 2012.

Zhong, Q., Huang, Y., Shen, H., Chen, Y., Chen, H., Huang, T., Zeng, E. Y., and Tao, S.: Global Estimates of Carbon Monoxide Emissions from 1960 to 2013, Environmental Science and Pollution Research, 24, 864–873, https://doi.org/10.1007/s11356-016-7896-2, 2017.

Zhou, M., Wang, P., Kumps, N., Hermans, C., and Nan, W.: TCCON Data from Xianghe, China, Release GGG2020.R0 (Version R0), https://doi.org/10.14291/tccon.ggg2020.xianghe01.R0, 2022.

5.2 Analysis of CO_2 and CO time series

Building on the CH_4 analysis presented in the previous section, this part focuses on both in situ and column observations of CO_2 and CO at Xianghe. Likewise, the goal is to better understand the causes of the observed temporal variability and to evaluate the model's ability to simulate these time series in northern China.
Initial insights into the observed CO_2 time series at Xianghe were provided by Yang et al. (2020, 2021). They found that the seasonal cycle of CO_2 at Xianghe aligns with patterns observed at other sites of similar latitude, showing higher concentrations in winter and lower levels in summer. This variation is driven by increased fossil fuel use from traffic and heating systems during winter and enhanced biospheric uptake in summer due to photosynthesis. Additionally, as mentioned in the CH_4 section, they observed a strong correlation between the column observations of CO_2, CH_4, and CO, which is influenced by pollution transport from the south and cleaner air masses from the north.
WRF-GHG has proven to be a valuable tool for studying CO_2 fluxes and variability in China, as demonstrated by previous studies (Dayalu et al., 2018; Liu et al., 2018; Li et al., 2020; Dong et al., 2021).
This section utilizes the same model simulations and methods described earlier, so they will not be repeated here.

The following aspects will be discussed: the model's performance in simulating the observed time series (Sect. 5.2.1), the monthly mean contributions of different source sectors (Sect. 5.2.2), the possible causes of the observed XCO_2 model bias (Sect. 5.2.3), and the impact of meteorological processes on the temporal variability of observed concentrations (Sect. 5.2.4). A summary of the conclusions for CO_2 and CO is provided in Sect. 5.2.5.

5.2.1 Model performance

Figure 5.1 provides an overview of the simulated and observed time series of CO_2 and CO concentrations at Xianghe, along with their respective differences.
Overall, WRF-GHG demonstrates a reasonable accuracy in replicating these measurements: the XCO_2 observations are slightly underestimated, with a mean bias error of -1.43 ppm (as detailed in Table 5.1), while the XCO simulations show a very minor overestimation, with a mean bias error of 0.42 ppb. As with CH_4 in Sect. 5.1, the data near the surface has been divided into afternoon (13:00 - 18:00 LT) and nighttime (03:00 - 08:00 LT) periods to evaluate model performance, as these time frames often yield different results. Indeed, WRF-GHG shows a smaller bias (-2.14 ppm) during the afternoon, when the lower atmosphere is well-mixed, compared to nighttime (6.02 ppm). Additionally, the mean bias error differs in sign between the two periods: in situ CO_2 levels tend to be underestimated in the afternoon but overestimated at night. This result will be further discussed in Section 5.2.4. Except for the moderate correlation observed for in situ CO_2 during nighttime (0.58), WRF-GHG achieves relatively high correlation coefficients (≥ 0.68) for other CO_2 and CO data, indicating satisfactory model performance.

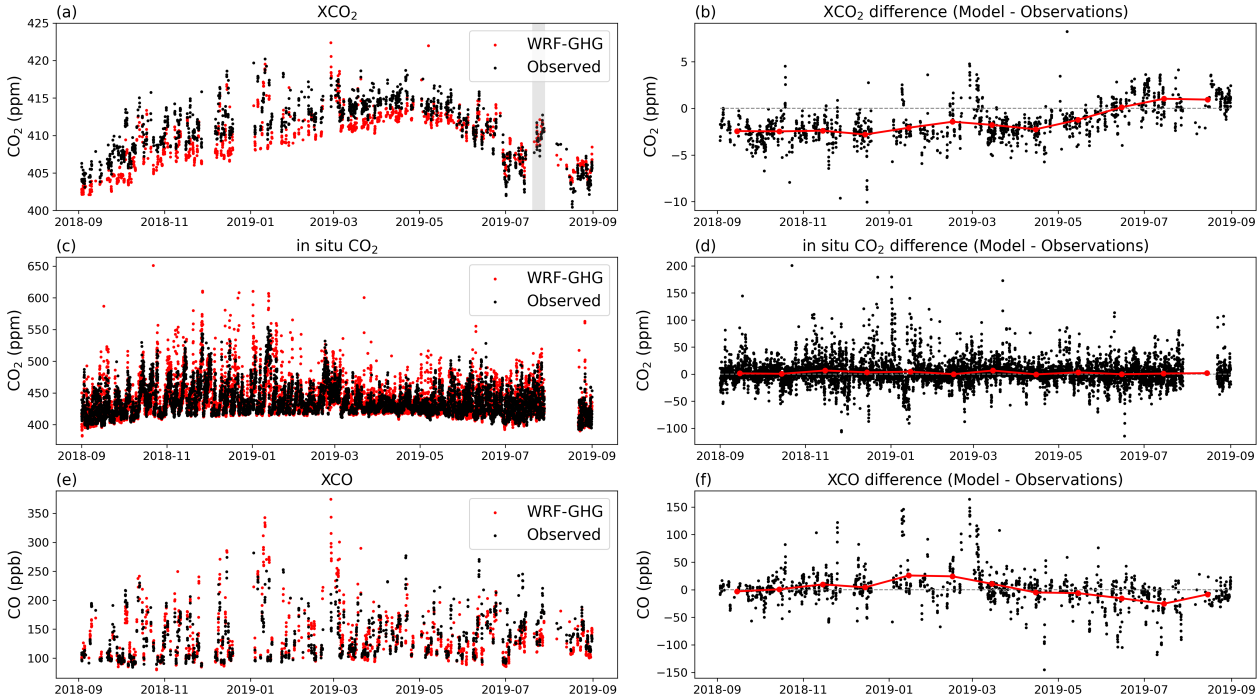

Figure 5.1: Time series of the observed (black) and simulated (red) (a) XCO_2, (c) insitu CO_2 and (e) XCO concentrations at the Xianghe site. Panels (b), (d) and (f) show the differences between WRF-GHG simulations and observations for XCO_2, in situ CO_2 and XCO, respectively. Data points are hourly. The red data points in (b), (d) and (f) represent the monthly mean differences.

	insitu CO_2 (afternoon)	insitu CO_2 (night)	XCO_2	XCO
BIAS	-2.14	6.02	-1.43	0.42
RMSE	14.50	24.93	2.45	31.85
CORR	0.75	0.58	0.70	0.69

Table 5.1: Statistics of the model-data comparison of the ground-based CO_2 and CO observations at the Xianghe site from 1 September 2018 until 1 September 2019. We present the mean bias error (BIAS), root mean square error (RMSE) and Pearson correlation coefficient (CORR). Note that the XCO_2 time series was de-trended before calculating the correlation coefficient in order to remove the effect of the seasonal variation. The mean bias error and root mean square error are given in ppm for CO_2 and in ppb for CO. For in situ observations, the data is split in afternoon (13-18 LT) and night (3-8 LT) hours.

Looking at the time series of XCO_2 in Fig. 5.1a and b, a few aspects stand out. Firstly, a clear model underestimation is observed between September 2018 and May 2019, after which the bias diminishes. Secondly, from May onward, XCO_2 concentrations generally decline, which is associated with the northern hemisphere's growing season and enhanced photosynthesis. However, a significant spike in XCO_2 levels occurs between 20-29 July, highlighted in gray in Fig. 5.1a. A more detailed analysis of this summer spike will be provided in Sect.5.2.4,

while the bias between September 2018 and May 2019 will be discussed in Sect. 5.2.3.

5.2.2 Sector contributions

WRF-GHG tracks all fluxes in separate tracers, enabling the decomposition of total simulated concentrations into contributions from different source sectors. This subsection will assess each sector's influence on the CO_2 and CO observations at Xianghe. Figure 5.2 shows the monthly mean values, while additionally the median and interquartile ranges are presented in Table 5.2 for CO_2 and Table 5.3 for CO.

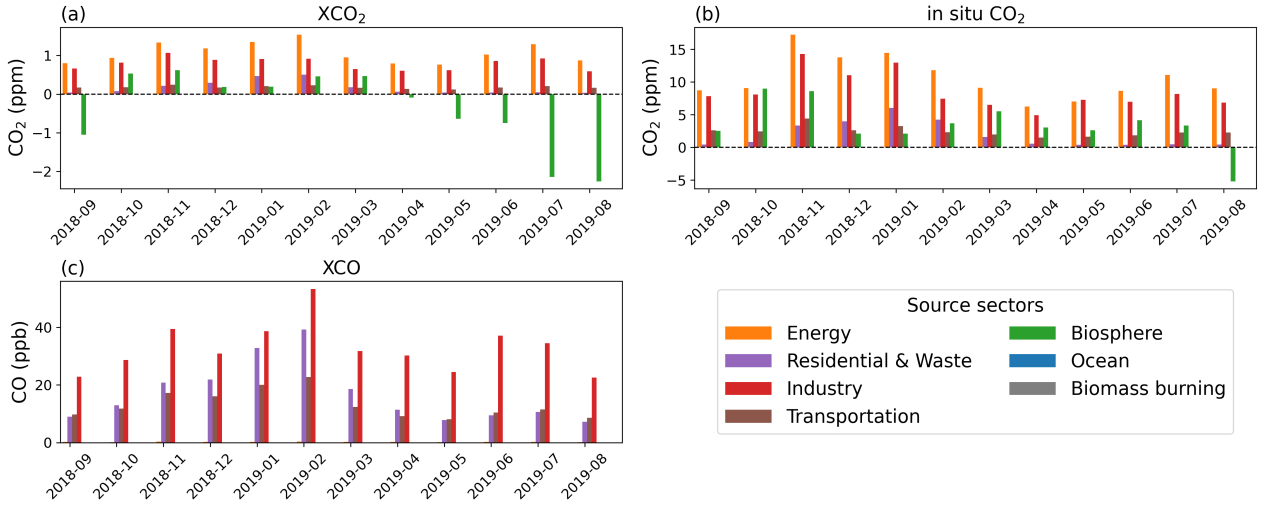

Figure 5.2: Monthly mean tracer contributions above the background for (a) XCO_2, (b) in situ CO_2 and (c) XCO simulated concentrations at Xianghe.

CO_2

The main sectors contributing to the modeled CO_2 variability at Xianghe are energy, industry, and the biosphere (Fig. 5.2a,b). For XCO_2, we find median values of 0.85 ppm and 0.63 ppm for the energy and industry sectors, respectively. Furthermore, the biosphere significantly influences the column-averaged CO_2 values, where it acts as a sink from April to September with a median value of -0.77 ppm during this period. During the rest of the year, the biogenic tracer acts as a small source (median value of 0.22 ppm).
Near the surface, median enhancements of in situ CO_2 concentrations are 6.85 ppm and 5.69 ppm for the energy and industry sectors, respectively. The biosphere generally acts as a minor source throughout the year, with a median contribution of 2.69 ppm, except in August, when it becomes a significant sink of -6.76 ppm.
The difference between the biosphere functioning as a sink in the column measurements for five months, but not in the in situ concentrations (except in August), might result from Xianghe's location relative to strong land sinks (e.g., forests) and the different sensitivities of the measurement techniques. In situ observations are typically less sensitive to distant sources and sinks compared to FTIR observations. VPRM-computed fluxes suggest that the

	XCO_2 (ppm)				in situ CO_2 (ppm)			
	Q1	median	mean	Q3	Q1	median	mean	Q3
Total	408.06	411.19	410.84	413.55	418.81	430.45	437.33	449.31
Background	407.09	409.20	409.01	411.37	396.59	411.52	410.55	413.79
Biomass burning	0.00	0.00	0.00	0.00	0.00	0.00	0.00	0.00
Energy	0.36	0.85	1.07	1.53	2.74	6.85	10.51	14.06
Residential	0.03	0.06	0.17	0.17	0.30	0.65	1.88	1.95
Industry	0.24	0.63	0.79	1.14	2.70	5.69	8.53	10.51
Transportation	0.08	0.16	0.18	0.25	0.81	1.73	2.43	3.19
Biosphere	-0.77	0.04	-0.38	0.31	-0.01	2.36	3.44	7.39
Ocean	-0.00	-0.00	-0.00	-0.00	-0.01	-0.00	-0.01	-0.00
Total tracers	0.33	1.23	1.82	2.80	7.36	18.99	26.78	38.30

Table 5.2: Statistics of the total simulated CO_2 concentrations and the different tracer contributions over the complete simulation period. Q1 and Q3 represent the first and third quartile, respectively, between which 50 % of the data fall.

local biosphere near Xianghe (cropland) acts primarily as a net source, except in August, while the forested mountains approximately 50 km north and 90 km east of the site serve as a strong sink (see Fig. 5.3).
Next to the biosphere, industry, and energy, also transportation and residential sources have a small but discernible influence on the Xianghe data. During winter, the contribution of residential sources increases, where the highest values for the column simulations are found in February (median of 0.45 ppm) while near the surface this occurs in January (4.28 ppm). This peak aligns with heightened residential emissions in winter, driven by increased heating demands correlated with air temperature (Guevara et al., 2021). Finally, no relevant impact was found from biomass burning and the ocean. Overall, the total tracer enhancement for the in situ concentrations is approximately ten times greater than that of the column-averaged values.

CO

Based on our model simulations, the CO column time series is primarily influenced by sources from the industry, residential and transportation sectors (see Fig. 5.2c). With a median value of 25.23 ppb, the industry sector is the largest contributor to XCO, followed by the residential and transportation sectors with values of 10.64 ppb and 10.54 ppb, respectively (see Table 5.3). Both residential and transportation tracers show larger values in winter, peaking in February with monthly median values of 33.03 ppb and 19.87 ppb, respectively. This increase is in agreement with higher emissions in that period of the year due to colder air temperatures (Guevara et al., 2021). Finally, energy sources and biomass burning are not important for the observations at Xianghe (< 1 ppb).
Note that due to CO's much shorter lifetime (a few weeks) compared to CO_2, the contribution of fluxes within the model domain constitutes a significantly larger portion of the total

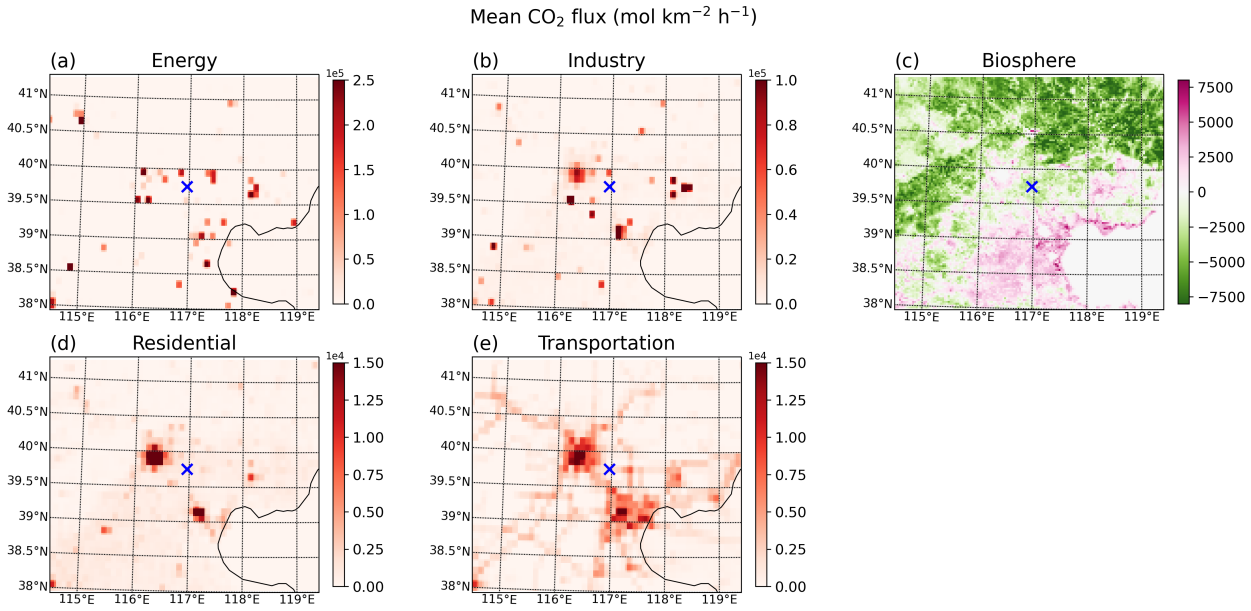

Figure 5.3: Map of the mean CO_2 flux (mol km^{-2} h^{-1}) in WRF-GHG domain d03 during the entire simulation period from September 2018 until September 2019, for the most important sectors. Remark that the panels have different color scales. The location of the Xianghe site is indicated by a blue cross.

	XCO (ppb)			
	Q1	median	mean	Q3
Total	119.10	146.07	161.67	184.85
Background	89.60	96.27	98.91	103.17
Biomass burning	0.00	0.00	0.00	0.00
Energy	0.09	0.21	0.26	0.37
Residential	4.75	10.64	16.68	20.45
Industry	11.83	25.23	32.72	45.39
Transportation	5.57	10.54	13.09	17.48
Total tracers	24.00	48.70	62.76	83.63

Table 5.3: Same as Table 5.2 but for XCO.

simulated column concentration for CO than for CO_2: on average 38.82% for XCO compared to just 0.44% for XCO_2.

5.2.3 XCO_2 bias

In Section 5.2.1, we observed that WRF-GHG underestimates XCO_2 by approximately 2 ppm until May 2019, after which the negative bias diminishes. This bias likely originates from a similar error in the background data, inaccuracies in representing the actual sources and sinks in the region, or a combination of both. Given that the background contributes

significantly to the total simulated XCO_2 concentration (see Table 5.2), it is probable that the bias originates from this source.

The CAMS validation report (Ramonet et al., 2021) presents "a very good agreement for all (TCCON) sites", suggesting that the CAMS reanalysis that is driving the WRF-GHG simulations is of good quality without known biases. However, their criteria for what constitutes "very good" appears to be relatively mild (within ±2 ppm). Moreover, the Xianghe site wasn't included in this report and the accompanying figure does not provide very detailed information. Therefore, we reproduced their analysis for several TCCON sites at similar latitudes for the period of our interest (September 2018 - September 2019): Karlsruhe (49.1° N), Orleans (48.0° N), Garmisch (47.5° N), Park Falls (45.9° N), Rikubetsu (43.5° N), Lamont (36.6° N), Tsukuba (36.0° N), Edwards (35.0° N), Pasadena (34.1° N), Saga (33.2° N), and Hefei (31.9° N). The results of this analysis are presented in Fig. 5.4.
We find an underestimation of the CAMS reanalysis XCO_2 at all TCCON sites between 30 - 50° N (except Pasadena) from October 2018 until May 2019. More specifically for Xianghe, monthly mean errors range from -2.20 (± 1.3) ppm in January 2019 to 3.38 (± 1.28) ppm in July 2019, which is of a similar order as the bias found with WRF-GHG (where the monthly mean differences with respect to the TCCON site of Xianghe range from -2.53 ± 1.7 ppm in December 2018 to 1.28 ± 1.57 ppm in July 2019).
Therefore, we assume that the error pattern detected in the XCO_2 time series is primarily the result of the same pattern in the background information. Moreover, this bias pattern is not found in the in situ CO_2 time series (Fig. 3b), likely because the mean tracer contribution to the in situ concentrations is larger than the size of this background bias (see Table 5.2).

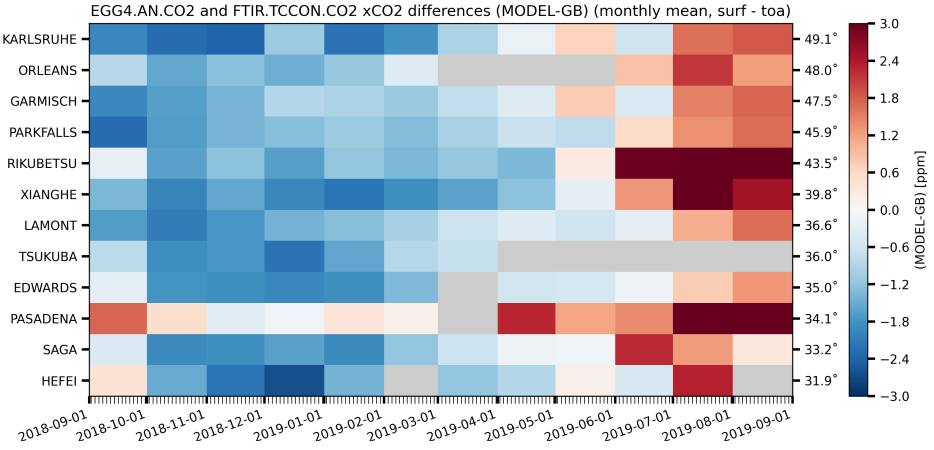

Figure 5.4: Monthly mean difference (in ppm) between CAMS reanalysis model and TCCON XCO_2 between 30 - 50° N over the simulation period of this study.

5.2.4 Impact of meteorology

Similarly as for CH_4 in Sect. 5.1, we additionally want to discuss the meteorological factors that influence the temporal variability of the time series by focusing on the impact of large-

scale phenomena, the planetary boundary layer and local winds.

Synoptic scale winds

For CH_4, we found that synoptic weather conditions significantly influence the temporal variability of the observations: higher XCH_4 values are associated with winds from the southwest (bringing polluted air from the North China Plain), while lower XCH_4 concentrations correspond with winds from the northwest (see Sect. 5.1). This finding aligns with the results of Yang et al. (2020), who demonstrated that the day-to-day variability of XCH_4, and simultaneously XCO_2 and XCO, is closely linked to wind direction.
Consistent with this, we observe significant differences in XCO_2 and XCO concentrations depending on the 800 hPa wind direction, as shown in Fig. 5.5. The median XCO_2 (XCO) enhancement during polluted days is 2.35 ppm (79.50 ppb), compared to 0.42 ppm (18.53 ppb) on clean days. This indicates that air masses from the southwest transport polluted air from the North China Plain to the Xianghe site, and that this transport is reflected in the column concentrations of all three species: CH_4, CO_2 and CO. Conversely, when winds shift to the northwest, a decrease in column concentrations is observed across all species.

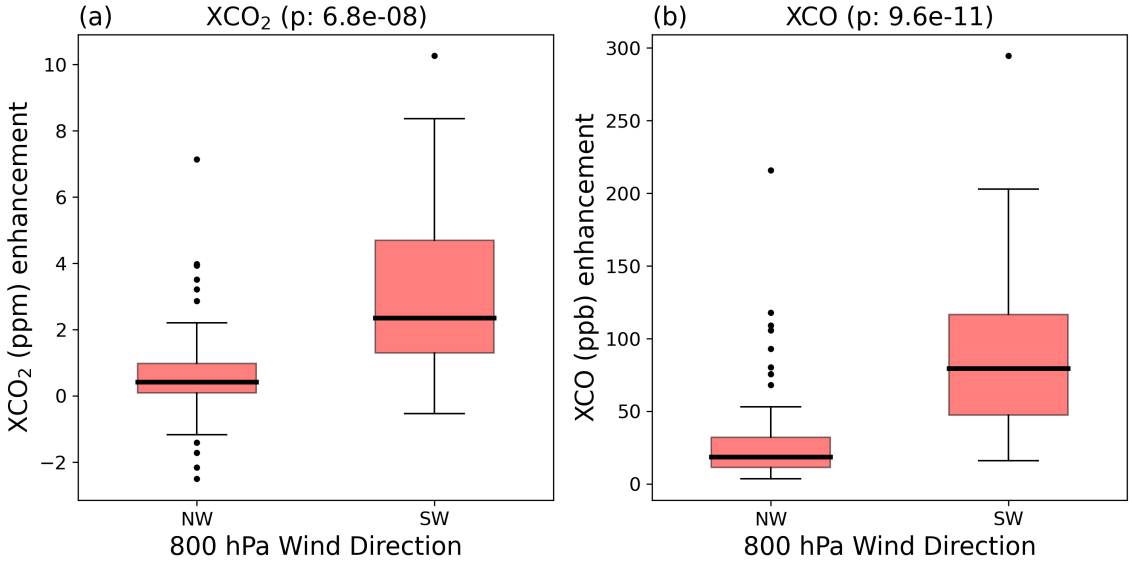

Figure 5.5: The distribution of the daily mean simulated column tracers above the background per 800 hPa wind direction category and species. NW is for winds with an angle of 292.5 to 337.5 ° from north, while SW represents the angles between 202.5 and 247.5°. There are 72 days with NW winds and 33 days with SW winds. The colored boxes indicate the range between the first and third quartile, while the thick solid line is the median. Outliers (values that are 1.5 times the interquartile range above (below) the third (first) quartile) are shown by black dots.

Additionally, we find a strong correlation of 0.79 between daily mean CO_2 enhancements at the surface and in the columns, similar to the correlation observed for CH_4. This indicates

that the variability in in situ concentrations is also influenced by the clean or polluted nature of the air masses.

Finally, as observed for CH_4, the month-to-month variability in the tracer contributions for CO_2 and CO is more pronounced than the variability in their emissions. For example, the monthly mean CO_2 energy emissions over the entire model domain have a coefficient of variation (CV) of 6.93%, while the corresponding tracer fields exhibit a CV of 20.12% in the columns and 32.61% near the surface. Similarly, for CO, while the CV of monthly industry emissions is just 2.95%, the column tracer contributions show a much larger variability, with a CV of 29.6%. It is worth noting that both CO_2 and CO show similar monthly variability, with higher contributions in February and lower in May, which is very likely influenced by shifts in meteorological conditions.
Among the observed variability, the previously highlighted episode of elevated XCO_2 concentrations stands out (see Sect. 5.2.1), and is possibly linked to synoptic weather conditions. The next section delves deeper into this period, aiming to uncover the mechanisms driving this summertime increase.

Focus on a specific event in July 2019

A notable spike in XCO_2 levels is observed between 20-29 July (see Fig. 5.1a), diverging from the typical decreasing trend of XCO_2 from May to September, which is linked to the northern hemisphere's growing season and increased photosynthesis. We will focus on the model simulations between 7 July 2019 and 30 August 2019 to explain the causes of this XCO_2 summer spike, as WRF-GHG correlates well with the observations during this period (correlation coefficient of 0.84).

The total simulated XCO_2 increases from 407.43 ($\pm$ 1.19) ppm before to 410.76 ($\pm$ 1.19) ppm during the summer spike (20-29 July), and then decreases to 405.75 ($\pm$ 0.98) ppm after, as shown in Fig. 5.6a. This sudden increase of more than 3 ppm is significant and warrants further investigation. Figure 5.6 shows the simulated background and tracer contributions during this period. Figure 5.6a shows that the background XCO_2 remains relatively constant in July (408.69 $\pm$ 0.78 ppm), and decreases to 406.67 $\pm$ 0.73 ppm in August. It further clearly indicates an enhancement of the tracers from below the background before and after the summer spike to above the background during the spike period. Looking at the different tracers in Fig. 5.6b, we see that it is mainly the biogenic tracer that has a different behavior in the spike period compared to the periods before and after. Thus, the increase in XCO_2 between 20-29 July is mainly linked to a less strong biogenic sink (-0.33 $\pm$ 0.57 ppm) compared to the periods before (-2.88 $\pm$ 0.71 ppm) and after (-1.76 $\pm$ 1.11 ppm).

Further analysis reveals that during the spike, a heatwave with surface temperatures up to 39°C occurred, together with 800 hPa winds predominantly from the west (see Fig. 5.6a and c). The biogenic tracer also shows increased values across a large vertical extent in the troposphere (Fig. 5.6c), indicating advection from other regions. Synoptic maps (not shown) suggest eastward advection of a warm air mass with high biogenic CO_2 levels, originating

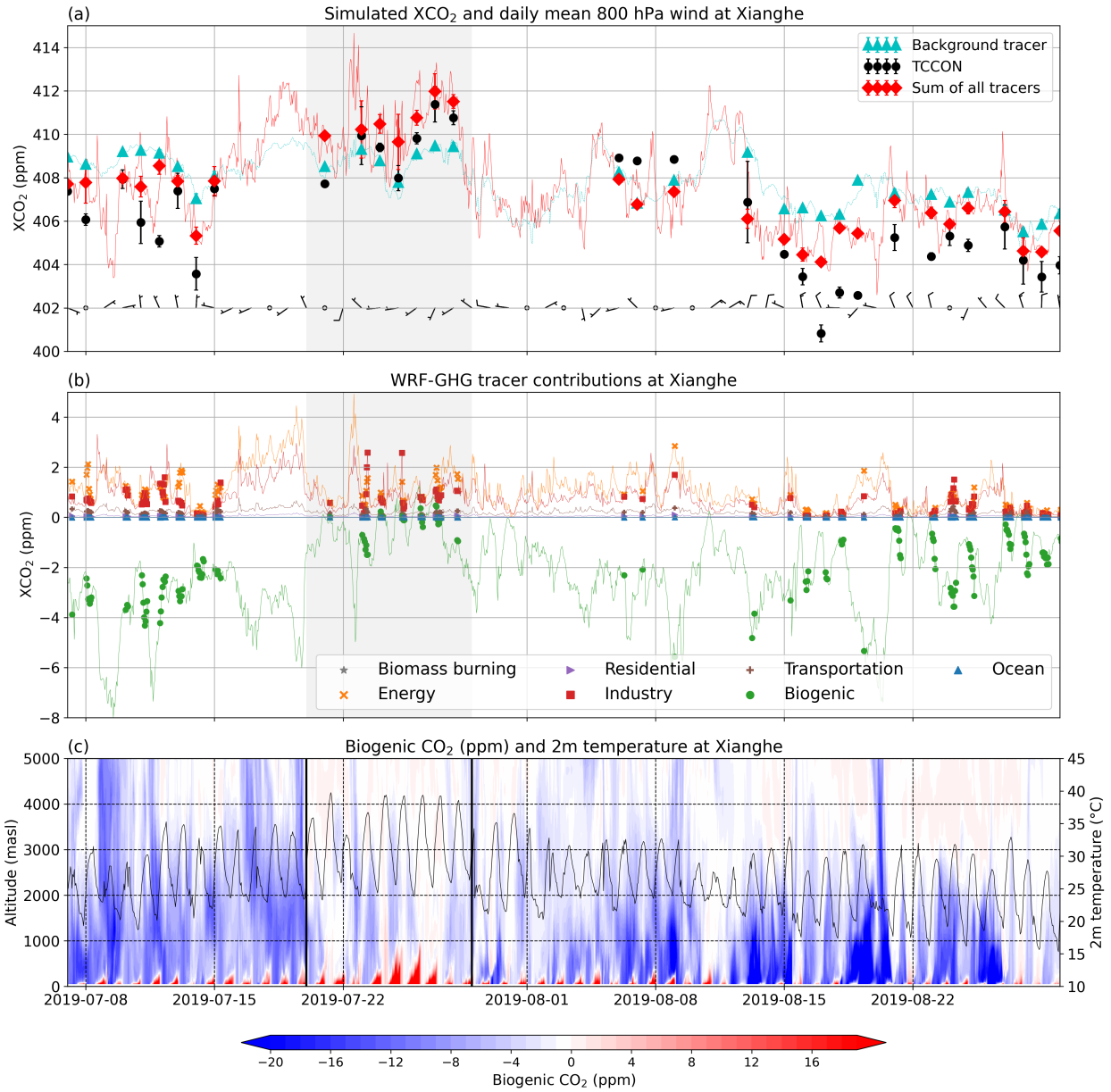

Figure 5.6: Simulated time series of XCO_2 at Xianghe from 7 July 2019 to 30 August 2019, with the spike period highlighted in all panels. Daily mean (a) background tracer (cyan triangles) and total tracers (red diamonds) from WRF-GHG at Xianghe, and TCCON values (black dots). Error bars represent the standard deviation of the daily mean. Daily mean 800 hPa wind direction is indicated by wind barbs at the bottom. (b) Time series of different tracer contributions at Xianghe ,with hourly values shown as thin lines and points for TCCON observation times. (c) Color coded vertical profiles of the biogenic CO_2 contributions (left y-axis) shown in red and blue, and surface temperature (right y-axis) in black.

from the Gobi Desert and grasslands in Inner Mongolia, both areas that are characterized

by sparse vegetation and elevated temperatures.
Additionally, the mean biogenic CO_2 flux around Xianghe, as calculated by VPRM, is slightly higher between 20 and 29 July (average of -5 941 mol km^{-2} h^{-1} over domain d03) compared to the periods before and after (respectively -9 153 and -12 785 mol km^{-2} h^{-1}). In VPRM, the respiration component is linearly dependent on surface temperature, and the gross ecosystem exchange also has a temperature dependency representing the temperature sensitivity of photosynthesis, with CO_2 uptake decreasing at temperatures higher than optimal (Mahadevan et al., 2008). Indeed, it has been shown that extreme temperatures impact CO_2 fluxes (Xu et al., 2020; Ramonet et al., 2020; Gupta et al., 2021).
Therefore, we conclude that the spike was caused by an atmospheric circulation anomaly resulting in the advection of a warm air mass with high biogenic CO_2 levels, along with a locally reduced ecosystem exchange due to the resulting hot temperatures.

PBL

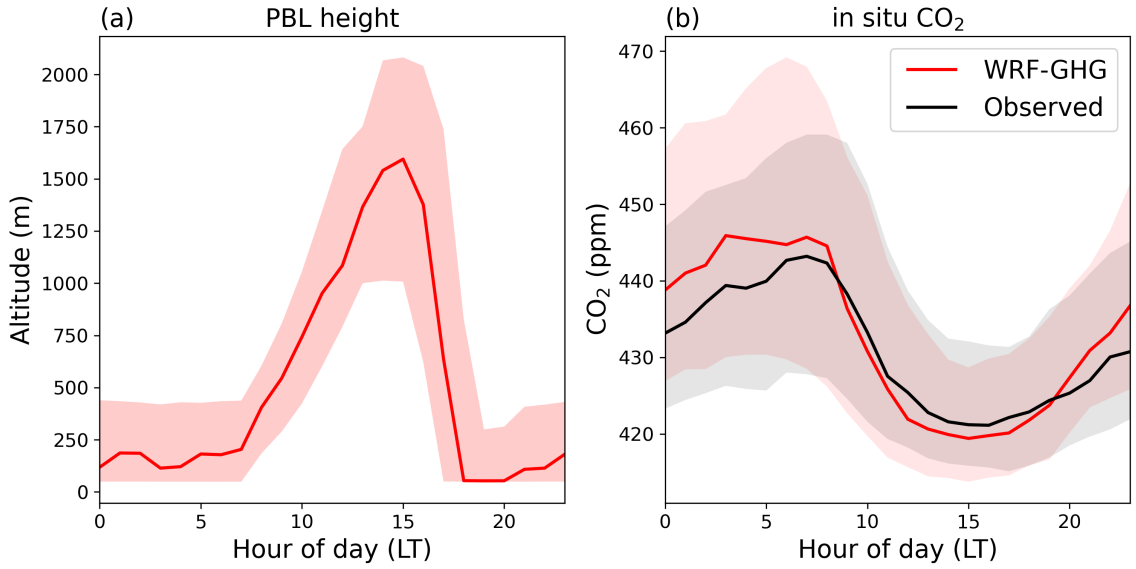

Figure 5.7: Hourly median and interquartile range of the (a) simulated planetary boundary layer height, and observed and simulated surface (b) CO_2 concentration at Xianghe.

The planetary boundary layer (PBL) plays a crucial role in regulating near-surface CO_2 concentrations. Figure 5.7 displays the diurnal variation of the PBL height as simulated by WRF-GHG, along with the corresponding CO_2 concentrations near the surface (both simulated and observed).
During the day, the PBL height increases due to solar radiation and enhanced turbulent mixing, leading to lower CO_2 concentrations near the surface. As observed for CH_4, the PBL reaches its maximum height around 15:00 local time, coinciding with the lowest simulated surface CO_2 concentrations, with median (and interquartile) values of 419.41 (413.75 - 428.69) ppm. Conversely, during the night, radiative cooling leads to the formation of a stable, shallow PBL, trapping CO_2 near the surface and causing concentrations to rise. The

peak CO_2 concentrations in WRF-GHG are reached at 3:00, with values of 445.91 (430.03 - 461.75) ppm. However, unlike CH_4, the simulated CO_2 concentrations remain relatively stable between 3:00 and 8:00. As the sun rises and the PBL height begins to increase again, the CO_2 concentrations drop, giving rise to a characteristic diurnal cycle.

WRF-GHG is able to replicate this diurnal pattern in CO_2 in situ observations, but some biases are present. For instance, a slight underestimation is observed during the daytime, as the lowest observed concentrations typically occur at 16:00, with a median (and interquartile) value of 421.13 (415.62 - 431.56) ppm. A more pronounced overestimation is noted during the night, with observed concentrations peaking at 7:00 with values of 443.21 (427.81 - 459.10) ppm. This leads to an overestimation of the CO_2 diurnal amplitude in WRF-GHG by 4.42 ppm.

WRF-GHG is overestimating surface CO_2 during much of the night, a discrepancy not observed for CH_4. This suggests a potential bias in the representation of CO_2 fluxes rather than in the model dynamics.
In the special case of CO_2, its distinct diurnal cycle near the surface is actually determined by a combination of PBL dynamics and biogenic fluxes. During the day, photosynthesis in vegetation results in negative CO_2 fluxes, leading to a reduction in CO_2 concentrations near the surface. At night, however, photosynthesis ceases, and plants release CO_2 through respiration. These biogenic fluxes can therefore amplify the impact of PBL dynamics on near-surface concentrations. This correlation between PBL dynamics and biogenic CO_2 fluxes is driven by solar radiation and is commonly referred to as the atmospheric CO_2 *rectifier effect*. Therefore, incorrect biogenic CO_2 fluxes can also result in biases of the diurnal cycle.
Several uncertainties in the online calculation of biogenic CO_2 fluxes can be identified. First of all, the VPRM parameters in the current study are taken from Li et al. (2020) but were optimized for the United States. An update on these parameters for China is essential to reduce the uncertainties on the biogenic CO_2 fluxes (Li et al., 2020; Dong et al., 2021). Furthermore, the simplicity of the linear respiration model could introduce inaccuracies, as suggested by Li et al. (2020); Dong et al. (2021); Hu et al. (2021). Finally, another potential source of error may arise from the misclassification of land cover types. VPRM fluxes are calculated as a weighted average of biogenic fluxes across seven vegetation classes, combined with the fractional vegetation cover for each grid cell. This classification is based on the 1-km global land cover product SYNMAP by Jung et al. (2006), where the region surrounding the Xianghe site is categorized as 100% cropland. While this aligns with the general landscape, the omission of significant urbanization in this product, likely due to its dated nature, could lead to discrepancies. Since built-up areas in WRF-GHG result in zero biogenic fluxes, this oversight could contribute to the observed overestimation of nighttime respiration and daytime photosynthesis near Xianghe.
While errors in biogenic fluxes are a likely contributor, the overestimation of nighttime CO_2 concentrations could also originate from inaccuracies in the representation of anthropogenic emission heights, particularly given the strong influence of such sources at the site. In the WRF-GHG simulations, all emissions were released near the surface in the lowest model layer which is a simplification of reality since especially industrial and energy sources (power plants)

usually emit CO_2 at higher altitudes. As Brunner et al. (2019) demonstrated, neglecting this vertical distribution can lead to an overestimation of near-surface CO_2 concentrations.

Local winds

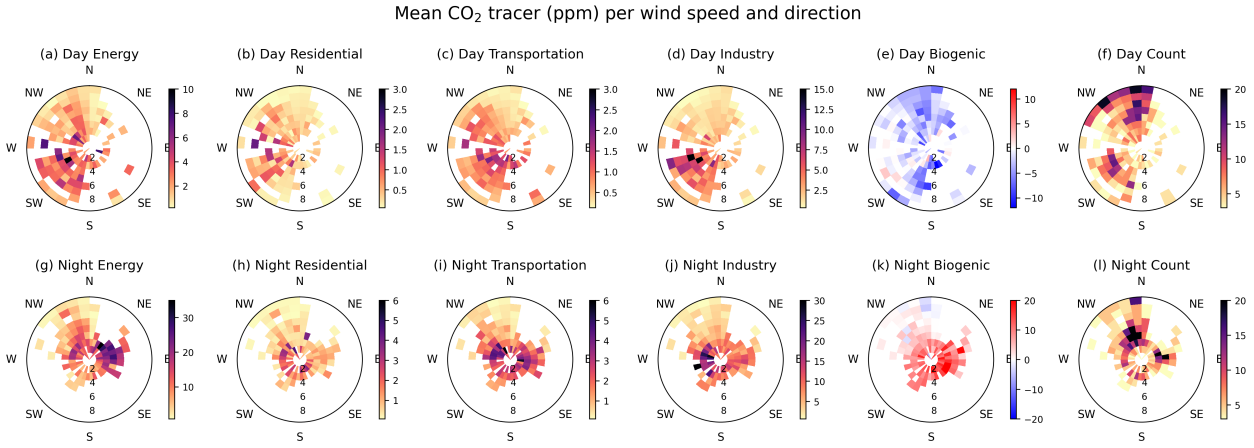

Figure 5.8: Mean CO_2 simulated tracer concentrations (indicated by color scale, in ppm) binned per wind speed and direction for the main sectors (a) energy, (b) residential, (c) transportation, (d) industry and the (f) biosphere on days without strong regional pollution. The first row represents afternoon hours (13h - 18h LT), while the second row represents nighttime hours (3h - 8h LT). Data is binned per 1 m s^{-1} and 11.25° wind direction. (f) Count of data points in each bin. Only bins with at least 3 points are included in the figure. Remark that the panels have different color scales.

To assess the impact of near-surface wind direction on in situ CO_2 concentrations at Xianghe, we analyze the correlations between the 10 m wind speed and direction and the simulated concentrations, following a similar approach as for CH_4 in Sect. 5.1. Figure 5.8 illustrates the mean WRF-GHG tracer contribution for CO_2 by wind direction and speed. To focus on this relationship specifically, we exclude polluted days based on the XCO enhancement and separate the data into afternoon and nighttime periods to minimize diurnal variability.
Afternoon winds tend to be stronger, originating from the north and southwest, while weaker nighttime winds generally come from the north and east. Given that CO_2 sources are distributed in nearly all directions around Xianghe (see Fig. 5.3), no strong correlation emerges between the 10m wind direction and in situ CO_2 concentration overall. However, for the residential sector, higher CO_2 levels are observed when winds come from the west, where Beijing is located. Similarly, elevated CO_2 concentrations are linked to industrial sources in the southwest, likely due to the influence of the strong point source around 39.55° N, 116.25° E (see Fig. 5.3). For biogenic sources, the observed pattern is as expected: negative contributions during the daytime due to photosynthesis and positive at night due to respiration. Additionally, slightly lower nighttime enhancements are observed when winds come from the north, which aligns with the more densely vegetated areas in that direction.

5.2.5 Conclusions

In the second part of this chapter, we analyzed CO_2 and CO time series from the Xianghe site, focusing on both column-averaged (XCO_2 and XCO) and in situ CO_2 observations to understand their variabilities through comparisons with WRF-GHG simulations.
The model shows good performance for CO_2, achieving correlation coefficients of 0.70 for XCO_2 and 0.75 for afternoon in situ concentrations. However, nighttime performance is weaker, with a correlation of 0.58 and a mean overestimation of 6.02 ppm. For XCO_2, a mean bias of -1.43 ppm relative to TCCON is found, primarily due to an underestimation from September 2018 to April 2019 linked to biases in the CAMS reanalysis. Accurate boundary conditions are found to be crucial for XCO_2 due to CO_2's long atmospheric lifetime, with emissions in the model domain contributing to a mean tracer enhancement of only 1.82 ppm. For near-surface CO_2, emissions within the domain play a larger role, resulting in a mean tracer enhancement of 26.78 ppm and mitigating the influence of biases in the background.

The model simulations further indicate that the industry and energy sectors are the primary contributors to CO_2 concentrations at Xianghe, with the biosphere playing a seasonal role. The biosphere acts as a sink for XCO_2 from April to September, averaging -0.77 ppm, and becomes a source of 0.22 ppm for the rest of the year. Near the surface, it acts as a sink only in August (-6.76 ppm) and a source during other months (2.69 ppm on average). These differences between column and surface measurements are likely due to the distance to strong land sinks and the varying sensitivity of each measurement method. The residential and transportation sectors contribute smaller amounts to CO_2, peaking in winter.
All tracers, however, are influenced by monthly variations in meteorological conditions, such as horizontal advection and atmospheric stability. This influence is particularly noticeable in the energy and industry sectors, whose emissions remain relatively stable throughout the year, but show larger enhancements in for example November and February. The analysis of CO_2 and CO, in line with earlier CH_4 findings, shows a strong correlation between tracer levels and the free tropospheric wind direction. Synoptic weather systems play a key role in transporting clean or polluted air to the site, making them a dominant factor in the variability of column-averaged data. This influence is evident in events like the July 2019 heatwave, where XCO_2 significantly increased over a period of 10 days due to advection of a hot, CO_2-rich air mass.
Near the surface, smaller-scale circulations also impact variability, with the diurnal cycle of the planetary boundary layer being especially important. WRF-GHG generally captures these changes well, though it overestimates the average daily amplitude of 22.08 ppm by 4.42 ppm, mainly due to an overestimation of nighttime concentrations. This discrepancy likely stems from inaccuracies in biogenic CO_2 fluxes from VPRM or in the release height of anthropogenic emissions.
Finally, since major CO_2 sources surround Xianghe from all directions, no distinct correlation between in situ concentrations and local wind direction can be found. However, some regional patterns emerge, such as elevated residential tracer values from the west, where Beijing is located, and increased tracer enhancements due to a strong industrial source to the southwest.

For CO, the analysis is limited to column observations, resulting in fewer conclusions. Nevertheless, CO's shorter atmospheric lifetime, compared to CH_4 and CO_2, makes it a useful tracer for identifying pollution events. Emissions within the model domain contribute on average about 62 ppb (or almost 40%) to the total XCO concentration at Xianghe. Overall, WRF-GHG is able to capture the variability in XCO quite well, showing a correlation coefficient of 0.69 and no under-or overestimation with mean bias of 0.42 ppb. Lastly, we could identify that the main sources contributing to XCO are industry (with an average of about 25 ppb), residential combustion and transportation (both about 10 ppb).
This analysis enhances our understanding of the regional drivers of CO_2 and CO variability at Xianghe, while emphasizing the critical role of accurate emission inventories and boundary conditions in regional modeling efforts.

Chapter 6

Conclusions and outlook

In this concluding chapter, we revisit the key insights gained from this study, tying them back to the broader goal of understanding greenhouse gas dynamics at Réunion Island and Xianghe, and assessing the effectiveness of the WRF-GHG model. The first section provides a concise overview of the main factors influencing the observed CO_2, CH_4, and CO concentrations, focusing on the roles of emissions, sinks, and meteorological processes at both sites. This is followed by a reflection on the model's overall performance, offering a balanced perspective on its strengths and limitations. The second section looks ahead to potential future research directions and finally, the chapter concludes with a set of recommendations for future applications of the WRF-GHG model.

6.1 Conclusions

In this study, we simulated CO_2, CH_4, and CO observations at two sites on Réunion Island: Saint-Denis and Maïdo, each equipped with a remote sensing FTIR instrument and an in situ CRDS instrument. The main conclusions of this study are presented below, starting with an overview of the processes affecting column observations, and then discussing the in situ measurement results.

Given that FTIR instruments measure the entire atmospheric column, their sampling volumes are significantly larger compared to the localized observations made by the in situ instruments. As a result, the column observations at Saint-Denis and Maïdo, which sample similar air masses, yield similar conclusions.
Previous studies have demonstrated that the wind inversion above Réunion leads to distinct footprints for surface versus column measurements. Near the surface, the prevailing eastern trade winds transport air parcels primarily from the Indian Ocean. In contrast, at higher altitudes, the westerlies bring air from Africa or South America. This phenomenon enables the column observations at Réunion to effectively capture tracer enhancements associated with the biomass burning season in Africa and South America, which is generally between August and December. Our model simulations support this, revealing biomass burning-related enhancements in the tracer contributions for all three species, particularly for CO, which is the primary emission from biomass burning, during this part of the year.

Moreover, the WRF-GHG simulations indicate a positive contribution from the biosphere during this period, likely associated with the coinciding dry season when biospheric CO_2 uptake is reduced. During the austral summer, on the other hand, our simulations reveal only a minor biogenic CO_2 sink, which is likely due to changing wind patterns that cause the column observations at Réunion to be less sensitive to the African biosphere, as originally suggested by Frey et al. (2021). Additionally, a small wetland signal is detected in the CH_4 columns during the austral summer, corresponding to the rainy season.
This source attribution analysis, combined with the fact that Réunion Island lacks major local emission sources, and that model performance remains consistent at resolutions of 50 km compared to 10 km or 2 km, indicates that the primary sources influencing the column observations are located further away, particularly in continental Africa. Furthermore, the relatively small tracer contributions above the background level throughout the year (smaller than 0.5% for CO_2 and CH_4) and the fact that the largest variations in the time series are already captured by the background tracer emphasize the importance of boundary information to simulate these column measurements at Réunion Island. This further confirms the strategic location of Réunion for studying atmospheric background concentrations.

The in situ observations of CO_2 and CH_4 at Saint-Denis were simulated and analyzed in detail for the first time. Our analysis highlights the influence of local emissions and various meteorological processes on the observed variations. One key factor is the diurnal variation in the planetary boundary layer height, which leads to higher concentrations at night compared to daytime, due to tracer accumulation near the surface at night versus vertical mixing during the day. This effect is more pronounced for CO_2 than for CH_4, likely due to stronger local CO_2 emissions.
Both species are influenced by anthropogenic activities in the capital city, but a notable biogenic CO_2 tracer enhancement is also identified, originating from outside the city. Despite Saint-Denis' coastal location, the contribution from oceanic sources is negligible. Furthermore, our findings indicate that the strength of the nocturnal buildup of CO_2 is highly dependent on local wind speed and direction. Stronger winds result in greater dispersion, reduced accumulation, and lower concentrations. Typically, these stronger winds originate from the east-southeast, whereas weaker winds, associated with significant nocturnal CO_2 buildup, come from the south. This might indicate that the stronger east-southeast winds can advect CO_2-depleted air from outside the city.

Finally, we analyzed the in situ time series at the Maïdo Observatory. Previous research has highlighted the unique location of the Maïdo Observatory: at high altitude, it is often situated in the free troposphere at night, while during the day, anabatic winds transport air from the lower coastal regions upslope to the mountain top. Our model simulations capture these patterns to some extent, as reflected in the partitioning of tracer contributions.
Despite the absence of local sources, small anthropogenic contributions to CO_2 and CO are detected, likely originating from the coastal regions. Additionally, a small biomass burning contribution is observed for CO, suggesting an influence from distant sources and indicating the presence of the instrument in the free troposphere. Further, a distinct diurnal cycle is identified for CO_2, driven by the biogenic tracer, with local vegetation contributing to CO_2

uptake during the day and respiration at night.

6.1.1 Xianghe

In this study, we simulated the time series of CO_2, CH_4 and CO at Xianghe, analyzing both near-surface observations and those from the atmospheric column above. Unlike the distinct circulation patterns observed at Réunion Island, where surface and column observations are influenced by different air masses, the air masses affecting both surface and column measurements at Xianghe are largely similar. Consequently, the relative distribution of tracer contributions to both in situ concentrations and column-averaged values is comparable and can be discussed per species.

For CO_2, the primary contributing sectors at Xianghe are energy and industry, followed by the biosphere. CH_4 concentrations are mainly influenced by the energy sector, residential activities, waste management, and agriculture. Meanwhile, CO levels at Xianghe are mainly driven by emissions from industry, residential areas, and transportation.
A notable difference between the in situ and column-averaged observations is the magnitude of the tracer enhancements. The in situ measurements, conducted close to the surface where emission sources are concentrated, show significantly higher enhancements: up to ten times greater than those in the column-averaged measurements. This is because remote sensing captures an average over the entire atmospheric column, diluting the effect of surface emissions. Our model simulations also indicate a relatively stronger biogenic CO_2 sink in the column-averaged measurements compared to the surface observations. Similarly, the energy sector shows a relatively larger contribution to the XCH_4 time series than to the in situ concentrations. These discrepancies are likely due to the distance of major source regions from Xianghe: while distant sources are less likely to impact surface measurements directly, they can still influence column data when air masses carrying these tracers are advected at higher altitudes.

The in situ observations at Xianghe exhibit a distinct diurnal cycle, characterized by lower concentrations during the day and higher values at night, driven by variations in the planetary boundary layer height. Additionally, both surface and column observations are heavily influenced by the prevailing winds: polluted air from the North China Plain is typically brought in by southwestern winds, while cleaner air from Inner Mongolia is advected by northern winds. These wind patterns are a dominant factor contributing to the substantial day-to-day variability observed in the remote sensing time series.
Furthermore, the XCO_2 time series is subject to significant variations due to anomalous weather conditions, such as the advection of CO_2-rich air during a summer heatwave. This highlights the impact of episodic meteorological events on atmospheric composition at Xianghe.

6.1.2 WRF-GHG evaluation

WRF-GHG is a sophisticated tool designed for simulating the transport and concentration of greenhouse gases and other atmospheric tracers. Its versatility and high resolution make it suitable for a range of atmospheric studies. However, like any model, WRF-GHG has its strengths and weaknesses, which must be considered when interpreting its results. Through our application of the model to the observations at Réunion Island and Xianghe, we have identified several key insights as listed below.

Strengths of the WRF-GHG Model

- **Versatility**: One of the key strengths of the WRF-GHG model is its versatility. It offers a wide array of configuration options that allow users to tailor the model to their specific research needs. This includes the ability to define alternative passive tracers with only minor modifications to the model's source code. Such flexibility enables researchers to, for example, test multiple emission inventories simultaneously or to incorporate additional tracers, providing greater detail and precision in identifying and analyzing emission sources. Moreover, the capability to separately track different components of the signal allows researchers to identify the key sources driving observed variability.

- **Integration of tracers and meteorological data**: WRF-GHG simulates tracer concentrations simultaneously with meteorological data, allowing for in-depth analysis of the correlations between them. This integrated approach is crucial for understanding the transport mechanisms and dispersion of tracers, providing insights into how meteorological conditions impact greenhouse gas concentrations.

- **Good overall performance**: As demonstrated by various studies and confirmed in the current work, the WRF-GHG model displays a good overall performance. It effectively captures the main temporal variations in the time series, particularly for CO and CO_2, as evidenced by high correlation values. These temporal variations are driven by a combination of emission changes and meteorological phenomena, which are well-represented by the model. Additionally, the model accurately simulates the diurnal cycles of in situ observations and replicates specific transport patterns, such as tracer advection from coastal regions to the Maïdo mountain. Although some discrepancies in local wind simulations were noted, the model still performed well in representing these complex dynamics at Réunion Island.

- **VPRM integration**: The integration of the Vegetation Photosynthesis and Respiration Model (VPRM) within WRF-GHG is another strength. VPRM allows the simulation of hourly varying biogenic CO_2 fluxes, providing a more dynamic and accurate representation of biospheric contributions to atmospheric CO_2 levels. This capability is particularly important for studies focused on carbon cycle dynamics and land-atmosphere interactions.

- **High spatial resolution**: WRF-GHG offers users the flexibility to choose spatial resolutions as high as 1 km or even finer. This level of detail is significantly higher than that of most global models, enabling more precise simulations of local transport patterns and emission dispersion, especially when high-resolution emission data is available to match.

- **Evaluating input datasets**: By identifying discrepancies between observed greenhouse gas concentrations and model simulations, WRF-GHG can reveal inaccuracies in existing emission inventories. This study specifically highlighted inaccuracies in CH_4 emissions from EDGAR at Réunion and CAMS-GLOB-ANT around Xianghe.

Remark that it is common to use Lagrangian models for studies tracing backward trajectories to link observations at a specific site to potential source regions or to estimate the influence of sources on a receptor (source-receptor analysis). This type of models, of which FLEXPART (FLEXible PARTicle dispersion mode) or STILT (Stochastic Time-Inverted Lagrangian Transport model) are widely used examples, follow individual air parcels as they move through the atmosphere, based on wind fields and turbulence. They represent a different approach compared to Eulerian models, such as WRF-GHG, that simulate the movement of gases on a fixed spatial grid, allowing for a detailed representation of physical processes across a continuous domain. One of the objectives of this study was to assess the usefulness of WRF-GHG in simulating ground-based measurements, both in situ and remote, at specific observation sites. While it was not an explicit goal to compare it with Lagrangian models, the strengths and weaknesses of WRF-GHG revealed in this analysis, and as stated above, provide insights for future users to make thoughtful choices when selecting between modeling approaches. WRF-GHG offers several advantages, including its ability to simulate online biogenic CO_2 fluxes, its continuous domain-wide concentration fields, and its high-resolution representation of meteorological processes influencing GHG variability. Additionally, WRF-GHG simplifies the comparison with both in situ and remote sensing data by allowing direct extraction from relevant grid cells, as well as the possibility to compare with satellite products.

Weaknesses of the WRF-GHG Model

- **Complexity**: While the versatility of WRF-GHG is a strength, the vast number of configuration options can also be a drawback. Users may spend considerable time on sensitivity tests, trying to identify the optimal settings for their specific study, which can make it challenging to choose the best configuration and lead to delays. Additionally, the model requires a substantial amount of preprocessing to correctly prepare input data for ingestion into the model, involving several steps and multiple programs that must be run before the actual forward integration begins. This lengthy and intricate process demands considerable effort to navigate and understand, increasing the risk of errors along the way. If the model fails or produces unexpected results, pinpointing the specific source of the error can be particularly challenging.

- **Dependency on accurate emission data**: The accuracy of WRF-GHG simulations is directly influenced by the quality of the used emission data. Errors in the spatial,

temporal, or quantitative aspects of these datasets can lead to significant errors in the model output. For instance, the EDGAR dataset was found to overestimate CH_4 emissions at Réunion, likely due to its low spatial resolution. Similarly, CAMS-GLOB-ANT emissions around Xianghe showed an incorrect seasonality for CH_4, possibly linked to agricultural or waste management sources, and a potential overestimation of CH_4 from large point sources in the energy sector.

- **Reliance on accurate boundary conditions**: As a limited-area model, WRF-GHG relies on accurate initial and lateral boundary conditions provided by global models. This dependency is especially crucial for long-lived tracers like CO_2 and CH_4, where enhancements due to emissions within the model domain are often small compared to the total atmospheric concentrations. This reliance is especially significant for remote regions such as Réunion Island, where local emissions are very low. Any biases in the boundary conditions can propagate through the simulations, leading to errors in the results. For example, seasonal biases in CH_4 from the CAMS reanalysis were observed at both Réunion and Xianghe. Additionally, a bias in the CAMS reanalysis for CO_2 over Asia was identified during a large part of the simulation period, further highlighting the importance of accurate boundary information for reliable model outcomes.

- **Surface wind speed overestimation**: WRF-GHG has a known tendency to overestimate surface wind speeds, a common issue documented in other WRF studies. At Réunion Island, this overestimation was particularly evident at Saint-Denis. Unfortunately, we could not evaluate this issue at Xianghe due to the lack of reliable meteorological data at the site.

- **Lack of CH_4 and CO chemistry**: The absence of CH_4 and CO chemistry in WRF-GHG can introduce biases in the model simulations, especially in long-term studies or those involving very large domains. While the impact of this limitation may vary depending on the specific study, it remains a potential source of error that researchers must consider.

- **Challenges in optimizing VPRM parameters**: Optimizing the VPRM parameters for a specific region is a complex task that often requires a separate, dedicated study. Unfortunately, this process has not been undertaken for many regions, potentially contributing to the errors observed in in situ CO_2 simulations at Maïdo and Xianghe. Region-specific parameters will likely improve the accuracy of biogenic CO_2 flux simulations in these areas.

WRF-GHG is a powerful tool with significant strengths that make it highly valuable for atmospheric research, particularly in studies that require high spatial resolution and detailed tracer analysis. However, its weaknesses—such as its dependence on accurate input data and the complexity of its configuration—highlight the need for careful application and thorough validation. Understanding these strengths and weaknesses is crucial for interpreting model results accurately and for making informed decisions about the model's application in future research studies.

6.2 Outlook

This section explores potential avenues for future research aimed at enhancing model accuracy and deepening our understanding of the observations at Réunion Island, Xianghe or elsewhere.

1. If a more accurate representation of the in situ observations at Réunion Island is required for further analysis, it may be beneficial to explore model resolutions finer than the 2 km used in the current study. Increasing the spatial resolution could lead to better-resolved local wind patterns, such as those around Maïdo, and better representation of the weak winds near Saint-Denis. However, for research focused on the remote sensing observations, a higher spatial resolution is likely not beneficial.

2. For future studies concentrating on the surface CH_4 observations at Réunion Island, obtaining a more precise anthropogenic emission inventory with higher spatial resolution is essential. Improving the EDGAR v5.0 inventory, which has shown inaccuracies in our study, is expected to lead to more accurate simulations for these observations.

3. The observed bias in the CAMS reanalysis for CH_4 in the Réunion domain underscores the need for a better understanding of CH_4 sources and sinks in the Southern Hemisphere in general.

4. Similarly, research into the seasonal cycle of CH_4 in the wide region around Xianghe is needed. Previous studies, such as Yang et al. (2020), have noted the unique seasonality of XCH_4 at Xianghe compared to other sites at similar latitudes. Our study faced difficulties in simulating CH_4 due to potential inaccuracies in both CAMS reanalysis and CAMS-GLOB-ANT emissions, emphasizing the need for focused research on regional CH_4 sources and sinks.

5. To gain further insights into the observations at Xianghe, it could be valuable to define new tracers linked to specific source regions rather than source sectors, as employed in the current study. This approach could illuminate the contributions of different countries, provinces or even targeted point sources to the observed atmospheric variabilities.

6. Implementing a vertical distribution to CO_2 emission sources could result in a more accurate representation of reality.

7. The VPRM model's treatment of vegetation respiration has been highlighted as oversimplified in several studies. Further evaluation of the proposed modifications by for example Gourdji et al. (2022) to incorporate EVI, water stress and a more complex dependence on temperature, might lead to an updated WRF-GHG distribution and more accurate simulations of biogenic CO_2 fluxes in the future. Further, more region-specific VPRM parameter optimization is also needed, as current studies are limited to Europe, the United States, and the Amazon region. Other tropical regions and Asia would benefit from updated parameters to improve biogenic CO_2 flux simulations, underscoring the importance of establishing more extensive flux observations in these areas.

8. The Kaplan model for simulating biogenic CH_4 fluxes from wetlands, has not been thoroughly evaluated since its inclusion in WRF-GHG. Evaluating this model over regions with extensive wetland areas could provide valuable insights. Similarly, a formal evaluation and potential modification of the online soil uptake model for CH_4 fluxes should be considered to enhance WRF-GHG's relevance.

9. Application of WRF-GHG in Belgium: I am currently involved in the VERBE project (https://verbe.aeronomie.be/) which aims at establishing a top-down, spatially explicit GHG emission monitoring and verification system (MVS) for Belgium. This project will apply WRF-GHG in an inversion framework, to evaluate the existing inventories of GHG emissions in Belgium, while interacting with the local stakeholders. This initiative will ultimately support government policies and EU strategies to reduce CO_2 and CH_4 emissions.

6.3 Recommendations for future WRF-GHG applications

Based on my experience, I wish to conclude this thesis with several recommendations for future applications of WRF-GHG.

- Select appropriate emission data and boundary conditions: Ensure that emission data matches the model resolution as closely as possible and that boundary conditions are as accurate as possible to minimize errors that can propagate through the model. Avoid biases, such as those encountered with CH_4 in our study.

- Optimize model domain size: The model domain should be sufficiently large to include a comprehensive range of emission sources. This is particularly important for CO_2 and CH_4 simulations, where insufficient domain size can lead to under-representation of tracer contributions.

- Update fixed data sets for online biogenic fluxes: This includes for example using a more recent land cover classification for the VPRM model, as the SYNMAP dataset is outdated, at least for China as shown in our study over Xianghe. The recently distributed pyVPRM preprocessor can be used for smooth ingestion into WRF-GHG. Moreover, this tool can additionally include newer satellite products (as MODIS will be decommissioned soon), offering improved accuracy. Further, it may also be beneficial to evaluate whether the relatively old termite database from Sanderson (1996) is still relevant.

- Allocate sufficient time for study design: Carefully consider which tagged tracers are most relevant to your research objectives. Thorough study design is crucial for obtaining meaningful results.

- Consider higher model top height: Increasing the model top above 50 hPa could benefit CH_4 column simulations, as this species is significantly influenced by processes in the

upper atmosphere. However, extending the model top may introduce new inaccuracies, as chemical processes become more significant at higher altitudes, potentially affecting the CH_4 simulations. Therefore, it is essential to find a balance between extending the model top to capture the complete atmospheric profile, which may lead to inaccuracies due to neglected chemistry and an increased computation time, and maintaining a lower model top that might miss important stratospheric contributions.

- Select suitable model resolution: For studies focused on column observations, a model resolution similar to that of the emission inventory is generally sufficient. Higher resolution may not be necessary unless specific details are required.

Appendix A

List of Acronyms

ADS	Atmospheric Data Store
AR6	Sixth Assessment Report
BIRA-IASB	Royal Belgian Institute for Space Aeronomy
CAMS	Copernicus Atmosphere Monitoring Service
CAMS-GLOB-ANT	Global Anthropogenic emission database of the European CAMS
CAS	Chinese Academy of Science
CDO	Climate Data Operator
CDS	Climate Data Store
COCCON	Collaborative Carbon Column Observing Network
CRDS	Cavity Ring-Down Spectroscopy
CTM	Chemical Transport Model
DOAS	Differential Optical Absorption Spectroscopy
DOF	Degrees Of Freedom
ECCAD	Emissions of atmospheric Compounds and Compilation of Ancillary Data
ECMWF	European Centre for Medium-Range Weather Forecasts
EDGAR	Emissions Database for Global Atmospheric Research
ESRL	Earth Systems Resource Laboratories
EVI	Enhanced Vegetation Index
FFDAS	Fossil Fuel Data Assimilation System
FINN	Fire Inventory from NCAR
FLEXPART	FLEXible PARTicle dispersion model
FTIR	Fourier Transform Infrared
GAW	Global Atmosphere Watch
GEE	Gross Ecosystem Exchange
GHG	Greenhouse Gas
GOSAT	Greenhouse gas Observing SATellite
HPC	High-Performance Computing
IAP	Institute of Atmospheric Physics
IC-BC	Initial and lateral Boundary Condition

ICOS	Integrated Carbon Observing System
IFS	Integrated Forecast System
IPCC	Intergovernmental Panel of Climate Change
IRWG	Infrared Working Group
IR	Infrared
LSCE	Laboratoire des Sciences du Climat et de l'Environnement
LSWI	Land Surface Water Index
LULUCF	Land Use, Land-Use Change and Forestry
LW	Longwave
MEIC-China	Multi-resolution Emission Inventory for China
MIR	Mid-infrared
MODIS	Moderate Resolution Imaging Spectroradiometer
MPI-BGC	Max Planck Institute for Biogeochemistry
NASA	National Aeronautics and Space Administration
NCAR	National Center for Atmospheric Research
NDACC	Network for the Detection of Atmospheric Composition Change
NDIR	Non-Dispersive Infrared
NEE	Net Ecosystem Exchange
NIR	Near-infrared
NOAA	National Oceanic and Atmospheric Administration
NWP	Numerical Weather Prediction
OCO	Orbiting Carbon Observatory
ODIAC	Open-source Data Inventory for Anthropogenic CO_2
OE	Optimal Estimation
OPAR	Observatoire de Physique de l'Atmosphère de La Réunion
PAR	Photosynthetically Active Radiation
PBL	Planetary Boundary Layer
PKU	Peking University
REAS	Regional Emission inventory in ASia
RES	Ecosystem respiration
SW	Shortwave
SZA	Solar Zenith Angle
TC	Total Column
TCCON	Total Carbon Column Observing Network
TIMES	Temporal Improvements for Modeling Emissions by Scaling
TROPOMI	Tropospheric Monitoring Instrument
UNFCCC	United Nations Framework Convention on Climate Change
UV	Ultraviolet
VPRM	Vegetation Photosynthesis and Respiration Model
WMO	World Meteorological Organization
WPS	WRF Preprocessing System
WRF	Weather Research and Forecasting model
WRF-Chem	WRF coupled with Chemistry
WRF-GHG	WRF for Greenhouse Gases

Appendix B

Describing atmospheric composition

The concentration of a species G in the atmosphere can be expressed as a mixing ratio ν_G or mole fraction, which is defined as the number of moles of species G per mole of air (mol mol^{-1}). Note that for species with very small amounts in the atmosphere, the mixing ratio is usually expressed as parts per million by volume (ppmv) or parts per billion by volume (ppbv). For example, a CO_2 mixing ratio of 400 ppm indicates that there are 400 moles of CO_2 per 10^6 mole of air.
Alternatively, the concentration can be described as number density ρ_G, which is the number of moles of species G per unit volume of air (mol m^{-3}). They are related through the number density of air ρ_a (mol m^{-3}):

$$\rho_G = \nu_G \rho_a \tag{B.1}$$

Both measures can be expressed with respect to wet air or dry air (i.e. wet air without H_2O), whereby we add a or da as sub-/superscript, respectively: $\rho_G^a = \nu_G^a \rho_a$ and $\rho_G^{da} = \nu_G^{da} \rho_{da}$. The number density of wet air can be calculated according to the ideal gas law:

$$\rho_a = \frac{P}{RT},$$

where P is the pressure (in Pa), T the temperature (in K) and R the ideal gas constant (8.314 $JK^{-1}mol^{-1}$).
We can derive a formula for the number density of dry air, using the fact that $\nu_{H_2O}^a \rho_a = \nu_{H_2O}^{da} \rho_{da}$:

$$\begin{aligned}
\rho_a &= \rho_{da} + \rho_{H_2O}^a \\
&= \rho_{da} + \nu_{H_2O}^a \rho_a \\
&= \rho_{da} + \nu_{H_2O}^{da} \rho_{da} \\
&= \left(1 + \nu_{H_2O}^{da}\right) \rho_{da} \\
\Leftrightarrow \rho_{da} &= \rho_a \frac{1}{1 + \nu_{H_2O}^{da}} \\
&= \rho_a \frac{1}{1 + \frac{M_{da}}{M_{H2O}} q} \\
&= \rho_a \frac{1}{1 + 1.6075 q}.
\end{aligned}$$

In the last two equations, q is the mass mixing ratio of water vapor (kg kg^{-1}) with respect to dry air, while $M_{da} = 28.96$ (g mol^{-1}) is the molar mass of dry air and $M_{H_2O} = 18.015$ (g mol^{-1}) is the molar mass of H_2O. So, with the atmospheric variables of water vapor, pressure and temperature, the number density of dry air can be computed: $\rho_{da} = \frac{P}{RT}\frac{1}{1+1.6075q}$, and we can easily convert the dry air number density of a species G to its mixing ratio and vice versa.

In this thesis, concentration quantities are always mentioned with respect to dry air, unless otherwise specified, and thus the superscript *da* is dropped.

When working with remotely sensed data, other concentration measures are often used, such as the partial and total column concentration (mol m^{-2}).
In a partial column profile, the thickness of the several atmospheric layers are taken into account. It can be expressed for a species G as :

$$\boldsymbol{PC}_G = (PC_{G,0} \dots PC_{G,n}) \text{, where } PC_{G,i} = \nu_{G,i}\frac{P_i}{RT_i}\frac{1}{1+1.6075q_i}\Delta z_i, \tag{B.2}$$

with $\nu_{G,i}$ the volume mixing ratio of species G, P_i the atmospheric pressure, T_i the air temperature, q_i the water vapour mass mixing ratio and Δz_i the thickness of layer i (in m). Note that the partial column of dry air ($\boldsymbol{PC}_{da}$) is calculated as in Eq. B.2 without the volume mixing ratio profile of G. As a result, we can state the following for any layer i:

$$PC_{G,i} = \nu_{G,i}PC_{da,i} = \nu_{G,i}\rho_{da,i}\Delta z_i = \rho_{G,i}\Delta z_i$$

The total column concentration is then simply the sum of partial columns over all vertical layers:

$$TC_G = \sum_i PC_{G,i} = \sum_i \nu_{G,i}\frac{P_i}{RT_i}\frac{1}{1+1.6075q_i}\Delta z_i. \tag{B.3}$$

Further, the column-averaged dry air mole fraction X_G or $Xgas$ is very frequently used. It can be calculated by dividing the total column concentration of G by the total column of dry air:

$$X_G = \frac{TC_G}{TC_{da}} = \frac{\sum_i PC_{G,i}}{\sum_i PC_{da,i}} = \frac{\sum_i \nu_{G,i}\rho_{da,i}\Delta z_i}{\sum_i \rho_{da,i}\Delta z_i} \tag{B.4}$$

Appendix C

Running WRF-GHG at BIRA-IASB: procedure

This section outlines the steps involved in creating WRF-GHG simulations within the IT infrastructure of BIRA-IASB.

To ensure that atmospheric transport in the center of the domain remains consistent with the ERA5 reanalysis used at the lateral boundaries, meteorological fields are re-initialized with ERA5 data every 24 hours, after a 6-hour spin-up period. In practice, this results in the workflow illustrated in Fig. C.1 and summarized below:

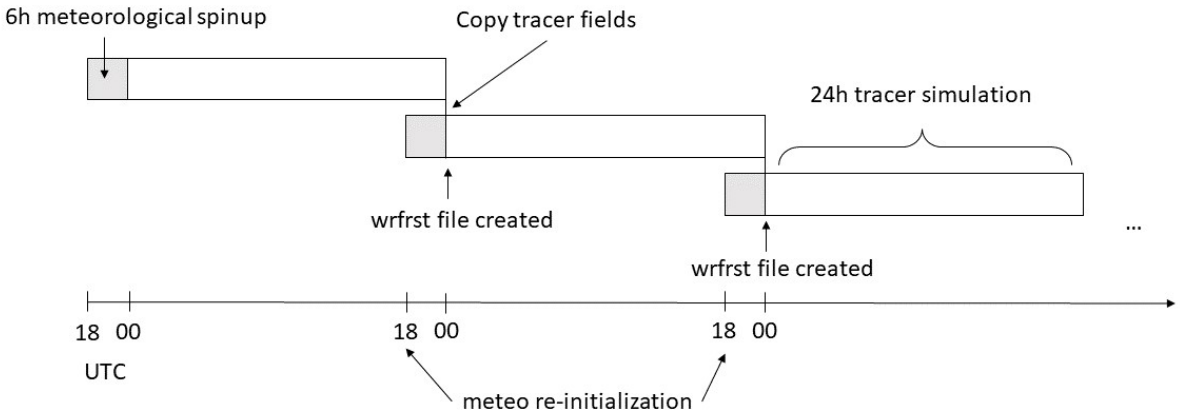

Figure C.1: Schematic diagram on the process of meteorological re-initialization.

- Run the model without emissions for a 6-hour period each day throughout the simulation timeframe, from 18:00 to 00:00 UTC. Use the `restart_interval = 360` setting in *namelist.input* to generate a WRF restart file (`wrfrst`) at 00:00.

- Copy the tracer fields from the previous day's WRF-GHG simulation (`wrfout` files) into the corresponding fields in the restart file, ensuring continuity of the tracer field.
- Run WRF-GHG for a 24-hour period, starting from the modified restart file (using `restart = true` in *namelist.input*).

Technically, this approach results in a series of separate meteorological simulations of 30 hours each (from 18:00 UTC the previous day until 00:00 UTC the following day), but with continuous tracer advection.

To perform WRF-GHG simulations at BIRA-IASB, follow these steps (see Fig. 3.3 for the different programs that are called):

1. Download external datasets, including ERA5 reanalysis data and emission inventories for the selected area and simulation period. The CAMS analysis data is already available on BIRA-IASB servers.
2. Define the model domain, resolution, and nesting configuration by adjusting the WPS configuration file *namelist.wps*, and then execute the *geogrid* program.
3. Use the `geo_em` files generated by *geogrid* to regrid the external emission inventories and CAMS data to the model domain. Apply temporal profiles to the anthropogenic emissions if needed (see Sec 3.2.3). This step is conducted using Python scripts on the BIRA-IASB compute servers.
4. Prepare the meteorological fields from ERA5 by running a Bash script on the HPC, which locates the required input data and launches the *ungrib* program.
5. Generate the final meteorological input files (`met_em` files) by running a Bash script on the HPC, which queues a job to execute *metgrid* and completing WPS.
6. Define the model settings by adjusting a Bash script that creates the *namelist.input* file. This script also queues a job to launch the *real* program, which performs vertical interpolation of the meteorological data (`met_em` files) and generates initial and lateral boundary condition files (`wrfinput` and `wrfbdy`).
7. Prepare additional input data, that require the `wrfinput` files generated by *real*: biomass burning emissions from FINN (handled by the *fire_emis* program) and VPRM input files created by the *VPRM preprocessor* and *VPRM shapeshifter* (see Sec. 3.1.3). This step creates `wrffire` and `vprm_input` files.
8. Transfer the regridded CAMS and emission data from the BIRA-IASB servers to the HPC for use in the model.
9. Execute a script on the HPC for the first simulation. This script: 1) reads regridded CAMS data and fills the corresponding tracer fields in `wrfinput` and `wrfbdy` files, 2) reads regridded emission data and creates `wrfchemi` and `wrfoce` files, 3) adjusts *namelist.input* to include these auxiliary files, and 4) queues a job on the HPC to execute *wrf*.

10. Launch scripts for the meteorological spin-up runs: a 6-hour simulation without emissions is run every 24 hours. Since these runs only require WPS-processed ERA5 data (`met_em` files) for the entire simulation period, they can be executed all at once. For each day, these scripts generate a *namelist.input* file with the same settings as the chemistry run and launch *real* and *wrf*.

11. After the spin-up simulations and the initial 24-hour WRF-GHG simulations are complete, start a cronjob (a Unix command that automatically runs specified scripts). The initial job from step 9 is necessary to fill the lateral boundary conditions with CAMS data and create the emission files for the complete period. The cronjob follows a text file listing dates for sequential simulations, checks if the previous day's simulation was successful, starts from the spin-up meteorological data (`wrfrst` files), transfers the tracer fields from the previous simulation into these files, and launches *wrf* for the next 24-hour simulation. Monitor this process through a logfile for errors. For the setup in this thesis, a 24-hour simulation of three nested domains typically takes 1-2 hours to complete. The cronjob also cleans up successful simulations by deleting large logfiles and copying the output to the BIRA-IASB servers.

Appendix D

Bibliography

Ahmadov, R., Gerbig, C., Kretschmer, R., Koerner, S., Neininger, B., Dolman, A. J., and Sarrat, C.: Mesoscale Covariance of Transport and CO2 Fluxes: Evidence from Observations and Simulations Using the WRF-VPRM Coupled Atmosphere-Biosphere Model, Journal of Geophysical Research: Atmospheres, 112, doi: 10.1029/2007JD008552, 2007.

Ahmadov, R., Gerbig, C., Kretschmer, R., Körner, S., Rödenbeck, C., Bousquet, P., and Ramonet, M.: Comparing High Resolution WRF-VPRM Simulations and Two Global CO2 Transport Models with Coastal Tower Measurements of CO2, Biogeosciences (Online), 6, 807–817, doi: 10.5194/bg-6-807-2009, 2009.

Ahrens, C. and Henson, R.: Meteorology Today: An Introduction to Weather, Climate, and the Environment, MindTap Course List Series, Cengage, ISBN 978-0-357-45207-3, 2021.

Asefi-Najafabady, S., Rayner, P. J., Gurney, K. R., McRobert, A., Song, Y., Coltin, K., Huang, J., Elvidge, C., and Baugh, K.: A Multiyear, Global Gridded Fossil Fuel CO $_2$ Emission Data Product: Evaluation and Analysis of Results: GLOBAL FOSSIL FUEL CO2 EMISSIONS, Journal of Geophysical Research: Atmospheres, 119, 10,213–10,231, doi: 10.1002/2013JD021296, 2014.

Ballav, S., Naja, M., Patra, P. K., Machida, T., and Mukai, H.: Assessment of Spatio-Temporal Distribution of CO2 over Greater Asia Using the WRF–CO2 Model, Journal of Earth System Science, 129, 80, doi: 10.1007/s12040-020-1352-x, 2020.

Beck, V., Koch, T., Kretschmer, R., Marshall, J., Ahmadov, R., Gerbig, C., Pillai, D., and Heimann, M.: The WRF Greenhouse Gas Model (WRF-GHG), Tech. rep., 2011.

Beck, V., Gerbig, C., Koch, T., Bela, M. M., Longo, K. M., Freitas, S. R., Kaplan, J. O., Prigent, C., Bergamaschi, P., and Heimann, M.: WRF-Chem Simulations in the Amazon Region during Wet and Dry Season Transitions: Evaluation of Methane Models and Wetland Inundation Maps, Atmospheric Chemistry and Physics, 13, 7961–7982, doi: 10.5194/acp-13-7961-2013, 2013.

Bloom, A. A., Bowman, K. W., Lee, M., Turner, A. J., Schroeder, R., Worden, J. R., Weidner, R., McDonald, K. C., and Jacob, D. J.: A Global Wetland Methane Emissions and

Uncertainty Dataset for Atmospheric Chemical Transport Models (WetCHARTs Version 1.0), Geoscientific Model Development, 10, 2141–2156, doi: 10.5194/gmd-10-2141-2017, 2017.

Borsdorff, T., aan de Brugh, J., Pandey, S., Hasekamp, O., Aben, I., Houweling, S., and Landgraf, J.: Carbon Monoxide Air Pollution on Sub-City Scales and along Arterial Roads Detected by the Tropospheric Monitoring Instrument, Atmospheric Chemistry and Physics, 19, 3579–3588, doi: 10.5194/acp-19-3579-2019, 2019.

Brunner, D., Kuhlmann, G., Marshall, J., Clément, V., Fuhrer, O., Broquet, G., Löscher, A., and Meijer, Y.: Accounting for the Vertical Distribution of Emissions in Atmospheric CO_2 Simulations, Atmospheric Chemistry and Physics, 19, 4541–4559, doi: 10.5194/acp-19-4541-2019, 2019.

Bushinsky, S. M., Landschützer, P., Rödenbeck, C., Gray, A. R., Baker, D., Mazloff, M. R., Resplandy, L., Johnson, K. S., and Sarmiento, J. L.: Reassessing Southern Ocean Air-Sea CO2 Flux Estimates With the Addition of Biogeochemical Float Observations, Global Biogeochemical Cycles, 33, 1370–1388, doi: 10.1029/2019GB006176, 2019.

Callewaert, S.: WRF-GHG User Guide, doi: 10.18758/Q6RAPNEU, 2024.

Callewaert, S., Brioude, J., Langerock, B., Duflot, V., Fonteyn, D., Müller, J.-F., Metzger, J.-M., Hermans, C., Kumps, N., Ramonet, M., Lopez, M., Mahieu, E., and De Mazière, M.: Analysis of CO_2, CH_4, and CO Surface and Column Concentrations Observed at Réunion Island by Assessing WRF-Chem Simulations, Atmospheric Chemistry and Physics, 22, 7763–7792, doi: 10.5194/acp-22-7763-2022, 2022.

Callewaert, S., Zhou, M., Langerock, B., Wang, P., Wang, T., Mahieu, E., and De Mazière, M.: A WRF-Chem Study of the Greenhouse Gas Column and in Situ Surface Concentrations Observed at Xianghe, China. Part 1: Methane (CH_4), EGUsphere, pp. 1–39, doi: 10.5194/egusphere-2024-3228, 2024.

Crippa, M., Solazzo, E., Huang, G., Guizzardi, D., Koffi, E., Muntean, M., Schieberle, C., Friedrich, R., and Janssens-Maenhout, G.: High Resolution Temporal Profiles in the Emissions Database for Global Atmospheric Research, Scientific Data, 7, 121, doi: 10.1038/s41597-020-0462-2, 2020a.

Crippa, M., Solazzo, E., Huang, G., Guizzardi, D., Koffi, E., Muntean, M., Schieberle, C., Friedrich, R., and Maenhout, G. J.: High Resolution Temporal Profiles in the Emissions Database for Global Atmospheric Research (EDGAR), doi: 10.6084/m9.figshare.c.4780547.v1, 2020b.

Dayalu, A., Munger, J. W., Wofsy, S. C., Wang, Y., Nehrkorn, T., Zhao, Y., McElroy, M. B., Nielsen, C. P., and Luus, K.: Assessing Biotic Contributions to CO_2 Fluxes in Northern China Using the Vegetation, Photosynthesis and Respiration Model (VPRM-CHINA) and Observations from 2005 to 2009, Biogeosciences (Online), 15, 6713–6729, doi: 10.5194/bg-15-6713-2018, 2018.

De Mazière, M., Thompson, A. M., Kurylo, M. J., Wild, J. D., Bernhard, G., Blumenstock, T., Braathen, G. O., Hannigan, J. W., Lambert, J.-C., Leblanc, T., McGee, T. J., Nedoluha, G., Petropavlovskikh, I., Seckmeyer, G., Simon, P. C., Steinbrecht, W., and Strahan, S. E.: The Network for the Detection of Atmospheric Composition Change (NDACC): History, Status and Perspectives, Atmospheric Chemistry and Physics, 18, 4935–4964, doi: 10.5194/acp-18-4935-2018, 2018.

Dekker, I. N., Houweling, S., Aben, I., Röckmann, T., Krol, M., Martínez-Alonso, S., Deeter, M. N., and Worden, H. M.: Quantification of CO Emissions from the City of Madrid Using MOPITT Satellite Retrievals and WRF Simulations, Atmospheric Chemistry and Physics, 17, 14 675–14 694, doi: 10.5194/acp-17-14675-2017, 2017.

Dekker, I. N., Houweling, S., Pandey, S., Krol, M., Röckmann, T., Borsdorff, T., Landgraf, J., and Aben, I.: What Caused the Extreme CO Concentrations during the 2017 High-Pollution Episode in India?, Atmospheric Chemistry and Physics, 19, 3433–3445, doi: 10.5194/acp-19-3433-2019, 2019.

Dong, X., Yue, M., Jiang, Y., Hu, X.-M., Ma, Q., Pu, J., and Zhou, G.: Analysis of CO_2 Spatio-Temporal Variations in China Using a Weather–Biosphere Online Coupled Model, Atmospheric Chemistry and Physics, 21, 7217–7233, doi: 10.5194/acp-21-7217-2021, 2021.

Feng, S., Lauvaux, T., Newman, S., Rao, P., Ahmadov, R., Deng, A., Díaz-Isaac, L. I., Duren, R. M., Fischer, M. L., Gerbig, C., Gurney, K. R., Huang, J., Jeong, S., Li, Z., Miller, C. E., O'Keeffe, D., Patarasuk, R., Sander, S. P., Song, Y., Wong, K. W., and Yung, Y. L.: Los Angeles Megacity: A High-Resolution Land–Atmosphere Modelling System for Urban CO_2 Emissions, Atmospheric Chemistry and Physics, 16, 9019–9045, doi: 10.5194/acp-16-9019-2016, 2016.

Foken, T.: Micrometeorology, Springer, ISBN 978-3-540-74665-2, 2008.

Frey, M. M., Hase, F., Blumenstock, T., Dubravica, D., Groß, J., Göttsche, F., Handjaba, M., Amadhila, P., Mushi, R., Morino, I., Shiomi, K., Sha, M. K., de Mazière, M., and Pollard, D. F.: Long-Term Column-Averaged Greenhouse Gas Observations Using a COCCON Spectrometer at the High-Surface-Albedo Site in Gobabeb, Namibia, Atmospheric Measurement Techniques, 14, 5887–5911, doi: 10.5194/amt-14-5887-2021, 2021.

Friedlingstein, P., O'Sullivan, M., Jones, M. W., Andrew, R. M., Bakker, D. C. E., Hauck, J., Landschützer, P., Le Quéré, C., Luijkx, I. T., Peters, G. P., Peters, W., Pongratz, J., Schwingshackl, C., Sitch, S., Canadell, J. G., Ciais, P., Jackson, R. B., Alin, S. R., Anthoni, P., Barbero, L., Bates, N. R., Becker, M., Bellouin, N., Decharme, B., Bopp, L., Brasika, I. B. M., Cadule, P., Chamberlain, M. A., Chandra, N., Chau, T.-T.-T., Chevallier, F., Chini, L. P., Cronin, M., Dou, X., Enyo, K., Evans, W., Falk, S., Feely, R. A., Feng, L., Ford, D. J., Gasser, T., Ghattas, J., Gkritzalis, T., Grassi, G., Gregor, L., Gruber, N., Gürses, Ö., Harris, I., Hefner, M., Heinke, J., Houghton, R. A., Hurtt, G. C., Iida, Y., Ilyina, T., Jacobson, A. R., Jain, A., Jarníková, T., Jersild, A., Jiang, F., Jin, Z., Joos, F., Kato, E., Keeling, R. F., Kennedy, D., Klein Goldewijk, K., Knauer, J., Korsbakken,

J. I., Körtzinger, A., Lan, X., Lefèvre, N., Li, H., Liu, J., Liu, Z., Ma, L., Marland, G., Mayot, N., McGuire, P. C., McKinley, G. A., Meyer, G., Morgan, E. J., Munro, D. R., Nakaoka, S.-I., Niwa, Y., O'Brien, K. M., Olsen, A., Omar, A. M., Ono, T., Paulsen, M., Pierrot, D., Pocock, K., Poulter, B., Powis, C. M., Rehder, G., Resplandy, L., Robertson, E., Rödenbeck, C., Rosan, T. M., Schwinger, J., Séférian, R., Smallman, T. L., Smith, S. M., Sospedra-Alfonso, R., Sun, Q., Sutton, A. J., Sweeney, C., Takao, S., Tans, P. P., Tian, H., Tilbrook, B., Tsujino, H., Tubiello, F., van der Werf, G. R., van Ooijen, E., Wanninkhof, R., Watanabe, M., Wimart-Rousseau, C., Yang, D., Yang, X., Yuan, W., Yue, X., Zaehle, S., Zeng, J., and Zheng, B.: Global Carbon Budget 2023, Earth System Science Data, 15, 5301–5369, doi: 10.5194/essd-15-5301-2023, 2023.

Gourdji, S. M., Karion, A., Lopez-Coto, I., Ghosh, S., Mueller, K. L., Zhou, Y., Williams, C. A., Baker, I. T., Haynes, K. D., and Whetstone, J. R.: A Modified Vegetation Photosynthesis and Respiration Model (VPRM) for the Eastern USA and Canada, Evaluated With Comparison to Atmospheric Observations and Other Biospheric Models, Journal of Geophysical Research: Biogeosciences, 127, doi: 10.1029/2021JG006290, 2022.

Granier, C., Darras, S., Denier van der Gon, H., Doubalova, J., Elguindi, N., Galle, B., Gauss, M., Guevara, M., Jalkanen, J.-P., Kuenen, J., Liousse, C., Quack, B., Simpson, D., and Sindelarova, K.: The Copernicus Atmosphere Monitoring Service Global and Regional Emissions (April 2019 Version), doi: 10.24380/D0BN-KX16, 2019.

Grell, G. A., Peckham, S. E., Schmitz, R., McKeen, S. A., Frost, G., Skamarock, W. C., and Eder, B.: Fully Coupled "Online" Chemistry within the WRF Model, Atmospheric Environment, 39, 6957–6975, doi: 10.1016/j.atmosenv.2005.04.027, 2005.

Guevara, M., Jorba, O., Tena, C., Denier van der Gon, H., Kuenen, J., Elguindi, N., Darras, S., Granier, C., and Pérez García-Pando, C.: Copernicus Atmosphere Monitoring Service TEMPOral Profiles (CAMS-TEMPO): Global and European Emission Temporal Profile Maps for Atmospheric Chemistry Modelling, Earth System Science Data, 13, 367–404, doi: 10.5194/essd-13-367-2021, 2021.

Gulev, S., Thorne, P.W., Ahn, J., Dentener, F.J., Domingues, C.M., Gerland, S., Gong, D., Kaufman, D.S., Nnamchi, H.C., Quaas, J., Rivera, J.A., Sathyendranath, S., Smith, S.L., Trewin, B., van Schuckmann, K., and Vose, R.S.: IPCC, 2021: Chapter 2. In: Climate Change 2021: The Physical Science Basis. Contribution of Working Group I to the Sixth Assessment Report of the Intergovernmental Panel on Climate Change, Tech. rep., 2021.

Gupta, S., Tiwari, Y. K., Revadekar, J. V., Burman, P. K. D., Chakraborty, S., and Gnanamoorthy, P.: An Intensification of Atmospheric CO2 Concentrations Due to the Surface Temperature Extremes in India, Meteorology and Atmospheric Physics, 133, 1647–1659, doi: 10.1007/s00703-021-00834-w, 2021.

Hersbach, H., Bell, B., Berrisford, P., Biavati, G., Horányi, A., Munoz Sabater, J., Nicolas, J., Peubey, C., Radu, R., Rozum, I., Schepers, D., Simmons, A., Soci, C., Dee, D., and Thépaut, J.-N.: ERA5 Hourly Data on Pressure Levels from 1940 to Present., doi: 10.24381/cds.bd0915c6, 2023a.

Hersbach, H., Bell, B., Berrisford, P., Biavati, G., Horányi, A., Munoz Sabater, J., Nicolas, J., Peubey, C., Radu, R., Rozum, I., Schepers, D., Simmons, A., Soci, C., Dee, D., and Thépaut, J.-N.: ERA5 Hourly Data on Single Levels from 1940 to Present., doi: 10.24381/cds.adbb2d47, 2023b.

Hu, X.-M., Crowell, S., Wang, Q., Zhang, Y., Davis, K. J., Xue, M., Xiao, X., Moore, B., Wu, X., Choi, Y., and DiGangi, J. P.: Dynamical Downscaling of CO2 in 2016 Over the Contiguous United States Using WRF-VPRM, a Weather-Biosphere-Online-Coupled Model, Journal of Advances in Modeling Earth Systems, 12, e2019MS001 875, doi: 10.1029/2019MS001875, 2020.

Hu, X.-M., Gourdji, S. M., Davis, K. J., Wang, Q., Zhang, Y., Xue, M., Feng, S., Moore, B., and Crowell, S. M. R.: Implementation of Improved Parameterization of Terrestrial Flux in WRF-VPRM Improves the Simulation of Nighttime CO2 Peaks and a Daytime CO2 Band Ahead of a Cold Front, Journal of Geophysical Research: Atmospheres, 126, e2020JD034 362, doi: 10.1029/2020JD034362, 2021.

Inness, A., Ades, M., Agustí-Panareda, A., Barré, J., Benedictow, A., Blechschmidt, A.-M., Dominguez, J. J., Engelen, R., Eskes, H., Flemming, J., Huijnen, V., Jones, L., Kipling, Z., Massart, S., Parrington, M., Peuch, V.-H., Razinger, M., Remy, S., Schulz, M., and Suttie, M.: The CAMS Reanalysis of Atmospheric Composition, Atmospheric Chemistry and Physics, 19, 3515–3556, doi: 10.5194/acp-19-3515-2019, 2019.

Jacobson, A. R., Schuldt, K. N., Mille, r. J. B., Oda, T., Tans, P., Andrews, A., J, M., Ott, L., Collatz, G. J., Aalto, T., et al.: CarbonTracker CT2019B, doi: 10.25925/20201008, 2020.

Jung, M., Henkel, K., Herold, M., and Churkina, G.: Exploiting Synergies of Global Land Cover Products for Carbon Cycle Modeling, Remote Sensing of Environment, 101, 534–553, doi: 10.1016/j.rse.2006.01.020, 2006.

Kaiser, J. W., Heil, A., Andreae, M. O., Benedetti, A., Chubarova, N., Jones, L., Morcrette, J.-J., Razinger, M., Schultz, M. G., Suttie, M., and van der Werf, G. R.: Biomass Burning Emissions Estimated with a Global Fire Assimilation System Based on Observed Fire Radiative Power, Biogeosciences (Online), 9, 527–554, doi: 10.5194/bg-9-527-2012, 2012.

Kaplan, J. O.: Wetlands at the Last Glacial Maximum: Distribution and Methane Emissions: WETLANDS AT THE LAST GLACIAL MAXIMUM, Geophysical Research Letters, 29, 3–1–3–4, doi: 10.1029/2001GL013366, 2002.

Keppel-Aleks, G., Wennberg, P. O., and Schneider, T.: Sources of Variations in Total Column Carbon Dioxide, Atmospheric Chemistry and Physics, 11, 3581–3593, doi: 10.5194/acp-11-3581-2011, 2011.

Kurokawa, J. and Ohara, T.: Long-Term Historical Trends in Air Pollutant Emissions in Asia: Regional Emission Inventory in ASia (REAS) Version 3, Atmospheric Chemistry and Physics, 20, 12 761–12 793, doi: 10.5194/acp-20-12761-2020, 2020.

Landschützer, P., Bushinsky, S., and Gray, A.: A Combined Globally Mapped CO2 Flux Estimate Based on the Surface Ocean CO2 Atlas Database (SOCAT) and Southern Ocean Carbon and Climate Observations and Modeling (SOCCOM) Biogeochemistry Floats from 1982 to 2017 (NCEI Accession 0191304). Version 2.2., doi: 10.25921/9hsn-xq82, 2019.

Langerock, B., De Mazière, M., Hendrick, F., Vigouroux, C., Desmet, F., Dils, B., and Niemeijer, S.: Description of Algorithms for Co-Locating and Comparing Gridded Model Data with Remote-Sensing Observations, Geoscientific Model Development, 8, 911–921, doi: 10.5194/gmd-8-911-2015, 2015.

Laughner, J. L., Toon, G. C., Mendonca, J., Petri, C., Roche, S., Wunch, D., Blavier, J.-F., Griffith, D. W. T., Heikkinen, P., Keeling, R. F., Kiel, M., Kivi, R., Roehl, C. M., Stephens, B. B., Baier, B. C., Chen, H., Choi, Y., Deutscher, N. M., DiGangi, J. P., Gross, J., Herkommer, B., Jeseck, P., Laemmel, T., Lan, X., McGee, E., McKain, K., Miller, J., Morino, I., Notholt, J., Ohyama, H., Pollard, D. F., Rettinger, M., Riris, H., Rousogenous, C., Sha, M. K., Shiomi, K., Strong, K., Sussmann, R., Té, Y., Velazco, V. A., Wofsy, S. C., Zhou, M., and Wennberg, P. O.: The Total Carbon Column Observing Network's GGG2020 Data Version, Earth System Science Data, 16, 2197–2260, doi: 10.5194/essd-16-2197-2024, 2024.

Levin, I., Karstens, U., Eritt, M., Maier, F., Arnold, S., Rzesanke, D., Hammer, S., Ramonet, M., Vítková, G., Conil, S., Heliasz, M., Kubistin, D., and Lindauer, M.: A Dedicated Flask Sampling Strategy Developed for Integrated Carbon Observation System (ICOS) Stations Based on CO_2 and CO Measurements and Stochastic Time-Inverted Lagrangian Transport (STILT) Footprint Modelling, Atmospheric Chemistry and Physics, 20, 11 161–11 180, doi: 10.5194/acp-20-11161-2020, 2020.

Li, M., Liu, H., Geng, G., Hong, C., Liu, F., Song, Y., Tong, D., Zheng, B., Cui, H., Man, H., Zhang, Q., and He, K.: Anthropogenic Emission Inventories in China: A Review, National Science Review, 4, 834–866, doi: 10.1093/nsr/nwx150, 2017.

Li, X., Hu, X.-M., Cai, C., Jia, Q., Zhang, Y., Liu, J., Xue, M., Xu, J., Wen, R., and Crowell, S. M. R.: Terrestrial CO2 Fluxes, Concentrations, Sources and Budget in Northeast China: Observational and Modeling Studies, Journal of Geophysical Research: Atmospheres, 125, e2019JD031 686, doi: 10.1029/2019JD031686, 2020.

Liu, Y., Yue, T., Zhang, L., Zhao, N., Zhao, M., and Liu, Y.: Simulation and Analysis of XCO2 in North China Based on High Accuracy Surface Modeling, Environmental Science and Pollution Research International, 25, 27 378–27 392, doi: 10.1007/s11356-018-2683-x, 2018.

Liu, Z., Guan, D., Wei, W., Davis, S. J., Ciais, P., Bai, J., Peng, S., Zhang, Q., Hubacek, K., Marland, G., Andres, R. J., Crawford-Brown, D., Lin, J., Zhao, H., Hong, C., Boden, T. A., Feng, K., Peters, G. P., Xi, F., Liu, J., Li, Y., Zhao, Y., Zeng, N., and He, K.: Reduced Carbon Emission Estimates from Fossil Fuel Combustion and Cement Production in China, Nature, 524, 335–338, doi: 10.1038/nature14677, 2015.

Maahn, M., Turner, D. D., Löhnert, U., Posselt, D. J., Ebell, K., Mace, G. G., and Comstock, J. M.: Optimal Estimation Retrievals and Their Uncertainties: What Every Atmospheric Scientist Should Know, Bulletin of the American Meteorological Society, 101, E1512–E1523, doi: 10.1175/BAMS-D-19-0027.1, 2020.

Mahadevan, P., Wofsy, S. C., Matross, D. M., Xiao, X., Dunn, A. L., Lin, J. C., Gerbig, C., Munger, J. W., Chow, V. Y., and Gottlieb, E. W.: A Satellite-Based Biosphere Parameterization for Net Ecosystem CO2 Exchange: Vegetation Photosynthesis and Respiration Model (VPRM), Global Biogeochemical Cycles, 22, doi: 10.1029/2006GB002735, 2008.

Martin, C. R., Zeng, N., Karion, A., Mueller, K., Ghosh, S., Lopez-Coto, I., Gurney, K., Oda, T., Prasad, K., Liu, Y., Dickerson, R., and Whetstone, J.: Investigating Sources of Variability and Error in Simulations of Carbon Dioxide in an Urban Region, Atmospheric Environment, 199, 55–69, doi: 10.1016/j.atmosenv.2018.11.013, 2019.

Masson-Delmotte, V., Zhai, P., Pirani, A., Connors, S. L., Péan, C., Berger, S., Caud, N., Chen, Y., Goldfarb, L., Gomis, M. I., Huang, M., Leitzell, K., Lonnoy, E., Matthews, J. B. R., Maycock, T. K., Waterfield, T., Yelekçi, O., Yu, R., and Zhou (eds.), a. B.: IPCC, 2021: Climate Change 2021: The Physical Science Basis. Contribution of Working Group I to the Sixth Assessment Report of the Intergovernmental Panel on Climate Change, Tech. rep., 2021.

Monforti-Ferrario, F., Oreggioni, G., Schaaf, E., Guizzardi, D., Olivier, J. G. J., Solazzo, E., Lo Vullo, E., Crippa, M., Muntean, M., Vignati, E., and Commission), J. R. C. E.: Fossil CO2 and GHG Emissions of All World Countries: 2019 Report, Publications Office of the European Union, LU, ISBN 978-92-76-11100-9, 2019.

Nassar, R.: Scaling Factors to Improve the Temporal and Spatial Distribution of CO2 Emissions from Global Fossil Fuel Emission Datasets, doi: 10.15485/1463822, 2013.

Nassar, R., Napier-Linton, L., Gurney, K. R., Andres, R. J., Oda, T., Vogel, F. R., and Deng, F.: Improving the Temporal and Spatial Distribution of CO2 Emissions from Global Fossil Fuel Emission Data Sets, Journal of Geophysical Research: Atmospheres, 118, 917–933, doi: 10.1029/2012JD018196, 2013.

Oda, T. and Maksyuto, S.: A Very High-Resolution (1 Km×1 Km) Global Fossil Fuel CO_2 Emission Inventory Derived Using a Point Source Database and Satellite Observations of Nighttime Lights, Atmospheric Chemistry and Physics, 11, 543–556, doi: 10.5194/acp-11-543-2011, 2011.

Oda, T. and Maksyuto, S.: ODIAC Fossil Fuel CO_2 Emissions Dataset (ODIAC2020b), Center for Global Environmental Research, National Institute for Environmental Studies, doi: 10.17595/20170411.001, 2020.

Oda, T., Maksyuto, S., and Andres, R. J.: The Open-source Data Inventory for Anthropogenic CO_2, Version 2016 (ODIAC2016): A Global Monthly Fossil Fuel CO_2 Gridded Emissions Data Product for Tracer Transport Simulations and Surface Flux Inversions, Earth System Science Data, 10, 87–107, doi: 10.5194/essd-10-87-2018, 2018.

Park, C., Gerbig, C., Newman, S., Ahmadov, R., Feng, S., Gurney, K. R., Carmichael, G. R., Park, S.-Y., Lee, H.-W., Goulden, M., Stutz, J., Peischl, J., and Ryerson, T.: CO2 Transport, Variability, and Budget over the Southern California Air Basin Using the High-Resolution WRF-VPRM Model during the CalNex 2010 Campaign, Journal of Applied Meteorology and Climatology, 57, 1337–1352, doi: 10.1175/JAMC-D-17-0358.1, 2018.

Pillai, D., Gerbig, C., Ahmadov, R., Rödenbeck, C., Kretschmer, R., Koch, T., Thompson, R., Neininger, B., and Lavrié, J. V.: High-Resolution Simulations of Atmospheric CO₂ over Complex Terrain – Representing the Ochsenkopf Mountain Tall Tower, Atmospheric Chemistry and Physics, 11, 7445–7464, doi: 10.5194/acp-11-7445-2011, 2011.

Pörtner, Roberts, D.C., Tignor, M., Poloczanska, E.S., Mintenbeck, K., Alegria, A., Craig, M., Langsdorf, S., Löschke, S., Möller, V., Okem, A., and Rama, B.: Climate Change 2022 – Impacts, Adaptation and Vulnerability: Working Group II Contribution to the Sixth Assessment Report of the Intergovernmental Panel on Climate Change, Cambridge University Press, 1 edn., ISBN 978-1-00-932584-4, doi: 10.1017/9781009325844, 2023.

Powers, J. G., Klemp, J. B., Skamarock, W. C., Davis, C. A., Dudhia, J., Gill, D. O., Coen, J. L., Gochis, D. J., Ahmadov, R., Peckham, S. E., Grell, G. A., Michalakes, J., Trahan, S., Benjamin, S. G., Alexander, C. R., Dimego, G. J., Wang, W., Schwartz, C. S., Romine, G. S., Liu, Z., Snyder, C., Chen, F., Barlage, M. J., Yu, W., and Duda, M. G.: The Weather Research and Forecasting Model: Overview, System Efforts, and Future Directions, doi: 10.1175/BAMS-D-15-00308.1, 2017.

Ramonet, M., Ciais, P., Apadula, F., Bartyzel, J., Bastos, A., Bergamaschi, P., Blanc, P. E., Brunner, D., Caracciolo di Torchiarolo, L., Calzolari, F., Chen, H., Chmura, L., Colomb, A., Conil, S., Cristofanelli, P., Cuevas, E., Curcoll, R., Delmotte, M., di Sarra, A., Emmenegger, L., Forster, G., Frumau, A., Gerbig, C., Gheusi, F., Hammer, S., Haszpra, L., Hatakka, J., Hazan, L., Heliasz, M., Henne, S., Hensen, A., Hermansen, O., Keronen, P., Kivi, R., Komínková, K., Kubistin, D., Laurent, O., Laurila, T., Lavric, J. V., Lehner, I., Lehtinen, K. E. J., Leskinen, A., Leuenberger, M., Levin, I., Lindauer, M., Lopez, M., Myhre, C. L., Mammarella, I., Manca, G., Manning, A., Marek, M. V., Marklund, P., Martin, D., Meinhardt, F., Mihalopoulos, N., Mölder, M., Morgui, J. A., Necki, J., O'Doherty, S., O'Dowd, C., Ottosson, M., Philippon, C., Piacentino, S., Pichon, J. M., Plass-Duelmer, C., Resovsky, A., Rivier, L., Rodó, X., Sha, M. K., Scheeren, H. A., Sferlazzo, D., Spain, T. G., Stanley, K. M., Steinbacher, M., Trisolino, P., Vermeulen, A., Vítková, G., Weyrauch, D., Xueref-Remy, I., Yala, K., and Yver Kwok, C.: The Fingerprint of the Summer 2018 Drought in Europe on Ground-Based Atmospheric CO2 Measurements, Philosophical Transactions of the Royal Society B: Biological Sciences, 375, 20190 513, doi: 10.1098/rstb.2019.0513, 2020.

Ramonet, M., Langerock, B., Warneke, T., and Eskes, H.: Validation Report of the CAMS Greenhouse Gas Global Reanalysis, Years 2003-2020, doi: 10.24380/438C-4597, 2021.

Ridgwell, A. J., Marshall, S. J., and Gregson, K.: Consumption of Atmospheric Methane by Soils: A Process-Based Model, Global Biogeochemical Cycles, 13, 59–70, doi: 10.1029/1998GB900004, 1999.

Rodgers, C. D.: Inverse Methods for Atmospheric Sounding: Theory and Practice, no. v. 2 in Series on Atmospheric, Oceanic and Planetary Physics, World Scientific, Singapore ; [River Edge, N.J.], ISBN 978-981-02-2740-1, oCLC: ocm45098450, 2000.

Rodgers, C. D. and Connor, B. J.: Intercomparison of Remote Sounding Instruments, Journal of Geophysical Research: Atmospheres, 108, n/a–n/a, doi: 10.1029/2002JD002299, 2003.

Sanderson, M. G.: Biomass of Termites and Their Emissions of Methane and Carbon Dioxide: A Global Database, Global Biogeochemical Cycles, 10, 543–557, doi: 10.1029/96GB01893, 1996.

Saunois, M., Martinez, A., Poulter, B., Zhang, Z., Raymond, P., Regnier, P., Canadell, J. G., Jackson, R. B., Patra, P. K., Bousquet, P., Ciais, P., Dlugokencky, E. J., Lan, X., Allen, G. H., Bastviken, D., Beerling, D. J., Belikov, D. A., Blake, D. R., Castaldi, S., Crippa, M., Deemer, B. R., Dennison, F., Etiope, G., Gedney, N., Höglund-Isaksson, L., Holgerson, M. A., Hopcroft, P. O., Hugelius, G., Ito, A., Jain, A. K., Janardanan, R., Johnson, M. S., Kleinen, T., Krummel, P., Lauerwald, R., Li, T., Liu, X., McDonald, K. C., Melton, J. R., Mühle, J., Müller, J., Murguia-Flores, F., Niwa, Y., Noce, S., Pan, S., Parker, R. J., Peng, C., Ramonet, M., Riley, W. J., Rocher-Ros, G., Rosentreter, J. A., Sasakawa, M., Segers, A., Smith, S. J., Stanley, E. H., Thanwerdas, J., Tian, H., Tsuruta, A., Tubiello, F. N., Weber, T. S., van der Werf, G., Worthy, D. E., Xi, Y., Yoshida, Y., Zhang, W., Zheng, B., Zhu, Q., Zhu, Q., and Zhuang, Q.: Global Methane Budget 2000–2020, Earth System Science Data Discussions, pp. 1–147, doi: 10.5194/essd-2024-115, 2024.

Schulzweida, U.: Climate Data Operators (CDO) User Guide, 2020/2023.

Soulie, A., Granier, C., Darras, S., Zilbermann, N., Doumbia, T., Guevara, M., Jalkanen, J.-P., Keita, S., Liousse, C., Crippa, M., Guizzardi, D., Hoesly, R., and Smith, S.: Global Anthropogenic Emissions (CAMS-GLOB-ANT) for the Copernicus Atmosphere Monitoring Service Simulations of Air Quality Forecasts and Reanalyses, Earth System Science Data Discussions, pp. 1–45, doi: 10.5194/essd-2023-306, 2023.

Vellalassery, A., Pillai, D., Marshall, J., Gerbig, C., Buchwitz, M., Schneising, O., and Ravi, A.: Using TROPOspheric Monitoring Instrument (TROPOMI) Measurements and Weather Research and Forecasting (WRF) CO Modelling to Understand the Contribution of Meteorology and Emissions to an Extreme Air Pollution Event in India, Atmospheric Chemistry and Physics, 21, 5393–5414, doi: 10.5194/acp-21-5393-2021, 2021.

Wang, R., Tao, S., Ciais, P., Shen, H. Z., Huang, Y., Chen, H., Shen, G. F., Wang, B., Li, W., Zhang, Y. Y., Lu, Y., Zhu, D., Chen, Y. C., Liu, X. P., Wang, W. T., Wang, X. L., Liu, W. X., Li, B. G., and Piao, S. L.: High-Resolution Mapping of Combustion Processes and Implications for CO_2 Emissions, Atmospheric Chemistry and Physics, 13, 5189–5203, doi: 10.5194/acp-13-5189-2013, 2013.

Wiedinmyer, C., Quayle, B., Geron, C., Belote, A., McKenzie, D., Zhang, X., O'Neill, S., and Wynne, K. K.: Estimating Emissions from Fires in North America for Air Quality Modeling, Atmospheric Environment, 40, 3419–3432, doi: 10.1016/j.atmosenv.2006.02.010, 2006.

Wiedinmyer, C., Akagi, S. K., Yokelson, R. J., Emmons, L. K., Al-Saadi, J. A., Orlando, J. J., and Soja, A. J.: The Fire INventory from NCAR (FINN): A High Resolution Global Model to Estimate the Emissions from Open Burning, Geoscientific Model Development, doi: 10.5194/gmd-4-625-2011, 2011.

Wiedinmyer, C., Kimura, Y., McDonald-Buller, E. C., Emmons, L. K., Buchholz, R. R., Tang, W., Seto, K., Joseph, M. B., Barsanti, K. C., Carlton, A. G., and Yokelson, R.: The Fire Inventory from NCAR Version 2.5: An Updated Global Fire Emissions Model for Climate and Chemistry Applications, Geoscientific Model Development, 16, 3873–3891, doi: 10.5194/gmd-16-3873-2023, 2023.

WMO: WMO Greenhouse Gas Bulletin, World Meteorological Organization, No. 19, 2023.

Wunch, D., Toon, G. C., Blavier, J.-F. L., Washenfelder, R. A., Notholt, J., Connor, B. J., Griffith, D. W. T., Sherlock, V., and Wennberg, P. O.: The Total Carbon Column Observing Network, Philosophical Transactions of the Royal Society A: Mathematical, Physical and Engineering Sciences, 369, 2087–2112, doi: 10.1098/rsta.2010.0240, 2011.

Xu, H., Xiao, J., and Zhang, Z.: Heatwave Effects on Gross Primary Production of Northern Mid-Latitude Ecosystems, Environmental Research Letters, 15, 074 027, doi: 10.1088/1748-9326/ab8760, 2020.

Yang, Y., Zhou, M., Langerock, B., Sha, M. K., Hermans, C., Wang, T., Ji, D., Vigouroux, C., Kumps, N., Wang, G., De Mazière, M., and Wang, P.: New Ground-Based Fourier-transform near-Infrared Solar Absorption Measurements of XCO_2, XCH_4 and XCO at Xianghe, China, Earth System Science Data, 12, 1679–1696, doi: 10.5194/essd-12-1679-2020, 2020.

Yang, Y., Zhou, M., Wang, T., Yao, B., Han, P., Ji, D., Zhou, W., Sun, Y., Wang, G., and Wang, P.: Spatial and Temporal Variations of CO_2 Mole Fractions Observed at Beijing, Xianghe, and Xinglong in North China, Atmospheric Chemistry and Physics, 21, 11 741–11 757, doi: 10.5194/acp-21-11741-2021, 2021.

Zhang, X., Zhou, C., Zhang, Y., Lu, X., Xiao, X., Wang, F., Song, J., Guo, Y., Leung, K. K. M., Cao, J., and Gao, M.: Where to Place Methane Monitoring Sites in China to Better Assist Carbon Management, npj Climate and Atmospheric Science, 6, 1–8, doi: 10.1038/s41612-023-00359-6, 2023.

Zhao, X., Marshall, J., Hachinger, S., Gerbig, C., Frey, M., Hase, F., and Chen, J.: Analysis of Total Column CO_2 and CH_4 Measurements in Berlin with WRF-GHG, Atmospheric Chemistry and Physics, 19, 11 279–11 302, doi: 10.5194/acp-19-11279-2019, 2019.

Zheng, B., Tong, D., Li, M., Liu, F., Hong, C., Geng, G., Li, H., Li, X., Peng, L., Qi, J., Yan, L., Zhang, Y., Zhao, H., Zheng, Y., He, K., and Zhang, Q.: Trends in China's Anthropogenic Emissions since 2010 as the Consequence of Clean Air Actions, Atmospheric Chemistry and Physics, 18, 14 095–14 111, doi: 10.5194/acp-18-14095-2018, 2018.

Zhong, Q., Huang, Y., Shen, H., Chen, Y., Chen, H., Huang, T., Zeng, E. Y., and Tao, S.: Global Estimates of Carbon Monoxide Emissions from 1960 to 2013, Environmental Science and Pollution Research, 24, 864–873, doi: 10.1007/s11356-016-7896-2, 2017.

Zhou, M., Langerock, B., Vigouroux, C., Sha, M. K., Ramonet, M., Delmotte, M., Mahieu, E., Bader, W., Hermans, C., Kumps, N., Metzger, J.-M., Duflot, V., Wang, Z., Palm, M., and De Mazière, M.: Atmospheric CO and CH_4 Time Series and Seasonal Variations on Reunion Island from Ground-Based in Situ and FTIR (NDACC and TCCON) Measurements, Atmospheric Chemistry and Physics, 18, 13 881–13 901, doi: 10.5194/acp-18-13881-2018, 2018.